



**NAVAL
POSTGRADUATE
SCHOOL**

MONTEREY, CALIFORNIA

DISSERTATION

**USE OF SYMMETRICAL NUMBER SYSTEMS IN
ELECTRONIC WARFARE**

by

Thomas W. Tedesso

December 2013

Dissertation Supervisor:

Phillip E. Pace

Approved for public release; distribution is unlimited

THIS PAGE INTENTIONALLY LEFT BLANK

REPORT DOCUMENTATION PAGE

Form Approved
OMB No. 0704-0188

The public reporting burden for this collection of information is estimated to average 1 hour per response, including the time for reviewing instructions, searching existing data sources, gathering and maintaining the data needed, and completing and reviewing the collection of information. Send comments regarding this burden estimate or any other aspect of this collection of information, including suggestions for reducing this burden to Department of Defense, Washington Headquarters Services, Directorate for Information Operations and Reports (0704-0188), 1215 Jefferson Davis Highway, Suite 1204, Arlington, VA 22202-4302. Respondents should be aware that notwithstanding any other provision of law, no person shall be subject to any penalty for failing to comply with a collection of information if it does not display a currently valid OMB control number. **PLEASE DO NOT RETURN YOUR FORM TO THE ABOVE ADDRESS.**

1. REPORT DATE (DD-MM-YYYY) 9-12-2013			2. REPORT TYPE Dissertation		3. DATES COVERED (From — To) 2010-09-01—2013-12-20	
4. TITLE AND SUBTITLE USE OF SYMMETRICAL NUMBER SYSTEMS IN ELECTRONIC WARFARE					5a. CONTRACT NUMBER	
					5b. GRANT NUMBER	
					5c. PROGRAM ELEMENT NUMBER	
6. AUTHOR(S) Thomas W. Tedesso					5d. PROJECT NUMBER	
					5e. TASK NUMBER	
					5f. WORK UNIT NUMBER	
7. PERFORMING ORGANIZATION NAME(S) AND ADDRESS(ES) Naval Postgraduate School Monterey, CA 93943					8. PERFORMING ORGANIZATION REPORT NUMBER	
9. SPONSORING / MONITORING AGENCY NAME(S) AND ADDRESS(ES) Department of the Navy					10. SPONSOR/MONITOR'S ACRONYM(S)	
					11. SPONSOR/MONITOR'S REPORT NUMBER(S)	
12. DISTRIBUTION / AVAILABILITY STATEMENT Approved for public release; distribution is unlimited						
13. SUPPLEMENTARY NOTES The views expressed in this dissertation are those of the author and do not reflect the official policy or position of the Department of Defense or the U.S. Government. IRB Protocol number: N/A						
14. ABSTRACT The use of symmetrical number systems and wideband technologies is investigated to develop novel concepts for use in electronic warfare (EW) receivers. A computationally efficient algorithm for determining the dynamic range of the robust symmetrical number system (RSNS) is used to derive additional closed-form expressions for the RSNS dynamic range, using a curve-fitting method. A photonic direction-finding array employing dual-electrode Mach-Zehnder modulators with RSNS preprocessing is developed and validated through simulations and experimental testing. Additional EW receiver concepts using the symmetrical number system (SNS) and CS are also examined. An SNS-CS cueing receiver is proposed that places a multichannel undersampling receiver, based on the SNS, into a CS framework and applies CS recovery algorithms to resolve the signal's frequency components. The SNS-CS cueing receiver's performance is evaluated through Monte Carlo simulations. The final concept examined is a multichannel Nyquist folding receiver (NYFR) with SNS-based uniform sampling rates (NYFR-B). The NYFR-B's performance is evaluated through Monte Carlo simulations and performance curves are presented.						
15. SUBJECT TERMS Symmetrical Number Systems, Robust Symmetrical Number System, Compressive Sensing, Photonics, Mach-Zehnder Modulator, Direction Finding Array, Electronic Warfare						
16. SECURITY CLASSIFICATION OF:			17. LIMITATION OF ABSTRACT UU	18. NUMBER OF PAGES 229	19a. NAME OF RESPONSIBLE PERSON	
a. REPORT Unclassified	b. ABSTRACT Unclassified	c. THIS PAGE Unclassified			19b. TELEPHONE NUMBER (include area code)	

THIS PAGE INTENTIONALLY LEFT BLANK

Approved for public release; distribution is unlimited

USE OF SYMMETRICAL NUMBER SYSTEMS IN ELECTRONIC WARFARE

Thomas W. Tedesso
Commander, United States Navy
B.S.E.E., Illinois Institute of Technology, 1990
M.S.E.E., Naval Postgraduate School, 1998

Submitted in partial fulfillment of the
requirements for the degree of

DOCTOR OF PHILOSOPHY IN ELECTRICAL ENGINEERING
from the

NAVAL POSTGRADUATE SCHOOL
December 2013

Author: Thomas W. Tedesso

Approved by: Phillip E. Pace
Professor of Electrical and
Computer Engineering
Dissertation Committee Chair

Frank E. Kragh
Associate Professor of Electrical
and Computer Engineering

Monique P. Fargues
Professor of Electrical and
Computer Engineering

Ric A. Romero
Assistant Professor of Electrical
and Computer Engineering

James H. Newman
Professor of Space Systems

Approved by: R. Clark Robertson
Chair, Department of Electrical and Computer Engineering

Approved by: Douglas Moses, Vice Provost for Academic Affairs

THIS PAGE INTENTIONALLY LEFT BLANK

ABSTRACT

The use of symmetrical number systems and wideband technologies is investigated to develop novel concepts for use in electronic warfare (EW) receivers. A computationally efficient algorithm for determining the dynamic range of the robust symmetrical number system (RSNS) is used to derive additional closed-form expressions for the RSNS dynamic range, using a curve-fitting method. A photonic direction-finding array employing dual-electrode Mac-Zehnder modulators with RSNS preprocessing is developed and validated through simulations and experimental testing. Additional EW receiver concepts using the symmetrical number system (SNS) and CS are also examined. An SNS-CS cueing receiver is proposed that places a multichannel undersampling receiver, based on the SNS, into a CS framework and applies CS recovery algorithms to resolve the signal's frequency components. The SNS-CS cueing receiver's performance is evaluated through Monte Carlo simulations. The final concept examined is a multichannel Nyquist folding receiver (NYFR) with SNS-based uniform sampling rates (NYFR-B). The NYFR-B's performance is evaluated through Monte Carlo simulations and performance curves are presented.

THIS PAGE INTENTIONALLY LEFT BLANK

Table of Contents

1	Introduction	1
1.1	Primary Contributions	3
1.2	Dissertation Outline	5
2	Compressive Sensing	7
2.1	Compressive Sensing Theory	7
2.2	Compressive Sensing Electronic Warfare Receivers	14
3	Symmetrical Number Systems	39
3.1	Symmetrical Number System	39
3.2	The Relationship Between the Symmetrical Number System and the Discrete Fourier Transform	41
3.3	Optimum Symmetrical Number System	42
3.4	Robust Symmetrical Number System	43
3.5	Robust Symmetrical Number System N-Sequence Ambiguity Analysis	46
4	Determining Additional Closed-Form Expressions for the Dynamic Range of the Robust Symmetrical Number System	53
4.1	Efficient Algorithm for Determining the Dynamic Range of the Robust Symmetrical Number System	53
4.2	Efficient Algorithm Complexity Analysis	63
4.3	Additional Closed-Form Expressions for the Dynamic Range of the Robust Symmetrical Number System	65
4.4	Concluding Remarks	91

5 Photonic Direction Finding Array with Robust Symmetrical Number System Preprocessing	93
5.1 Use of a Dual Electrode Mach Zehnder Modulator in Phase Interferometry . . .	95
5.2 Photonic Implementation of a Robust Symmetrical Number System-based Direction Finding Array	105
5.3 Simulation Results for Photonic Direction Finding Array with Robust Symmetrical Number System Preprocessing	111
5.4 Experimental Results.	119
5.5 Simulation of Multiple Pulsed Signals	126
5.6 Concluding Remarks	133
6 Symmetrical Number System - Compressive Sensing Cueing Receiver	135
6.1 Symmetrical Number System - Compressive Sensing Cueing Receiver Concept and Theoretical Development	136
6.2 Monte Carlo Simulations	141
6.3 Concluding Remarks	149
7 Symmetrical Number System - Nyquist Folding Receiver	155
7.1 Symmetrical Number System - Nyquist Folding Receiver (NYFR-B) Concept . .	155
7.2 Detection of Multiple Signals Using the Symmetrical Number System	159
7.3 Symmetrical Number System - Nyquist Folding Receiver (NYFR-B) Detection and Frequency Resolution Using an Envelope Approximation Detector with Greatest of Constant False Alarm Rate Processing	160
7.4 Simulation Results.	165
7.5 Concluding Remarks	168
8 Concluding Remarks	171
List of References	175
Initial Distribution List	185

List of Figures

Figure 1.1	Air defense weapons	2
Figure 2.1	Pictorial depiction of sparsity.	8
Figure 2.2	Pictorial representation of the combined sampling and compressing steps.	9
Figure 2.3	Geometric representation of ℓ_p norm minimization.	12
Figure 2.4	Random demodulator block diagram.	15
Figure 2.5	Random filter implementations.	18
Figure 2.6	Random sampling architecture.	19
Figure 2.7	Random analog-to-digital converter implementations.	20
Figure 2.8	Compressive multiplexer block diagram.	21
Figure 2.9	Modulated wideband converter block diagram.	23
Figure 2.10	Modulate wideband converter—relation between the signal frequency spectrum $Z(f)$ and the vector $x(f)$	24
Figure 2.11	Block diagram of nonlinear affine signal processing receiver.	25
Figure 2.12	Nonlinear affine processing encoder.	26
Figure 2.13	Non-linear affine processing encoding/decoding process.	27
Figure 2.14	Nyquist analog-to-information folding receiver block diagram.	28
Figure 2.15	Nyquist folding receiver compressive sensing model.	30
Figure 2.16	Nyquist folding receiver detection methods.	32
Figure 2.17	Nyquist folding receiver - modulation scale factor.	33

Figure 2.18	Time encoding machine block diagram.	34
Figure 2.19	Time encoding machine receiver architecture.	34
Figure 2.20	Time encoding machine implementations.	36
Figure 3.1	Graphical representation of a symmetrical number system for moduli $m_i = \{3, 4\}$	40
Figure 3.2	Graphical depiction of a three-sequence robust symmetrical number system for moduli $m_i = \{3, 4, 5\}$	45
Figure 3.3	Graphical representation of the single sequence ambiguity types for a robust symmetrical number system ($N=3, m=5$).	46
Figure 4.1	Comparison of efficient and naïve algorithm run time.	65
Figure 4.2	Curve fitting results for the dynamic range of the robust symmetrical number system \hat{M}_{RSNS} when $m_i = \{m-1, m+1, m+3\}$ where $m \equiv 0 \pmod{4}$	67
Figure 4.3	Curve fitting results for the dynamic range of the robust symmetrical number system \hat{M}_{RSNS} when $m_i = \{m-1, m+1, m+3\}$ and $m \equiv 2 \pmod{4}$	69
Figure 4.4	Curve fitting results for the dynamic range of the robust symmetrical number system \hat{M}_{RSNS} when $m_i = \{m, m+1, m+3\}$ where $m \equiv 2 \pmod{4}$ and $m \geq 14$	71
Figure 4.5	Curve fitting results for the dynamic range of the robust symmetrical number system \hat{M}_{RSNS} when $m_i = \{m-3, m-1, m\}$ where $m \not\equiv 0 \pmod{6}$ and m is even.	72
Figure 4.6	Curve fitting results for the dynamic range of the robust symmetrical number system \hat{M}_{RSNS} when $m_i = \{m, m+4, m+8\}$ where $m \equiv 1 \pmod{8}$ and $m \geq 7$	74
Figure 4.7	Curve fitting results for the dynamic range of the robust symmetrical number system \hat{M}_{RSNS} when $m_i = \{m, m+4, m+8\}$ where $m \equiv 3 \pmod{8}$ and $m \geq 7$	75
Figure 4.8	Curve fitting results for the dynamic range of the robust symmetrical number system \hat{M}_{RSNS} when $m_i = \{m, m+4, m+8\}$ where $m \equiv 5 \pmod{8}$ and $m \geq 7$	76

Figure 4.9	Curve fitting results for the dynamic range of the robust symmetrical number system \hat{M}_{RSNS} when the moduli $m_i = \{m, m+4, m+8\}$ where $m \equiv 7 \pmod{8}$ and $m \geq 7$	77
Figure 4.10	Curve fitting results plotted against algorithm results for the dynamic range of the robust symmetrical number system \hat{M}_{RSNS} when the moduli $m_i = \{m-1, m, m+2, m+4\}$ where $m \equiv 3 \pmod{6}$ or $m \equiv 5 \pmod{6}$ and $m \geq 15$	79
Figure 4.11	Curve fitting results plotted against algorithm results for the dynamic range of the robust symmetrical number system \hat{M}_{RSNS} when the moduli $m_i = \{m, m+1, m+2, m+4\}$ where $m \equiv 1 \pmod{6}$ or $m \equiv 3 \pmod{6}$ and $m \geq 15$	81
Figure 4.12	Curve fitting results plotted against algorithm results for the dynamic range of the robust symmetrical number system \hat{M}_{RSNS} when the moduli $m_i = \{m, m+2, m+3, m+4\}$ where $m = \{25 + 12k, 29 + 12k, 31\}$ where $k = 0, 1, 2, \dots$	83
Figure 4.13	Curve fitting results plotted against algorithm results for the dynamic range of the robust symmetrical number system \hat{M}_{RSNS} when the moduli $m_i = \{m, m+2, m+3, m+4\}$ where $m = \{25 + 12k, 29 + 12k, 31\}$ where $k = 0, 1, 2, \dots$	85
Figure 4.14	Curve fitting results plotted against algorithm results for the dynamic range of the robust symmetrical number system \hat{M}_{RSNS} when the moduli $m_i = \{m, m+2, m+4, m+5\}$ where with m is odd, $m \geq 39$, and $\gcd(m, 5) = 1$	88
Figure 4.15	Curve fitting results plotted against algorithm results for \hat{M}_{RSNS} when the moduli $m_i = \{m, m+2, m+4, m+6\}$ where with m is odd, $m \geq 13$, and $\gcd(m, 3) = 1$	89
Figure 4.16	Curve fitting results and algorithm results for \hat{M} when the moduli $m_i = \{m, m+2, m+3, m+4, m+6\}$ when $m = 109 + 72k$ and $m = 133 + 72k$ and $k = 0, 1, 2, \dots$	92
Figure 5.1	Block diagram of a two-element photonic direction finding linear array.	96
Figure 5.2	Dual electrode Mach-Zehnder modulator in phase interferometry - theoretical and simulation results for the normalized output versus the direction of arrival.	100

Figure 5.3	Dual electrode Mach-Zehnder modulator output and photo detector output for a direction of arrival of 90 deg	101
Figure 5.4	Block diagram of experimental setup for testing of a dual electrode Mach-Zehnder modulator in phase interferometry application.	101
Figure 5.5	Experimental results for two element photonic direction finding array (bench test).	102
Figure 5.6	Dual electrode Mach-Zehnder modulator (DE-MZM) normalized transmission coefficient versus phase angle when DE-MZM is biased at minimum transmission point.	104
Figure 5.7	Block diagram of the photonic direction finding antenna array using a robust symmetrical number system preprocessing.	105
Figure 5.8	Robust symmetrical number system residues versus direction of arrival, θ deg.	106
Figure 5.9	Photonic direction finding array - alignment of linear array folding waveforms with the robust symmetrical number system's folding waveforms.	108
Figure 5.10	Comparison of folding waveforms for different signal frequencies.	109
Figure 5.11	Effect of signal frequency on the transfer function of a photonic direction finding array with robust symmetrical number system preprocessing.	110
Figure 5.12	Simulation results for photonic direction finding array with robust symmetrical number system preprocessing using ideal components.	113
Figure 5.13	Estimated direction of arrival θ_{est} deg versus direction of arrival θ deg using ideal components.	114
Figure 5.14	Simulation using non-ideal components and $SNR = 30$ dB: (a) normalized envelope detector output voltages, (b) residues versus direction of arrival, theoretical data is the blue solid line, the simulated data is the red dashed line.	115
Figure 5.15	Transfer function of photonic direction finding array with robust symmetrical number system for $SNR=30$ dB.	116
Figure 5.16	Simulation results for nonideal components and $SNR = 20$ dB, (a) normalized envelope detector output, (b) residues versus direction of arrival. Blue solid line represents the theoretical values, and the red dashed line represents the simulation results.	117

Figure 5.17	Transfer function of photonic direction finding array with robust symmetrical number system preprocessing for $SNR = 20\text{dB}$. Blue solid line is theoretical transfer function, red dashed line represents the simulation results.	118
Figure 5.18	Block diagram of equipment setup for bench testing.	119
Figure 5.19	Block diagrams for support circuits used in experimental bench test. . .	120
Figure 5.20	Phase Shifter transfer functions, (a) ψ_7 , (b) ψ_8 and (c) ψ_9	121
Figure 5.21	Theoretical residues versus experimental residues.	123
Figure 5.22	Theoretical direction finding array transfer function versus experimental results is displayed in (a). (b) and (c) display details of (a).	124
Figure 5.23	Experimental results - error between estimated direction of arrival and the actual direction of arrival $\theta_{est} - \theta$	125
Figure 5.24	Simulation flow chart for multiple emitter direction of arrival determination.	128
Figure 5.25	Multiple pulsed signals example 1—input signal.	129
Figure 5.26	Multiple pulsed signals example 1—spectrogram and periodogram. . . .	129
Figure 5.27	Multiple pulsed signal example 1—direction of arrival versus time. . . .	130
Figure 5.28	Multiple pulsed signals example 2—input signal.	131
Figure 5.29	Multiple pulsed signals example 2—spectrogram and periodogram. . . .	131
Figure 5.30	Multiple pulsed signals example 2—direction of arrival versus time. . . .	132
Figure 5.31	Multiple pulsed signals example 3—input signal.	132
Figure 5.32	Multiple pulsed signals example 3—spectrogram and periodogram. . . .	133
Figure 5.33	Multiple pulsed signals example 3—direction of arrival versus time. . . .	133
Figure 6.1	Block diagram of a symmetrical number system—compressive sensing cueing receiver.	137
Figure 6.2	Example of symmetrical number system based undersampling.	140
Figure 6.3	Symmetrical number system—compressive sensing cueing receiver performance for $m_i = \{21, 22, 23\}$ and $SNR = 30\text{ dB}$	142

Figure 6.4	Symmetrical number system–compressive sensing cueing receiver performance for $m_i = \{21, 22, 23\}$ and $SNR = 20$ dB.	142
Figure 6.5	Symmetrical number system–compressive sensing cueing receiver performance for $m_i = \{21, 22, 23\}$ and $SNR = 10$ dB.	143
Figure 6.6	Symmetrical number system–compressive sensing cueing receiver performance $m_i = \{21, 22, 23, 25\}$ and $SNR = 30$ dB	144
Figure 6.7	Symmetrical number system–compressive sensing cueing receiver performance for $m_i = \{21, 22, 23, 25\}$ and a $SNR = 20$ dB.	144
Figure 6.8	Symmetrical number system–compressive sensing cueing receiver performance for $m_i = \{21, 22, 23, 25\}$ and $SNR = 10$ dB.	145
Figure 6.9	Symmetrical number system–compressive sensing cueing receiver performance for $m_i = \{21, 22, 23, 25, 29\}$ and $SNR = 30$ dB.	146
Figure 6.10	Symmetrical number system–compressive sensing cueing receiver performance for $m_i = \{21, 22, 23, 25, 29\}$ and $SNR = 20$ dB.	146
Figure 6.11	Symmetrical number system–compressive sensing cueing receiver performance for $m_i = \{21, 22, 23, 25, 29\}$, and $SNR = 10$ dB.	147
Figure 6.12	Symmetrical number system–compressive sensing cueing receiver performance: (a) $N = 1024$ and $f_{max} = 64$, (b) $N = 2048$ and $f_{max} = 128$	147
Figure 6.13	Probability of detection for a symmetrical number system–compressive sensing cueing receiver with $m_i = \{21, 22, 23, 25, 29\}$ and $N = 2048$	151
Figure 6.14	Probability of detection for a symmetrical number system–compressive sensing cueing receiver with $m_i = \{21, 22, 23, 25\}$ and $N = 2048$	152
Figure 6.15	Probability of detection for symmetrical number system–compressive sensing cueing receiver with $m_i = \{21, 22, 23\}$ and $N = 2048$	153
Figure 7.1	L -channel symmetrical number system undersampling receiver.	156
Figure 7.2	Symmetrical number system-based Nyquist folding receiver	157
Figure 7.3	Comparison of the symmetrical residues resulting from a symmetrical number system (SNS) undersampling receiver and a SNS - Nyquist Folding Receiver (NYFR-B) architecture.	159
Figure 7.4	Greatest of constant false alarm rate processing.	162

Figure 7.5	Four channel NYFR-B: one transmitted tone, (a) probability of detection, (b) probability of a missed detection.	166
Figure 7.6	Four channel NYFR-B: two transmitted tones, (a) probability of detection, (b) probability of a missed detection.	166
Figure 7.7	Six channel NYFR-B: one transmitted tone, (a) probability of detection, (b) probability of a missed detection.	166
Figure 7.8	Six channel NYFR-B: two transmitted tones, (a) probability of detection, (b) probability of a missed detection.	167
Figure 7.9	Six channel NYFR-B: three transmitted tones, (a) probability of detection, (b) probability of a missed detection.	167
Figure 7.10	Comparison of 4 and 6 channel NYFR-B	168

THIS PAGE INTENTIONALLY LEFT BLANK

List of Tables

Table 2.1	Analytical expressions for the required number of samples for the sensing matrix to satisfy the restricted isometry property based on the measurement matrix distribution.	14
Table 2.2	Modulation Scale Factor for various Nyquist Zones	31
Table 2.3	Comparison of compressive sensing receivers.	37
Table 3.1	Symmetrical number system for moduli, $m_i = \{3, 4\}$	40
Table 3.2	Optimum symmetrical number system with moduli, $m_i = \{3, 4\}$ and dynamic range, $M = 12$	43
Table 3.3	Three sequence robust symmetrical number system structure for moduli $m_i = \{3, 4, 5\}$	44
Table 3.4	Single sequence of a three-sequence robust symmetrical number system illustrating the decomposition into subsequences.	47
Table 3.5	Parity (e = even, o = odd) of residue vectors.	47
Table 3.6	N-sequence robust symmetrical number system summary of congruence equation solutions for ambiguity locations.	49
Table 4.1	Comparison of the dynamic range for a three-sequence robust symmetrical number system to that of a three-sequence residue number system.	57
Table 4.2	Calculation of ambiguity locations for all ambiguity cases for a three sequence robust symmetrical number system with moduli $m_i = \{3, 4, 5\}$ and $a \in \mathbb{Z}$	61
Table 4.3	Robust symmetrical number system efficient search algorithm example - determination of all consecutive minimal pairs for $N = 3$ and $m_i = \{3, 4, 5\}$	62

Table 4.4	Sample of data used in curve fitting for a three sequential odd coprime moduli, $m \equiv 0 \pmod{4}$	67
Table 4.5	Sample of data used in curve fitting for sequential odd coprime moduli, with $m \equiv 2 \pmod{4}$	68
Table 4.6	Sample of data used in curve fitting for sequential coprime moduli of form, $\{m, m+1, m+3\}$, with $m \equiv 2 \pmod{4}$ and $m \geq 14$	70
Table 4.7	Sample of data used in curve fitting for sequential coprime moduli of form, $\{m-3, m-1, m\}$, with $m \not\equiv 0 \pmod{6}$	72
Table 4.8	Sample of data used in curve fitting for sequential coprime moduli of form, $\{m, m+4, m+8\}$, with m odd and $m \geq 7$	73
Table 4.9	New closed-form expressions for three sequence robust symmetrical number system (RSNS) dynamic range.	78
Table 4.10	Sample of data used in curve fitting for sequential coprime moduli of form, $\{m, m+1, m+2, m+4\}$, with $m \equiv 3 \pmod{6}$ or $m \equiv 5 \pmod{6}$ and $m \geq 15$	79
Table 4.11	Sample of data used in curve fitting for sequential coprime moduli of form, $\{m, m+1, m+2, m+4\}$, with $m \equiv 1 \pmod{6}$ or $m \equiv 3 \pmod{6}$ and $m \geq 15$	80
Table 4.12	Sample of data used in curve fitting for sequential coprime moduli of form, $\{m, m+1, m+2, m+4\}$, with $m \equiv 1 \pmod{6}$ or $m \equiv 3 \pmod{6}$ and $m \geq 15$	82
Table 4.13	Sample of data used in curve fitting for sequential coprime moduli of form, $\{m, m+2, m+4, m+5\}$, with m odd, $m \geq 39$, and $\gcd(m, 5) = 1$	87
Table 4.14	Sample of data used in curve fitting for sequential coprime moduli odd moduli of form, $m_i = \{m, m+2, m+4, m+6\}$, with m odd, $m \geq 13$, and $\gcd(m, 3) = 1$	89
Table 4.15	New closed-form expressions for the dynamic range of four-sequence robust symmetrical number systems.	90
Table 5.1	Required phase shifts to match folding wave forms to robust symmetrical number system's waveforms for $m_i = \{7, 8, 9\}$	107
Table 5.2	Multiple pulsed emitters—example 1: signal parameters.	127

Table 5.3	Multiple pulsed emitters—example 2: signal parameters.	130
Table 5.4	Multiple pulsed emitters—example 3: signal parameters.	131
Table 6.1	Number of sinusoids that can be detected with a probability of detection $P_D \geq 0.9$ with $N = 1024$, $f_{max} = 32$ Hz.	145
Table 6.2	Number of sinusoids that can be detected with a probability of detection $P_D \geq 0.9$ with $N = 1024$, $f_{max} = 64$ Hz.	146
Table 6.3	Comparison of performance of the symmetrical number system—compressive sensing cueing receiver and a Chinese remainder theorem-based algorithm.	148
Table 6.4	Number of sinusoids that can be detected with a probability of detection $P_D \geq 0.9$ with $N = 2048$, $f_{max} = 128$ Hz.	148
Table 6.5	Number of sinusoids that can be detected with probability of detection $P_D \geq 0.9$ with $N = 2048$, $f_{max} = 64$ Hz.	149

THIS PAGE INTENTIONALLY LEFT BLANK

List of Acronyms and Abbreviations

AD	Air defense
AC	Alternating current
ADC	Analog-to-digital converter
AWGN	Additive white Gaussian noise
BCR	Block coordinate relaxation
BP	Basis pursuit
BW	Bandwidth
CDMA	Code division multiple access
CFAR	Constant false alarm rate
CMUX	Compressive multiplexer
CoSaMP	Compressive sampling matching pursuit
COA	Centers of ambiguity
CRD	Constrained random demodulator
CRT	Chinese remainder theorem
CS	Compressive sensing
CW	Continuous wave
DAC	Digital-to-analog converter
DC	Direct current
DF	Direction finding
DFB	Distributed feedback
DE-MZM	Dual electrode Mach-Zehnder modulator
DFT	Discrete Fourier transform
DOA	Direction-of-arrival
DSP	Digital signal processing

DTFT	Discrete time Fourier transform
EA	Electronic attack
EAD	Envelope approximation detector
EMI	Electromagnetic interference
ES	Electronic support
ESPRIT	Estimation of signal parameters via rotational invariance techniques
EW	Electronic warfare
FPGA	Field programmable logic device
FIR	Finite impulse response
FFT	Fast Fourier transform
FOV	Field of view
GP	Gradient pursuit
GO-CFAR	Greatest of constant false alarm rate
HP	Hewlett Packard
IDFT	Inverse discrete Fourier transform
IID	Independent identically distributed
IFT	Inverse Fourier transform
IFFT	Inverse fast Fourier transform
LASSO	Least absolute shrinkage and selection operator
LTI	Linear time invariant
LNA	Low noise amplifier
LPF	Low pass filter
MP	Matching pursuit
ML	Maximum likelihood
MW	Microwave

MWC	Modulated wideband converter
MUSIC	Multiple signal classification
MZM	Mach-Zehnder modulator
NLEQ	Nonlinear equalization
NoLAff	Nonlinear affine processing
NYFR	Nyquist analog-to-information folding receiver
OSNS	Optimum symmetrical number system
OMP	Orthogonal matching pursuit
PD	Photodetector
pdf	Probability density function
PFA	Probability of false alarm
PRF	Pulse repetition frequency
PW	Pulse width
QMFB	Quadrature mirror filter bank
RADC	Random sampling analog-to-digital converter
RF	Radio frequency
RD	Random demodulator
RIP	Restricted isometry property
RLL	Run-length limited
RNS	Residue number system
RSNS	Robust symmetrical number system
SOI	Signal of interest
SNR	Signal-to-noise ratio
SNS	Symmetrical number system
SNS-CS	Symmetrical number system - compressive sensing

SpaRSA	Sparse reconstruction by separable approximation
StRIP	Statistical restricted isometry property
TEM	Time encoding machine
TOA	Time-of-arrival
VNA	Vector network analyzer

Executive Summary

Threat weapon system sensors and missile seekers continue to evolve by adopting wide bandwidth low-probability-of-intercept signals and by migrating to the millimeter wavelength band as missile seekers adopt imaging radar technology to discriminate between targets and decoys. As a result, electronic warfare (EW) receivers are required to monitor an increasingly wide bandwidth, stressing the capabilities of existing EW receivers. To reduce analog hardware requirements and eliminate the inter-modulation products that result from down converting microwave (MW) signals, digital receiver trends have been towards direct digitization. However, the bandwidth (BW) and resolution of current analog-to-digital converter (ADC) technology [1]–[4] limits the ability to directly digitize MW signals. Wideband technologies have been adopted in EW receivers including photonics, compressive sensing (CS), and the use of symmetrical number systems to address the limitations of ADC technology.

In MW photonics, the Mach-Zehnder modulator (MZM) using $LiNbO_3$ technology plays a significant role in modern direction finding (DF) and digital receiver architectures. Several applications of the MZM in DF arrays are presented in the literature. In [5], the MZM is used in a wideband fiber-optic DF application as an optical down conversion circuit at the antenna. Another photonic approach is used to measure the direction-of-arrival (DOA) for a MW signal by cascading two MZMs as discussed in [6]. Similarly, CS has been introduced to combine sampling and compression into a single operation to allow the recovery of sparse high-dimensional signals from incomplete measurements through the use of efficient algorithms [7]. Wideband receivers suitable for EW applications using CS techniques have been introduced in literature. The majority of the CS receivers introduce randomness into the sampling process to provide theoretical assurances that the recovery algorithm will accurately recover the sparse signal. Examples of these receivers include: a random demodulator [8], random filtering [9], random sampling [10], and a compressive multiplexer [11]. Other CS receiver architectures take advantage of the structure of the signal space such as the modulated wideband converter [12], [13], Nyquist folding receiver (NYFR) [14]–[16], and nonlinear affine signal processing [17].

Other methods explored to resolve frequency aliasing involve the use of multi-channel under-sampling with coprime sampling rates. Symmetrical number systems based on a set of coprime moduli were developed to extract information from symmetrical folding waveforms that appear frequently in nature. Symmetrical number systems include the symmetrical number system (SNS) that was demonstrated to have the same structure as the discrete Fourier transform (DFT) for real signals [18], [19] and the robust symmetrical number system (RSNS) that has an inherent integer Gray code property allowing error detection and correction [20]–[23]. Both the SNS and RSNS have found many applications including DF arrays, undersampling receivers, and ADCs.

In this work, several wideband EW receiver concepts are developed that combine the use of symmetrical number systems with photonics and CS. The first concept investigates a four-

element photonic DF array with RSNS preprocessing using dual electrode MZMs (DE-MZMs) in an phase interferometry application. This concept is developed theoretically and verified through simulation and experimental testing. Closed-form analytical expressions for the dynamic range of the RSNS \hat{M}_{RSNS} are also developed for several families of coprime moduli sets through the application of a computationally efficient search algorithm. Two EW receiver concepts are also examined that use the SNS in CS receiver architectures. The first concept applies CS theory and recovery algorithms to a multi-channel undersampling receiver based on the SNS in a cueing receiver application. The SNS is also applied to a multi-channel NYFR architecture allowing determination of the SNS residues via a fast Fourier transform (FFT) and resolving frequency ambiguities through the properties of the SNS and the NYFR.

Background

Compressive Sensing

Compressive sensing is a new area of digital signal processing that allows sampling a signal that is sparse in some orthonormal basis at a rate much lower than the Nyquist sampling rate and enables the successful recovery of the signal via convex optimization algorithms or greedy algorithms. Compressive sensing can be viewed as combining sampling and compression into one operation and can be mathematically expressed as

$$\mathbf{y} = \mathbf{A}\mathbf{x}, \quad (1)$$

where the measurement vector \mathbf{y} is an $L \times 1$ vector, \mathbf{x} is the $N \times 1$ signal vector which is sparse, and \mathbf{A} is an $L \times N$ sensing matrix [24]. The sensing matrix \mathbf{A} is

$$\mathbf{A} = \Phi\Psi \quad (2)$$

where Ψ is $N \times N$ orthonormal basis matrix and Φ is the $L \times N$ measurement basis matrix.

In order to recover \mathbf{x} , \mathbf{A} must satisfy the restricted isometry principle (RIP) which is equivalent to the matrices Φ and Ψ being incoherent. It was proven that sensing matrices based on Gaussian or Bernoulli distributions satisfy RIP and can recover an S -sparse signal \mathbf{x} provided [24]

$$L \geq CS \ln(N/S). \quad (3)$$

It was also demonstrated that if sensing matrices are formed by randomly selecting the rows of an unitary DFT matrix that RIP is statistically satisfied if [25]

$$L > S \ln N. \quad (4)$$

Symmetrical Number Systems

The SNS is a modular number system that consists of N separate periodic symmetrically folded sequences based on a set of coprime moduli $m_i = \{m_1, m_2, \dots, m_N\}$. Each SNS sequence is periodic and consists of a row vector of the symmetrical residues defining the sequence,

$$\mathbf{b}_m = \begin{cases} [0, 1, \dots, \lfloor \frac{m}{2} \rfloor, \lfloor \frac{m}{2} \rfloor, \dots, 2, 1], & m \text{ is odd} \\ [0, 1, \dots, \frac{m}{2}, \frac{m}{2} - 1, \dots, 2, 1], & m \text{ is even} \end{cases} \quad (5)$$

where $\lfloor \bullet \rfloor$ is the floor operator [18]. Each integer h is represented by a vector $\mathbf{B}_h = [b_h^1, b_h^2, \dots, b_h^N]^T$ composed of the N symmetrical residues for that integer. The symmetrical residues for a SNS with $m_i = \{3, 4\}$, are listed in Table 1. The ambiguous results are annotated in Table 1 using bold font. The span of integer values where each vector, \mathbf{B}_h , uniquely defines an integer is the dynamic range of the SNS \hat{M}_{SNS} which is defined in [18].

Table 1: Symmetrical Number System for $m_i = \{3, 4\}$.

q	0	1	2	3	4	5	6	...
$m_i = 3$	0	1	1	0	1	1	0	...
$m_i = 4$	0	1	2	1	0	1	2	...
	$\leftarrow \hat{M}_{SNS} \rightarrow$							

The property of the SNS that makes it powerful in resolving single frequency ambiguities resulting from aliasing due to undersampling is the direct mapping of the symmetrical residues of the SNS into the DFT digital frequencies for real signals. This property is demonstrated in an undersampling receiver architecture in [18].

Another powerful symmetrical number system is the RSNS. The RSNS is a modular-based number system consisting of $N \geq 2$ integer sequences with each sequence associated with a coprime modulus. The RSNS is based on the following sequence:

$$\{x'_m\} = [0, 1, 2, \dots, m-1, m, m-1, \dots, 2, 1]. \quad (6)$$

To form the N -sequence RSNS, each term in Equation (6) is repeated N times in succession. Therefore, the integers within one folding period of a sequence are:

$$\{x_m\} = [0, \dots, 0, 1, 1, \dots, 1, \dots, m-1, \dots, m-1, m, \dots, m, m-1, \dots, m-1, \dots, 1, \dots, 1]. \quad (7)$$

This results in a periodic sequence with a period of $P_m = 2Nm$ [21], [26]. Each sequence corresponding to m_i is also shifted left (or right) by $s_i = i-1$ where $i \in \{1, 2, \dots, N\}$ and the shift values, $s_i = \{s_1, s_2, \dots, s_N\}$, form a complete residue system modulo N . The resulting structure of the N sequences ensures that two successive RSNS vectors when considered together, differ by only one integer resulting in an integer Gray code property [21].

Each RSNS sequence is extended periodically with period, $2Nm$, as $x_{h+n2Nm} = x_h$, where $n \in \{0, \pm 1, \pm 2, \dots\}$. Therefore, x_h is a symmetrical residue of $(h+n2Nm)$ modulo $2Nm$. An integer h is represented by a vector, $X_h = [x_{1,h}, x_{2,h}, \dots, x_{N,h}]^T$, of N paired integers from each sequence at h . An example of a left shifted $N = 3$ RSNS with $m_i = \{3, 4, 5\}$ is displayed in Table 2.

Closed-form expressions for the dynamic range of the RSNS \hat{M}_{RSNS} exists for only few specific cases. In [20], [21], a closed-form expression for two-sequence RSNSs is reported. The other published closed-form expression for \hat{M}_{RSNS} is for three-sequence RSNSs when $m_i = \{m-1, m, m+1\}$ with m even and $m > 3$ [21], [27].

Table 2: Three-sequence RSNS structure for $m_i = \{3, 4, 5\}$, after [21]

h	0	1	2	3	4	5	6	7	8	9	10	11	12	13	14	15	16...
$m_1 = 3$	0	0	0	1	1	1	2	2	2	3	3	3	2	2	2	1	1...
X_h $m_2 = 4$	0	0	1	1	1	2	2	2	3	3	3	4	4	4	3	3	3...
$m_3 = 5$	0	1	1	1	2	2	2	3	3	3	4	4	4	5	5	5	4...

Closed-Form Expressions for \hat{M}_{RSNS}

A computationally efficient search algorithm for determining \hat{M}_{RSNS} is presented, and its computational complexity is derived and compared to that of a naïve search algorithm. The complexity of the efficient algorithm is shown to be independent of the moduli values. Additional closed-form expressions were derived by generating data sets for different families of coprime moduli through use of the efficient algorithm. The data was curve fitted to determine closed-form analytical expressions for \hat{M}_{RSNS} , and the resulting analytical expressions were verified to satisfy the theoretical solutions to the congruence equations defining the ambiguity locations for the beginning and ending points of the sequence defining \hat{M}_{RSNS} .

The additional closed-form expressions for \hat{M}_{RSNS} for three-sequence RSNSs are summarized in Table 3. Also, closed-form expressions were developed and verified for four-sequence RSNSs that are summarized in Table 4. Future research in this area includes developing additional specific closed-form expressions for \hat{M}_{RSNS} with the aim of developing a general closed-form expression for an arbitrary set of N coprime moduli.

 Table 3: New closed-form expressions for \hat{M}_{RSNS} for three-sequence RSNSs, from [28].

m_i	\hat{M}_{RSNS}	m
$\{m-1, m+1, m+3\}$	$\frac{3}{2}m^2 + \frac{15}{2}m + 7$	$m \equiv 0 \pmod{4}$
	$\frac{3}{2}m^2 + \frac{15}{2}m + 5$	$m \equiv 2 \pmod{4}$
$\{m, m+1, m+3\}$	$\frac{3}{2}m^2 + \frac{27}{2}m + 6$	$m \equiv 2 \pmod{4}$ and $m \geq 14$
$\{m-3, m+1, m\}$	$\frac{3}{2}m^2 + \frac{3}{2}m$	m is even and $m \neq 6k$ where $k = 1, 2, \dots$
$\{m, m+4, m+8\}$	$\frac{9}{4}m^2 + \frac{63}{4}m + 48$	$m \equiv 1 \pmod{8}$
	$\frac{3}{2}m^2 + \frac{33}{2}m + 35$	$m \equiv 3 \pmod{8}$
	$\frac{3}{2}m^2 + \frac{33}{2}m + 34$	$m \equiv 5 \pmod{8}$
	$\frac{9}{4}m^2 + \frac{57}{4}m + 45$	$m \equiv 7 \pmod{8}$

Table 4: Closed-form expressions for \hat{M}_{RSNS} for four-sequence RSNSs, from [28].

m_i	\hat{M}_{RSNS}	m
$\{m-1, m, m+2, m+4\}$	$10m^2 + 6m + 20$	$m \equiv 3 \pmod{6}$ or $m \equiv 5 \pmod{6}$ with $m \geq 15$ and $m \neq \{29, 33\}$
$\{m, m+1, m+2, m+4\}$	$10m^2 + 22m + 20$	$m \equiv 1 \pmod{6}$ or $m \equiv 3 \pmod{6}$ and $m \geq 15$
$\{m, m+2, m+3, m+4\}$	$10m^2 + 30m - 6$ $10m^2 + 30m - 8$	$m = \{25 + 12k, 29 + 12k, 31\}$ where $k = 0, 1, 2, \dots$, $m = \{43 + 12k, 47 + 12k\}$ and $k = 0, 1, 2, \dots$
$\{m, m+2, m+4, m+5\}$	$10m^2 + 54m + 20$	$m \geq 39$, $\gcd(m, 5) = 1$, and m is odd
$\{m, m+2, m+4, m+6\}$	$10m^2 + 38m + 56$	$m \geq 13$ and $\gcd(m, 3) = 1$

Photonic Direction Finding Array with RSNS Preprocessing

For the two-element photonic DF linear array shown in Figure 1, the DOA of a MW emitter is determined by detecting the phase difference between the narrow band signals received at a reference antenna element and a measurement antenna element separated by a distance d . The phase angle ψ between the signals arriving at the two antennas is related to the DOA θ by

$$\psi = \frac{2\pi}{\lambda} d \sin \theta, \quad (8)$$

where λ is the wavelength of the incident MW signal. The normalized value of V_{out} can be approximated as

$$\frac{V_{out}}{\max(V_{out})} \approx |\sin(\psi/2)| \quad (9)$$

and can be used to determine the DOA, provided the input signal magnitude $V \ll V_\pi$ where V_π is the half-wave switching voltage of the dual electrode DE-MZM. This theoretical result was verified through simulation results that are presented in Figure 2. Equation (9) is used to design and test a four-element photonic DF array with RSNS preprocessing. Simulations and experimental testing were conducted to validate the concept.

The theoretical transfer function of the array and the experimental results are shown in Figure 3. Invalid RSNS codes resulted for $\theta = \{-24.6, -10.4, -10.2, -7.8, 7.6, 15.2, 60\}$ and were set to 0 deg. Note that the use of the RSNS preprocessing quantizes the DOA and that the angular resolution of the DOA bins is reduced as the DOA moves from broadside. The error between the estimated DOA and the actual DOA is plotted in Figure 4 along with the envelope of the theoretical maximum error signal. The results demonstrate that the DE-MZM can be used in phase interferometry applications and the viability of a wideband photonic DF array using

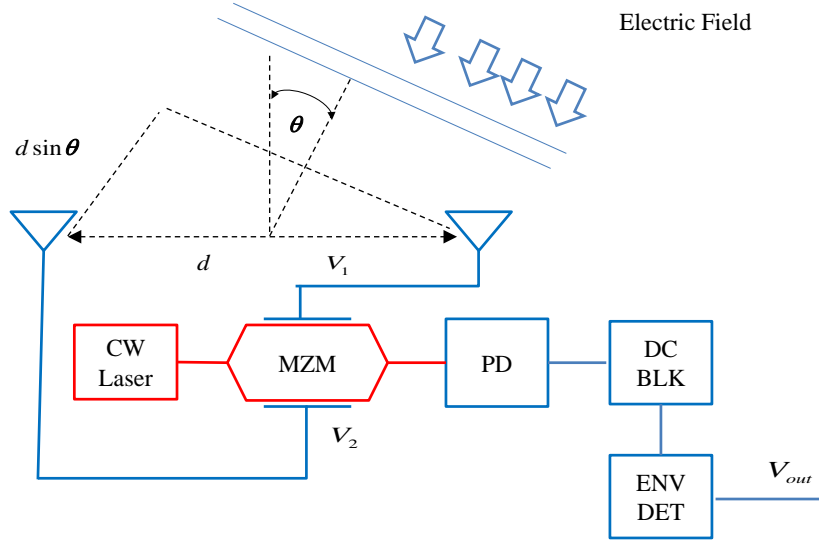


Figure 1: Block diagram of a two-element photonic DF linear array. Abbreviations used in diagram , photo detector (PD), DC blocking capacitor (DC BLK), envelope detector (ENV DET), continuous wave (CW).

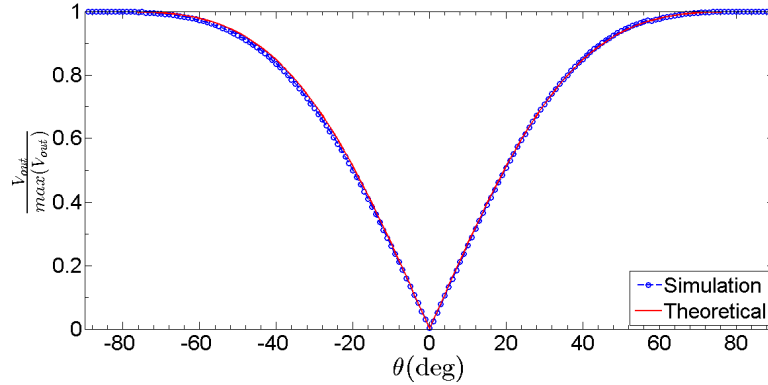


Figure 2: Normalized transmission coefficient vs. phase angle for DE-MZM biased at quadrature point, $V_b = V_\pi/2$. Red solid line graphs the theoretical results, the blue dashed line plots the simulation results.

RSNS preprocessing. Additional research is required to mature this concept including implementation and testing of the array using wideband components and integration with a wideband EW receiver.

SNS - CS Cueing Receiver

A novel SNS-CS cueing receiver architecture is presented that allows signal frequency identification in a sparse signal environment. The SNS-CS cueing receiver forms a measurement vector \mathbf{y} by collating the samples obtained through coprime undersampling with sampling rates

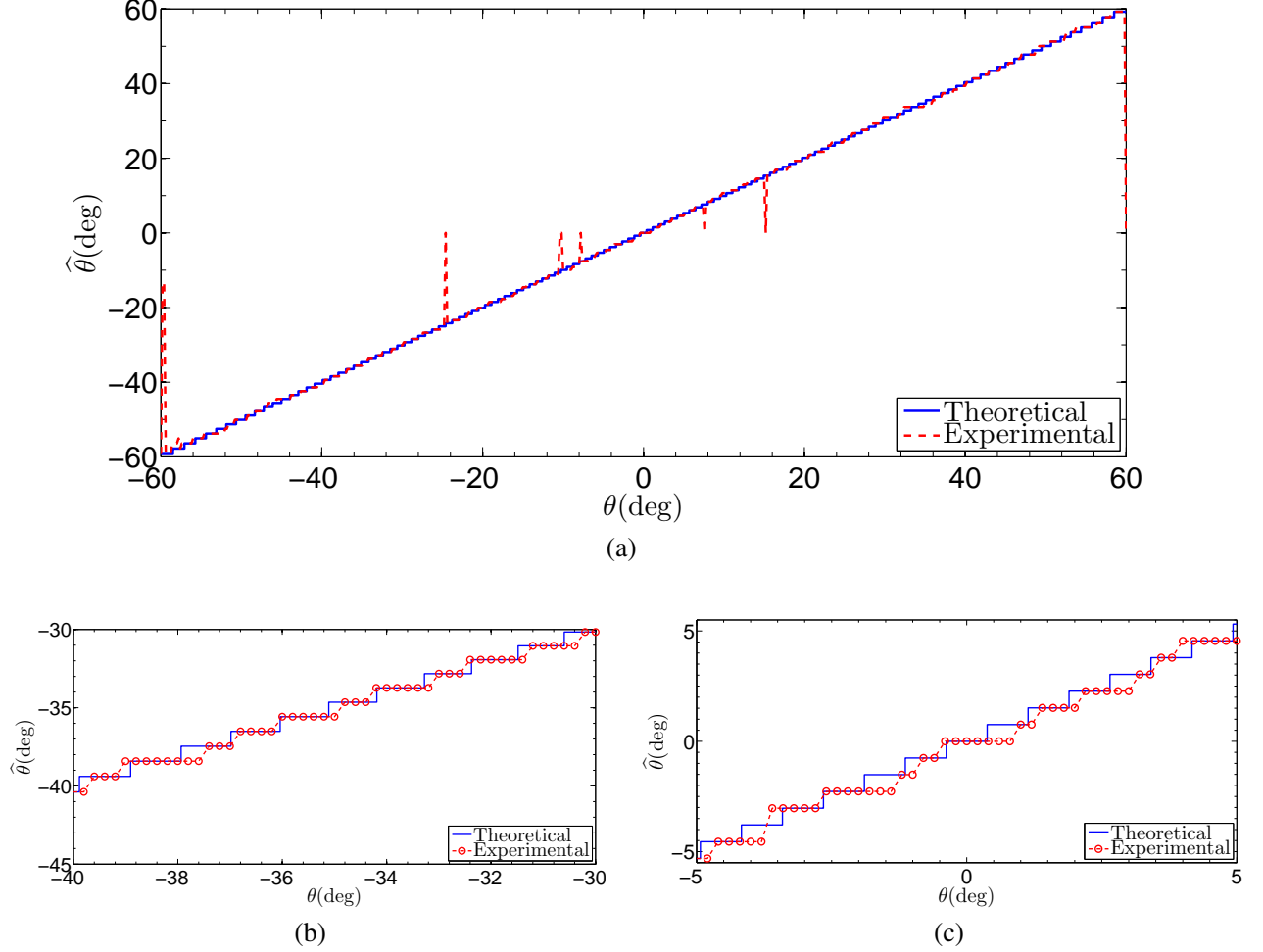


Figure 3: Theoretical DF array transfer function v.s. experimental results is displayed in (a), (b) and (c) display details of (a).

equal to the SNS moduli m_i . The SNS-CS cueing receiver also forms a deterministic partial inverse DFT (IDFT) sensing matrix \mathbf{A} based on the receiver's sampling rates, and applies CS recovery algorithms to estimate the frequency spectrum \mathbf{X} . The SNS-CS cueing receiver's performance is examined through Monte Carlo simulations and are compared to the performance achieved when a random sensing matrix is used in the CS recovery algorithm. The performance of the SNS-CS cueing receiver is shown to be comparable to that of a random sensing CS receiver architectures in identifying the frequencies of sinusoids in a sparse signal environment and is consistent with the theoretical predictions of [25]. The SNS-CS cueing receiver is also demonstrated to allow the identification of an increased number of sinusoids than the Chinese Remainder Theorem (CRT)-based algorithm described in [29] and the algorithm in [18] for a fixed number of coprime sampling rates. The results are summarized for three separate SNS-CS cueing receiver architectures in Table 5 and is compared to that of a CRT-based algorithm in Table 6.

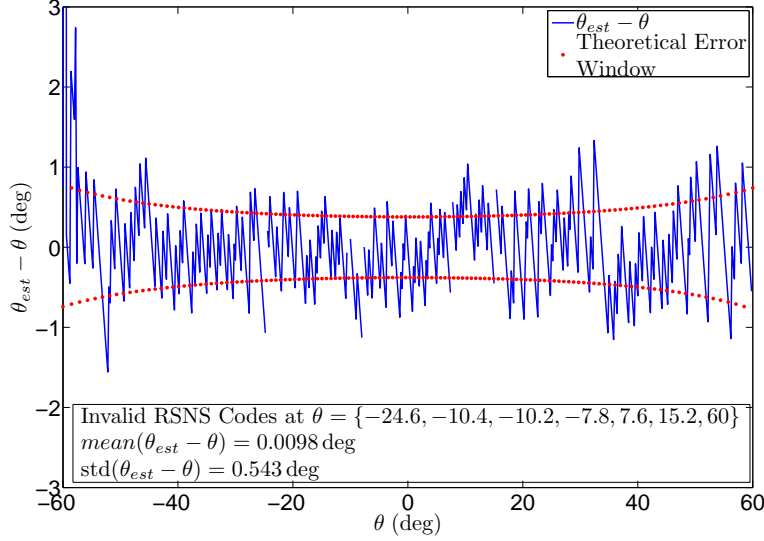


Figure 4: Experimental Results - $\theta_{est} - \theta$. Experimental data are represented by the solid blue line, theoretical error envelope represented by red dots.

Table 5: Number of sinusoids that can be detected with $P_D \geq 0.9$ with $N = 2048$, $f_{max} = 128$ Hz.

m_i	SNR			From Equation (4)
	30 dB	20 dB	10 dB	
$\{21, 22, 23\}$	3	3	2	4
$\{21, 22, 23, 25\}$	5	5	3	5
$\{21, 22, 23, 25, 29\}$	7	7	4	7

Table 6: Comparison of the maximum number of sinusoids that are able to be detected by the SNS-CS cueing receiver to the performance of the CRT based algorithm of [29].

m_i	SNS-CS Cueing Receiver		CRT Algorithm of [29]			
	Frequencies	f_{max}	Frequencies	f_{max}	Frequencies	f_{max}
$\{21, 22, 23\}$	3	128	3	23		
$\{21, 22, 23, 25\}$	5	128	4	25	2	462
$\{21, 22, 23, 25, 29\}$	7	128	5	29	2	462

Symmetrical Number System - Folding Receiver (NYFR-B)

A multi-channel NYFR architecture (shown in Figure 5) with uniform coprime sampling (NYFR-B) is proposed as an alternate architecture to a single channel NYFR architecture using a non-uniform sampling. The NYFR-B architecture uses uniform sampling based on coprime moduli

and resolves the signal's frequency using the properties of the SNS and the folding receiver. The relationship between the frequency spectrum obtained using an SNS-based undersampling receiver and that obtained using the NYFR-B architecture is examined. It is demonstrated that the NYFR-B architecture and the SNS undersampling receiver architecture produce frequency spectra for each channel where the signal's energy is concentrated in the identical positive digital frequency bin k representing the same baseband frequency for both receiver architectures. This fact allows the use of a constant radix FFT for all channels allowing faster computations and signal processing compared to that of a multi-channel undersampling receiver architecture using different radix DFTs. An envelope approximation detector (EAD) with greatest of constant false alarm rate (GO-CFAR) processing [30] is adapted to estimate the magnitude spectrum and detect the peak values. The use of GO-CFAR processing provides an adaptive detection threshold to compensate for either a colored noise spectra, band limited barrage noise jamming, or a noise distribution that is not wide sense stationary. The use of the SNS to resolve multiple frequencies is also examined and the conditions for unambiguous frequency identification are presented. The receiver's performance is shown in Figure 6.

Concluding remarks

In this work, wideband EW receiver concepts were examined that couple the use of symmetrical number systems and wideband technologies such as CS and MW photonics. Also, closed-form expressions for \hat{M}_{RSNS} were generated for several families of moduli sets for three sequence and four sequence RSNSs. The new closed-form expressions were verified to satisfy the solutions to the congruence equations defining the ambiguity locations [21]. Closed-form expressions for

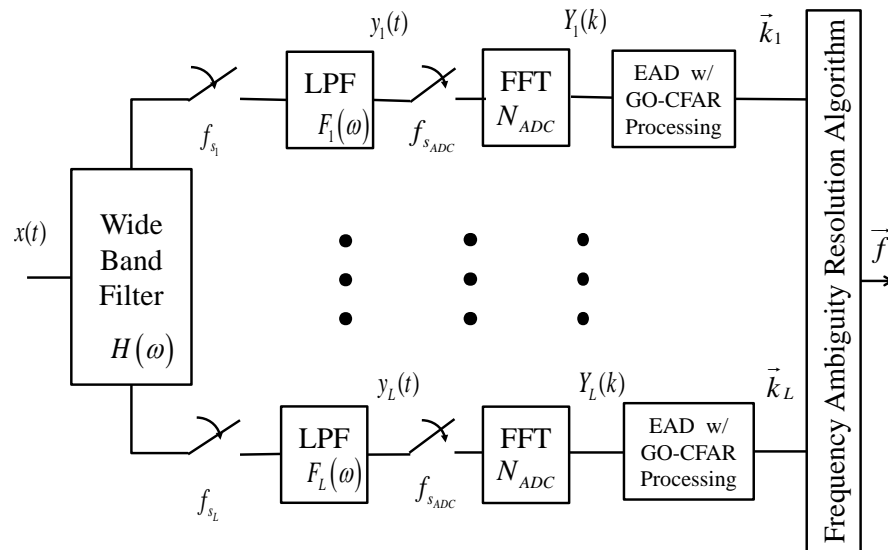


Figure 5: NYFR-B block diagram.

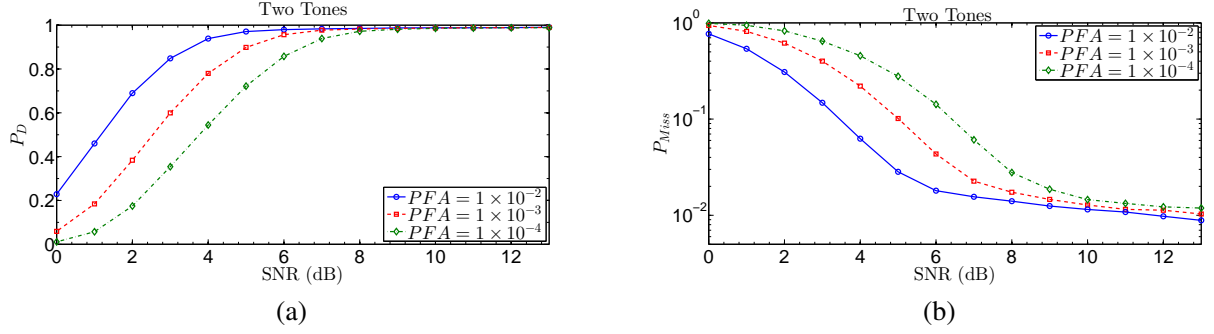


Figure 6: Four channel NYFR-B: two transmitted tones, (a) probability of detection, (b) probability of a missed detection. Monte Carlo simulations conducted: 1×10^5 .

four additional moduli families for a three-sequence RSNSs were developed. Also, closed-form expressions for five different families of moduli sets for four-sequence RSNSs were developed and presented. These expressions are the only closed-form expressions for \hat{M}_{RSNS} that have been developed for four-sequence RSNSs. Future work in this area includes identifying additional specific closed-form expressions for \hat{M}_{RSNS} for different families of moduli sets focused upon identifying a general closed-form expression for the \hat{M}_{RSNS} for a general set of N coprime moduli.

A photonic DF array with RSNS preprocessing was also examined. It was demonstrated theoretically and verified through simulations and experimentation that a DE-MZM can be used to perform phase interferometry. Using DE-MZMs, a linear four-element photonic DF antenna array with RSNS preprocessing was designed and its performance was examined through simulations and experimental testing. It was demonstrated that the photonic DF array provided accurate DOA estimation with fine DOA resolution while maintaining a small array size. The simulations and experimental testing were performed for a narrow band CW signal at 2.4 GHz. The results successfully demonstrate the concept of a photonic DF array with RSNS preprocessing, which warrants future investigation and development for use in EW receiver systems. Future work to further develop and mature this concept include anechoic chamber testing using narrow band components, modification of the circuit to use wideband components followed by bench testing and anechoic chamber testing. Experimental testing with multiple pulsed emitters is also required. Also, integration of the photonic DF array with RSNS preprocessing with a wide band CS receiver such as the NYFR and further development of pulse sorting signal processing algorithms provide additional avenues for future research.

The use of the SNS was examined in CS receivers to take advantage of the relationship between the SNS and the DFT [18]. A SNS-CS cueing receiver was investigated. The performance of the SNS-CS cueing receiver was examined through Monte Carlo simulations, and the results were compared to those obtained when a random orthonormal sensing matrix was used. The results demonstrated that the SNS-CS cueing receiver was capable of accurately resolving the number of frequencies predicted by CS theory and was comparable to that of random sensing

techniques. Future work includes determining the SNS-CS cueing receiver's performance when using greedy recovery algorithms and hardware implementation.

A multi-channel NYFR architecture using deterministic coprime sampling based on the moduli of a SNS was examined. The use of a NYFR architecture enabled use of a common radix FFT to calculate the residues in each channel instead of different radix DFTs in each channel. The constant sampling rates in also allowed for a simpler implementation of the sampling process when compared to the conventional NYFR architecture that uses a modulated RF sampling clock. Due to the possibility that permutations of the residues could represent more than one valid SNS code, the full dynamic range of the SNS could not be exercised and a smaller dynamic range was used based on applying the results from [29] to the SNS. Monte Carlo simulations were conducted and performance curves were presented for a four-channel and six-channel NYFR-B receiver architecture. Future research in this area includes examining methods that can be employed to allow taking advantage of the entire bandwidth provided by the \hat{M}_{SNS} of all moduli used. By doing so, the number of channels required to identify multiple signals can be reduced significantly. One potential method is to apply a modulation to one of the channels of the NYFR to isolate the Nyquist zone in which each sinusoid resides to allow resolution of each signal's frequency and eliminate permutations of the symmetrical residues that correspond to frequencies outside of the identified Nyquist zone. Simulations and hardware testing can also be accomplished to further develop this CS receiver concept.

THIS PAGE INTENTIONALLY LEFT BLANK

List of References

- [1] R. H. Walden, “Analog-to-digital converter survey and analysis,” *IEEE J. Sel. Areas Commun.*, vol. 17, pp. 539–550, Apr. 1999.
- [2] —, “Performance trends for analog to digital converters,” *IEEE Commun. Mag.*, vol. 37, pp. 96–101, Feb. 1999.
- [3] B. Murmann, “A/D converter trends: Power dissipation, scaling and digitally assisted architectures,” *Proc. IEEE Custom Integrated Circuits Conf.*, pp. 105–112, 2008.
- [4] B. Jonsson, “A survey of A/D-converter performance evolution,” *Proc. 17th IEEE Int. Conf. Electronics, Circuits, and Systems (ICECS ’10)*, pp. 766–769, Dec. 2010.
- [5] P. D. Biernacki, R. Madara, L. T. Nichols, A. Ward, and P. J. Mathews, “A four channel angle of arrival detector using optical downconversion,” *IEEE MTT-S Int. Microwave Symp. Dig.*, vol. 3, pp. 885–888, 1999.
- [6] X. Zou, W. Li, W. Pan, B. Luo, L. Yan, and J. Yao, “Photonic approach to the measurement of time-difference-of-arrival and angle-of-arrival of a microwave signal,” *Opt. Lett.*, vol. 37, pp. 755–757, Feb. 2012.
- [7] Y. C. Eldar and E. G. Kutyniok, *Compressed Sensing: Theory and Applications*. New York: Cambridge University Press, 2012.
- [8] J. A. Tropp, J. N. Laska, M. F. Duarte, J. K. Romberg, and R. G. Baraniuk, “Beyond nyquist: Efficient sampling of sparse bandlimited signals,” *IEEE Trans. Inf. Theory*, vol. 56, pp. 520–544, Jan. 2010.
- [9] J. A. Tropp, M. B. Wakin, M. F. Duarte, D. Baron, and R. G. Baraniuk, “Random filters for compressive sampling and reconstruction,” *Proc. IEEE Int. Conf. on Acoustics, Speech and Signal Processing*, vol. 3, pp. 872–875, 2006.
- [10] J. Laska, S. Kirolos, Y. Massoud, R. Baraniuk, A. Gilbert, M. Iwen, and M. Strauss, “Random sampling for analog-to-information conversion of wideband signals,” *IEEE Dallas/CAS Workshop on Design, Application, Integration and Software (DCAS ’06)*, pp. 119–122, Oct. 2006.
- [11] J. P. Slavinsky, J. N. Laska, M. A. Davenport, and R. G. Baraniuk, “The compressive multiplexer for multi-channel compressive sensing,” *Proc. IEEE Int. Conf. Acoustics, Speech and Signal Processing*, pp. 3980–3983, 2011.
- [12] M. Mishali, Y. C. Eldar, O. Dounaevsky, and E. Shoshan, “Xampling: Analog to digital at sub-nyquist rates,” *IET Circuits, Devices & Syst.*, vol. 5, no. 1, pp. 8–20, 2011.

- [13] M. Mishali and Y. C. Eldar, "From theory to practice: Sub-nyquist sampling of sparse wideband analog signals," *IEEE J. Sel. Topics Signal Process.*, vol. 4, pp. 375–391, Apr. 2010.
- [14] G. L. Fudge, R. E. Bland, M. A. Chivers, S. Ravindran, J. Haupt, and P. E. Pace, "A Nyquist folding analog-to-information receiver," *Conf. Rec. 42nd Asilomar Conf. on Signals, Systems and Computers*, pp. 541–545, 2008.
- [15] R. Maleh, G. L. Fudge, F. A. Boyle, and P. E. Pace, "Analog-to-information and the Nyquist folding receiver," *IEEE J. Emerging Select. Topics Circuits Syst.*, vol. 2, pp. 564–578, Sep. 2012.
- [16] P. E. Pace, A. Kusmanoff, and G. L. Fudge, "Nyquist folding analog-to-information receiver: Autonomous information recovery using quadrature mirror filtering," *Conf. Rec. 43rd Asilomar Conf. Signals, Systems. and Computers*, pp. 1581–1585, 2009.
- [17] K. W. Forsythe, J. I. Goodman, M. R. Green, B. A. Miller, G. M. Raz, and J. H. Jackson, MIT Lincoln Laboratory, Tech. Rep. PR-A21- 1, Oct. 2007.
- [18] P. E. Pace, R. E. Leino, and D. Styer, "Use of the symmetrical number system in resolving single-frequency undersampling aliases," *IEEE Trans. Signal Process.*, vol. 45, pp. 1153–1160, May 1997.
- [19] P. E. Pace and D. D. Styer, "High-resolution encoding process for an integrated optical analog-to-digital converter," *Opt. Eng.*, vol. 33, pp. 2638–2645, Aug. 1994. [Online]. Available: <http://dx.doi.org/10.1117/12.173559>
- [20] D. Styer and P. E. Pace, "Two-channel RSNS dynamic range," *IEEE Trans. Circuits Syst. I*, vol. 49, pp. 395–397, Mar. 2002.
- [21] B. L. Luke and P. E. Pace, "N-sequence RSNS ambiguity analysis," *IEEE Trans. Inf. Theory*, vol. 53, pp. 1759–1766, May 2007.
- [22] —, "N-sequence RSNS redundancy analysis," *Proc. IEEE Int. Symp. Information Theory*, pp. 2744–2748, 2006.
- [23] —, "Computation of the robust symmetrical number system dynamic range," *Proc. IEEE Information Theory Workshop*, pp. 1–5, 2010.
- [24] E. J. Candes and M. B. Wakin, "An introduction to compressive sampling," *IEEE Signal Processing Mag.*, vol. 25, pp. 21–30, Mar. 2008.
- [25] R. Calderbank, S. Howard, and S. Jafarpour, "Construction of a large class of deterministic sensing matrices that satisfy a statistical isometry property," *IEEE J. Sel. Topics Signal Process.*, vol. 4, pp. 358–374, Apr. 2010.

- [26] M. R. Arvizo, J. Calusdian, K. B. Hollinger, and P. E. Pace, "Robust symmetrical number system preprocessing for minimizing encoding errors in photonic analog-to-digital converters," *Optical Engineering*, vol. 50, pp. 084 602–1–084 602–11, Aug. 2011.
- [27] P. E. Pace, D. Wickersham, D. C. Jenn, and N. S. York, "High-resolution phase sampled interferometry using symmetrical number systems," *IEEE Trans. Antennas Propag.*, vol. 49, pp. 1411–1423, Oct. 2001.
- [28] P. E. Pace, P. Stănică, B. L. Luke, and T. W. Tedesso, "Extended closed-form expressions for the robust symmetrical number system dynamic range and an efficient algorithm for its computation," *IEEE Trans. Inf. Theory*, accepted for publication.
- [29] X.-G. Xia, "On estimation of multiple frequencies in undersampled complex valued waveforms," *IEEE Trans. Signal Process.*, vol. 47, pp. 3417–3419, Dec. 1999.
- [30] P. E. Pace and L. L. Taylor, "False alarm analysis of the envelope detection GO-CFAR processor," *IEEE Trans. Aerosp. Electron. Syst.*, vol. 30, pp. 848–864, Jul. 1994.

THIS PAGE INTENTIONALLY LEFT BLANK

Acknowledgements

I would like to thank my advisor, Professor Phillip E. Pace for his guidance and support in completing my doctoral research and dissertation. I would also like to thank the members of my Dissertation Committee, Professor Monique Fargues, Professor Frank Kragh, Professor Ric Romero, and Professor James Newman, for their assistance during my research and their thoughtful and insightful comments during the various committee meetings. Additionally, I would like to thank Dr. Gerald Fudge of L-3 Communications Integrated Systems, Mission Integration Division, who taught a course on compressive sensing electronic warfare receivers at Naval Postgraduate School and sparked my interest in the topic. I also would like to thank Professor Pantelimon Stănică and CAPT Brian L. Luke, USN, for their assistance in the work on the Robust Symmetrical Number System. Also, I wish to recognize Dr. James Calusdian and LCDR(ret) Bob Broadston, USN, who provided me with invaluable assistance during the experimental testing portions of my research. Additionally, I am grateful to Dr. David Garren for his support in obtaining the hardware components required for the experimental testing conducted in this work.

I would like to thank my wife, Keiko, for her unwavering support throughout my Naval career, culminating in my selection as a permanent military professor at the United States Naval Academy. Without her sacrifice and support during my many years of arduous sea duty, I would not have achieved the many successes in my career. I also would like to acknowledge my parents, Frank and Joan Tedesso, who provided me with the tools required to succeed in life, both personally and professionally.

Also, I would like to acknowledge the many great leaders and role models whom I have served with during my Naval career and the faculty and staff at the Naval Postgraduate School (NPS) whose tireless efforts make the NPS an institution of higher learning which is second to none. Lastly, I would like to dedicate this work to the heroic men and women of the United States Armed Forces who selflessly serve of our great nation.

This work was supported in part by the Naval Research Laboratories, Washington, DC, and L-3 Communications Integrated Systems, Mission Integration Division, Greenville, TX.

THIS PAGE INTENTIONALLY LEFT BLANK

CHAPTER 1:

Introduction

Military search and fire control radars cover a wide bandwidth (BW) of frequencies (2-18 GHz) and have expanded into the millimeter wavelength range as missile seekers employ imaging radars to discriminate between targets and decoys during terminal homing. Electronic warfare (EW) receivers intercept threat emitters and determine their parameters, including frequency, pulse width (PW), pulse repetition frequency (PRF), PRF jitter or modulation, and direction-of-arrival (DOA). Based on these parameters, EW receivers classify intercepted signals by comparing their parameters to a database or emitter library [1]. Passive detection and classification of threat radars through electronic support (ES) allow modern integrated combat systems to respond with electronic attack (EA), by deploying decoys and by conducting active radar jamming, or employing air defense (AD) weapon systems. These weapon systems include the Standard Missile, the Evolved Sea Sparrow Missile, the Rolling Airframe Missile, and the Phalanx Close-in Weapon System, shown in Figure 1.1.

As threat weapon systems migrate to the millimeter wavelength band and adopt low-probability-of-intercept techniques, EW receivers must be capable of monitoring wider BWs to intercept emerging threat emitters. Most wideband receivers channelize the received signal and then down-convert the signal in each channel to an intermediate frequency prior to conducting analog-to-digital conversion. This approach is costly in terms of analog hardware, space limitations, and power consumption. Therefore, trends in receiver design have been toward digitizing the analog signal as far forward in the receiver as possible to eliminate analog down-conversion stages and filters. This technique reduces inter-modulation products and increases the EW receiver's dynamic range. If direct digitization at the antenna is achieved, digital signal processing (DSP) can be used to conduct demodulation, filtering, etc., which takes advantage of the advances in digital microprocessor speeds. However, to digitize an analog signal without aliasing, the sampling rate must be greater than or equal to the Nyquist sampling rate [3]. Analog-to-digital converter (ADC) technology, has lagged behind the advances in digital microprocessor technology hindering the ability to directly digitize received radio frequency (RF) and microwave (MW) signals [4]–[7].

To address the limitations of ADC technology, several undersampling techniques based on co-prime sampling rates and symmetrical number systems have been introduced. Symmetrical

number systems based on coprime moduli sets were developed to extract the maximum amount of information from symmetrical folding waveforms that are common in many engineering and scientific applications [8]. The use of symmetrical number systems has also been proposed to resolve frequency ambiguities due to aliasing in undersampled receivers and to increase the resolution of high speed ADCs. Compressive sensing (CS), has also emerged that combines several disciplines in mathematics and engineering to allow signal recovery while sampling at rates much less than the Nyquist sampling rate provided the signal is sparse in an orthonormal basis. Several CS receiver architectures have been proposed in the literature for use in numerous applications including EW receivers.

Photonic technology has also been introduced to modern radars and EW receivers due to the



(a) Standard Missile.



(b) Evolved Sea Sparrow.



(c) Phalanx Close-in Weapon System.



(d) Rolling Airframe Missile.

Figure 1.1: Air defense weapons from [2].

advantages of fiber-optic systems over metallic waveguides or coaxial cables including wide BWs, low electrical losses, low weight, and the immunity to electromagnetic interference (EMI) [9]. Microwave photonic systems also permit the use of narrow band optical signal processing techniques due to the high frequency of the optical carrier, $f_{opt} \approx 193$ THz for a 1550 nm wavelength laser, compared to the bandwidth of a wideband MW signal, i.e several GHz. The most common electro-optic modulator used in MW photonic systems is the Mach-Zehnder modulator (MZM) based on $LiNbO_3$ technology. Possessing an extremely wide BW, MZMs are ideally suited for use in wideband EW receiver applications.

In this work, several wideband EW receiver concepts are developed that combine the use of symmetrical number systems and advanced technologies such as photonics and CS theory. The first concept investigates a four-element photonic direction finding (DF) array with robust symmetrical number system (RSNS) preprocessing. This concept is first developed theoretically and then verified through simulation and experimental testing. Closed-form analytical expressions for the dynamic range of the RSNS \hat{M}_{RSNS} are also developed for several families of coprime moduli sets through the application of a computationally efficient search algorithm. Two EW receiver concepts are also examined which use the symmetrical number system (SNS) in CS receiver architectures. The first of these two concepts applies CS theory and recovery algorithms to a multi-channel undersampling receiver based on the SNS in a cueing receiver application. The SNS is also applied to a multi-channel Nyquist analog-to-information folding receiver (NYFR) architecture allowing determination of the SNS residues via a fast Fourier transform (FFT) and resolving frequency ambiguities through the properties of the SNS and the NYFR. Through examination of these concepts several contributions are made.

1.1 Primary Contributions

The first major contribution in this work is the development of several new closed-form analytical expressions for \hat{M}_{RSNS} for various families of coprime moduli sets. The closed-form expressions are developed by curve fitting data produced using a computationally efficient search algorithm. The computational complexity of the efficient search algorithm is compared to that of a naïve search algorithm and is demonstrated to be less complex by several orders of magnitude. These closed-form expressions are also demonstrated to satisfy the solutions to congruence equations that apply to the ambiguity locations. As a result of these new analytical expressions, the dynamic range of a greatly increased number of moduli sets can be easily calculated without the use of computer search algorithms. Additional closed-form expressions are

developed for both three sequence and four sequence RSNSs. The method used to determine and validate the new closed-form expressions for \hat{M}_{RSNS} is also presented allowing follow-on research in this area.

The second major contribution contained in this manuscript is that the dual electrode Mach-Zehnder modulator (DE-MZM) is proven mathematically to be capable of being used in phase interferometry applications. The theoretical results are also demonstrated through simulation and experimentation. Building upon this result, a small baseline four-element photonic DF array with RSNS preprocessing is designed, and its performance is investigated through the use of computer simulations and experimental testing, which proves the viability of the concept. The impact of signal frequency on system performance is also examined demonstrating the decreased spatial resolution that results when the signal frequency is below the design frequency of the photonic DF array. The photonic DF array's performance, when more than one pulsed emitter is present, is also examined through computer simulations. The simulation results for three separate cases are presented, and the signal processing algorithm used to sort the pulses is discussed.

The third major contribution is that a SNS-based CS cueing receiver is presented. The symmetrical number system - compressive sensing (SNS-CS) cueing receiver applies CS theory to an undersampled receiver using SNS-based sampling rates. The SNS is placed in a CS framework by collating the time domain samples from each channel to form the measurement vector, and deterministically forming the sensing matrix by selecting the rows of a unitary inverse discrete Fourier transform (IDFT) matrix that correspond to the SNS-based sample times. The frequency spectrum of the signal is estimated by applying a CS recovery algorithm, sparse reconstruction by separable approximation (SpaRSA) [10]. The results of Monte Carlo simulations are presented for different SNS-CS cueing receiver architectures. The probability of correctly identifying the frequency components of the signal is determined and compared to that of a CS receiver architecture using a random sensing matrix. The performance of the SNS-CS cueing receiver is also compared to the theoretical predictions for Fourier-based sensing matrices. It is shown that the SNS-CS cueing receiver's performance is comparable to the performance of CS receivers using random sensing matrices as well as the theoretical predictions. The SNS-CS cueing receiver also provides significant improvement over the performance of other undersampled receivers based on coprime sample rates that use Chinese remainder theorem (CRT)-based recovery algorithms.

The fourth major contribution is demonstrating the use of SNS-based undersampling in a NYFR architecture using an envelope approximation detector (EAD) with greatest of constant false alarm rate (GO-CFAR) processing to identify the peaks in the magnitude spectrum. The SNS structure is shown to be maintained by the NYFR architecture allowing use of the FFT for signal processing as opposed to different length discrete Fourier transforms (DFTs). The necessary modifications to the conditions required to implement an EAD with GO-CFAR processing to detect the peaks in the frequency spectrum are presented. Probability of detection curves are determined through Monte Carlo simulations to demonstrate the ability of a undersampled folding receiver to intercept multiple signals in a sparse signal environment. The required restrictions on the bandwidth of the receiver are also presented that prevent ambiguities in the resolved frequencies due to the permutations of the symmetrical residues.

1.2 Dissertation Outline

The remainder of this document is structured as follows. Background material is provided in Chapter 2 and Chapter 3. In Chapter 2, the important theoretical concepts in CS theory are presented, and a comprehensive review of the CS receiver architectures proposed in the literature is presented. In Chapter 3, three different symmetrical number systems are presented to provide the reader with a basic understanding of the structure of the symmetrical number systems and their applications. The SNS, optimum symmetrical number system (OSNS), and RSNS are presented showing the structure of the number systems and the analytical expressions for the dynamic range that exist. Specific properties of each symmetrical number system are discussed and applications are presented.

In Chapter 4, a computationally efficient search algorithm is presented for determining \hat{M}_{RSNS} , and its computational complexity is compared to that of a naïve search algorithm. The efficient search algorithm is used to generate data sets for different families of coprime moduli from which closed-form analytical expressions are developed via curve fitting techniques. The new closed-form expressions for \hat{M}_{RSNS} are subsequently verified to satisfy the solution to the congruence equations that define the ambiguity locations. Additional closed-form expressions are developed for different families of three coprime moduli. Also, several closed-form expressions are developed for families of four coprime moduli, where none have previously been identified. The methodology for determining the closed-form expressions for \hat{M}_{RSNS} is presented, and its application to additional moduli sets is discussed.

In Chapter 5, it is first proven, then demonstrated via simulations and experimental testing that

a DE-MZM can be used in phase interferometry applications to determine the DOA of an RF emitter. This concept is then applied to design, simulate and experimentally test a four-element photonic DF array with RSNS preprocessing based on moduli $m_i = \{7, 8, 9\}$. It is demonstrated through simulations that the system's performance closely correlates with the theoretical predictions. Experimental testing also closely approximated the theoretical predictions. Simulations are also presented to demonstrate the DOA processing of two or more intercepted pulsed emitters.

In Chapter 6, CS theory is applied to an undersampling receiver based on the SNS. The SNS-CS cueing receiver concept is developed in Section 6.1, and the performance of the SNS-CS cueing receiver is examined through Monte Carlo simulations in Section 6.2. The performance of the SNS-CS cueing receiver is compared to that of a CS receiver employing a random sensing matrix simulating a general random sampling approach. The SNS-CS receiver's ability to resolve multiple frequency tones is also compared to that of undersampled receivers using coprime sampling rates and a CRT based algorithm to resolve ambiguities resulting from aliasing.

In Chapter 7, the use of constant SNS-based undersampling in a multi-channel NYFR architecture is presented. It is proven that the SNS structure is maintained by the NYFR architecture allowing the use of an FFT instead of a DFT to determine the residue values increasing the computation speed. The peaks in the magnitude spectrum formed through use of an EAD with GO-CFAR processing is used to provide a variable threshold based on a constant false alarm rate (CFAR). Through the properties of the folding receiver, the frequency values are calculated based upon the residues in each channel. The results of Monte Carlo simulations are presented for a four channel and six channel receiver. Concluding remarks follow in Chapter 8.

CHAPTER 2:

Compressive Sensing

Compressive sensing is a recent development in DSP that combines sampling and compression into a single operation allowing the recovery of sparse high-dimensional signals from incomplete measurements by using efficient algorithms [11]. The primary impetus for the adoption of CS is that ADC speeds have lagged the increases in microprocessor speeds [4]–[7], limiting the ability to directly digitize wideband signals. Compressive sensing has found numerous applications in imaging [12], [13], medical imaging [14], [15], remote sensing [16], [17], analog-to-information conversion [18], [19], communications [20], [21], and radar [22], [23] by drawing from a variety of other fields including convex optimization, numerical linear algebra, random matrix theory, and signal processing [11]. An introduction to CS theory and a comprehensive summary of the CS receiver architectures that have been proposed in the literature are provided in this chapter.

2.1 Compressive Sensing Theory

Compressive sensing theory permits the recovery of sparse signals and images using significantly fewer samples than required by the Nyquist sampling theorem [24]. An $N \times 1$ signal vector \mathbf{z} can be expressed as a linear combination of the columns of an $N \times N$ orthonormal basis matrix Ψ as

$$\mathbf{z} = \sum_{i=1}^N x_i \psi_i = \Psi \mathbf{x}, \quad (2.1)$$

where \mathbf{x} is a $N \times 1$ vector of weighting coefficients. The weighting coefficients are

$$x_i = \langle \mathbf{z}, \psi_i \rangle = \psi_i^T \mathbf{z}' \quad (2.2)$$

where $\langle \bullet \rangle$ is the inner product and ψ_i is the i -th column vector of Ψ . The signal \mathbf{z} is considered to be S -sparse in Ψ if all but S of the N weighting factors x_i are equal to zero and $S \ll N$. Similarly, a signal is considered to be compressible if all but S of the N weighting factors are negligible in value compared to the S largest valued weighting factors and $S \ll N$ [25]. For example, a sinusoidal tone is sparse in a Fourier basis. Equation (2.1) is displayed pictorially in Figure 2.1 where the shaded blocks indicate that $x_i \neq 0$ and the unshaded blocks indicate that $x_i = 0$.

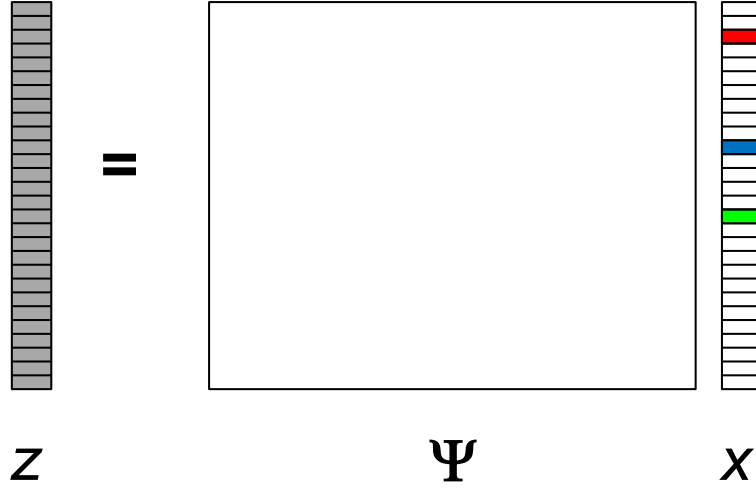


Figure 2.1: Pictorial depiction of sparsity.

In conventional transform coding, signals are sampled at or above the Nyquist sampling rate and are then transformed to a compressible or sparse representation (for example via eigenvalue decomposition). The compressed data is then used to represent the signal. This sample-then-compress framework suffers from three inherent inefficiencies: the initial number of samples N may be large even if the desired S is small; the set of all N transform coefficients x_i must be computed even though $(N - S)$ of them will be discarded, and the locations of the S largest coefficients must be encoded introducing additional overhead [25]. Compressive sensing resolves these inefficiencies by combining the separate sampling and compressing operations into a single function. Compressive sensing encodes (sample/compress) an S -sparse signal \mathbf{z} by taking L measurements to form an $L \times 1$ measurement vector \mathbf{y} where $S < L \ll N$. The measurement vector \mathbf{y} is expressed as

$$\mathbf{y} = \mathbf{A}\mathbf{x}, \quad (2.3)$$

where the $L \times N$ sensing matrix \mathbf{A} is the product of an $L \times N$ fixed measurement basis matrix Φ and an $N \times N$ orthonormal basis matrix Ψ [24],

$$\mathbf{A} = \Phi\Psi. \quad (2.4)$$

Equation (2.3) is represented pictorially in Figure 2.2.

The CS problem, therefore, consists of determining a stable measurement basis Φ that retains the salient information in the S -sparse or compressible signal while reducing the dimensional-

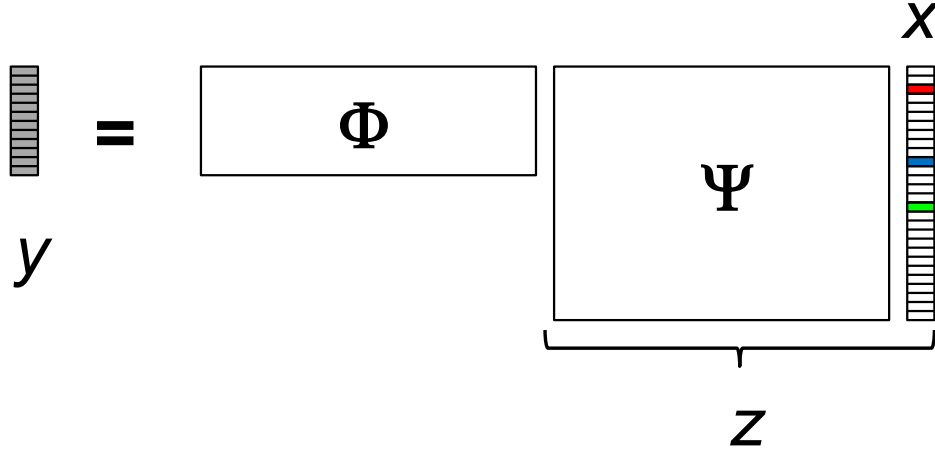


Figure 2.2: Pictorial representation of the combined sampling and compressing steps.

ity from $\mathbf{z} \in \mathbb{R}^N$ to $\mathbf{y} \in \mathbb{R}^L$, and determining a reconstruction algorithm that allows recovery of \mathbf{z} from only $L \cong S$ (\cong is approximately equal to) measurements that form \mathbf{y} . For the problem posed in Equation (2.3) to have a stable solution, i.e., a solution that does not change appreciably due to small perturbations from additive noise, the Euclidean distance (ℓ_2 norm) between the vectors in \mathbb{R}^N space and \mathbb{R}^L space must be preserved. The ℓ_p norm is defined as

$$\|\mathbf{x}\|_p = \begin{cases} \sqrt[p]{\sum_1^N |x_k|^p}, & p \in [1, \infty) \\ \max_{i=1,2,\dots,N} |x_i|, & p = \infty \end{cases}. \quad (2.5)$$

In the literature, reference is also made to an ℓ_0 pseudo-norm,

$$\|x\|_0 = \lim_{p \rightarrow 0} \|x\|_p = |\text{supp}(x)|, \quad (2.6)$$

where the absolute value of the support of \mathbf{x} , $|\text{supp}(\mathbf{x})|$, is the cardinality of $\text{supp}(\mathbf{x})$ [11]. More simply stated, $\|x\|_0$ is the number of elements in \mathbf{x} where $x_i \neq 0$.

Sensing matrices that satisfy restricted isometry property (RIP) of order S approximately preserve the Euclidean distance of S -sparse signals between the vectors in \mathbb{R}^N space and \mathbb{R}^L space and have columns that are nearly orthogonal [24], [25]. Therefore, if a sensing matrix satisfies RIP of order S , an efficient and robust reconstruction algorithm exists that allows for recon-

struction of an S -sparse signal \mathbf{x} from \mathbf{y} [24]. The RIP is defined as

$$(1 - \delta_S) \|\mathbf{x}\|_{\ell_2}^2 \leq \|\mathbf{A}\mathbf{x}\|_{\ell_2}^2 \leq (1 + \delta_S) \|\mathbf{x}\|_{\ell_2}^2 \quad (2.7)$$

where $\delta_S \in (0, 1)$ is the isometry constant of \mathbf{A} and is the smallest value for which Equation (2.7) is satisfied [24]. Sensing matrices that satisfy RIP of order S also satisfy RIP of order $\tilde{S} < S$. If \mathbf{A} satisfies RIP, Φ and Ψ must have low coherence where coherence is defined as

$$\mu(\Phi, \Psi) = \sqrt{N} \max_{1 \leq k, j \leq N} |\langle \phi_k, \psi_j \rangle| \quad (2.8)$$

and measures the largest absolute inner product between any two columns of Φ and Ψ [11], [24]. The coherence μ and RIP are related. If \mathbf{A} has unit length column vectors, \mathbf{A} satisfies RIP of order S provided

$$\delta_S = (S - 1) \mu(A), \quad (2.9)$$

for all $S < 1/\mu$ [11]. Gaussian or Bernoulli distributed random matrices are typically used as Φ because they are known to be incoherent with any fixed Ψ , and therefore, produce sensing matrices satisfying the RIP [11], [24], [25].

To recover \mathbf{z} or equivalently the weighting factors \mathbf{x} from \mathbf{y} , the recovery algorithm must solve Equation (2.3). However, there are an infinite number of possible solutions $\hat{\mathbf{x}}$ because any vector, $\mathbf{x} + \mathbf{r}$ where $\mathbf{r} \in \mathcal{N}(\mathbf{A})$ ($\mathcal{N}(\mathbf{A})$ is the Null Space of the matrix \mathbf{A}) solves Equation (2.3). Therefore, the signal reconstruction algorithm must determine the sparsest solution. Reconstruction algorithms typically rely on convex optimization algorithms that minimize a ℓ_p norm. Of the possible reconstruction algorithms, typically, minimization of the ℓ_2 norm fails to provide a sparse result. Also, minimizing the ℓ_0 pseudo-norm is numerically unstable and NP -complete requiring an exhaustive enumeration of all

$$\binom{N}{S} = \frac{N!}{S!(N-S)!} \quad (2.10)$$

possible solutions to determine the sparsest solution $\hat{\mathbf{x}}$ [25]. In complexity theory, an NP -complete class of problems have the property that if any of the problems can be solved by a polynomial worst-case time algorithm, then all of the problems can be solved by polynomial worst-case time algorithms [26].

Optimizing based on the ℓ_1 norm, however, allows exact recovery of the S -sparse signal from

the L measurements. The ℓ_1 minimizer is determined as

$$\hat{\mathbf{x}} = \arg \min \|\mathbf{x}'\|_1 \text{ such that } \mathbf{A}\mathbf{x}' = \mathbf{y} \quad (2.11)$$

and can exactly recover \mathbf{z} by using

$$L \geq CS \ln(N/S) \quad (2.12)$$

independent identically distributed (IID) Gaussian measurements where C is a constant depending on each instance [24], [25], [27]. As an example, if \mathbf{A} satisfies RIP of order $2S$ and $\delta_{2S} \in (0, 1/2]$, $C = 1 / \left(2 \ln \left(\sqrt{24} + 1 \right) \right) \approx 0.28$ [11].

Examining the geometry of the CS problem in \mathbb{R}^N helps to visualize why the ℓ_2 norm fails to identify the sparse solution and why ℓ_1 minimization succeeds. The set of all S -sparse vectors $\mathbf{x} \in \mathbb{R}^N$ is a highly nonlinear space consisting of all S -dimensional hyperplanes that are aligned with the coordinate axes as shown in Figure 2.3a. The translated null space $\mathcal{H} = \mathbb{N}(\mathbf{A}) + \mathbf{x}$ is oriented at a random angle due to the randomness in the matrix \mathbf{A} as shown in Figure 2.3b. The ℓ_2 minimizer,

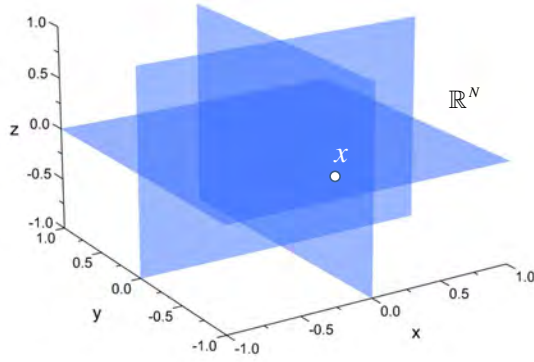
$$\hat{\mathbf{x}} = \arg \min \|\mathbf{x}'\|_2 \text{ such that } \mathbf{A}\mathbf{x}' = \mathbf{y} \quad (2.13)$$

is the point on \mathcal{H} closest to the origin. This point can be found by blowing up a hypersphere (the ℓ_2 ball) until it contacts \mathcal{H} . Due to the random orientation of \mathcal{H} , the estimate $\hat{\mathbf{x}}$ will be away from the coordinate axes with high probability and, therefore, will be neither sparse nor accurate. In contrast, the ℓ_1 ball shown in Figure 2.3c is convex and has its vertices aligned with the coordinate axes. Therefore, when the ℓ_1 ball is blown up, it will first contact the translated null space \mathcal{H} at a point near the coordinate axes, which is precisely where the sparse vector, \mathbf{x} , is located [25]. This can also be seen in two dimensions in Figure 2.3d.

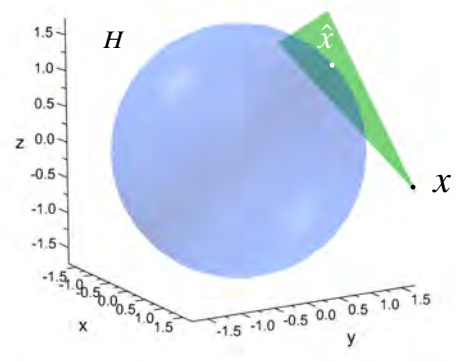
To accurately recover a sparse signal using CS, a sufficient number of samples must be obtained. Different conditions have been placed on the required number of samples based on the distribution of the measurement basis Φ . If L samples of an S -sparse signal \mathbf{z} are chosen uniformly at random, \mathbf{z} may be recovered exactly with overwhelming probability using ℓ_1 minimization if

$$L \geq C\mu^2(\Phi, \Psi) S \ln N \quad (2.14)$$

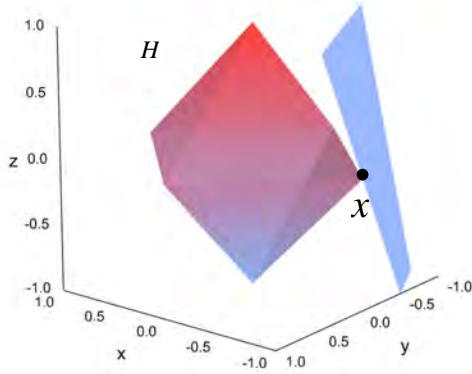
where C is positive constant. Also, for a Φ based on a Gaussian or a symmetrical Bernoulli



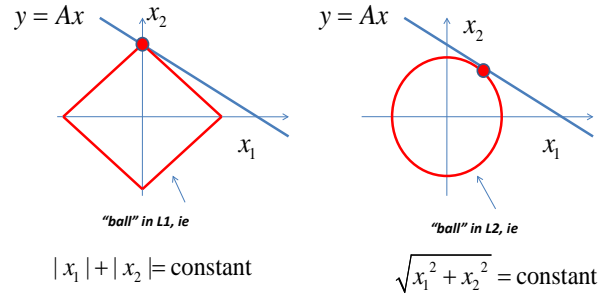
(a)



(b)



(c)



(d)

Figure 2.3: Geometric representation of ℓ_p norm minimization. (a) The subspaces containing two sparse vectors in \mathbb{R}^3 lie close to the coordinate axes. (b) Visualization of the ℓ_2 minimization that finds the nonsparse point-of-contact, $\hat{\mathbf{x}}$ between the ℓ_2 hypersphere and the translated measurement matrix null space. (c) Visualization of the ℓ_1 minimization solution that finds the sparse point-of-contact \mathbf{x} with high probability due to the pointedness of the ℓ_1 ball. (d) displays the ℓ_1 ball and ℓ_2 ball in two dimensions. After [25].

distribution, the number of samples acquired must satisfy Equation (2.12).

In a signal environment corrupted by additive white Gaussian noise (AWGN), the ℓ_1 minimization problem described by Equation (2.11) is recast as an ℓ_1 minimization with relaxed constraints for reconstruction. This algorithm is commonly referred to as the least absolute

shrinkage and selection operator (LASSO) algorithm and is formulated as

$$\min \|x\|_{\ell_1} \text{ subject to } \|\mathbf{Ax} - \mathbf{y}\|_{\ell_2} < \varepsilon \quad (2.15)$$

where ε bounds the amount of noise in the data [10], [24], [28]. The ℓ_1 minimization problems of Equation (2.11) and Equation (2.15) can be solved via convex optimization such as basis pursuit (BP) that applies algorithms such as interior-points methods for linear programming [27], [29], [30] or block coordinate relaxation (BCR) [30]. Besides convex optimization there are several greedy algorithms that have been developed to solve the ℓ_1 minimization problem described by Equation (2.11) as well as the noise corrupted problem of Equation (2.15). Greedy algorithms rely on iterative approximation of the signal coefficients and support either by iteratively identifying the support of the signal until a convergence criterion is met, or alternatively by obtaining an improved estimate of the sparse signal at each iteration that attempts to account for the mismatch to the measured data [11]. These algorithms include matching pursuit (MP) [11], [31], orthogonal matching pursuit (OMP) [31], [32], gradient pursuit (GP) [33], and compressive sampling matching pursuit (CoSaMP) [34].

While the use of random sensing matrices and ℓ_1 minimization is a near-optimal sensing strategy [24], random sensing matrices have some drawbacks. These drawbacks include: (1) the efficiency of sampling is offset by increased complexity in the reconstruction algorithm, (2) significant storage requirements can exist, and (3) no efficient algorithm exists for verifying that \mathbf{A} satisfies RIP [35]. Deterministic sensing matrices address these drawbacks by allowing dynamic construction of the sensing matrix eliminating the need for storage. Also, deterministic sensing matrices permit signal recovery using lower complexity algorithms and provide easily verifiable conditions to ensure successful signal recover for all but an infinitesimally small fraction of S -sparse signals [35]. The performance of deterministic sensing matrices, however, is only guaranteed in expectation. In [35], instead of considering whether the sensing matrix satisfies RIP a weaker condition, statistical restricted isometry property (StRIP), is imposed. A sensing matrix \mathbf{A} is defined as a (S, δ, ε) -StRIP matrix if

$$(1 - \delta) \|\mathbf{x}\|_2^2 \leq \left| \frac{1}{\sqrt{N}} \mathbf{Ax} \right|^2 \leq (1 + \delta) \|\mathbf{x}\|_2^2 \quad (2.16)$$

with probability $1 - \varepsilon$ with respect to a uniform distribution of the vectors \mathbf{x} among all S -sparse vectors in \mathbb{R}^N with the same fixed magnitudes. A large class of deterministic sensing matrices were examined in [35] including those based on partial DFT or IDFT matrices. It was

Table 2.1: Analytical expressions for the required number of samples for the sensing matrix to satisfy the restricted isometry property based on the measurement matrix distribution.

Measurement Matrix Distribution	Required Number of Samples
Uniform	$L \geq C\mu^2(\Phi, \Psi)S\ln N$
Gaussian or Bernoulli	$L \geq CS\ln(\frac{N}{S})$
Fourier (rows chosen uniformly at random)	$L > S\ln N$

demonstrated that partial DFT or IDFT sensing matrices satisfy StRIP, provided

$$L > S\ln(N), \quad (2.17)$$

and the rows of the matrix are chosen uniformly at random [35]. Deterministic partial DFT sensing matrices, formed by selecting the rows of the DFT matrix that correspond to the integer outputs of certain polynomial functions modulo N , were also shown to satisfy RIP in [36]. Equation (2.17) is applied in Chapter 6 to determine the theoretical maximum number of tones that the receiver can detect. A summary of the required number of samples based on the measurement matrix distribution is provided in Table 2.1.

While the focus above has been on discrete-time signals \mathbf{z} , CS also applies to sparse or compressible analog signals $z(t)$ that can be represented or approximated using only S of N possible elements from a continuous basis or dictionary $\psi_i(t)_{i=1}^N$. While each $\psi_i(t)$ may have large bandwidth, the signal $z(t)$ has only S degrees of freedom and thus can be measured at a much lower rate than the Nyquist sampling rate [25]. Thus, if a sparse signal can be represented by a structured signal models or union of subspaces, the signal can be recovered using less samples than required by Equation (2.12) [37], [38]. Examples of structured signal sparsity models that can be incorporated into CS recovery algorithms include wavelet trees and block sparsity models [37].

2.2 Compressive Sensing Electronic Warfare Receivers

Several CS receiver architectures have been proposed in the literature. The majority of CS receiver architectures introduce randomness into the sampling process to generate sensing matrices that have a high probability of satisfying RIP. Examples of CS receiver architectures that introduce randomness into the sampling process are the random filter [39], random demodulator (RD) [40], and the compressive multiplexer (CMUX) [41]. Other CS architectures, such as

the NYFR [18], [42], [43] and those using nonlinear affine processing (NoLAff) [44], preserve the signal's structure and allow determination of signal characteristics (frequency, BW, PRF, PW, modulation type, etc.) via less complex algorithms.

2.2.1 Random Demodulator

A RD, shown in Figure 2.4, is a new type of sampling system that can be used to acquire sparse, band limited signals. One of the major advantages of the RD is that it bypasses the need for a high-rate ADC and allows sampling at a much lower frequency than required by the Nyquist sampling theorem. The RD consists of a pseudo-random number generator that generates a chipping sequence, $p_c(t)$, a mixer, an accumulator, and a sampler. The RD demodulates the incoming signal $z(t)$ by multiplying it with a pseudo-random chipping sequence $p_c(t)$ that switches between ± 1 at or above the Nyquist sampling rate of N samples per second (sps) [40]. This operation spreads the input signal frequency spectrum through the convolution of the signal and the chipping sequence frequency spectra $Z(f) * P_c(f)$ where f represents frequency. The resulting signal is then passed through an integrate and dump circuit prior to being converted to a digital signal at a sampling rate of L sps, where $L \ll N$. [40].

To better illustrate the functioning of the RD, it can be recast in a discrete time format problem where the signal $z(t)$ is a multi-tonal continuous signal sparse in the frequency domain and is represented by a Nyquist rate sampled signal \mathbf{z} . From Equation (2.1), $\mathbf{z} = \Psi \mathbf{x}$ where Ψ is a

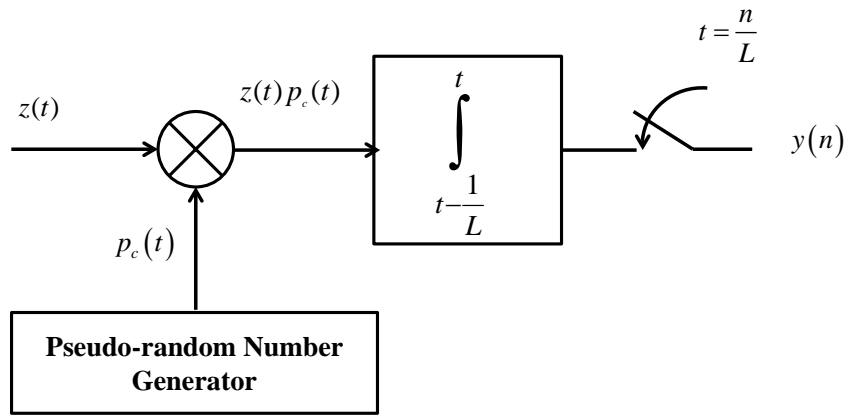


Figure 2.4: Random demodulator block diagram. After [40].

unitary DFT matrix,

$$\Psi = \frac{1}{\sqrt{N}} \left[e^{\frac{-j2\pi nk}{N}} \right]_{n,k}, \quad (2.18)$$

where $n = 0, 1, \dots, N-1$ and $k = 0, \pm 1, \pm 2, \dots, \pm(N/2-1), N/2$. The RD can be expressed as a discrete time representation in matrix form as

$$\mathbf{y} = \Phi \Psi \mathbf{x}. \quad (2.19)$$

The action of the demodulator on the discrete signal can be expressed as

$$\Phi = \mathbf{H} \mathbf{D} \quad (2.20)$$

where each row of Φ yields a separate sample of the input signal. The matrix, \mathbf{H} , is an $L \times N$ matrix with N/L consecutive unit entries ($h = 1$) starting in column $lN/L + 1$ for $l = 0, 1, \dots, L-1$,

$$\mathbf{H} = \begin{bmatrix} h_{N/L-1} & \cdots & h_0 & 0 & \cdots & \cdots & \cdots & \cdots & \cdots & 0 & 0 \\ 0 & \cdots & 0 & h_{N/L-1} & \cdots & h_0 & 0 & \cdots & \vdots & 0 & 0 \\ \vdots & \ddots & \ddots & 0 & \cdots & \cdots & h_{N/L-1} & \cdots & h_0 & 0 & 0 \\ 0 & \cdots & \cdots & \cdots & \cdots & \cdots & 0 & \cdots & 0 & h_{N/L-1} & \cdots \end{bmatrix}, \quad (2.21)$$

and represents the action of the integrate and dump circuit. The matrix, \mathbf{D} , is a $N \times N$ matrix with elements equal to the value of the chipping sequence and represents the action mixer multiplying the input signal by the chipping sequence, $\varepsilon_i = \pm 1$,

$$\mathbf{D} = \begin{bmatrix} \varepsilon_0 & 0 & \cdots & 0 \\ 0 & \ddots & \ddots & \vdots \\ \vdots & \ddots & \ddots & 0 \\ 0 & \cdots & 0 & \varepsilon_{N-1} \end{bmatrix}. \quad (2.22)$$

The RD can now be expressed as

$$\mathbf{y} = \mathbf{H} \mathbf{D} \Psi \mathbf{x} \quad (2.23)$$

where \mathbf{y} is the vector of samples acquired by the RD that represent \mathbf{z} . Recovery of the signal is accomplished through algorithms such as ℓ_1 norm minimization or greedy pursuit algo-

rithms [40].

Empirical results provided in [40] demonstrate that the RD requires a sampling rate of

$$L \approx 1.7S \ln \left(\frac{N}{S} + 1 \right). \quad (2.24)$$

In [40], theoretical guarantees are also provided for recovery of a sparse signal composed of S randomly selected uniformly spaced tones by ℓ_1 minimization when

$$L \geq C (S \ln N + \ln^3 N) \quad (2.25)$$

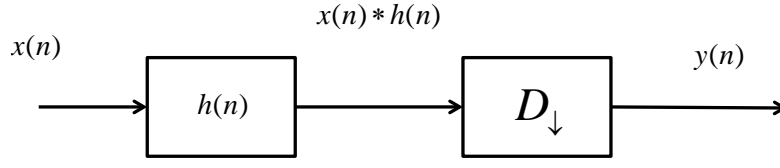
and L divides N .

In [45], a constrained random demodulator (CRD) is presented that is a modification of the RD. The CRD replaces the random waveform $p_c(t)$ with a constrained random waveform that limits its switching rate because fast switching waveforms may be difficult to generate cleanly. The CRD replaces the modulating waveform of the RD with a (d, k) -constrained waveform generated from a run-length limited (RLL) sequence. The RLL constraints specify the minimum separation d and the maximum separation k between transitions from one symbol to another to reduce the number of transitions in the waveform by a factor of $(d + 1)$, resulting in an increase in the signal energy captured by the hardware. The performance of the CRD using RLL sequences based on repetition coded sequences and Markov chains are examined in [45] and compared to that of the RD. Poor performance was seen when using the repetition coded sequences. However, the performance of the CRD when using the Markov-based RLL was comparable to the performance of the RD [45].

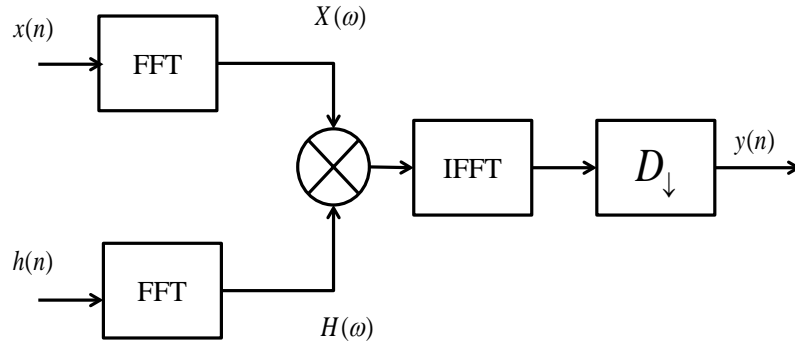
2.2.2 Random Filter

A random filter, shown in Figure 2.5, is new technique for efficiently acquiring and reconstructing signals based on convolution with a fixed finite impulse response (FIR) filter of length B where the filter taps are IID random variables [39]. The filter tap distributions examined in [39] are a zero mean Gaussian distribution with a variance of one $\mathcal{N}(0, 1)$ and a Bernoulli/Rademacher distribution $\{\pm 1\}$'s. The signal is encoded by performing linear convolution and down sampling by a rate of N/L where N is the length of the sparse signal vector \mathbf{x} , and L is the number samples in the vector \mathbf{y} used to represent \mathbf{x} . This operation can be represented as

$$\mathbf{y} = D_{\downarrow}(h * \mathbf{x}) \quad (2.26)$$



(a)



(b)

Figure 2.5: Random filter implementations. (a) is a block diagram of a time domain implementation using convolution. (b) is a FFT based implementation. After [39].

where D_{\downarrow} down samples by a factor of $\lfloor N/L \rfloor$. The combined operation of linear convolution and down sampling is displayed in Figure 2.5a and is represented mathematically as

$$y(n) = \sum_{j=0}^{B-1} x\left(n \left\lfloor \frac{N}{L} \right\rfloor + j\right) h(B-j) \quad (2.27)$$

where $n = 0, 1, \dots, L-1$ and $\lfloor \bullet \rfloor$ is the floor operator that rounds the argument down to the nearest integer. This method is useful when the input signal is streaming since the input signal is localized in time and the system is linear time invariant (LTI). Alternately, the convolution may be accomplished using the FFT as shown in Figure 2.5b. This method can be expressed mathematically as:

$$y = D_{\downarrow} \mathcal{F}^{-1} \{H(\omega)X(\omega)\} \quad (2.28)$$

where D_{\downarrow} represents down sampling by a factor of $\lfloor N/L \rfloor$ and \mathcal{F}^{-1} is the inverse fast Fourier transform (IFFT) operator. Greedy algorithms, such as OMP, or convex optimization based

algorithms, such as ℓ_1 minimization, are used to reconstruct the signal.

The principal advantage of the random filter receiver architecture is that the random filter requires less storage for measurement and reconstruction than standard CS techniques. Also, due to the random filter being time invariant and time localized, it is well suited for application with streaming or continuous time inputs [39].

2.2.3 Random Sampling

A random sampling analog-to-digital converter (RADC), shown in Figure 2.6, is implemented by randomly sampling the incoming signal at an average rate that is significantly lower than the Nyquist sampling rate. The samples are chosen using a pseudo-random chipping sequence $p_c(t)$ based on an arithmetic progression designed to have a low probability of samples being chosen consecutively, i.e., at the Nyquist rate.

The random sampler is the challenging portion of the architecture to implement due to the potential to have some samples close to each other, i.e., at the Nyquist sampling rate. Two implementations of the RADC are shown in Figure 2.7. In the first implementation, illustrated in Figure 2.7a, a parallel bank of low-rate ADCs that have equal shifts between their starting conversion points is used. This creates a shift in the samples that are produced from each of the parallel ADCs. The switching mechanism is controlled pseudorandomly. This approach faces challenges with minimizing the jitter effect when controlling the switches.

A second approach, shown in Figure 2.7b, employs an analog register and an analog demultiplexer/multiplexer. The demultiplexer is controlled by a pseudorandom digital control signal with an average rate corresponding to the measurement rate while the output multiplexer is

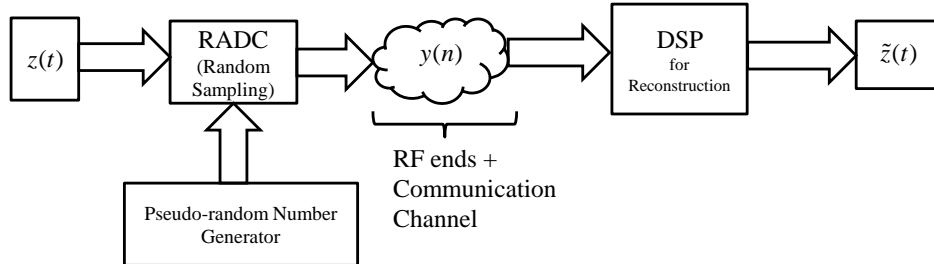
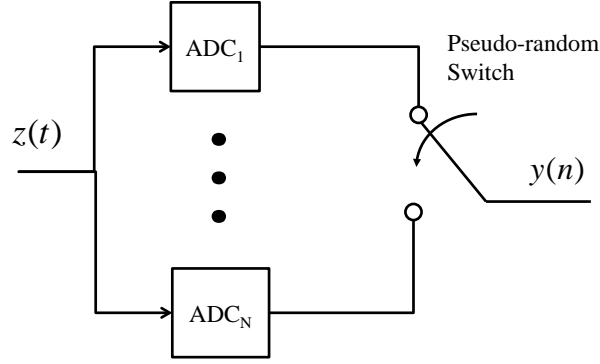
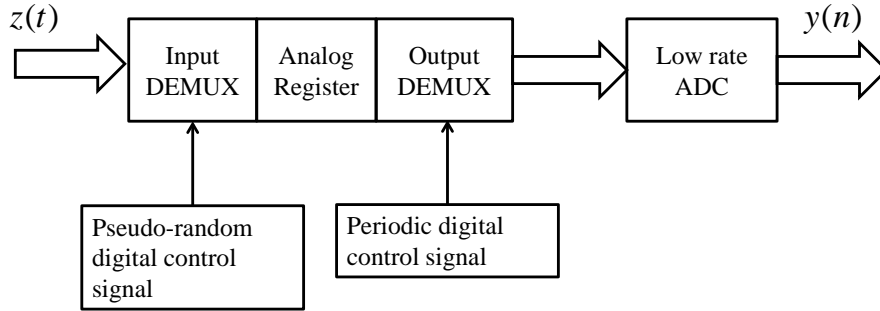


Figure 2.6: Random sampling architecture. After [46].



(a)



(b)

Figure 2.7: Random ADC implementations. (a) random ADC implementation using a parallel bank of ADCs, (b) random ADC implementation using an analog register and a demultiplexer/multiplexer. After [46].

controlled by a periodic signal with the same rate. The storage control signal is pseudorandom in order to sample the signal at pseudorandom time instances. Recovery of the signal is accomplished through greedy pursuit algorithms [46].

The principal advantage of the RADC is that it allows for signal acquisition of locally Fourier sparse signals while sampling at rates significantly less than the Nyquist sampling rate. The implementation of the random sampling, however, is challenging due to the possibility that consecutive random samples can be located closely spaced in time and near the Nyquist rate. Also, the pseudorandom number generator clock in the second implementation is required to be at or above the Nyquist sampling rate to allow capturing samples that are closely spaced in time [46].

2.2.4 Compressive Multiplexer

A CMUX, shown in Figure 2.8, is a CS receiver architecture for sub-Nyquist acquisition of multiple channels that are not contiguous. The CMUX acquires J independent signal channels of equal bandwidth $W/2$ Hz and mixes the channels with orthogonal pseudo-random chipping sequences $p_j(t)$. It then combines the resulting signals into a single channel by adding across channels prior to sampling at the chipping rate which is greater than or equal to the Nyquist sampling rate of any one baseband signal. The CMUX is analogous to coded digital communication schemes such as code division multiple access (CDMA); however, rather than coding signals with orthogonal codes and transmitting the signals onto a common channel as in CDMA, the CMUX codes the channels and records them onto the same samples [41]. The principal advantages of the CMUX architecture are that it requires only a single ADC and all of its components operate below the Nyquist sampling rate of the total acquired BW.

The CMUX architecture can be expressed as a $W \times JW$ matrix, Φ , formed by concatenating diagonal $W \times W$ sub-matrices, Φ_j , whose diagonal elements are ± 1 Rademacher variables and $j = 1, \dots, J$. That is

$$\Phi = [\Phi_1, \Phi_2, \dots, \Phi_J], \quad (2.29)$$

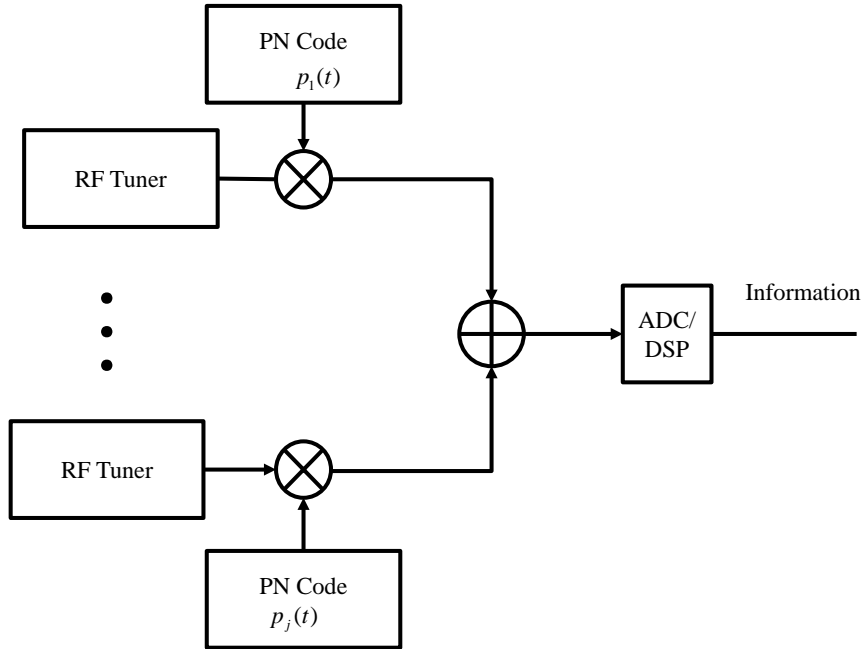


Figure 2.8: Compressive multiplexer block diagram. After [41].

where

$$\Phi_j = \begin{bmatrix} \varepsilon_0 & & 0 \\ & \ddots & \\ 0 & & \varepsilon_W \end{bmatrix} \quad (2.30)$$

and $\varepsilon_w = \pm 1$.

The sparsity basis matrix Ψ is a $JW \times JW$ block diagonal matrix with a $W \times W$ unitary DFT basis \mathcal{F} along the diagonal,

$$\Psi = \begin{bmatrix} \mathcal{F}_1 & & 0 \\ & \ddots & \\ 0 & & \mathcal{F}_J \end{bmatrix}. \quad (2.31)$$

The goal is to recover an S -sparse vector, $\mathbf{x} \in \mathbb{R}^{JW}$, such that $\mathbf{y} = \mathbf{A}\mathbf{x}$, where $\mathbf{A} = \Phi\Psi$. Signal recovery can be accomplished by demodulating the signal with each chipping sequence or via the BCR algorithm [41].

In [47], the recovery of correlated signals is examined. The CMUX architecture is modified by placing a random LTI filter after the random modulation in each leg of the CMUX architecture. The addition of the LTI filters forces the signal energy to be equally distributed among the channels allowing recovery of an ensemble of correlated signals regardless of the initial energy distribution [47].

2.2.5 Modulated Wideband Converter

A modulated wideband converter (MWC) is an analog wideband CS receiver that exploits spread spectrum communication techniques to allow sampling sparse wideband signals at rates much less than the Nyquist sampling rate [19], [48]. A block diagram of the MWC is displayed in Figure 2.9. The MWC front-end pre-processes a multi-band analog signal, $z(t)$, by using L channels. The term multi-band refers to an analog signal with the frequency spectrum concentrated on N frequency bands with individual BWs no greater than B Hz [19]. In each channel, $z(t)$ is mixed with a periodic signal $p_i(t)$, where $i = 1, 2, \dots, L$, with period, $T_p = 1/f_p$. In each channel, the resulting signal $\tilde{z}_i(t)$ is low pass filtered by filter $h(t)$ with a cutoff frequency of $f_s/2$ and uniformly sampled at a rate of f_s Hz.

The mixing operation scrambles the frequency spectrum of $z(t)$ so that a portion of the signal's energy in all of the bands appears in base band. Since the mixing signals are periodic, the signal

can be expressed as a Fourier series expansion,

$$p_i(t) = \sum_{l=-\infty}^{\infty} c_{il} e^{j\frac{2\pi l t}{T_p}}. \quad (2.32)$$

Therefore, the mixing results in a weighted sum of f_p -shifted copies of the signal's frequency spectrum,

$$\tilde{Z}(f) = \sum_{l=-\infty}^{\infty} c_{il} Z(f - l f_p), \quad (2.33)$$

where

$$c_{il} = \frac{1}{T_p} \int_0^{T_p} p_i(t) e^{-j\frac{2\pi}{T_p} l t} dt. \quad (2.34)$$

Since the filter's frequency response $H(f)$ is an ideal rectangular function, only the frequencies in the interval $[-f_s/2, +f_s/2]$ are contained in the uniformly sampled sequence $y_i[n]$. Therefore, the discrete time Fourier transform (DTFT) of $y_i[n]$ equals

$$Y_i(e^{j2\pi f T_s}) = \sum_{l=-L_0}^{+L_0} c_{il} Z(f - l f_p), \quad (2.35)$$

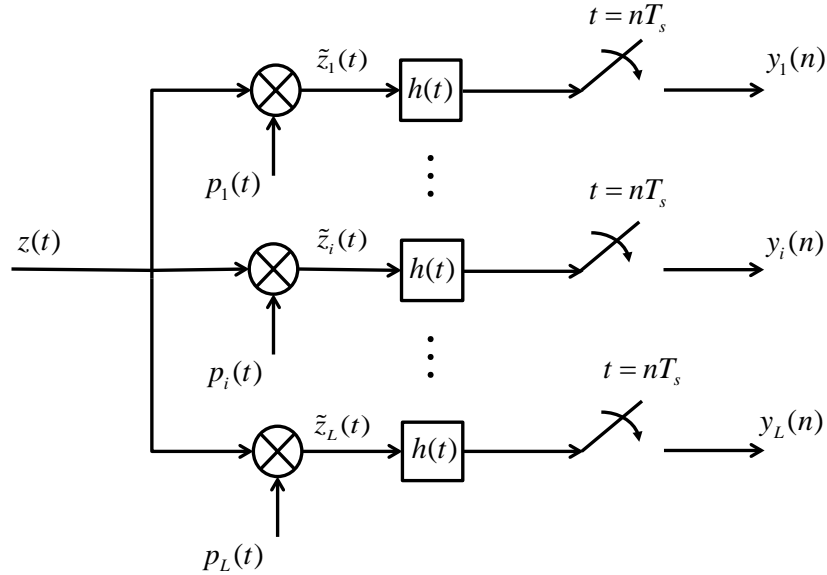


Figure 2.9: Modulated wideband converter block diagram, after [48].

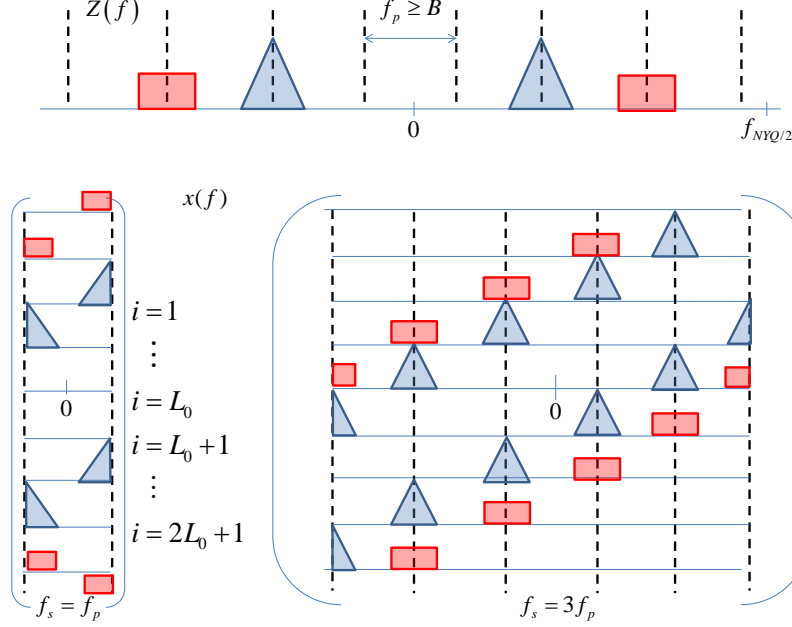


Figure 2.10: Modulate wideband converter–relation between $\mathbf{Z}(f)$ and $\mathbf{x}(f)$. After [48].

$L_0 = \lceil (f_{NQ} + f_s)/2f_p \rceil - 1$, and $\lceil \bullet \rceil$ is the ceiling function that rounds the argument to the next highest integer value. Expressing the above relationship in matrix form,

$$\mathbf{y}(f) = \mathbf{A}\mathbf{x}(f), \quad (2.36)$$

where $x_i(f) = Z(f + (i - L_0 - 1)f_p)$ for $1 \leq i \leq 2L_0 + 1$ and $A_{il} = c_{il}^*$. The relationship between $\mathbf{x}(f)$ and $\mathbf{Z}(f)$ is shown in Figure 2.10. Figure 2.10 depicts the vector $\mathbf{x}(f)$ and the effect of aliasing $\mathbf{Z}(f)$ in f_p -shifted copies for $M = 4$ bands, aliasing rate $f_p \geq B$, and two sampling rates, $f_s = f_p$ and $f_s = 3f_p$. Each entry of $\mathbf{x}(f)$ represents a frequency slice of $Z(f)$ whose length is f_s . Thus, to recover $z(t)$, it is sufficient to determine $\mathbf{x}(f)$. The signal is recovered from the channel outputs by determining the sparsest solution for $\mathbf{x}(f)$ that satisfies Equation (2.36).

2.2.6 Nonlinear Affine Processing

Another novel approach to undersampling is through the use of NoLAff processing, which provides a means of reducing the sampling rate to near the information rate for a sparse signal by exploiting nonlinearities and nonlinear signal artifacts to increase the signal diversity of weak sparse signals. In a NoLAff receiver shown in Figure 2.11, a large probe signal, with characteristics that are known a priori, is added to the signal of interest (SOI). The resulting signal is passed through a polynomial filter after which the probe signal and its harmonic distortions are

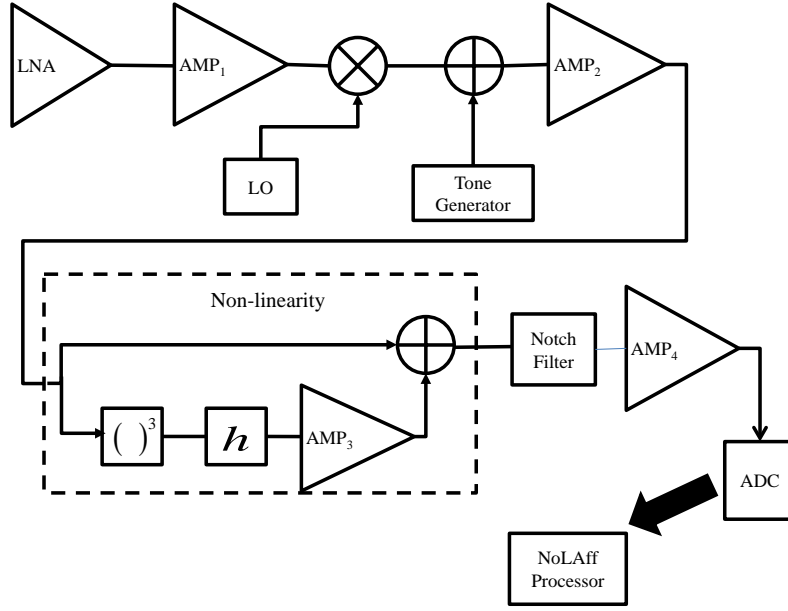


Figure 2.11: Block diagram of a nonlinear affine signal processing receiver. After [44].

removed from the signal, leaving the SOI and the intermodulation products between the probe signal and the SOI [44].

In an undersampled signal, the original signal will alias into the frequency spectrum defined by the sampling frequency. Nonlinear affine processing encoding allows for recovery of the original signal by spreading the signal into more frequency locations and filtering the result. The signal spreading creates extra copies of the original signal at deterministic frequency locations in the full spectrum; however, these frequency locations are ambiguous after undersampling. Filtering imparts alterations to the images that are unique based upon the signal frequency location in full spectrum. These alterations are used to decode the signal using hypothesis testing [44].

A system diagram for a general analog NoLAff encoder front-end is displayed in Figure 2.12. The encoding process can be represented as a nonlinear function expressed as

$$f(x) = g(x + p) - g(p) \quad (2.37)$$

where p represents the probe signal and $x(t)$ is the input signal. The function $g(\bullet)$ represents a

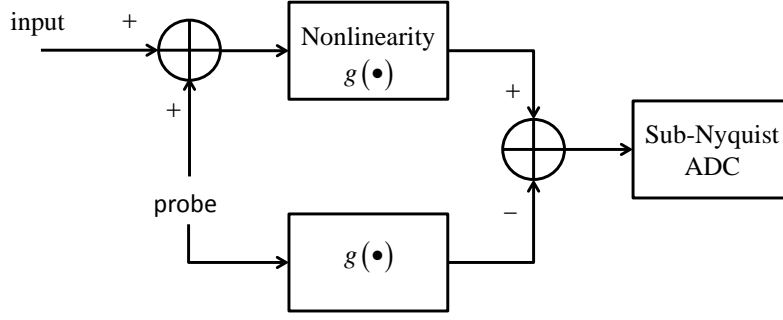


Figure 2.12: Nonlinear affine processing encoder. After [44].

general nonlinearity represented by a polynomial filter

$$g(\bullet) = \sum_{i=1}^{\infty} a_i(\bullet)^i \quad (2.38)$$

where “ $\cdot(\star)$ ” represents an element-wise operation. Assuming that $|p| \gg |x|$, the following expression is obtained

$$f(x) = x \cdot \sum_{k=1}^{\infty} a_k p^{(k-1)}. \quad (2.39)$$

Nonlinear affine processing is linear with respect to the input vector, \mathbf{x} [44]. The encoding and undersampling process is depicted in Figure 2.13a. The input signal and the encoded nonlinearities are folded into the Nyquist band of the low-rate ADC. Filtering is accomplished prior to undersampling and encodes the intermodulation products by altering amplitude and phase values of the distortions based on their frequency location in the full spectrum. The encoded nonlinearities and the phase differences resulting from the filtering process are exploited in the NoLAff decoding process [44].

The NoLAff decoding process is depicted in Figure 2.13b. The encoded signal is passed through an iterative nonlinear equalization (NLEQ) process and hypothesis signals are generated across the full frequency spectrum. These signals are then encoded with the probe signal added and maximum likelihood (ML) testing is conducted to determine which hypothesis is the closest match to the input signal prior to encoding [44].

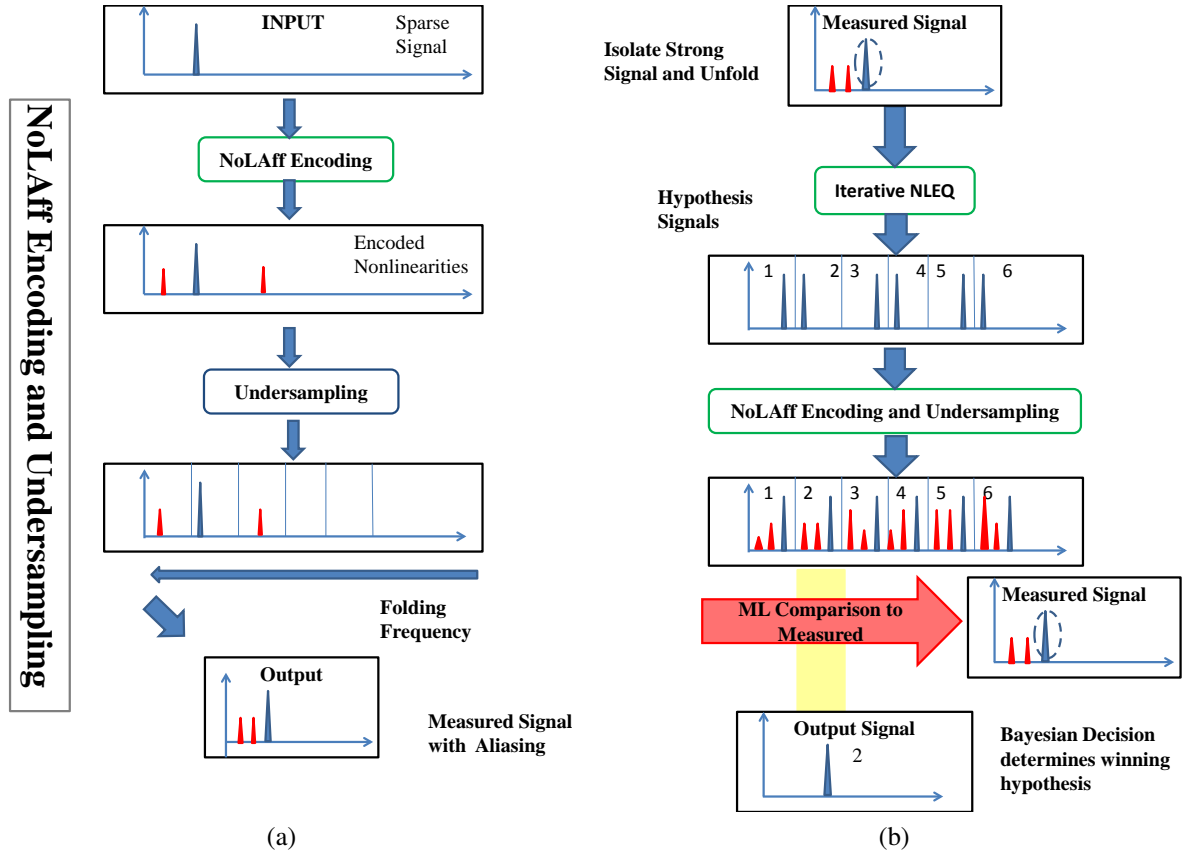


Figure 2.13: NoLAff encoding/decoding process, (a) displays the NoLAff encoding process. (b) displays the NoLAff decoding process. After [44].

2.2.7 Nyquist Folding Receiver

A NYFR uses deterministic *non-uniform sampling* where the sampling time corresponds to the positive slope zero crossings of a linear frequency modulated sinusoidal waveform. A block diagram of the NYFR architecture is shown in Figure 2.14. The NYFR architecture provides for a wide analog input BW without the requirement for high speed sample and hold circuits or Nyquist rate components. If the input signal $z(t) = \cos(\omega_c t + \psi(t))$ the normalized interpolation filter output is

$$y(t) \approx \cos(|\omega_c - \omega_{s1} k_H| t + \beta \psi(t) - \chi \theta(t)), \quad (2.40)$$

where $k_H = \lceil (\omega_c / \omega_{s1}) \rceil$, $\beta = \text{sgn}(\omega_c - \omega_{s1} k_H)$, $\chi = \beta k_H$, and $\lceil \bullet \rceil$ rounds the argument to the closest integer value. The signal $y(t)$ has an induced modulation $\chi \theta(t)$ of the same form as the RF clock modulation scaled by the modulation scale factor χ and its orientation β depending on the Nyquist zone of the signal. These features allow recovery of signal information in a sparse

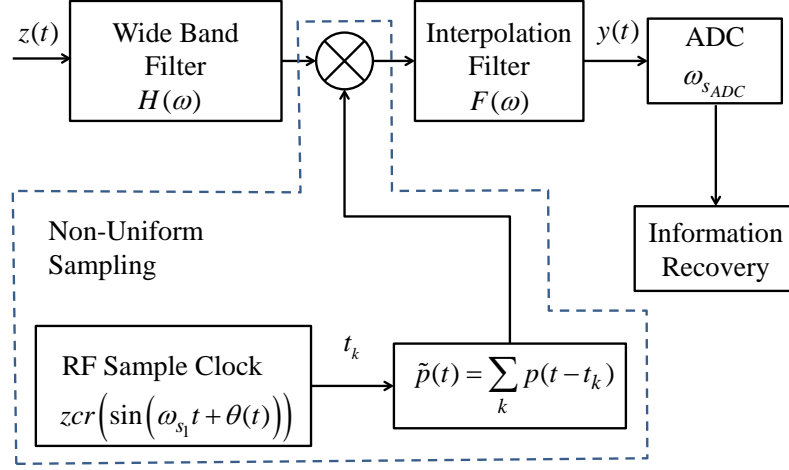


Figure 2.14: Nyquist analog-to-information folding receiver block diagram. After [18].

environment without solving a computationally intensive convex optimization problem [18].

For the case where the interpolation filter is an ideal filter with transfer function,

$$F(\omega) = \begin{cases} 1, & |\omega| < |\omega_{s1}| \\ 0 & , \text{ otherwise} \end{cases}, \quad (2.41)$$

$\varphi(t)$ is a narrow band phase (or frequency) modulation centered at

$$\varphi(t) = \omega_{s1}t + \theta(t), \quad (2.42)$$

and the input signal is a narrow band signal with carrier frequency ω_c and information modulation $\psi(t)$,

$$z(t) = \cos(\omega_c t + \psi(t)), \quad (2.43)$$

the normalized interpolation filter output $Y(\omega)$ is

$$Y(\omega) = ((Z(\omega)H(\omega)) * \tilde{P}(\omega)) F(\omega) / 2\pi \quad (2.44)$$

where $\tilde{P}(\omega)$ is the Fourier transform of the non-uniform pulse train, and $H(\omega)$ is the pre-select

input filter frequency response. The Fourier transform of the pulse train is

$$\tilde{P}(\omega) \approx P(\omega) \omega_{s_1} \sum_k \left(\delta(\omega - k\omega_{s_1}) * \mathcal{F} \left\{ e^{jk\theta(t)} \right\} \right) \quad (2.45)$$

which can be expressed as

$$\tilde{P}(\omega) = \sum_k T_k(\omega - k\omega_{s_1}) \quad (2.46)$$

where

$$T_k(\omega) = \omega_{s_1} P(k\omega_{s_1}) \mathcal{F} \left\{ e^{jk\theta(t)} \right\}. \quad (2.47)$$

Taking the Fourier transform of Equation (2.43) results in

$$Z(\omega) = \begin{cases} \frac{1}{2} \delta(\omega + \omega_c) * \mathcal{F} \left\{ e^{-j\psi(t)} \right\}, & \omega < 0 \\ \frac{1}{2} \delta(\omega - \omega_c) * \mathcal{F} \left\{ e^{-j\psi(t)} \right\}, & \omega > 0 \end{cases}. \quad (2.48)$$

Substituting Equation (2.46) and Equation (2.48) into Equation (2.44) yields

$$Y(\omega) = \frac{1}{4\pi} \delta(\omega + \omega_c - k_H \omega_{s_1}) * \mathcal{F} \left\{ e^{-j\psi(t)} \right\} * T_{k_H}(\omega) + \frac{1}{4\pi} \delta(\omega - \omega_c + k_H \omega_{s_1}) * \mathcal{F} \left\{ e^{j\psi(t)} \right\} * T_{-k_H}(\omega). \quad (2.49)$$

And, taking the inverse Fourier transform of Equation (2.49) provides the desired result:

$$y(t) \approx \cos(|\omega_c - \omega_{s_1} k_H| t + \beta \psi(t) - \Psi \theta(t)). \quad (2.50)$$

A detailed derivation of the above results can be located in the Appendix of [42].

The NYFR can also be modeled with CS and the signal recovered via ℓ_1 minimization or greedy algorithms. The input signal $z(t)$ is a wideband signal covering P Nyquist zones and is sparse in the frequency domain. The input signal $z(t)$ is represented as a Nyquist rate sampled vector \mathbf{z} over \mathbb{R}^{2N} or \mathbb{C}^N . The compressive sampling can be expressed as

$$\mathbf{y} = \mathbf{A} \boldsymbol{\zeta} \quad (2.51)$$

where \mathbf{A} is the $L \times N$ sensing matrix and $\boldsymbol{\zeta}$ is the DFT of the input signal. The sensing matrix

\mathbf{A} is

$$\mathbf{A} = \mathbf{R}\Sigma\Psi \quad (2.52)$$

where the induced sample modulation matrix, Σ is a $N \times N$ diagonal matrix whose entries are partitioned into $L \times L$ blocks and \mathbf{R} is the horizontal concatenation of P identity matrices, each of size $L \times L$. Also, Ψ is a $N \times N$ matrix given by

$$\Psi = \mathbf{I}_P \otimes \Psi_L \quad (2.53)$$

where \mathbf{I}_P is an identity matrix with dimension P equal to the number of folds, Ψ_L is an $L \times L$ IDFT matrix, and \otimes denotes the Kronecker product. Each block represents a Nyquist zone and contains entries of the form $\exp(j\chi\theta(t))$ where χ is the corresponding modulation scale factor for the Nyquist zone and $\theta(t)$ is the RF sample clock modulation function [18]. The format of the matrices is displayed in Figure 2.15.

In addition to solving the ℓ_1 minimization problem, recovery of signal characteristics (frequency, BW, PRF, PW, modulation type) from the NYFR can be accomplished by examining the time-frequency relationship of the signal. A spectrogram representation of the signal allows identification of the aliased frequency, the modulation scaling factor χ from the slope of the linear frequency modulation, and its orientation β . As a result, the Nyquist zone of the aliased frequency can be determined, and the true signal frequency can be calculated. An example of a spectrogram produced from a NYFR receiver is displayed in Figure 2.16a. In Figure 2.16a, the linear frequency modulation imparted onto the aliased signals is apparent. Also, the magnitude and orientation differences of the modulation based on the Nyquist zone in which the aliased signals reside are clearly shown in Figure 2.16a. The even and odd numbered Nyquist zones

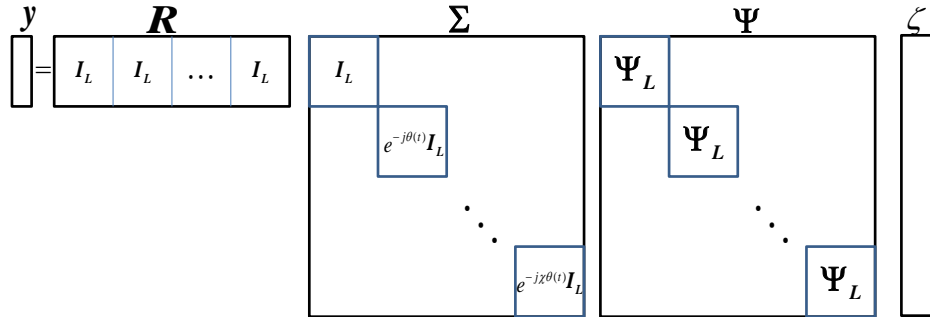


Figure 2.15: NYFR CS model. After [18]

Table 2.2: Modulation Scale Factor for various Nyquist Zones

Analog Frequency	Index	Nyquist Zone	χ
$0 \leq \omega \leq \frac{\omega_{s1}}{2}$	1	0	0
$\frac{\omega_{s1}}{2} \leq \omega \leq \omega_{s1}$	2	1	-1
$\omega_{s1} \leq \omega \leq \frac{3\omega_{s1}}{2}$	3	2	1
$\frac{3\omega_{s1}}{2} \leq \omega \leq 2\omega_{s1}$	4	3	-2
$2\omega_{s1} \leq \omega \leq \frac{5\omega_{s1}}{2}$	5	4	2
$\frac{5\omega_{s1}}{2} \leq \omega \leq 3\omega_{s1}$	6	5	-3
$3\omega_{s1} \leq \omega \leq \frac{7\omega_{s1}}{2}$	7	6	3

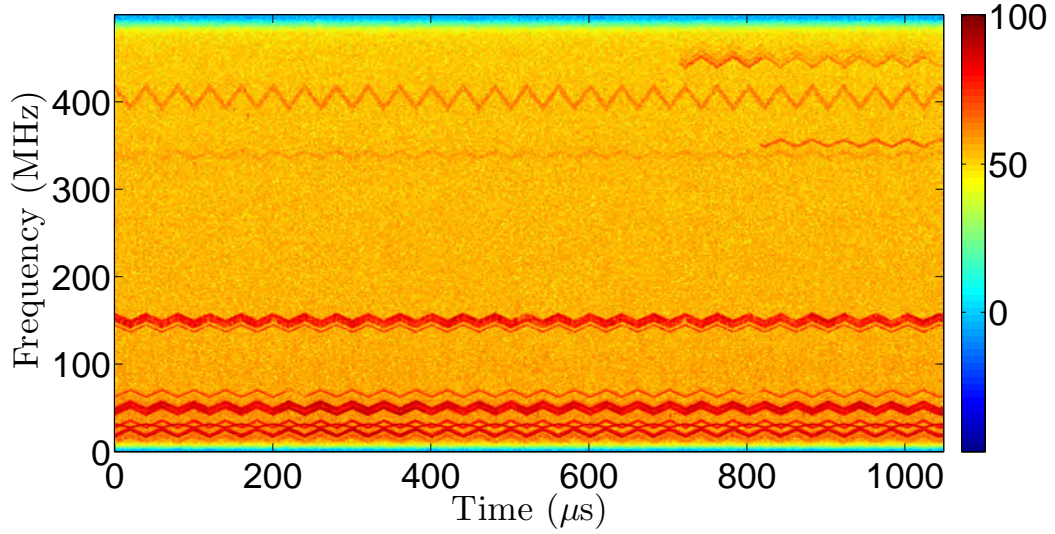
are 180 degrees out of phase with each other, and the magnitude of signals increases with χ .

Another method used to determine the signal frequency is by plotting an X-gram for the received signal. The X-gram, shown in Figure 2.16b, is produced by demodulating the received signal using integer values of χ , for instance from -20 to 20, determining the time-averaged power spectrum of the demodulated signal, and plotting the resulting data as an image. Signals can be identified at the mid-point of the X shapes from which the X-gram derives its name. Figure 2.16b displays the X-gram representation of the data from which Figure 2.16a was derived. The correlation between the signals in the spectrogram and the X-gram can be clearly observed. An example of the various Nyquist Zones and values for χ are shown in Table 2.2 and Figure 2.17.

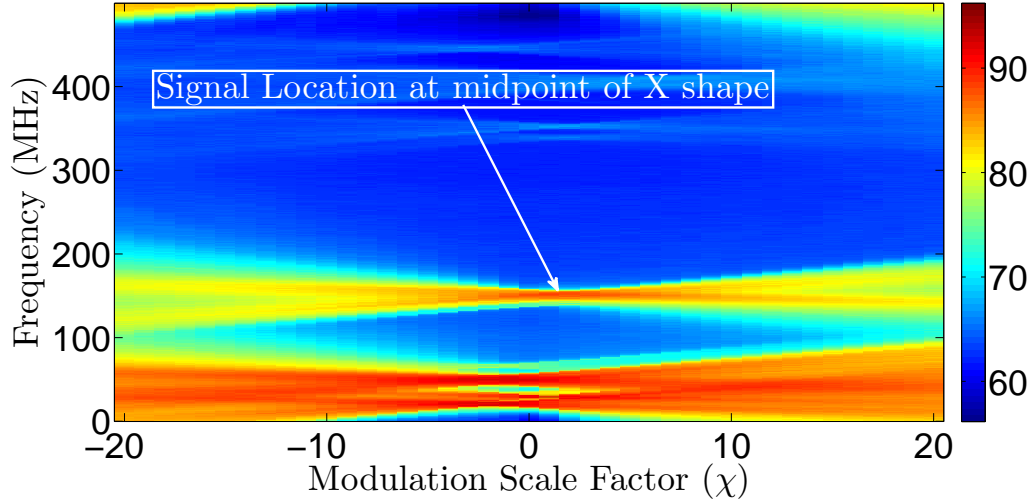
If the RF sample clock is a linear frequency modulated sinusoid and the modulation is known, the slope of the waveform, the modulation scale factor χ and its orientation β can be used to determine the Nyquist zone of a signal and subsequently resolve the aliased frequency. If a general narrow band modulation signal is used, the derivative of the waveform in the time-frequency plane would be used in place of the slope (provided the derivative was not equal to zero). It was demonstrated in [43] that the Nyquist zone N_z can be determined by finding

$$\min (S_p - \chi(i) S_t)^2 \quad (2.54)$$

where the slope of the pulse analyzed is equal to S_p , the slope of the modulation clock is S_t , and $\chi(i)$ are the possible modulation scale factors corresponding to the system bandwidth. The



(a)



(b)

Figure 2.16: NYFR detection methods. (a) shows an example of a spectrogram representation of the received signal. (b) shows an example of an X-gram representation of the signal. After [18].

Nyquist zone is equal to

$$N_z = i_{\min} - 1. \quad (2.55)$$

where i_{\min} is the index corresponding to the modulation scale factor that satisfies Equation (2.54). This feature of the NYFR simplifies signal information recovery in a sparse environment without solving a computationally intensive ℓ_1 minimization problem [18]. An autonomous detection scheme to determine the signal parameters including the pulse slope using a quadrature

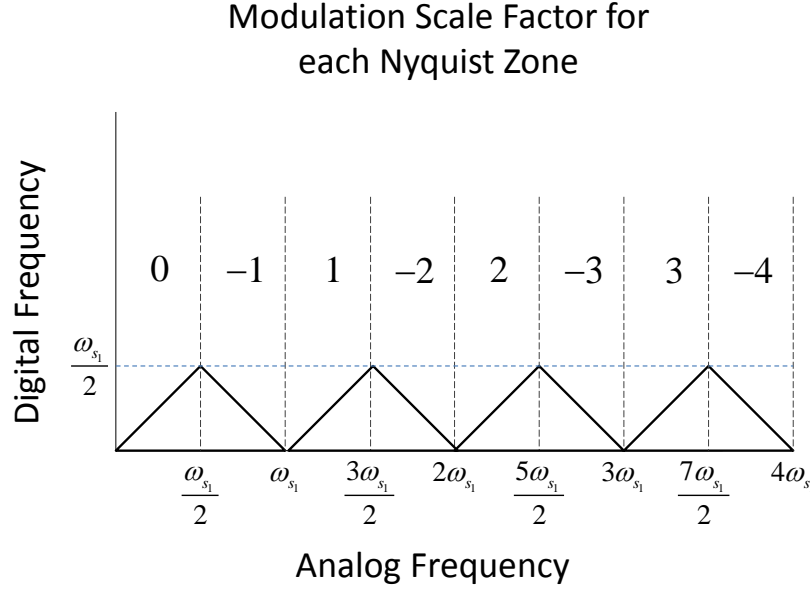


Figure 2.17: NYFR - modulation scale factor. After [18].

mirror filter bank (QMFB) to execute the wavelet decomposition of the signal was presented in [43].

2.2.8 Time encoding machine

A time encoding machine (TEM) is a unique implementation of CS that converts an analog signal $z(t)$ with a continuous voltage range to a binary amplitude signal and encodes the information of $z(t)$ in the time points when the binary signal $x(t)$ switches sign. The basic structure of a TEM is shown in Figure 2.18. It consists of an input transconductance amplifier, a feedback 1-bit digital-to-analog converter (DAC), an integrator, and a hysteresis quantizer [49], [50]. The relationship between the signal and the time sequence $\{t_k\}$ satisfies the relationship

$$\int_{t_k}^{t_{k+1}} \left(g_1 z(u) + (-1)^k g_3 \right) du = (-1)^k 2\delta, \quad (2.56)$$

where g_1 and g_3 are gain terms, $\{t_k\}$ is the encoded time sequence, and δ is as shown in Figure 2.18. The TEM transfer function exhibits the characteristics of a low pass filter due to the integrator. When there is no signal present at the input of the TEM, the output from the TEM is a square wave with a period $T_p = 4\delta/g_3$ with a 50% duty cycle. When the input is a bounded

signal such that $|z(t)| < b$, the intervals between time points, $T_k = t_{k+1} - t_k$ satisfy

$$\frac{2\delta}{g_3 + g_1 b} \leq T_k \leq \frac{2\delta}{g_3 - g_1 b}. \quad (2.57)$$

The time intervals are converted to voltage levels and measured through a sampler as shown in Figure 2.19 [49], [50].

This particular architecture requires sampling at above the Nyquist rate if the maximum interval between the time points T_k is less than half the minimum period of the signal's components. However, if the sample space is sparse, CS can be accomplished using a TEM. The signal

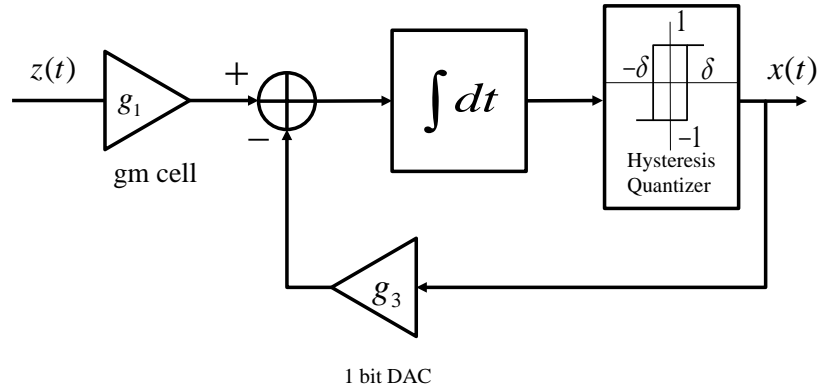


Figure 2.18: Time encoding machine block diagram. After [49].

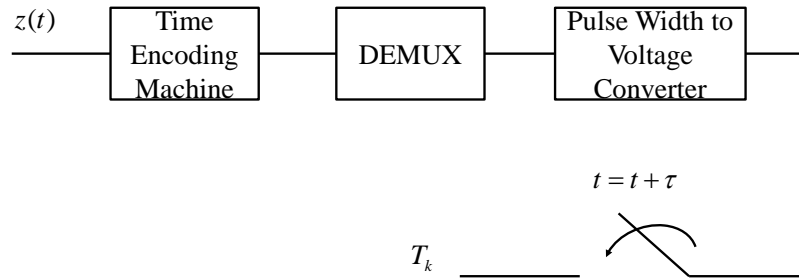


Figure 2.19: TEM receiver architecture. After [49], [50].

model can be expressed as

$$z(t) = \sum_{m=1}^{N-1} c_m \exp(j2\pi f m t) \quad (2.58)$$

where f is the fundamental frequency of the periodic signal $z(t)$. The compressive sensing problem can then be stated as

$$\mathbf{y} = \mathbf{P}\Phi_1 \mathbf{c}_1 \quad (2.59)$$

where P is a square matrix with entries

$$P_{i,j} = \begin{cases} -1, & i = j - 1 \\ 1, & i = j \\ 0, & \text{otherwise} \end{cases} \quad (2.60)$$

and

$$\Phi_{1k,m} = \exp(j2\pi f m t_k) \quad (2.61)$$

for $0 \leq k \leq n$, and $c_{1m} = \frac{g_1 c_m}{j2\pi m f}$ [49], [50].

In order to satisfy RIP, the measurement matrix is randomized by either randomizing the gain parameter, g_3 , shown in Figure 2.20a, or the switching threshold, δ , shown in Figure 2.20b. In both architectures, a pseudorandom number generator is triggered by the switching edge of the binary signal, $x(t)$. The advantage of the architecture in Figure 2.20b over that of Figure 2.20a is that the voltage level of the random number generator during the transition period between two random numbers does not affect the encoding or reconstruction process provided it reaches a steady state value prior to the hysteresis quantizer switching at the next time point [49], [50].

2.2.9 Comparison of Compressive Sensing Receivers

By comparing the various attributes of the major CS receivers, additional insight can be gained regarding the advantages and disadvantages of each receiver architecture. Several aspects were considered in [18], including whether exact CS signal reconstruction is possible, if Nyquist rate components are required, if single channel reconstruction is possible, if the data is easily visualized, if pseudo-random number generators are required, if the architecture is a folding architecture, and whether the architecture is linear. These attributes are summarized for each CS receiver architecture in Table 2.3.

The aspects examined help to determine which CS receiver architecture is best suited for an

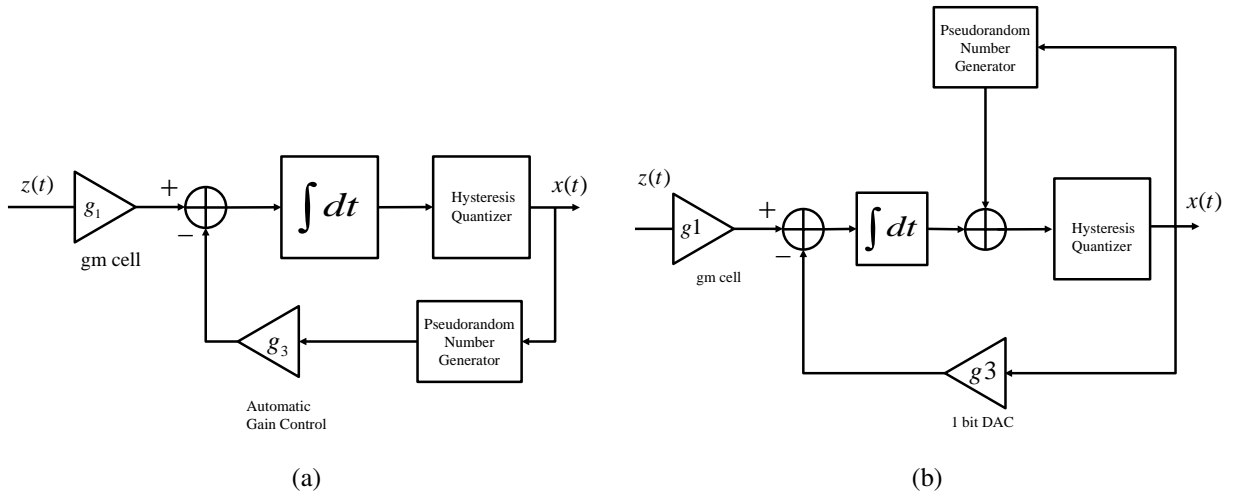


Figure 2.20: Time encoding machine random implementations (a) gain control, (b) random switching threshold. After [49], [50].

application. For instance, if a user interface requiring operator interpretation of the data is required, the NYFR, CMUX or MWC are well suited; however, the TEM or RD are not since the data is spread through use of a P-N code. Similarly, if it is desired to use a CS reconstruction algorithm in a linear receiver architecture, a receiver applying NoLAff processing or the TEM would not be a viable solutions; however, the other receiver architectures examined in Table 2.3 would be well suited for the application. If minimizing the amount of hardware required is the paramount consideration, then a single channel approach is desirable eliminating the RADC, CMUX, and MWC from consideration.

In this chapter, CS theory was introduced and different CS receiver architectures were presented. In Chapter 6 and Chapter 7, CS theory is applied to undersampled receiver architectures based on the SNS . In the following chapter, symmetrical number system theory is presented.

Table 2.3: Comparison of CS receivers. After [18].

Receiver	RD	Random Filter	RADC	CMUX	MWC	NoLAff	NYFR	TEM
Section	2.2.1	2.2.2	2.2.3	2.2.4	2.2.5	2.2.6	2.2.7	2.2.8
Is CS reconstruction possible?	Y	Y	Y	Y	Y	N ¹	Y	Y ²
Are all components sub-Nyquist?	N	N	N	Y	N	Y	Y	N
Is single channel reconstruction possible?	Y	Y	N	N ³	N	Y	Y	Y
Can data be easily visualized?	N	Y	N	Y	Y	Y	Y	N
Is a pseudo-random number generator required?	Y	N	Y	Y	Y	N	N	Y
Is the architecture a folding one?	N	Y	N	N	Y	Y	Y	N
Is the architecture linear?	Y	Y	Y	Y	Y	N	Y	N

¹ NoLAff output cannot be reconstructed using traditional CS algorithms, however, signal reconstruction is possible and is relatively straight forward.

² TEM requires a nonlinear transform in addition to CS reconstruction.

³ CMUX requires multiple RF tuner channels and mixing circuits.

THIS PAGE INTENTIONALLY LEFT BLANK

CHAPTER 3:

Symmetrical Number Systems

Symmetrical folding waveforms are the most common types of waveforms in engineering science and appear naturally in many engineering disciplines and system analysis techniques. Examples include sinusoidal signals in electrical engineering, symmetrical affine control systems in mechanical engineering, and symmetrical airfoil design in aeronautical engineering. To extract the maximum amount of information from symmetrical folding waveforms, symmetrical number systems were formulated that are based on a set of coprime moduli. Symmetrical number systems include the symmetrical number system (SNS) [51], [52], the optimum symmetrical number system (OSNS) [53], and robust symmetrical number system (RSNS) [8], [54]–[56]. In the following sections, the SNS, OSNS, and the RSNS are discussed.

3.1 Symmetrical Number System

The SNS is a modular number system that consists of N separate periodic symmetrically folded sequences based on a set of coprime moduli $m_i = \{m_1, m_2, \dots, m_N\}$. A symmetrical residue b_h is defined as

$$b_h = \min\{h, m - h\} \quad (3.1)$$

where h is an integer and $0 \leq h < m$ [51]. This function extends periodically with period m , such that

$$b_{h+nm} = b_h \quad (3.2)$$

where n is an integer and b_h is the symmetrical residue of $h + nm \bmod m$. If m is odd, the row vector consisting of the symmetrical residues is

$$\mathbf{b}_m = \left[0, 1, \dots, \left\lfloor \frac{m}{2} \right\rfloor, \left\lfloor \frac{m}{2} \right\rfloor, \dots, 2, 1\right], \quad (3.3)$$

where $\lfloor \bullet \rfloor$ is the floor operator. For m even,

$$\mathbf{b}_m = \left[0, 1, \dots, \frac{m}{2}, \frac{m}{2} - 1, \dots, 2, 1\right]. \quad (3.4)$$

The vector \mathbf{b}_m represents one period of a SNS folded sequence of length m .

Each integer h is represented by a vector,

$$\mathbf{B}_h = [b_h^1, b_h^2, \dots, b_h^N]^T, \quad (3.5)$$

composed of the N symmetrical residues b_h^i for that integer. For example, the symmetrical residues for a SNS with $m_i = \{3, 4\}$ are listed in Table 3.1 and graphically displayed in Figure 3.1. The ambiguous results are annotated in Table 3.1 using bold font.

Table 3.1: Symmetrical number system for moduli, $m_i = \{3, 4\}$.

h	0	1	2	3	4	5	6	...
$m_i = 3$	0	1	1	0	1	1	0	...
$m_i = 4$	0	1	2	1	0	1	2	...
	$\leftarrow \hat{M}_{SNS} \rightarrow$							

The span of integer values where each vector \mathbf{B}_h uniquely defines an integer is the dynamic range of the SNS \hat{M}_{SNS} . If one of the moduli is an even number, \hat{M}_{SNS} is defined as

$$\hat{M}_{SNS} = \min \left\{ \frac{m_1}{2} \prod_{l=2}^j m_{i_l} + \prod_{l=j+1}^N m_{i_l} \right\} \quad (3.6)$$

where j ranges from 1 to $N - 1$, $m_{i_2}, m_{i_3}, \dots, m_{i_N}$ range over all permutations of $\{2, 3, \dots, N\}$,

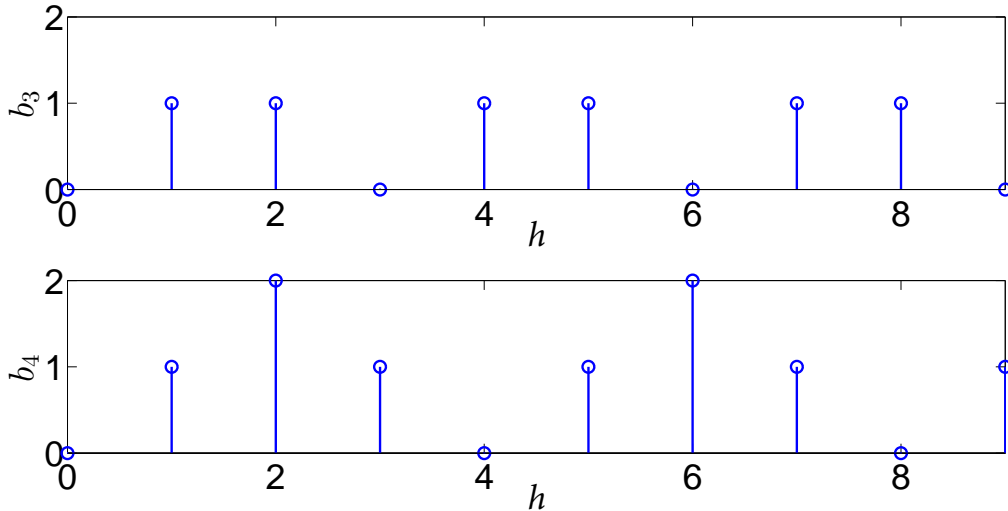


Figure 3.1: Graphical representation of a symmetrical number system for moduli $m_i = \{3, 4\}$.

and m_1 is the even modulus [51]. If all of the moduli are odd numbers,

$$\hat{M}_{SNS} = \min \left\{ \frac{1}{2} \prod_{l=1}^j m_{i_l} + \frac{1}{2} \prod_{l=j+1}^N m_{i_l} \right\} \quad (3.7)$$

where j ranges from 1 to $N-1$, and $m_{i_1}, m_{i_2}, \dots, m_{i_N}$ range over all permutations of $\{1, 2, \dots, N\}$ [51]. In the example shown in Table 3.1 and Figure 3.1, Equation (3.6) results in $\hat{M}_{SNS} = 5$.

3.2 The Relationship Between the Symmetrical Number System and the Discrete Fourier Transform

A fundamental principle in DSP is that an analog frequency f can be represented by a digital frequency ω in the z -domain where $\omega = (2\pi f)/f_s$ and $-\pi \leq \omega \leq \pi$. If $f > f_s/2$, it will map to a digital frequency equal to $\omega - 2\pi n$ where n is an integer. For example, if $f = 1.5f_s$ then $\omega = \pi$ which is indistinguishable from an analog frequency of $f = 0.5f_s$. This phenomenon is called aliasing.

The DFT of a discrete signal $x(p)$ is given by

$$X(k) = \sum_{p=0}^{P-1} x(p) e^{\frac{-j2\pi kp}{P}} \quad (3.8)$$

where $k = 0, 1, \dots, P-1$. Application of the DFT to a discrete time signal $x(p)$ yields a discrete power spectrum $|X(k)|^2$ where the energy in the signal is mapped to discrete digital frequencies, $\omega = (2\pi k)/P$. There are P discrete digital frequencies given by

$$\omega = \frac{2\pi}{P} \left[0, 1, \dots, \left\lfloor \frac{P}{2} \right\rfloor, \left\lceil \frac{P}{2} \right\rceil, \dots, P-2, P-1 \right] \quad (3.9)$$

for P odd and

$$\omega = \frac{2\pi}{P} \left[0, 1, \dots, \frac{P}{2}, \frac{P}{2} + 1, \dots, P-2, P-1 \right] \quad (3.10)$$

for P even.

For real signals, the digital frequencies in the range of $\pi \leq \omega \leq 2\pi$ are indistinguishable from

those between $0 \leq \omega \leq \pi$; therefore, Equation (3.9) and Equation (3.10) can be recast as

$$\omega = \frac{2\pi}{P} \left[0, 1, \dots, \left\lfloor \frac{P}{2} \right\rfloor, \left\lfloor \frac{P}{2} \right\rfloor, \dots, 1 \right] \quad (3.11)$$

for P odd, and

$$\omega = \frac{2\pi}{P} \left[0, 1, \dots, \frac{P}{2}, \frac{P}{2} - 1, \dots, 1 \right] \quad (3.12)$$

for P even. Comparing Equation (3.3) and Equation (3.4) to Equation (3.11) and Equation (3.12), the exact mapping of the DFT into the SNS format is observed [51]. This mapping of the DFT into the SNS structure allows receiver architectures based on SNS coprime undersampling to resolve single integer valued frequency ambiguities resulting from aliasing provided that $f < \hat{M}_{SNS}$.

3.3 Optimum Symmetrical Number System

Similar to the SNS, the OSNS is composed of N sequences based on a set of coprime moduli, $m_i = \{m_1, m_2, \dots, m_N\}$. The integers within each OSNS sequence form a symmetrically folded sequence with the period of the sequence equal to twice the coprime modulus $2m_i$. The integer values within the period of each individual OSNS sequence are given by the row vector

$$x_{m_i} = [0, 1, \dots, m_i - 1, m_i - 1, \dots, 1, 0]. \quad (3.13)$$

Due to the presence of ambiguities, the integers within Equation (3.13) do not form a complete system of length $2m_i$ by themselves. Similar to the SNS, the ambiguities that arise within the modulus are resolved by considering the paired values from all N sequences together. By considering the N paired sequences, the OSNS is rendered a complete system having a one-to-one correspondence with the residue number system (RNS).

The dynamic range of the OSNS equals the dynamic range of the RNS

$$M = \prod_{i=1}^N m_i, \quad (3.14)$$

which is also the location of the first repetitive vector [53]. As an example, $N = 2$ OSNS with $m_i = \{3, 4\}$ is displayed in Table 3.2. The ambiguous values are shown in bold font. In [53], the OSNS was shown to be an optimum scheme by using the multiplication principle. The OSNS has the largest dynamic range of the symmetrical number systems for a given moduli

Table 3.2: Optimum symmetrical number system with moduli, $m_i = \{3, 4\}$ and dynamic range, $M = 12$.

m_1	0	1	2	2	1	0	0	1	2	2	1	0	0
m_2	0	1	2	3	3	2	1	0	0	1	2	3	3
h	0	1	2	3	4	5	6	7	8	9	10	11	12

set, and therefore, requires the least number of comparators in folding ADC applications [53] or elements in DF antenna array applications [57]. However, the OSNS and the SNS can have the values of the symmetrical residues in each sequence change for an increment in the integer value represented by the N -tuple of symmetrical residues. Therefore, errors (invalid codes) can potentially occur if the circuitry (comparator circuits for example) do not change state simultaneously. To prevent this source of errors, the RSNS was developed which has an inherent integer Gray code property. The RSNS is discussed in the following section.

3.4 Robust Symmetrical Number System

The RSNS is a modular-based number system consisting of $N \geq 2$ integer sequences with each sequence associated with a coprime modulus m_i . The RSNS is based on the following sequence:

$$\{x'_m\} = [0, 1, 2, \dots, m-1, m, m-1, \dots, 2, 1]. \quad (3.15)$$

To form the N -sequence RSNS, each term in Equation (3.15) is repeated N times in succession. Therefore, the integers within one folding period of a sequence are:

$$\{x_m\} = [0, \dots, 0, 1, 1, \dots, 1, \dots, m-1, \dots, m-1, m, \dots, m, m-1, \dots, m-1, \dots, 1, \dots, 1]. \quad (3.16)$$

This results in a periodic sequence with a period of $P_m = 2Nm$ [8], [58]. Each sequence corresponding to m_i is also shifted left (or right) by $s_i = i - 1$ where $i \in \{1, 2, \dots, N\}$ and the shift values, $s_i = \{s_1, s_2, \dots, s_N\}$, form a complete residue system modulo N . The resulting structure of the N sequences ensures that two successive RSNS vectors (paired terms from all N sequences) when considered together, differ by only one integer resulting in an acyclic integer Gray code property [8], [59].

Each RSNS sequence is extended periodically with period $P_i = 2Nm$, as $x_{h+n2Nm} = x_h$, where $n \in \{0, \pm 1, \pm 2, \dots\}$. Therefore, x_h is a symmetrical residue of $(h + n2Nm)$ modulo $2Nm$. An

integer h is represented by a vector $X_h = [x_{1,h}, x_{2,h}, \dots, x_{N,h}]^T$ of N paired integers from each sequence at h . For example, the left shifted $N = 3$ RSNS with $m_i = \{3, 4, 5\}$, which is displayed in Table 3.3 and Figure 3.2, represents $h = 5$ with $X_h = [1, 2, 2]^T$. Examining Table 3.3 and Figure 3.2, the integer Gray code property is evident.

Since the integer values within each modulus consists of $2Nm$ integers, the symmetrical residues are determined by first subtracting an integer multiple of $2Nm$ from h as

$$n_i = h - \left\lfloor \frac{h}{2Nm_i} \right\rfloor 2Nm_i. \quad (3.17)$$

The symmetrical residue x_h is then calculated as [8], [58]

$$x_h = \begin{cases} \left\lfloor \frac{n_i - s_i}{N} \right\rfloor, & s_i \leq n_i \leq Nm_i + s_i + 1 \\ \left\lfloor \frac{2Nm_i + N - n_i + s_i - 1}{N} \right\rfloor, & Nm_i + s_i + 2 \leq n_i \leq 2Nm_i + s_i - 1 \end{cases}. \quad (3.18)$$

The N -sequence RSNS is periodic with a fundamental period of

$$P_f = 2NM, \quad (3.19)$$

where $M = \prod_{i=1}^N m_i$ is the dynamic range of a RNS [8], [56], [57].

Closed-form expressions for \hat{M}_{RSNS} exists for only few specific cases. In [8], [54], a closed-form

Table 3.3: Three sequence robust symmetrical number system structure for moduli $m_i = \{3, 4, 5\}$, after [8].

h	0	1	2	3	4	5	6	7	8	9	10	11	12	13	14	15	16 ...
$m_1 = 3$	0	0	0	1	1	1	2	2	2	3	3	3	2	2	2	1	1 ...
X_h $m_2 = 4$	0	0	1	1	1	2	2	2	3	3	3	4	4	4	3	3	3 ...
$m_3 = 5$	0	1	1	1	2	2	2	3	3	3	4	4	4	5	5	5	4 ...

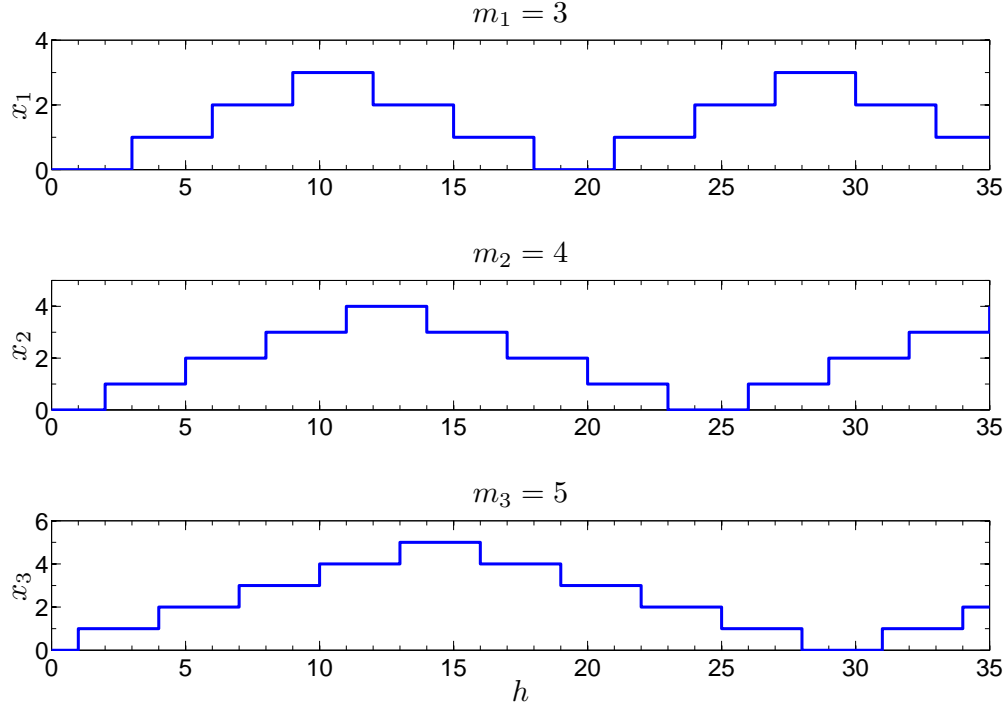


Figure 3.2: Graphical depiction of a three-sequence robust symmetrical number system for moduli $m_i = \{3, 4, 5\}$. After [8].

expression for a $N = 2$ RSNS is reported, where

$$\hat{M}_{RSNS} = 6m_1 - 3, \text{ and } m_2 = m_1 + 1 \text{ when } m_1 \geq 3 \quad (3.20)$$

$$\hat{M}_{RSNS} = \begin{cases} 4m_1 + 2m_2 - 5, & \text{when } m_2 \leq m_1 + 2 \\ 4m_1 + 2m_2 - 2, & \text{when } m_2 \geq m_1 + 3 \end{cases} \quad (3.21)$$

and $5 \leq m_1 < m_2$. The other published closed-form expression for \hat{M}_{RSNS} is when $N = 3$ and $m_i = \{m - 1, m, m + 1\}$ with m even and $m > 3$ [8], [57]. In this case,

$$\hat{M}_{RSNS} = \frac{3}{2}m^2 + \frac{15}{2}m + 7. \quad (3.22)$$

Additional closed-form expressions for \hat{M}_{RSNS} are developed and presented in Chapter 4.

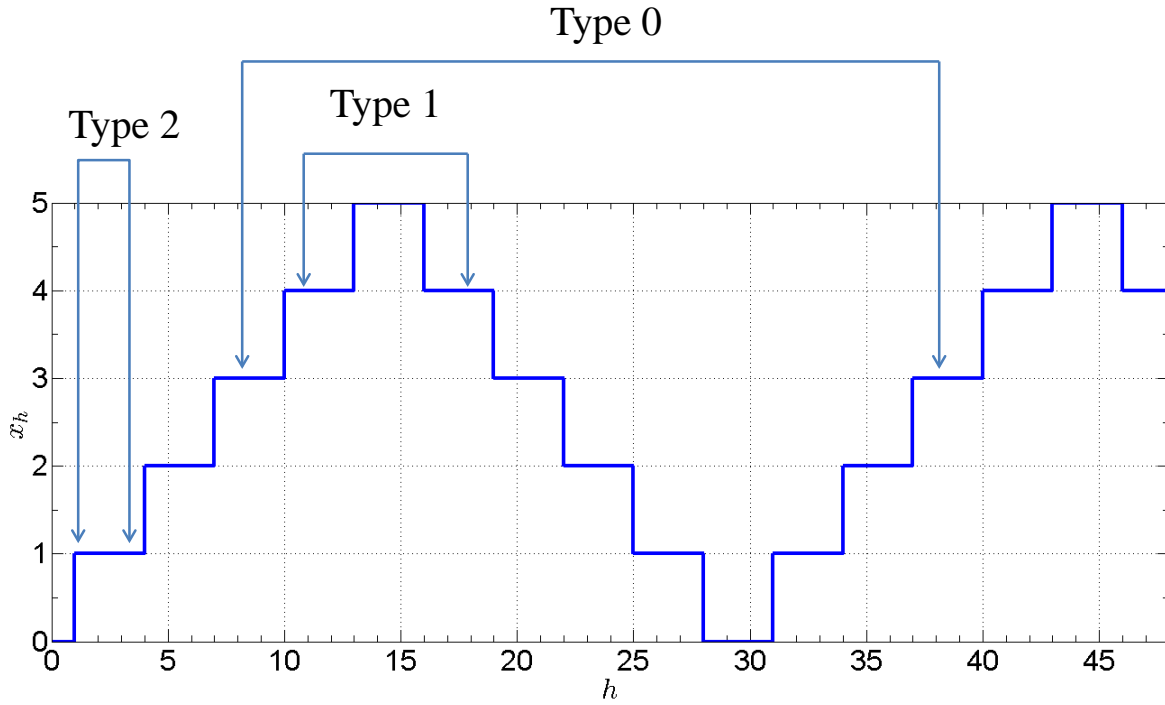


Figure 3.3: Graphical representation of the single sequence ambiguity types for a robust symmetrical number system ($N=3$, $m=5$), after [8].

3.5 Robust Symmetrical Number System N-Sequence

Ambiguity Analysis

In the fundamental period of an N -sequence RSNS, there are three types of ambiguities, Type 0, Type 1, and Type 2 that are illustrated in Figure 3.3. Type 0 ambiguities occur periodically in each RSNS sequence. Type 1 ambiguities occur across the folds of each sequence, and Type 2 ambiguities occur at the repetition of each number that results in the staircase sequence. Each RSNS sequence can be decimated into N subsequences where each subsequence is composed of values of the original sequences at $h \equiv 0 \pmod{N}$, $h \equiv 1 \pmod{N}$, \dots , and $h \equiv N - 1 \pmod{N}$. By examining these subsequences, the Type 2 ambiguities are eliminated leaving only Type 0 and Type 1 ambiguities. Table 3.4 illustrates the subsequence structure for a single sequence of a three-sequence RSNS. Each subsequence can be plotted and shown to have terms with the same arrangement as the SNS. Also, by analyzing the parity of the RSNS in Table 3.5, it can be shown that the parity of the sequence repeats at a period of $2N$; therefore, ambiguous vectors \mathbf{X}_h and \mathbf{X}_{h+k} occur at multiples of six for this example [8], [55], [60].

Table 3.4: Single sequence of a three-sequence RSNS illustrating the decomposition into subsequences, after [8].

$m_i = 3$	x_h	0	0	0	1	1	1	2	2	2	3	3	3	2	2	2	1	1
$h \equiv 0 \pmod 3$	x_h	0			1			2			3			2			1	
$h \equiv 1 \pmod 3$	x_h		0			1			2			3			2			1
$h \equiv 2 \pmod 3$	x_h			0			1			2			3			2		
	h	0	1	2	3	4	5	6	7	8	9	10	11	12	13	14	15	16

Table 3.5: Parity (e = even, o = odd) of residue vectors, after [8].

h	0	1	2	3	4	5	6	7	8	9	10	11	12	13	14	15	16
$m_1 = 3$	e	e	e	o	o	o	e	e	e	o	o	o	e	e	e	o	o
$m_2 = 4$	e	e	o	o	o	e	e	e	o	o	o	e	e	e	o	o	o
$m_3 = 5$	e	o	o	o	e	e	e	o	o	o	e	e	e	o	o	o	e

The ambiguity locations are determined by solving the congruence equations for each combination of Type 0 and Type 1 ambiguities that exist. The various ambiguity combinations are referred to by three digit *Case Numbers* where the first digit refers to the number of Type 1 ambiguities and ranges from zero to $N - 1$. The second digit represents the particular assignment of Type 0 and Type 1 ambiguities to specific sequences. For instance, for a three-sequence RSNS having one Type 1 ambiguity and two Type 0 ambiguities, the possible ambiguity combinations are

$$\{amb_3, amb_2, amb_1\} = \begin{cases} \{0, 0, 1\} \text{ Case11X} \\ \{0, 1, 0\} \text{ Case12X} , \\ \{1, 0, 0\} \text{ Case13X} \end{cases} \quad (3.23)$$

where amb_i is the ambiguity type for the i -th channel. The third digit of the case number represents the subsequence index and ranges from zero to $N - 1$ [8].

For an N -sequence RSNS, there are 2^N possible Type 0 and Type 1 ambiguity combinations. Each combination has N subsequences with the exception of when all ambiguities are Type 0 ambiguities so the total number of possible ambiguity combinations is $N2^N - N + 1$. The num-

ber of ambiguity combinations containing T_1 Type 1 ambiguities is

$$N \binom{N}{T_1} = N \frac{N!}{T_1! (N - T_1)!}. \quad (3.24)$$

To determine \hat{M}_{RSNS} , the ambiguity locations are determined by solving congruence equations for all combinations of Type 1 and Type 0 ambiguities, and the largest span of unambiguous values is identified which is equal to \hat{M}_{RSNS} . The location of the Type 0 ambiguity for a single i -th sequence is

$$\frac{k}{2N} \equiv 0 \pmod{m_i} \quad (3.25)$$

and for the Type 1 ambiguities, the congruence equations are of the form

$$\frac{k}{2N} \equiv \begin{cases} -\frac{h}{N} \pmod{m_i}, & \text{if } h \equiv 0 \pmod{N} \\ -\frac{h-1}{N} \pmod{m_i}, & \text{if } h \equiv 1 \pmod{N} \\ \vdots \\ -\frac{h+i-1}{N} \pmod{m_i}, & \text{if } h \equiv N-i+1 \pmod{N} \\ \vdots \\ -\frac{h+1}{N} \pmod{m_i}, & \text{if } h \equiv N-1 \pmod{N} \end{cases} \quad (3.26)$$

and account for each sequence i being shifted by $i-1$ positions to the left. Table 3.6 summarizes the solution to the congruence equations and defines the centers of ambiguity (COA) for all possible case numbers [8], [55], [60] for a N -sequence RSNS. The COA is defined as the midpoint between the ambiguous vector pairs and is presented in more detail in Chapter 4.

In Table 3.6, the value of h_s is solved for by solving a set of congruence equations using the CRT. For example, the congruence equations that represent the shift value h_{s_1} for a four-sequence

Table 3.6: N-sequence robust symmetrical number system summary of congruence equation solutions for ambiguity locations. Ambiguities exist at h and $h+k$. Index i denotes the sequences with Type 1 ambiguities and the index j denotes the sequences containing Type 0 ambiguities. After [8].

Case Number	h is	k is a multiple of	COA
010	Anywhere in fundamental period	$P_f = 2N \prod_{i=1}^N m_i$	None
1X0	$h = aNm_i - \frac{k}{2}$	$2N \frac{M}{m_i}$	aNm_i
1XX	$h = aNm_i + h_s - \frac{k}{2}$	$2N \frac{M}{m_i}$	$h_s + aNm_i$
$2X0 \cdots (N-1)X0$	$h = aN \prod_i m_i - \frac{k}{2}$	$2N \prod_j m_j$	$aN \prod_i m_i$
$2XX \cdots (N-1)XX$	$h = aN \prod_i m_i + h_s - \frac{k}{2}$	$2N \prod_j m_j$	$h_s + aN \prod_i m_i$
$N10$	$h = aN \prod_{n=1}^{n=N} m_n - \frac{k}{2}$	$2N$	$aN \prod_{n=1}^{n=N} m_n$
$N1X$	$h = aN \prod_{n=1}^{n=N} m_n + h_s - \frac{k}{2}$	$2N$	$h_s + aN \prod_{n=1}^{n=N} m_n$

RSNS are

$$\begin{aligned}
 \frac{h_{s1} - 1}{4} &\equiv 0 \pmod{m_1} \\
 \frac{h_{s1} - 1}{4} &\equiv 0 \pmod{m_2} \\
 \frac{h_{s1} - 1}{4} &\equiv 0 \pmod{m_3} \\
 \frac{h_{s1} + 3}{4} &\equiv 0 \pmod{m_4}
 \end{aligned} \quad . \tag{3.27}$$

The congruence equations are represented by a matrix that is formed by collecting the Type 1 symmetrical residue numerators into a matrix form with each column index corresponding to its corresponding modulus. This matrix will be referred to as a shift matrix. For example, Equation (3.27) is represented by the second row of the matrix. The shift matrix has a unique structure where the first column is $[0, -1, -2, \dots, N-1]^T$ and the subsequent columns are generated by circular shifting the previous column up and incrementing each value by one. An

example of the shift matrix for $N=4$ is

$$h_s \Rightarrow \begin{bmatrix} 0 & 0 & 0 & 0 \\ -1 & -1 & -1 & 3 \\ -2 & -2 & 2 & 2 \\ -3 & 1 & 1 & 1 \end{bmatrix}. \quad (3.28)$$

In general, the shift matrix is a $N \times N$ matrix defined as

$$h_s \Rightarrow \begin{bmatrix} 0 & 0 & \dots & \dots & \dots & 0 \\ -1 & -1 & \dots & \dots & -1 & N-1 \\ -2 & \dots & \dots & -2 & N-2 & \vdots \\ \vdots & \dots & \ddots & \ddots & \ddots & \vdots \\ -N+2 & -N+2 & \ddots & \ddots & \ddots & 2 \\ -N+1 & 1 & \dots & \dots & 1 & 1 \end{bmatrix}. \quad (3.29)$$

Note that the last column is of the form $[0, N-1, N-2, \dots, 1]$ and that the right to left diagonals are formed by subtracting one from the previous element on the diagonal. Subsequently, the main right to left diagonal is equal to the first column, that is

$$\begin{bmatrix} h_{s11} \\ h_{s21} \\ \vdots \\ h_{s(N-1)1} \\ h_{sN1} \end{bmatrix} = \begin{bmatrix} h_{s1N} \\ h_{s2(N-1)} \\ \vdots \\ h_{s(N-1)2} \\ h_{sN1} \end{bmatrix}. \quad (3.30)$$

The congruence equations are formed based on the sequences containing the Type 1 ambiguities and the subsequences that contain the ambiguities. For example, if $N = 4$ and the case number is 232, the sequences containing the Type 1 ambiguities would be those formed by moduli, m_2 and m_3 , and referring to Equation (3.28), the third row corresponds to the subsequence. The resulting system of congruence equations are

$$\begin{aligned} \frac{h_s - 2}{4} &\equiv 0 \pmod{m_2} \\ \frac{h_s + 2}{4} &\equiv 0 \pmod{m_3}. \end{aligned}$$

In this chapter, the SNS, OSNS, and RSNS were discussed. In the following chapter, an efficient search algorithm for determining \hat{M}_{RSNS} is presented that is applied to develop additional closed-form expressions for several families of moduli sets. The RSNS is applied to a photonic DF array in Chapter 5, and the SNS is applied to CS receiver architectures in Chapter 6 and Chapter 7.

THIS PAGE INTENTIONALLY LEFT BLANK

CHAPTER 4:

Determining Additional Closed-Form Expressions for the Dynamic Range of the Robust Symmetrical Number System

The RSNS has an inherent integer Gray code property that makes the RSNS particularly attractive for error control in both analog and digital signal processing applications. The RSNS has been shown to be useful in software radio systems for sample rate conversion [61], and in electronic [62], [63], photonic [58] and superconducting [64] folding ADCs. Due to the inherent symmetry within the modulus, a new theoretic transform for error detection and control was reported in [65] and applied to CDMA wireless communications [66]. The complexity of DF antenna systems is also reduced through use of the RSNS by decomposing the spatial filtering operation into a number of parallel sub-operations [57]. Consequently, each sub-operation only requires a complexity in accordance with that modulus and a much higher spatial resolution is achieved after the results of these less complex sub-operations are recombined. The use of the RSNS in radar waveform design has also been reported in [67] to extend the capabilities for target detection.

Despite the many diverse applications for the RSNS, the lack of a general closed-form expression for \hat{M}_{RSNS} has limited its wide-spread adoption. In this chapter, an efficient algorithm [8], [55] is presented for determining \hat{M}_{RSNS} , and the computational complexity of the efficient algorithm is compared to that of a naïve search algorithm. The efficient algorithm is then used to develop data sets for several groups of coprime moduli that are curve fitted to generate closed-form expressions for \hat{M}_{RSNS} . The closed-form analytical expressions generated from curve fitting are verified by generating them from the equations defining the ambiguity locations in Table 3.6.

4.1 Efficient Algorithm for Determining the Dynamic Range of the Robust Symmetrical Number System

In this section, an efficient algorithm is developed to efficiently compute \hat{M}_{RSNS} for N RSNS integer sequences with arbitrary coprime moduli, m_i , where $m_i \geq 2$, by first considering all

the minimal pair ambiguity locations (h_1, h_2) . For the general N -sequence RSNS case, let $C = \{(h_1, h_2) \mid 0 \leq h_1 < h_2 < P_f\}$ where $X_{h_1} = X_{h_2}$. A pair $(h_1, h_2) \in C$ is minimal if there does not exist a pair $(\tilde{h}_1, \tilde{h}_2) \in C$ such that $h_1 \leq \tilde{h}_1 < \tilde{h}_2 \leq h_2$ and the shorter sequence length, $\tilde{h}_2 - \tilde{h}_1 < h_2 - h_1$. The largest distance between *consecutive* minimal pairs, $h_2 - h_1 - 1$, is the \hat{M}_{RSNS} and $h_1 + 1$ is the starting position of \hat{M}_{RSNS} [56]. It then follows that $\hat{M}_{RSNS} < M = \prod m_i$, the dynamic range of the RNS [8].

In [8], it was demonstrated that the distance between ambiguous vector pairs is always odd; therefore, the COA is defined as the midpoint between the ambiguous vector pairs, $COA = (h_2 + h_1) / 2$. Given two minimal pairs $P_1 = (h_1, h_2) \in C$ with COA_{P_1} and $P_2 = (h'_1, h'_2) \in C$ with COA_{P_2} and $COA_{P_1} < COA_{P_2}$, the pairs are defined as consecutive if there does not exist a minimal pair $P_3 = (h''_1, h''_2) \in C$ with COA_{P_3} such that $COA_{P_1} < COA_{P_3} < COA_{P_2}$. Therefore, if $(h_1, h_2) \in C$ and $(h'_1, h'_2) \in C$ are consecutive minimal pairs, the maximal size $\hat{M}_{RSNS} = (h'_2 - 1) - (h_1 + 1) + 1 = h'_2 - h_1 - 1$ is the \hat{M}_{RSNS} . Furthermore, $h_1 + 1$ is the beginning position of the \hat{M}_{RSNS} . Since \hat{M}_{RSNS} is computed using consecutive minimal pairs $(h_1, h_2) \in C$ and $(h'_1, h'_2) \in C$, only the positions of the minimal pairs that can affect the length of \hat{M}_{RSNS} are required to be computed and the rest can be ignored [56], [68].

The algorithm for computing \hat{M}_{RSNS} relies on a number of lemmas, presented in Section 4.1.1, most of which are the result of an analysis of the locations of all vector ambiguities provided in [8]. Table 3.6 summarizes the N -channel RSNS vector ambiguity locations. The rows in Table 3.6 separate the locations of the ambiguity pairs into seven categories based on the *type* of ambiguity.

4.1.1 Theoretical Basis for Efficient Algorithm

In this section, the basis for the efficient algorithm for determining \hat{M}_{RSNS} is presented in a series of lemmas and theorems. From this theoretical foundation, the steps of the algorithm are developed and presented in Section 4.1.2.

Lemma 1. *There are 2^N distinct cases of repeated ambiguity pairs, each with a different ambiguity length and COA spacing. All but one of the 2^N cases have N subcases that have the same number of COAs and ambiguity lengths in P_f , but the COA for each of the subcases is shifted by a particular value, h_{s_i} .*

The N COA shifts (one for each subcase) are computed by solving a set of N congruence equations using the CRT. The subcase where $h_{s_0} = 0$ is called the base case and is shown in rows 2,

4, and 6 in Table 3.6 [56].

Proof. See the ambiguity analysis discussion in Section II of [8]. \square

Lemma 2. *Minimal pairs are computed using the first multiple of k from the third column in Table 3.6.*

Proof. Any vector pair computed using a higher multiple of k forms a vector pair that encompasses and is symmetric about the vector pair obtained using the lower multiple of k . Therefore, any vector pair computed using other than the first multiple of k is not minimal [8]. \square

Lemma 3. *For every ambiguity pair with a COA at h , there is an ambiguity pair with the same length at $h + P_f/2$.*

Proof. Given a general COA for any case at

$$h = a \left(N \prod_i m_i \right), \quad (4.1)$$

where the subscripts i are the indices of all vector elements with Type 1 ambiguity, there is also a COA at $h + P_f/2$ because

$$\begin{aligned} a \left(N \prod_i m_i \right) + \frac{P_f}{2} &= a \left(N \prod_i m_i \right) + N \prod_{n=1}^N m_n \\ &= a \left(N \prod_i m_i \right) + N \left(\prod_i m_i \prod_j m_j \right) \\ &= \left(a + \prod_j m_j \right) \left(N \prod_i m_i \right) \\ &= b \left(N \prod_i m_i \right), \end{aligned} \quad (4.2)$$

where a and b are any integers, j corresponds to the vector elements with Type 0 ambiguities, and i corresponds to the vector elements with Type 1 ambiguities. The result is that ambiguity pairs are symmetric about $P_f/2$ [56], [68]. \square

Lemma 4. *There is always an ambiguity with a COA at $h = 0$ and $h = P_f/2$ with a length of $2N + 1$, which is also the ambiguity with the smallest length.*

Proof. This is straightforward via inspection of row 6 in Table 3.6. \square

Lemma 5. *Using Lemma 3 and Lemma 4, only ambiguities from $-N$ to $P_f/2 + N$ need to be considered when computing \hat{M}_{RSNS} .*

Proof. Since Lemma 3 showed that ambiguity pairs are symmetric about $P_f/2$, and \hat{M}_{RSNS} is computed from minimal ambiguity pair locations, the same length \hat{M}_{RSNS} exists from $h = 0$ to $h = P_f/2$ as exists from $h = P_f/2$ to $h = P_f$ [56], [68]. \square

Lemma 6. *\hat{M}_{RSNS} is upper bounded by (using the complement notation $\bar{I} = \{1, \dots, n\} \setminus I$) [56], [68]*

$$\hat{M}_{RSNS} \leq B_{\hat{M}_{RSNS}} := N \min_{I \subseteq \{1, \dots, n\}} \left[\prod_{i \in I} m_i + 2 \prod_{j \in \bar{I}} m_j \right] - 1. \quad (4.3)$$

That is, each of the rows in Table 3.6 produce a unique set of minimal pairs and the row that has the smallest local \hat{M}_{RSNS} (the one that minimizes Equation (4.3)) provides an upper bound on \hat{M}_{RSNS} . Any ambiguity pair that has a length greater than $B_{\hat{M}_{RSNS}}$ does not affect \hat{M}_{RSNS} and can be ignored (i.e., \hat{M}_{RSNS} is smaller than the distance between the minimal pair and therefore cannot contain the vector pair) [8].

As an example, let $N = 3$ and $m_i = \{3, 4, 5\}$. Computing the expressions inside the minimum of Equation (4.3), for each of the 2^n subsets $I \subseteq \{1, 2, \dots, n\}$,

$$\begin{aligned} B_1 &= [1 + 2(3 \cdot 4 \cdot 5)] = 121 \\ B_2 &= [3 + 2(4 \cdot 5)] = 43 \\ B_3 &= [4 + 2(3 \cdot 5)] = 34 \\ B_4 &= [5 + 2(3 \cdot 4)] = 29 \\ B_5 &= [(3 \cdot 4) + 2(5)] = 22 \\ B_6 &= [(3 \cdot 5) + 2(4)] = 23 \\ B_7 &= [(4 \cdot 5) + 2(3)] = 26 \\ &\text{and} \\ B_8 &= [(3 \cdot 4 \cdot 5) + 2(1)] = 65. \end{aligned} \quad (4.4)$$

Applying Lemma 6,

$$B_{\hat{M}_{RSNS}} = 3 \min_i (B_i) - 1 = 3 \cdot 22 - 1 = 65. \quad (4.5)$$

Theorem 7. Assuming $M \geq 4$, an upper bound for \widehat{M}_{RSNS} is

$$B_{\widehat{M}_{RSNS}} \leq N \lceil 2\sqrt{2M} \rceil - 1. \quad (4.6)$$

Moreover, if $N \geq 3$, $\widehat{M}_{RSNS} < M$.

Proof. Setting $x = \prod_{i \in I} m_i$, the expression that must be minimized in the right-hand side of Equation (4.3) is the function

$$f(x) = x + \frac{2M}{x}, x \geq 1. \quad (4.7)$$

By examining the derivative of $f(x)$, a simple calculus analysis reveals that the function has a global minimum at $x = \sqrt{2M}$, namely $2\sqrt{2M}$, and the first inequality is shown [68].

The proof of $\widehat{M}_{RSNS} < M$ for $N = 3$ is contained in [8]. Examples when $N = 3$ are listed in lexicographical order in Table 4.1.

Table 4.1: Comparison of the dynamic range for a three-sequence robust symmetrical number system to that of a three-sequence residue number system, from [68].

$\mathbf{m_i}$	$\widehat{\mathbf{M}}_{\mathbf{RSNS}}$	\mathbf{M}
$\{2, 3, 5\}$	28	30
$\{2, 3, 7\}$	35	42
$\{2, 3, 11\}$	46	66
$\{3, 4, 5\}$	43	60

Now, assume that $N \geq 4$. The next step requires proving that $N \lceil 2\sqrt{2M} \rceil < M$, for $N \geq 4$. Starting with the simple inequality

$$N \lceil 2\sqrt{2M} \rceil \leq N(2\sqrt{2M} + 1), \quad (4.8)$$

it is sufficient to show that $N(2\sqrt{2M} + 1) \leq M$, which is equivalent to $N\sqrt{8M} \leq M - N$, and $8N^2M \leq M^2 + N^2 - 2MN$, that is, $M^2 - 2N(4N + 1)M + N^2 > 0$.

Looking at the previous inequality as the sign of a concave-up parabola in M , the inequality is true, as long as

$$M > 4N^2 + N + 2N\sqrt{4N^2 + 2N}. \quad (4.9)$$

If $N = 4$, then $M \geq 210$, and the right-hand side of Equation (4.9) is ~ 209.881 ; if $N = 5$, then $M \geq 2310$, and the right-hand side of Equation (4.9) is ~ 299.88 . Thus, the inequality Equation (4.9) is true for $4 \leq N \leq 5$.

Next, it is observed that for any $N \geq 3$ (use the fact that the moduli are coprime): if $N = 3$, then

$$M \geq \begin{cases} 2 \cdot 3 \cdot 5 = 30, & N = 3 \\ 2 \cdot 3 \cdot 5 \cdot 7 = 210, & N = 4 \\ \text{etc.} \end{cases} \quad (4.10)$$

$M \geq 2 \cdot 3 \cdot 5 = 30$; if $N = 4$, then $M \geq 2 \cdot 3 \cdot 5 \cdot 7 = 210$, etc. For arbitrary N , an easy inductive procedure reveals that $M \geq P_N\#$, where $P_N\# = \prod_{k=1}^N p_k$ is the primorial function, and p_k is the k th prime. It is well-known (and easily derivable by using the prime number theorem [69]) that $P_N\# = \exp[(1 + o(1))n \log n]$.

Assume $N \geq 6$. It is immediate that $P_N\# > (N + 1)!$.

For $N \geq 6$, the right hand side of the above inequality satisfies

$$(N + 1)! > 4N^2 + N + 2N\sqrt{4N^2 + 2N}, \quad (4.11)$$

which implies Equation (4.11).

Proving Equation (4.11) by induction on N , if $N = 6$, then

$$(6 + 1)! - \left(4 \cdot 6^2 + 6 + 2 \cdot 6\sqrt{4 \cdot 6^2 + 2 \cdot 6}\right) > 4740,$$

and so, the inequality Equation (4.11) is true in this case. Assuming that the inequality is true for N , it is shown for $N + 1$ to be true. Starting from Equation (4.11), multiply both sides by $N + 2$ to get

$$(N + 2)! > (N + 2) \cdot \left(4N^2 + N + 2N\sqrt{4N^2 + 2N}\right). \quad (4.12)$$

It will be sufficient to show that

$$(N + 2) \left(4N^2 + N + 2N\sqrt{4N^2 + 2N}\right) > 4(N + 1)^2 \quad (4.13)$$

$$+ (N + 1) + 2(N + 1)\sqrt{4(N + 1)^2 + 2(N + 1)}. \quad (4.14)$$

Since

$$(N+2)(4N^2+N) - 4(N+1)^2 - (N+1) = 4N^3 + 5N^2 - 7N - 5 \quad (4.15)$$

is increasing and greater than 0, for $N \geq 6$, the previous inequality will follow if

$$(N+2)2N\sqrt{4N^2+2N} > 2(N+1)\sqrt{4(N+1)^2+2(N+1)}, \quad (4.16)$$

which by squaring both sides transforms into

$$-24 - 88N - 120N^2 - 40N^3 + 80N^4 + 72N^5 + 16N^6 > 0, \quad (4.17)$$

which is true for $N \geq 6$. This concludes the proof of the theorem [56], [68]. \square

Lemma 8. *In the case of 3-channel RSNS of coprime moduli $m_1 < m_2 < m_3$, \hat{M}_{RSNS} is upper bounded by*

$$B_{\hat{M}_{RSNS}} = \begin{cases} N(m_1m_2 + 2m_3) - 1 & \text{if } m_1m_2 \geq m_3 \\ N(m_3 + 2m_1m_2) - 1 & \text{if } m_2m_3 < m_3. \end{cases} \quad (4.18)$$

Proof. Minimizing the expressions (from Equation (4.3)):

$$\begin{aligned} \alpha_1 &= m_1m_2 + 2m_3 \\ \alpha_2 &= m_1m_3 + 2m_2 \\ \alpha_3 &= m_2m_3 + 2m_1 \\ \alpha_4 &= m_1m_2m_3 + 2 \\ \alpha_5 &= 1 + 2m_1m_2m_3 \\ \alpha_6 &= m_1 + 2m_2m_3 \\ \alpha_7 &= m_2 + 2m_1m_3 \\ \alpha_8 &= m_3 + 2m_1m_2. \end{aligned} \quad (4.19)$$

By inspection, $\alpha_1 < \alpha_2 < \alpha_3 < \alpha_4$ and $\alpha_8 < \alpha_7 < \alpha_6 < \alpha_5$. Therefore, only α_1 and α_8 need to be compared, which is equivalent to comparing m_1m_2 and m_3 . \square

For instance, if $N = 3$, $m_i = \{3, 4, 5\}$, since $m_1m_2 \geq m_3$, then $B_{\hat{M}_{RSNS}} = 3(3 \cdot 4 + 2 \cdot 5) - 1 = 65$ [68].

4.1.2 Efficient Algorithm for Determining \hat{M}_{RSNS}

Using Lemmas 1 through 8 in Section 4.1.1, the efficient algorithm for computing \hat{M}_{RSNS} follows the steps below [68]

- S1. Define N as the number of coprime moduli $(m_i)_{1 \leq i \leq N}$, $M = \prod_{i=1}^N m_i$, and fundamental period of the RSNS, $P_f = 2MN$.
- S2. Compute the upper bound $B_{\hat{M}_{RSNS}}$ for the dynamic range, Equation (4.6) of Theorem 7, or Equation (4.18) of Lemma 8, if $N = 3$.
- S3. Compute the number of ambiguity cases for the particular RSNS using Table 3.6 and the limits imposed by Lemma 1. Compute the minimal-pair distance for all ambiguity pair cases using multiplication of corresponding entries in the matrix of size $N \times 2^N$, which is the matrix containing as columns all of the N subcases of the 2^N distinct cases of repeating ambiguity pairs, and eliminate all ambiguity pair cases that have a length greater than the dynamic range upper bound (step S2).
- S4. Compute the remaining minimal pair ambiguity locations (h_1, h_2) using Table 3.6 and Lemmas 2 and 5.
- S5. Sort the matrix of minimal pairs (h_1, h_2) such that h_2 is monotonically increasing. Vector subtract the start positions of consecutive minimal pairs $(h_1(p) - h_1(p+1))$ and remove all minimal pairs where the result is negative. The remaining minimal pairs are the only *consecutive* minimal pairs.
- S6. Compute the vector of distances between endpoints of consecutive minimal pairs $(h_2(p+1) - h_1(p) - 1)$. The dynamic range \hat{M}_{RSNS} is the largest value in the resulting vector.

As an example, consider the RSNS from Table 3.3 where $N = 3$, $m_i = \{3, 4, 5\}$. Table 3.6 provides the general N -sequence ambiguity expressions and Table I of reference [8] provides the general ambiguity pair equations for the $N = 3$ case.

- S1. Define $N = 3$, $M = \prod_{i=1}^N m_i = 60$, and $P_f = 360$.
- S2. Compute the dynamic range upper bound by using Theorem 7 (in which case, $\lceil 6\sqrt{120} \rceil - 1 = \lceil 65.7267 \rceil - 1 = 65$), or (since $N = 3$) Lemma 8 (in which case, $3(3 \cdot 4 + 2 \cdot 5) - 1 = 65$).
- S3. Table 4.2 shows all possible ambiguity cases (using Table 3.6, or Table I in [8]) and points out (above the double line) the rows that have ambiguity pairs with a length (min k) greater than $B_{\hat{M}_{RSNS}} = 65$, which can be ignored in the computation of \hat{M}_{RSNS} . The base cases (all cases ending in zero in Table 4.2) do not have shifts applied to the COA

Table 4.2: Calculation of ambiguity locations for all ambiguity cases for a three sequence robust symmetrical number system with moduli $m_i = \{3, 4, 5\}$ and $a \in \mathbb{Z}$, from [68]

Case Label	Ambiguities occur at h and $h + k$, where h is	min k
Case 010	Any position	360
Case 110	$h_{\text{Case 110}} = a \cdot 9 - 60$	120
Case 111	$h_{\text{Case 111}} = a \cdot 9 - 59$	
Case 112	$h_{\text{Case 112}} = a \cdot 9 - 58$	
Case 120	$h_{\text{Case 120}} = a \cdot 12 - 45$	90
Case 121	$h_{\text{Case 121}} = a \cdot 12 - 44$	
Case 122	$h_{\text{Case 122}} = a \cdot 12 - 46$	
Case 130	$h_{\text{Case 130}} = a \cdot 15 - 36$	72
Case 131	$h_{\text{Case 131}} = a \cdot 15 - 38$	
Case 132	$h_{\text{Case 132}} = a \cdot 15 - 37$	
Case 210	$h_{\text{Case 210}} = a \cdot 36 - 15$	30
Case 211	$h_{\text{Case 211}} = a \cdot 36 + h_{s1} - 15$	
Case 212	$h_{\text{Case 212}} = a \cdot 36 + h_{s2} - 15$	
Case 220	$h_{\text{Case 220}} = a \cdot 45 - 12$	24
Case 221	$h_{\text{Case 221}} = a \cdot 45 + h_{s1} - 12$	
Case 222	$h_{\text{Case 222}} = a \cdot 45 + h_{s2} - 12$	
Case 230	$h_{\text{Case 230}} = a \cdot 60 - 9$	18
Case 231	$h_{\text{Case 231}} = a \cdot 60 + h_{s1} - 9$	
Case 232	$h_{\text{Case 232}} = a \cdot 60 + h_{s2} - 9$	
Case 310	$h_{\text{Case 310}} = a \cdot 180 - 3$	6
Case 311	$h_{\text{Case 311}} = a \cdot 180 + h_{s1} - 3$	
Case 312	$h_{\text{Case 312}} = a \cdot 180 + h_{s2} - 3$	

(i.e., $h_{s0} = 0$). Using the procedure described in [8], the shifts, h_{s1} and h_{s2} in Table 4.2, are computed as the least positive solutions to the following two sets of congruence equations

$(h_{s_1} = 73, h_{s_2} = 119)$:

$$\begin{aligned}
\frac{h_{s_1}-1}{3} &\equiv 0 \pmod{3} & \frac{h_{s_2}-2}{3} &\equiv 0 \pmod{3} \\
\frac{h_{s_1}-1}{3} &\equiv 0 \pmod{4} & \frac{h_{s_2}+1}{3} &\equiv 0 \pmod{4} \\
\frac{h_{s_1}+2}{3} &\equiv 0 \pmod{5} & \frac{h_{s_2}+1}{3} &\equiv 0 \pmod{5}.
\end{aligned} \tag{4.20}$$

S4. Minimal pair ambiguity locations (h_1, h_2) are computed using Table 4.2 for $h = -3$ to $h = 183$. All minimal pairs are provided in Table 4.3.

S5. The *consecutive* minimal pairs are shown in Table 4.3.

Table 4.3: Robust symmetrical number system efficient search algorithm example - determination of all consecutive minimal pairs for $N = 3$ and $m_i = \{3, 4, 5\}$. *Consecutive* minimal pairs are shaded, the minimal consecutive minimal pairs used to determine \hat{M}_{RSNS} is in bold font. From [68].

h_1	COA	h_2	h_1	COA	h_2
-3	0	3	68	83	98
-14	1	16	78	90	102
-4	11	26	93	108	123
4	13	22	94	109	124
16	28	40	106	118	130
17	29	41	116	119	122
21	36	51	111	120	129
22	37	52	124	133	142
33	45	57	123	135	147
32	47	62	129	144	159
50	59	68	130	145	160
51	60	69	140	155	170
57	72	87	151	163	175
70	73	76	152	164	176
62	74	86	170	179	188
			177	180	183

S6. The consecutive minimal pairs that have the largest distance between them are displayed in **bold font** with a shaded background in Table 4.3. The result is $\hat{M}_{RSNS} = 43$ starting at

$h = 79$, and ending at $h = 121$, which agrees with the results in [8], [62].

4.2 Efficient Algorithm Complexity Analysis

In this section, the complexity of the computation of the upper bound, Equation (4.3), is computed, and the efficiency of the efficient algorithm described in Section 4.1.2 is compared to the naïve search algorithm of [56]. The “prime” big-oh notation $O'(\cdot)$ is used for functions in both M, N (to see the dependence on N), and the big-oh notation $O(\cdot)$ is used for functions in M , which is the relevant parameter (the O -constant will be dependent on N). For every $0 \leq k \leq N$, and every subset I of cardinality k , $k - 1$ multiplications are performed for the first term in the minimum computation of Equation (4.3), plus, a division and a doubling for the second term (since $2 \prod_{j \in \bar{I}} m_j = 2M / \prod_{i \in I} m_i$ reusing the previous computation). Including the sorting for a set of cardinality 2^N with complexity $O(N2^N)$, the complexity for the bound computation of Lemma 6 is

$$\begin{aligned} O \left(N2^N + N + \sum_{k=0}^N k \binom{N}{k} 2^k \right) \\ = O(N2^N + 2N3^{N-1}) \\ = O(N3^N), \end{aligned} \tag{4.21}$$

using the identity $\sum_{k=0}^n k \binom{n}{k} z^k = nz(z+1)^{n-1}$ [70]. Applying Equation (4.6) significantly reduces the above complexity to $O(1)$, as a function of M (at the expense of possibly increasing the upper bound) [68]. The \hat{M}_{RSNS} computation process described in Section 4.1.2 was implemented using MATLAB.

A search of current research did not reveal any existing efficient computational algorithms for finding and comparing *all* pairs of $N \times 1$ vectors in an $N \times P_f$ vector space, except for a naïve search algorithm used in [54]. The naïve search algorithm starts by creating an $N \times P_f$ matrix with each of the *columns* consisting of the integer values within each RSNS modulus sequence, as shown in Table 3.3. A double nested for-loop then determines the beginning position of each ambiguity, h_1 , which are then sorted. A second double nested for-loop is then used to determine the end position, h_2 , of each ambiguity where no other ambiguities are enclosed. The maximum length is then calculated and is \hat{M}_{RSNS} , with the matrix index corresponding to the correct beginning and end positions in the sequence.

The time complexities (arithmetical operations, and comparisons) of both algorithms in the modulus M (assuming N fixed) are compared. The naïve approach uses a matrix of size $N \times$

($2NM$) and for each column, it checks for the first match (ambiguity) in the remaining columns of the matrix, so it uses N comparisons (for each components of every vector) plus an addition for the range counter. Therefore, the worst case complexity of finding ambiguities and the distance between them would be

$$\ll \sum_{h=0}^{P_f-1} N(P_f - h) = NP_f^2 - N \frac{P_f(P_f - 1)}{2} \quad (4.22)$$

$$= \frac{NP_f(P_f + 1)}{2} = M(2MN + 1)N^2 = O'(M^2N^3), \quad (4.23)$$

(since the RSNS fundamental period is $P_f = 2NM$). Then, the obtained list of size $\ll P_f = 2NM$ is sorted, which can be done in $O'(MN(\log M + \log N))$, which brings the total time complexity for the dynamic range computation of [68]

$$\text{Naive Time Complexity} = O'(M^2N^3) = O(M^2). \quad (4.24)$$

Now, the time complexity of the efficient algorithm of Section 4.1.2 is examined. The first step is the same for both and its complexity is disregarded (as it is quite low, that is, $O'(N)$, compared to the other steps' complexities). The second step can be done in $O(1)$ using Theorem 7, Lemma 8. The third step uses a sorted bin of size $N \times 2^N$ and performs $O'(N^2 2^N)$ additions/multiplications on rows, and $O'(N 2^{2N})$ additions/multiplications on columns (see also [8] for further details on this step). The sorting of Step 3 is done in $O'(N 2^N)$ operations. Step 4 as well as Step 6 need $O'(2^N)$ operations, and Step 5 needs $O'(N 2^N)$, for a total worst case time complexity of [68]

$$\text{Improved Time Complexity} = O'(N 2^{2N}) = O(1). \quad (4.25)$$

The main advantage of the efficient algorithm is that it removes the apparent dependence on the size of the moduli in the number of operations needed to compute \hat{M}_{RSNS} [68].

Figure 4.1 shows a log-log plot of \hat{M}_{RSNS} versus computation time for the two algorithms using hundreds of N -channel moduli sets. Each “+” represents the \hat{M}_{RSNS} obtained using the algorithm presented in this paper, and has a corresponding “o” on the same horizontal axis (up to $\hat{M}_{RSNS} \approx 10^9$), which is the \hat{M}_{RSNS} computed using the naïve search algorithm. The results are displayed where the two computation methods produced the same results for \hat{M}_{RSNS} (up to

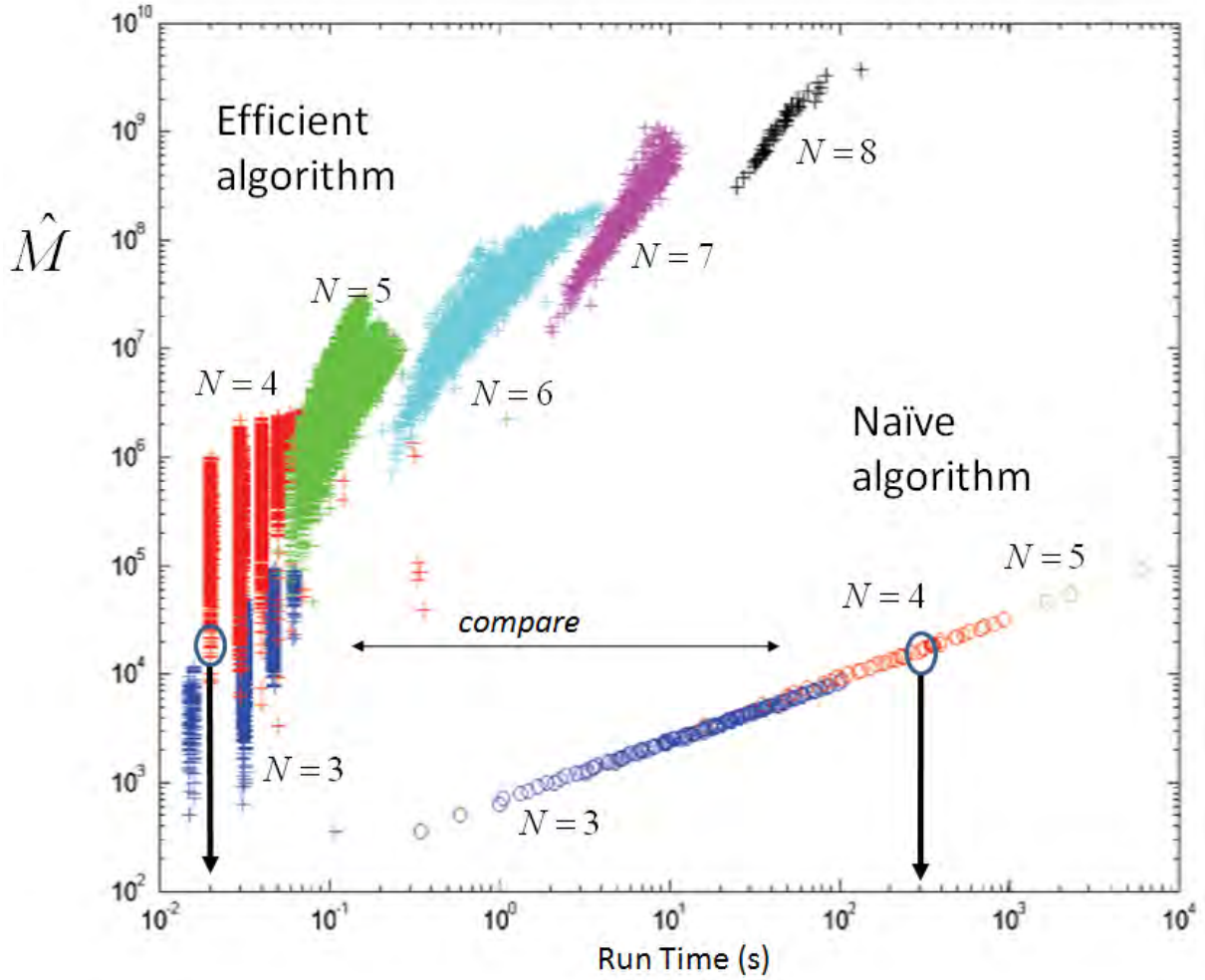


Figure 4.1: Comparison of efficient and naïve algorithm run time. From [56].

10^4 s). For example, with $N = 4$ moduli with $\hat{M}_{RSNS} = 2 \times 10^4$, the naïve algorithm takes 300 s to produce the answer, while it only takes the efficient algorithm described above 0.02 s.

4.3 Additional Closed-Form Expressions for the Dynamic Range of the Robust Symmetrical Number System

In this section, closed-form expressions for \hat{M}_{RSNS} are developed for additional families of moduli sets for $N = 3$ and $N = 4$ RSNS sequences to extend the solutions presented in [8]. The closed-form expressions were derived by generating different sets of coprime moduli and determining \hat{M}_{RSNS} , the corresponding sequence's beginning and ending positions as well as the corresponding case numbers using the efficient algorithm described in Section 4.1.2. The data

generated from the efficient algorithm were evaluated to determine the moduli sets that share common *start and stop case numbers*. The values of \hat{M}_{RSNS} for these moduli sets were then plotted versus the base modulus of the set of coprime moduli and curve fitting was conducted to determine an analytical solution. The resulting analytical solution was then verified to satisfy the solutions to the congruence equations shown in Table 3.6.

In the remainder of this section, additional closed-form expressions for \hat{M}_{RSNS} are presented for an $N = 3$ and an $N = 4$ RSNS, greatly expanding the number of cases for which closed-form expressions exist for \hat{M}_{RSNS} .

4.3.1 Three-Sequence Robust Symmetrical Number System

Three Sequential Odd Moduli

A set of three sequential, odd, coprime moduli were examined where $m_i = \{m - 1, m + 1, m + 3\}$ and $m > 2$ and even. The dynamic range \hat{M}_{RSNS} was determined using the efficient algorithm described in [8], [68] and Section 4.1.2 to generate a data set. The data set was examined, and it was determined that two distinct sets of case numbers were associated with the beginning and ending positions of \hat{M}_{RSNS} . When $m \equiv 0 \pmod{4}$, the case number associated with the beginning position (Start Case) of \hat{M}_{RSNS} is Case 211, and the case number associated with the ending position (Stop Case) of \hat{M}_{RSNS} is Case 220. The values of m were plotted against the values of \hat{M}_{RSNS} , and the data points were curve fitted to a quadratic polynomial using MATLAB's curve fitting toolbox, resulting in

$$\hat{M}_{RSNS} = \frac{3}{2}m^2 + \frac{15}{2}m + 7 \quad (4.26)$$

where $m \equiv 0 \pmod{4}$. A portion of the data that was curve fitted to derive Equation (4.26) is presented in Table 4.4. The data generated from the algorithm and the closed-form expression for \hat{M}_{RSNS} , Equation (4.26), are illustrated in Figure 4.2. The values of \hat{M}_{RSNS} derived from the algorithm are equal to the values resulting from Equation (4.26).

To verify Equation (4.26), the value of \hat{M}_{RSNS} was determined from the results of Table 3.6. For the Start Case,

$$h_{211} = a(3m_1m_2) + h_{s_{211}} - 3m_3. \quad (4.27)$$

The congruence equations generated from Equation (3.29),

$$\begin{aligned} \frac{h_{s_{211}} - 1}{3} &\equiv 0 \pmod{m_1} \\ \frac{h_{s_{211}} - 1}{3} &\equiv 0 \pmod{m_2} \end{aligned}, \quad (4.28)$$

were solved using the CRT to obtain $h_{s_{211}} = 1$. The value of a in Equation (4.27) was derived by solving for a using the values of the beginning position, $h_1 + 1$ and m . The results were curve fitted, resulting in $a = 0.75m + 2$. The expression for a was substituted into Equation (4.27) and

Table 4.4: Sample of data used in curve fitting for a three sequential odd coprime moduli, $m \equiv 0 \pmod{4}$.

$m - 1$	$m + 1$	$m + 3$	$h_1 + 1$	Start Case	$h_2 - 1$	Stop Case	\widehat{M}_{RSNS}
7	9	11	1481	211	1643	220	163
11	13	15	4676	211	4988	220	313
15	17	19	10655	211	11165	220	511
19	21	23	20282	211	21038	220	757
23	25	27	34421	211	35471	220	1051
27	29	31	53936	211	55328	220	1393
31	33	35	79691	211	81473	220	1783
35	37	39	112550	211	114770	220	2221
39	41	43	153377	211	156083	220	2707
43	45	47	203036	211	206276	220	3241
47	49	51	262391	211	266213	220	3823

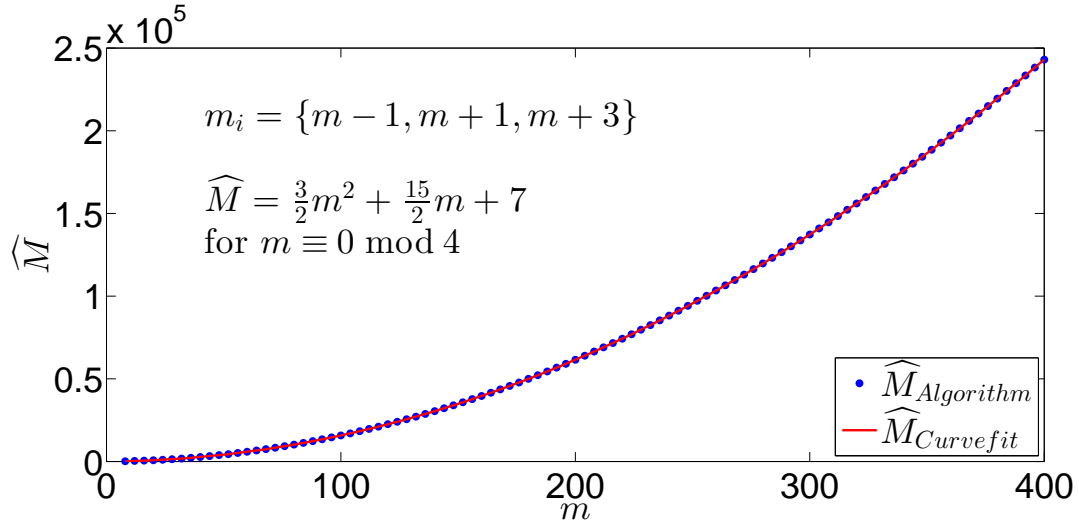


Figure 4.2: Curve fitting results for the dynamic range of the robust symmetrical number system \widehat{M}_{RSNS} when $m_i = \{m - 1, m + 1, m + 3\}$ where $m \equiv 0 \pmod{4}$.

simplified to provide the following result,

$$h_{211} = \frac{9}{4}m^3 + 6m^2 - \frac{21}{4}m - 14. \quad (4.29)$$

For the Stop Case,

$$h_{220} = a(3m_1m_3) + 3m_2. \quad (4.30)$$

By applying the same approach used in the previous cases examined, it was determined that $a = 0.75m + 1$ and

$$h_{220} = \frac{9}{4}m^3 + \frac{15}{2}m^2 + \frac{9}{4}m - 6. \quad (4.31)$$

By solving $\hat{M}_{RSNS} = h_{220} - h_{211} - 1$, the desired result, Equation (4.26), was obtained verifying the closed form expression for \hat{M}_{RSNS} .

When $m \equiv 2 \pmod{4}$, the Start Case is Case 211, and the Stop Case is Case 231. The data points were curve fitted resulting in

$$\hat{M}_{RSNS} = \frac{3}{2}m^2 + \frac{15}{2}m + 5. \quad (4.32)$$

A sample of the data used in the curve fitting process is listed in Table 4.5. In Figure 4.3, the data and closed-form expression generated from curve fitting, Equation (4.32), are displayed. To verify the Equation (4.32) it is derived from the applicable equations in Table 3.6. For the Start Case, Case 231,

$$h_{231} = a(3m_2m_3) + h_{s_{231}} + 3m_1. \quad (4.33)$$

Table 4.5: Sample of data used in curve fitting for sequential odd coprime moduli, with $m \equiv 2 \pmod{4}$.

$m - 1$	$m + 1$	$m + 3$	$h_1 + 1$	Start Case	$h_2 - 1$	Stop Case	\hat{M}_{RSNS}
5	7	9	395	211	498	231	104
9	11	13	1745	211	1974	231	230
13	15	17	4631	211	5034	231	404
17	19	21	9629	211	10254	231	626
21	23	25	17315	211	18210	231	896
25	27	29	28265	211	29478	231	1214
29	31	33	43055	211	44634	231	1580
33	35	37	62261	211	64254	231	1994
37	39	41	86459	211	88914	231	2456
41	43	45	116225	211	119190	231	2966
45	47	49	152135	211	155658	231	3524

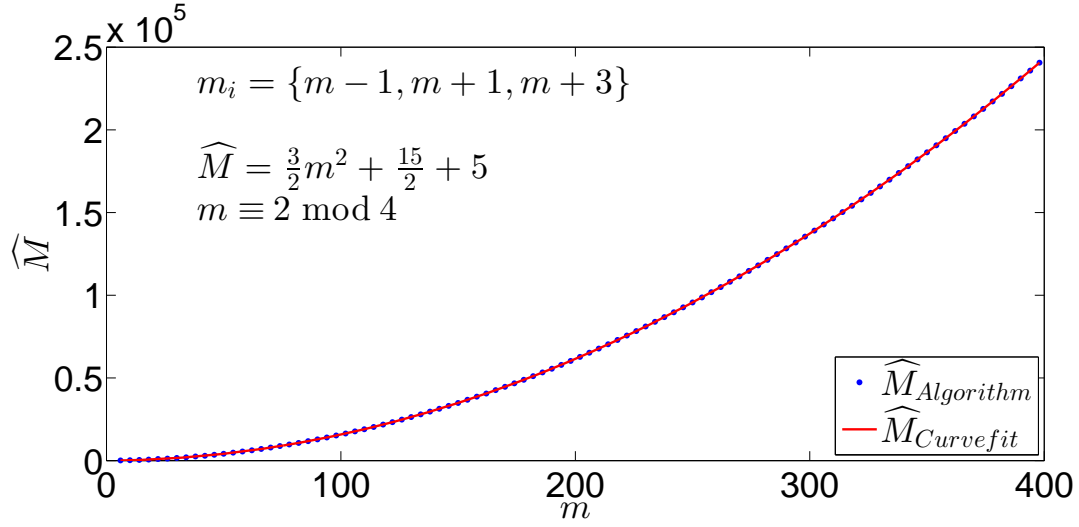


Figure 4.3: Curve fitting results for the dynamic range of the robust symmetrical number system \widehat{M}_{RSNS} when $m_i = \{m-1, m+1, m+3\}$ and $m \equiv 2 \pmod{4}$.

The shift value $h_{s_{231}}$ is determined by solving the congruence equations generated from Equation (3.29),

$$\begin{aligned} \frac{h_{s_{231}} - 1}{3} &\equiv 0 \pmod{m_2} \\ \frac{h_{s_{231}} + 2}{3} &\equiv 0 \pmod{m_3} \end{aligned}, \quad (4.34)$$

using the CRT. The resulting expression for the shift value is

$$h_{s_{231}} = \frac{3}{2}m^2 + \frac{15}{2}m + 7. \quad (4.35)$$

The value of a in Equation (4.33) was determined to be $a = 0.5m - 1$. These expressions were then used to determine that

$$h_{231} = \frac{3}{2}m^3 + \frac{9}{2}m^2 + 3m - 5. \quad (4.36)$$

By solving for $\widehat{M}_{RSNS} = h_{231} - h_{211} - 1$, the desired result is obtained verifying Equation (4.32).

Three Sequential Coprime Moduli (Even, Odd, Odd)

In [8], a closed-form expression for a three-sequence RSNS with coprime moduli of the form $\{m-1, m, m+1\}$, Equation (3.22), was presented where m is even and $m > 3$. This section examines the a set of sequential coprime moduli, $m_i = \{m, m+1, m+3\}$, where $m \equiv 2 \pmod{4}$ and $m \geq 14$. For this choice of moduli, the Start Case was Case 230, and the Stop Case was Case 231. A sample of the data obtained from using the algorithm of [8], [68] is displayed in

Table 4.6: Sample of data used in curve fitting for sequential coprime moduli of form, $\{m, m+1, m+3\}$, with $m \equiv 2 \pmod{4}$ and $m \geq 14$.

m	$m+1$	$m+3$	h_1+1	Start Case	h_2-1	Stop Case	\widehat{M}_{RSNS}
14	15	17	4549	230	5037	231	489
16	17	19	922	230	1527	231	606
20	21	23	11533	230	12408	231	876
22	23	25	1660	230	2688	231	1029
26	27	29	23413	230	24783	231	1371
28	29	31	2614	230	4173	231	1560
32	33	35	41485	230	43458	231	1974
34	35	37	3784	230	5982	231	2199
38	39	41	67045	230	69729	231	2685
40	41	43	5170	230	8115	231	2946
44	45	47	101389	230	104892	231	3504
46	47	49	6772	230	10572	231	3801

Table 4.6. The data points were curve fitted to obtain the following expression for \widehat{M}_{RSNS} ,

$$\widehat{M}_{RSNS} = \frac{3}{2}m^2 + \frac{27}{2}m + 6, \quad (4.37)$$

that is plotted against the data points in Figure 4.4. Next, Equation (4.37) is derived from the applicable equations of Table 3.6. The solution to \widehat{M}_{RSNS} reduces to

$$\widehat{M}_{RSNS} = h_{s_{231}} + 6m_1 - 1 \quad (4.38)$$

because h_{231} and h_{230} differ by the value of $h_{s_{231}}$. By solving the congruence equations, Equation (4.34),

$$h_{s_{231}} = \frac{3}{2}m^2 + \frac{15}{2}m + 7 \quad (4.39)$$

is obtained. The desired result, Equation (4.37), is produced by substituting Equation (4.39) into Equation (4.38) and simplifying the expression.

Three Sequential Coprime Moduli (Odd, Odd, Even)

Coprime moduli sets of the form, $\{m-3, m+1, m\}$ when m is even and $m \neq 6k$ where $k = 1, 2, \dots$ were examined. A sample of the data produced from the algorithm described in [8], [68] is displayed in Table 4.7. The data was curve fitted resulting in the following closed-form

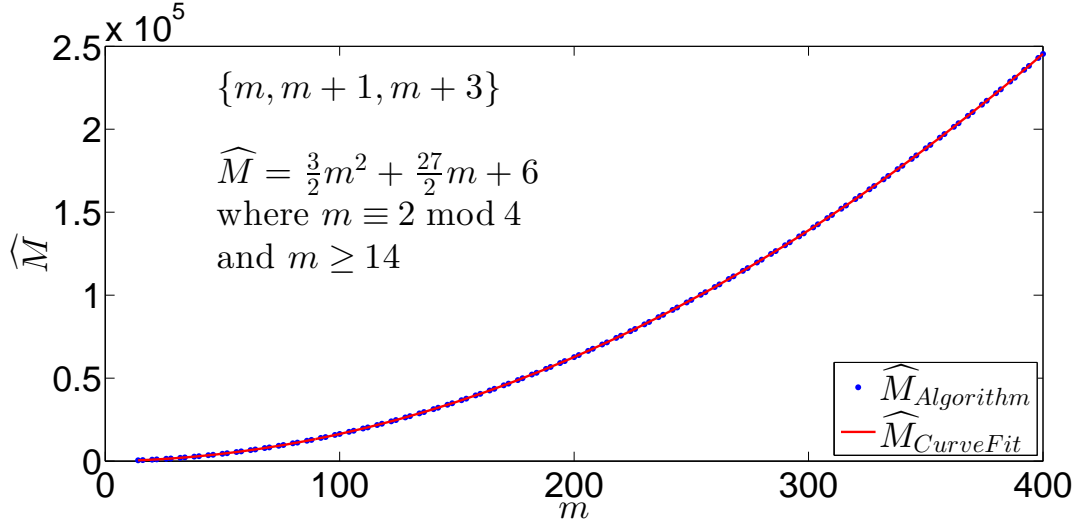


Figure 4.4: Curve fitting results for the dynamic range of the robust symmetrical number system \widehat{M}_{RSNS} when $m_i = \{m, m+1, m+3\}$ where $m \equiv 2 \pmod{4}$ and $m \geq 14$.

expression,

$$\widehat{M}_{RSNS} = \frac{3}{2}m^2 + \frac{3}{2}m, \quad (4.40)$$

which is plotted against the data generated from the algorithm of [8], [68] in Figure 4.5. The Start Case is Case 211, and the Stop Case is Case 212. Due to the solutions for h_{211} and h_{212} listed in Table 3.6 differing by the shift values, $h_{s_{211}}$ and $h_{s_{212}}$ the solution for \widehat{M}_{RSNS} is reduced to

$$\widehat{M}_{RSNS} = h_{s_{212}} + 6m - h_{s_{211}} - 1. \quad (4.41)$$

The shift value $h_{s_{211}}$ was determined by solving the congruence equations for $h_{s_{211}}$ in Equation (4.28) resulting in $h_{s_{211}} = 1$. The congruence equations for $h_{s_{212}}$ are

$$\begin{aligned} \frac{h_{s_{212}} - 2}{3} &\equiv 0 \pmod{m_1} \\ \frac{h_{s_{212}} + 1}{3} &\equiv 0 \pmod{m_2} \end{aligned} \quad (4.42)$$

The shift value $h_{s_{212}}$ is determined by using the CRT to solve Equation (4.42) resulting in

$$h_{s_{212}} = \frac{3}{2}m^2 - \frac{9}{2}m + 2. \quad (4.43)$$

By substituting the values for $h_{s_{211}}$ and $h_{s_{212}}$ into Equation (4.41) and simplifying the expression, Equation (4.40) is obtained verifying the closed-form expression for \widehat{M}_{RSNS} .

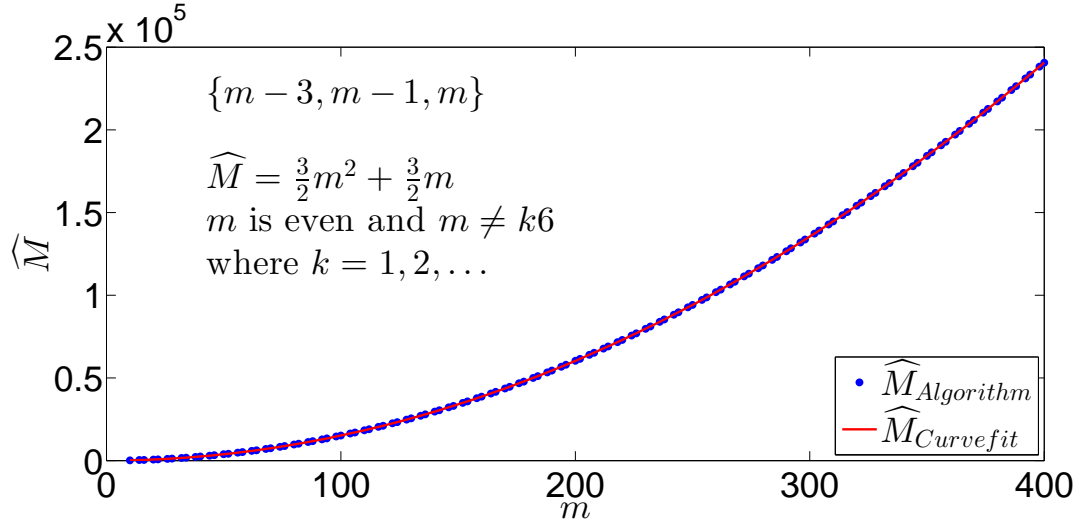


Figure 4.5: Curve fitting results for the dynamic range of the robust symmetrical number system \widehat{M}_{RSNS} when $m_i = \{m-3, m-1, m\}$ where $m \neq 0 \pmod{6}$ and m is even.

Three Odd Coprime Moduli, Every Other Odd Number

Three coprime odd moduli of the form $m_i = \{m, m+4, m+8\}$ were examined. By examining the data in Table 4.8, four separate Start and Stop Case combinations can be seen. The data was curve fitted for each Start and Stop Case combination which produced the following closed-

Table 4.7: Sample of data used in curve fitting for sequential coprime moduli of form, $\{m-3, m-1, m\}$, with $m \not\equiv 0 \pmod{6}$.

$m-3$	$m-1$	m	h_1+1	Start Case	h_2-1	Stop Case	\widehat{M}_{RSNS}
7	9	10	1673	211	1837	212	165
11	13	14	3392	211	3706	212	315
13	15	16	8144	211	8551	212	408
17	19	20	10601	211	11230	212	630
19	21	22	22679	211	23437	212	759
23	25	26	24074	211	25126	212	1053
25	27	28	48518	211	49735	212	1218
29	31	32	45755	211	47338	212	1584
31	33	34	88901	211	90685	212	1785
35	37	38	77588	211	79810	212	2223
37	39	40	147068	211	149527	212	2460
41	43	44	121517	211	124486	212	2970

Table 4.8: Sample of data used in curve fitting for sequential coprime moduli of form, $\{m, m+4, m+8\}$, with m odd and $m \geq 7$.

m	$m+4$	$m+8$	h_1+1	Start Case	h_2-1	Stop Case	\hat{M}_{RSNS}
7	11	15	714	212	968	210	255
9	13	17	1355	211	1726	212	372
11	15	19	5599	220	5996	210	398
13	17	21	8558	211	9059	220	502
15	19	23	4434	212	5198	210	765
17	21	25	6353	211	7318	212	966
19	23	27	21478	220	22367	210	890
21	25	29	28265	211	29306	220	1042
23	27	31	13434	212	14996	210	1563
25	29	33	17303	211	19150	212	1848
27	31	35	53773	220	55346	210	1574
29	33	37	65924	211	67697	220	1774
31	35	39	30018	212	32666	210	2649
33	37	41	36509	211	39526	212	3018
35	39	43	108244	220	110693	210	2450

form expressions,

$$\hat{M}_{RSNS} = \begin{cases} \frac{9}{4}m^2 + \frac{63}{4}m + 48, & m \equiv 1 \pmod{8} \\ \frac{3}{2}m^2 + \frac{33}{2}m + 35, & m \equiv 3 \pmod{8} \\ \frac{3}{2}m^2 + \frac{33}{2}m + 34, & m \equiv 5 \pmod{8} \\ \frac{9}{4}m^2 + \frac{57}{4}m + 45, & m \equiv 7 \pmod{8} \end{cases}. \quad (4.44)$$

The data points resulting from the algorithm are plotted along with the curve fit solutions in Figure 4.6 through Figure 4.9. For the first set of data, $m \equiv 1 \pmod{8}$, the Start Case is Case 211 and the Stop Case is Case 212. From Table 3.6, the solution to the congruence equations are

$$h_{211} = a_1 3m_1 m_2 + h_{s_{211}} - 3m_3 \quad (4.45)$$

$$h_{212} = a_2 3m_1 m_2 + h_{s_{212}} + 3m_3 \quad (4.46)$$

The shift values are determined to be

$$h_{s_{211}} = 1 \quad (4.47)$$

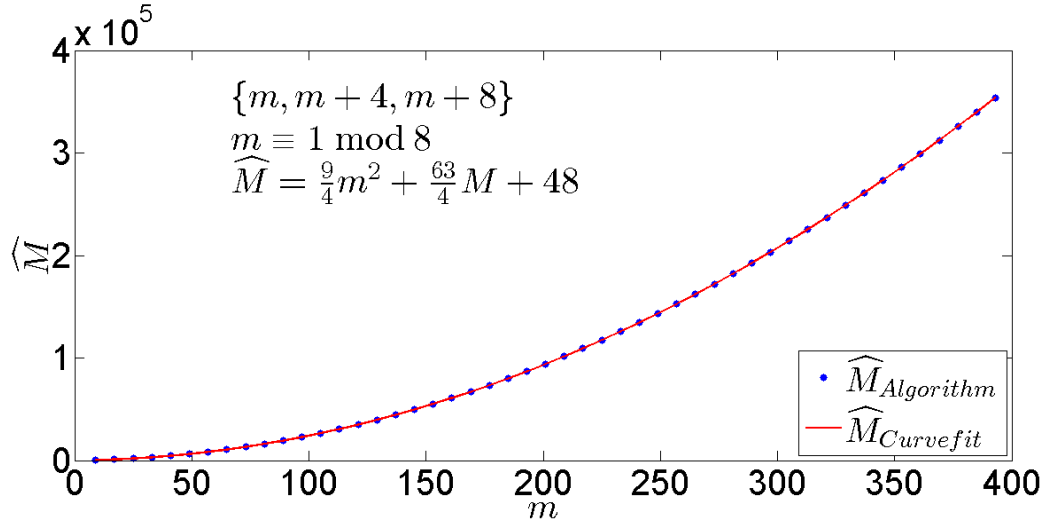


Figure 4.6: Curve fitting results for the dynamic range of the robust symmetrical number system \widehat{M}_{RSNS} when $m_i = \{m, m+4, m+8\}$ where $m \equiv 1 \pmod{8}$ and $m \geq 7$.

and

$$h_{s_{212}} = 2 - \frac{9}{4}m - \frac{3}{4}m^2. \quad (4.48)$$

The values of the a_1 and a_2 were determined to be

$$a_1 = \frac{1}{4}m + \frac{7}{4} \quad (4.49)$$

and

$$a_2 = \frac{1}{4}m + \frac{11}{4}. \quad (4.50)$$

The expressions of Equation (4.47) through Equation (4.50) are substituted into Equation (4.45) and Equation (4.46) resulting in

$$h_{211} = \frac{3}{4}m^3 + \frac{33}{4}m^2 + 18m - 23 \quad (4.51)$$

and

$$h_{212} = \frac{3}{4}m^3 + \frac{21}{2}m^2 + \frac{135}{4}m + 26. \quad (4.52)$$

From Equation (4.51) and Equation (4.52), the expression for $\widehat{M}_{RSNS} = h_{212} - h_{211} - 1$ results in the corresponding expression in Equation (4.44) verifying the result obtained through curve fitting.

When $m \equiv 3 \pmod{8}$, the Start Case is Case 220 and the Stop Case is Case 210. The solutions to

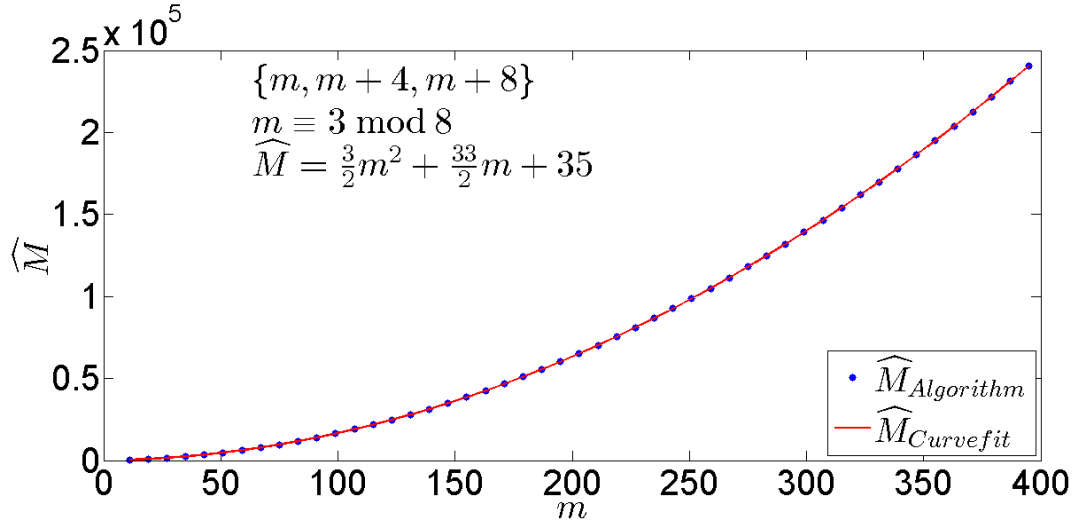


Figure 4.7: Curve fitting results for the dynamic range of the robust symmetrical number system \widehat{M}_{RSNS} when $m_i = \{m, m+4, m+8\}$ where $m \equiv 3 \pmod{8}$ and $m \geq 7$.

the congruence equations in Table 3.6 are

$$h_{210} = a_2 3m_1 m_2 + 3m_3 \quad (4.53)$$

$$h_{220} = a_1 3m_1 m_3 - 3m_2. \quad (4.54)$$

From the values of the beginning and ending positions and curve fitting,

$$a_1 = \frac{5}{8}m + \frac{17}{8}, \quad (4.55)$$

and

$$a_2 = \frac{5}{8}m + \frac{41}{8}. \quad (4.56)$$

The corresponding closed-form expression for \widehat{M}_{RSNS} in Equation (4.44) is obtained by substituting (4.55) and (4.56) into (4.53) and (4.54) and solving $\widehat{M}_{RSNS} = h_{210} - h_{220} - 1$.

When $m \equiv 5 \pmod{8}$, the Start Case is Case 211 and the Stop Case is Case 220. The solution to the congruence equations in Table 3.6 are

$$h_{211} = a_1 3m_1 m_2 + h_{s_{211}} - 3m_3 \quad (4.57)$$

and

$$h_{220} = a_2 3m_1 m_3 + 3m_3. \quad (4.58)$$

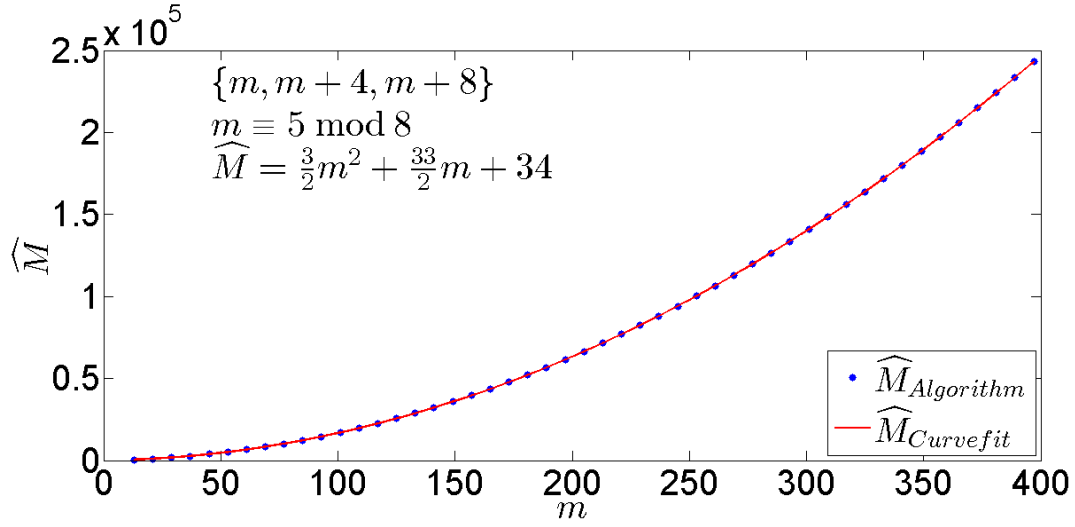


Figure 4.8: Curve fitting results for the dynamic range of the robust symmetrical number system \widehat{M}_{RSNS} when $m_i = \{m, m+4, m+8\}$ where $m \equiv 5 \pmod{8}$ and $m \geq 7$.

By solving the congruence equations based on the shift matrix, Equation (3.29), $h_{s_{211}} = 1$. Using the values of the beginning and ending positions of the sequence comprising \widehat{M}_{RSNS} ,

$$a_1 = \frac{5}{8}m + \frac{39}{8} \quad (4.59)$$

and

$$a_2 = \frac{5}{8}m + \frac{23}{8}. \quad (4.60)$$

After substituting Equation (4.59) and Equation (4.60) into Equation (4.57) and Equation (4.58) and solving $\widehat{M}_{RSNS} = h_{220} - h_{211} - 1$, the corresponding expression in Equation (4.44) is obtained.

When $m \equiv 7 \pmod{8}$, the Start Case is Case 212 and the Stop Case is Case 210. The solutions to the congruence equations from Table 3.6 are

$$h_{210} = a_1 m_1 m_2 + 3m_3 \quad (4.61)$$

and

$$h_{212} = a_2 m_1 m_2 + h_{s_{212}} - 3m_3. \quad (4.62)$$

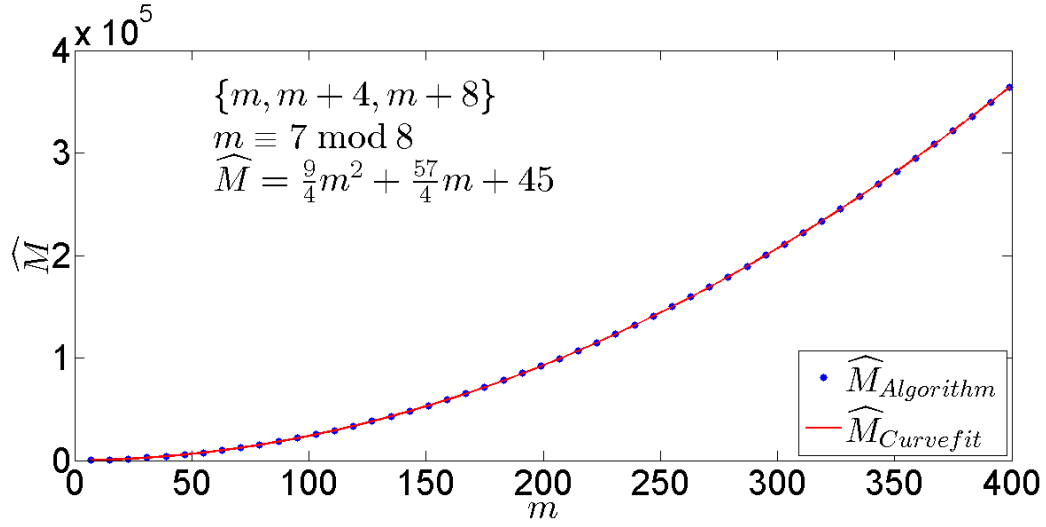


Figure 4.9: Curve fitting results for the dynamic range of the robust symmetrical number system \widehat{M}_{RSNS} when the moduli $m_i = \{m, m+4, m+8\}$ where $m \equiv 7 \pmod{8}$ and $m \geq 7$.

The congruence equations based on the shift matrix, Equation (3.29) are solved resulting in

$$h_{s_{212}} = \frac{3}{4}m^2 + \frac{15}{2}m + 2. \quad (4.63)$$

The expressions for a_1 and a_2 are determined to be

$$a_1 = \frac{1}{4}m + \frac{9}{4} \quad (4.64)$$

and

$$a_2 = \frac{1}{4}m + \frac{5}{4}. \quad (4.65)$$

Equation (4.64) and Equation (4.65) are substituted into Equation (4.61) and Equation (4.62), and $\widehat{M}_{RSNS} = h_{210} - h_{212} - 1$ is solved resulting in the corresponding expression in Equation (4.44) verifying the curve fitting results.

The new closed-form expressions for \widehat{M}_{RSNS} when $N = 3$ are summarized in Table 4.9.

4.3.2 Additional Closed-Form Solutions for a Four-sequence RSNS

In this section, several four-sequence RSNS moduli sets are examined and closed-form expressions to \widehat{M}_{RSNS} are derived based on the results of curve fitting using MATLAB's curve fitting toolbox. The closed-form expressions are verified by deriving the same expressions for \widehat{M}_{RSNS} using the equations in Table 3.6.

One Even and Three Odd Sequential Coprime Moduli (Even, Odd, Odd, Odd)

A set of coprime moduli was examined and the moduli were sequential coprime numbers of the format $m_i = \{m-1, m, m+2, m+4\}$ where m is an odd number. It was determined that when $m \equiv 3 \pmod{6}$ or $m \equiv 5 \pmod{6}$ with $m \geq 15$ and $m \neq \{29, 33\}$ that the Start Case was Case 260 and the Stop Case was Case 261. The data points obtained from applying the efficient algorithm described in Section 4.1.2 were curve fitted resulting in

$$\hat{M}_{RSNS} = 10m^2 + 6m + 20. \quad (4.66)$$

A sample of the data used in curve fitting is listed in Table 4.10, and the data and the closed-form expression for \hat{M}_{RSNS} , Equation (4.66), are displayed in Figure 4.10.

The closed-form expression in Equation (4.66) can be determined from the solutions to the congruence equations listed in Table 3.6. The solution for the Start Case is

$$h_{260} = a(4m_3m_4) - 4(m_1m_2), \quad (4.67)$$

and for the Stop Case, the solution to the congruence equations is

$$h_{261} = a(4m_3m_4) + h_{s_{261}} + 4(m_1m_2). \quad (4.68)$$

Table 4.9: New closed-form expressions for three sequence robust symmetrical number system (RSNS) dynamic range. From [68].

m_i	\hat{M}_{RSNS}	m
$\{m-1, m+1, m+3\}$	$\frac{3}{2}m^2 + \frac{15}{2}m + 7$	$m \equiv 0 \pmod{4}$
	$\frac{3}{2}m^2 + \frac{15}{2}m + 5$	$m \equiv 2 \pmod{4}$
$\{m, m+1, m+3\}$	$\frac{3}{2}m^2 + \frac{27}{2}m + 6$	$m \equiv 2 \pmod{4}$ and $m \geq 14$
$\{m-3, m+1, m\}$	$\frac{3}{2}m^2 + \frac{3}{2}m$	m is even and $m \neq 6k$ where $k = 1, 2, \dots$
$\{m, m+4, m+8\}$	$\frac{9}{4}m^2 + \frac{63}{4}m + 48$	$m \equiv 1 \pmod{8}$
	$\frac{3}{2}m^2 + \frac{33}{2}m + 35$	$m \equiv 3 \pmod{8}$
	$\frac{3}{2}m^2 + \frac{33}{2}m + 34$	$m \equiv 5 \pmod{8}$
	$\frac{9}{4}m^2 + \frac{57}{4}m + 45$	$m \equiv 7 \pmod{8}$

From Equation (4.67) and Equation (4.68),

$$\widehat{M}_{RSNS} = h_{s_{261}} + 8m_1m_2 - 1. \quad (4.69)$$

The shift value $h_{s_{261}}$ is obtained by solving the congruence equations for $h_{s_{261}}$,

$$\begin{aligned} \frac{h_{s_{261}} - 1}{4} &\equiv 0 \pmod{m_3} \\ \frac{h_{s_{261}} + 3}{4} &\equiv 0 \pmod{m_4} \end{aligned}, \quad (4.70)$$

Table 4.10: Sample of data used in curve fitting for sequential coprime moduli of form, $\{m, m+1, m+2, m+4\}$, with $m \equiv 3 \pmod{6}$ or $m \equiv 5 \pmod{6}$ and $m \geq 15$.

$m-1$	m	$m+2$	$m+4$	h_1+1	Start Case	h_2-1	Stop Case	\widehat{M}_{RSNS}
14	15	17	19	49549	260	51908	261	2360
16	17	19	21	93077	260	96088	261	3012
22	23	25	27	43877	260	49324	261	5448
26	27	29	31	212953	260	220424	261	7472
34	35	37	39	1455557	260	1468036	261	12480
38	39	41	43	4457989	260	4473452	261	15464
44	45	47	49	8540817	260	8561356	261	20540
46	47	49	51	3389993	260	3412384	261	22392
52	53	55	57	6384377	260	6412804	261	28428

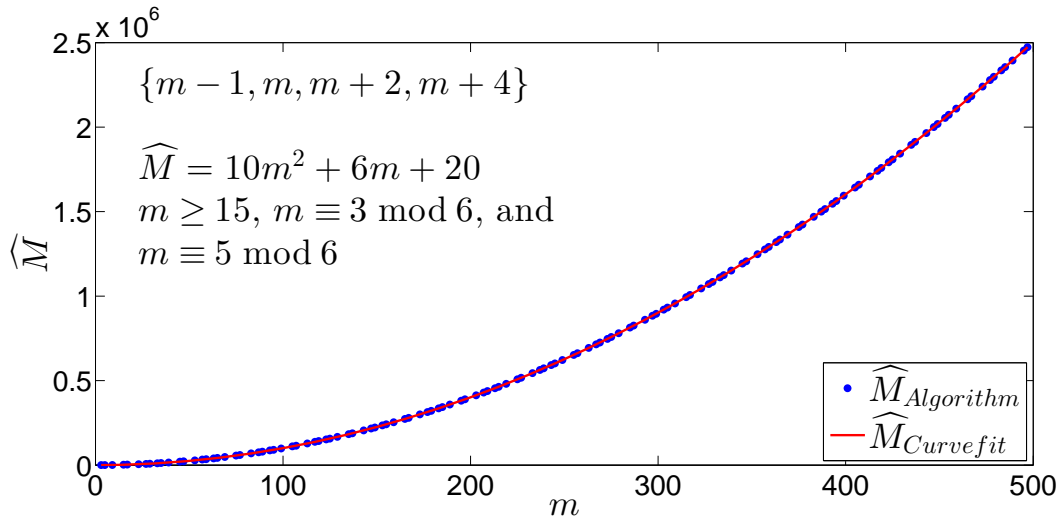


Figure 4.10: Curve fitting results plotted against algorithm results for the dynamic range of the robust symmetrical number system \widehat{M}_{RSNS} when the moduli $m_i = \{m-1, m, m+2, m+4\}$ where $m \equiv 3 \pmod{6}$ or $m \equiv 5 \pmod{6}$ and $m \geq 15$.

using the CRT, which results in

$$h_{s_{261}} = 2m^2 + 14m + 21. \quad (4.71)$$

Equation (4.71) is substituted into Equation (4.69) and the expression is simplified to obtain the closed-form expression for \hat{M}_{RSNS} , Equation (4.66).

One Even and Three Odd Sequential Coprime Moduli (Odd, Even, Odd, Odd)

The case where the four sequential coprime numbers are used as the moduli set of the form $m_i = \{m, m+1, m+2, m+4\}$ where $m \equiv 1 \pmod{6}$ or $m \equiv 3 \pmod{6}$ and $m \geq 15$ is examined. A sample of the data used in the curve fitting program is shown in Table 4.11. The data and the closed-form expression generated by curve fitting the data are displayed in Figure 4.11. The Start Case is Case 260, and the Stop Case is Case 261. Curve fitting the data in Table 4.11 results in a quadratic expression for \hat{M}_{RSNS} ,

$$\hat{M}_{RSNS} = 10m^2 + 22m + 20. \quad (4.72)$$

By applying the solutions to the congruence equations in Table 3.6, the values of h_{260} and h_{261}

Table 4.11: Sample of data used in curve fitting for sequential coprime moduli of form, $\{m, m+1, m+2, m+4\}$, with $m \equiv 1 \pmod{6}$ or $m \equiv 3 \pmod{6}$ and $m \geq 15$.

m	$m+1$	$m+2$	$m+4$	$h_1 + 1$	Start Case	$h_2 - 1$	Stop Case	\hat{M}_{RSNS}
15	16	17	19	41677	260	44276	261	2600
19	20	21	23	479549	260	483596	261	4048
21	22	23	25	407553	260	412444	261	4892
25	26	27	29	113285	260	120104	261	6820
27	28	29	31	7765	260	15668	261	7904
31	32	33	35	656693	260	667004	261	10312
33	34	35	37	529053	260	540688	261	11636
37	38	39	41	346157	260	360680	261	14524
39	40	41	43	1157341	260	1173428	261	16088
43	44	45	47	10220573	260	10240028	261	19456
45	46	47	49	6827025	260	6848284	261	21260
49	50	51	53	779477	260	804584	261	25108

can be derived. The solution for the Start Case is

$$h_{260} = a(4m_3m_4) - 4(m_1m_2), \quad (4.73)$$

and for the Stop Case, the solution to the congruence equations is

$$h_{261} = a(4m_3m_4) + h_{s_{261}} + 4(m_1m_2). \quad (4.74)$$

Based on Equation (4.73) and Equation (4.74),

$$\widehat{M}_{RSNS} = h_{s_{261}} + 8m^2 + 8m - 1. \quad (4.75)$$

The congruence equations used to solve for $h_{s_{261}}$ are

$$\begin{aligned} \frac{h_{s_{261}} - 1}{4} &\equiv 0 \pmod{m_3} \\ \frac{h_{s_{261}} + 3}{4} &\equiv 0 \pmod{m_4} \end{aligned} \quad (4.76)$$

The CRT is applied to Equation (4.76) to solve for $h_{s_{261}}$ and results in

$$h_{s_{261}} = 2m^2 + 14m + 21. \quad (4.77)$$

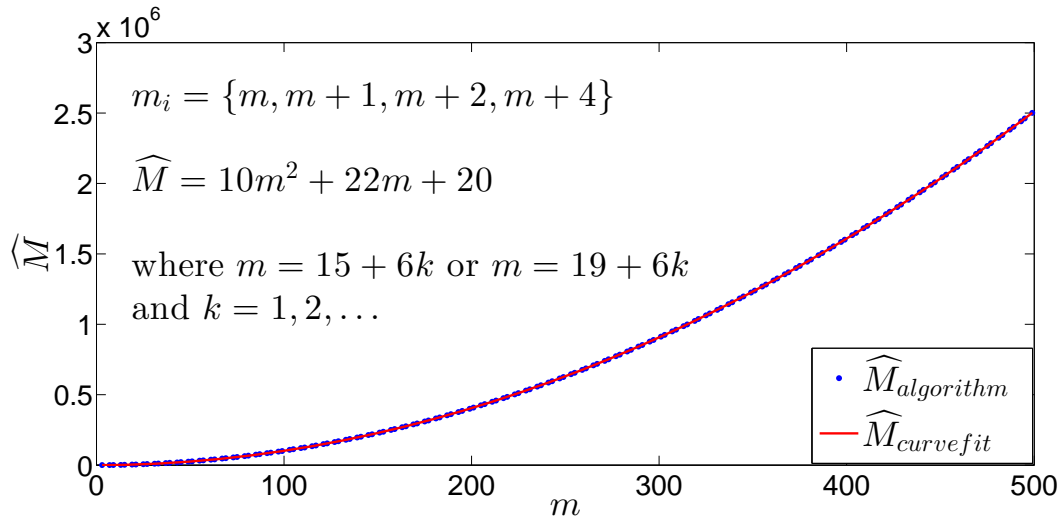


Figure 4.11: Curve fitting results plotted against algorithm results for the dynamic range of the robust symmetrical number system \widehat{M}_{RSNS} when the moduli $m_i = \{m, m+1, m+2, m+4\}$ where $m \equiv 1 \pmod{6}$ or $m \equiv 3 \pmod{6}$ and $m \geq 15$.

Table 4.12: Sample of data used in curve fitting for sequential coprime moduli of form, $\{m, m+1, m+2, m+4\}$, with $m \equiv 1 \pmod 6$ or $m \equiv 3 \pmod 6$ and $m \geq 15$.

m	$m+2$	$m+3$	$m+4$	$h_1 + 1$	Start Case	$h_2 - 1$	Stop Case	\hat{M}_{RSNS}
25	27	28	29	661185	250	668178	233	6994
29	31	32	33	3736377	250	3745650	233	9274
31	33	34	35	1968525	250	1979058	233	10534
35	37	38	39	880759	252	894050	233	13292
37	39	40	41	2949033	250	2963826	233	14794
41	43	44	45	13800945	250	13818978	233	18034
43	45	46	47	7398911	252	7418682	233	19772
47	49	50	51	14499895	252	14523386	233	23492
49	51	52	53	8725905	250	8751378	233	25474
53	55	56	57	36880809	250	36910482	233	29674
55	57	58	59	35117255	252	35149146	233	31892
59	61	62	63	6679999	252	6716570	233	36572
61	63	64	65	20459385	250	20498418	233	39034
65	67	68	69	81125217	250	81169410	233	44194

Equation (4.77) is substituted into Equation (4.75) resulting in Equation (4.72).

One Even and Three Odd Sequential Coprime Moduli (Odd, Odd, Even, Odd)

For the next case examined, the coprime moduli are in the form, $\{m, m+2, m+3, m+4\}$ and m is an odd number. A sample of the data examined is shown in Table 4.12. There are two distinct Start Cases, Case 250 and Case 252 for $m \geq 25$. The Stop Case is Case 233 for $m \geq 25$. For moduli sets where the Start Case is Case 250, $m = \{25 + 12k, 29 + 12k, 31\}$ where $k = 0, 1, 2, \dots$, the data points generated from the efficient algorithm described in Section 4.1.2 were curve fitted resulting in

$$\hat{M}_{RSNS} = 10m^2 + 30m - 6. \quad (4.78)$$

the data generated by the algorithm and the resulting quadratic function derived from curve fitting the data are displayed in Figure 4.12.

To verify Equation (4.78), it is derived from the solutions of the congruence equations listed in Table 3.6. From Table 3.6,

$$h_{250} = a_1 4m_2 m_4 - 4m_1 m_3, \quad (4.79)$$

and

$$h_{233} = a_2 4m_2 m_3 + h_{s_{233}} + 4m_1 m_4. \quad (4.80)$$

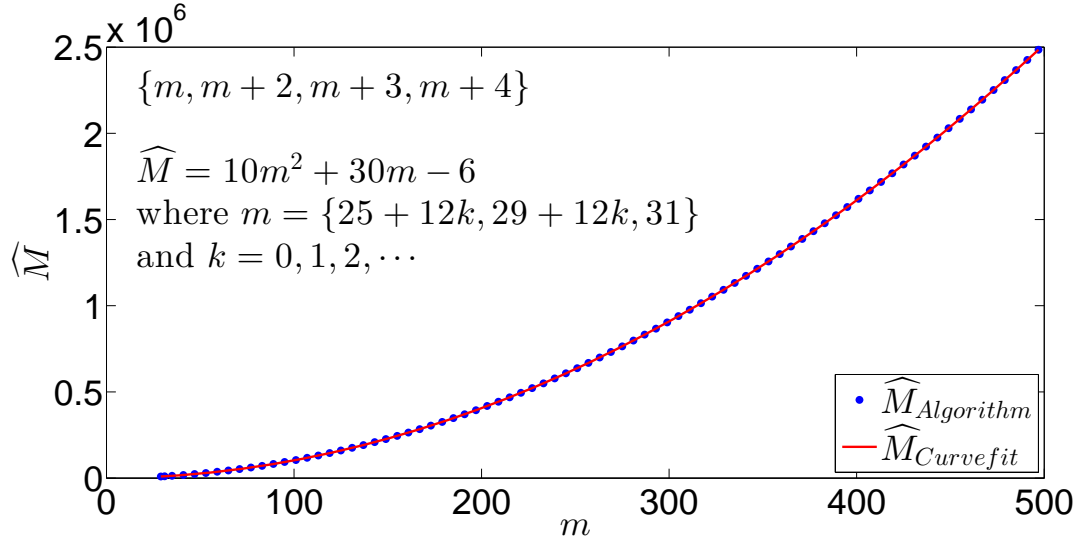


Figure 4.12: Curve fitting results plotted against algorithm results for the dynamic range of the robust symmetrical number system \widehat{M}_{RSNS} when the moduli $m_i = \{m, m+2, m+3, m+4\}$ where $m = \{25 + 12k, 29 + 12k, 31\}$ where $k = 0, 1, 2, \dots$.

To solve for h_{250} , the beginning position was used to solve Equation (4.79) for a_1 where

$$a_1 = \frac{h_1 + 4m(m+3)}{4(m+2)(m+4)} \quad (4.81)$$

and the data points were curve fitted. It was determined that

$$a_1 = \begin{cases} \frac{1}{3}m^2 + \frac{1}{6}m - \frac{1}{2}, & m = 25 + 12k \\ m^2 + \frac{5}{2}m + \frac{1}{2}, & m = 29 + 12k \end{cases} \quad (4.82)$$

resulting in

$$h_{250} = \begin{cases} \frac{4}{3}m^4 + \frac{26}{3}m^3 + \frac{26}{3}m^2 + \frac{34}{3}m - 21, & m = 25 + 12k \\ 4m^4 + 34m^3 + 90m^2 + 80m + 16, & m = 29 + 12k. \end{cases} \quad (4.83)$$

To solve for h_{233} , the shift value $h_{s_{233}}$ was determined from the congruence equations,

$$\begin{aligned} \frac{h_{s_{233}} + 1}{4} &\equiv 0 \pmod{m_2} \\ \frac{h_{s_{233}} + 1}{4} &\equiv 0 \pmod{m_3}, \end{aligned} \quad (4.84)$$

using the CRT resulting in $h_{s_{233}} = -1$. The expression for a_2 was then determined from the

ending position by solving

$$a_2 = \frac{h_2 + 1 + 4m(m+4)}{4(m+2)(m+3)}. \quad (4.85)$$

It was determined that

$$a_2 = \begin{cases} \frac{1}{3}m^2 + \frac{1}{2}m - \frac{5}{6}, & m = 25 + 12k \\ m^2 + \frac{7}{2}m + \frac{1}{2}, & m = 29 + 12k \end{cases}, \quad (4.86)$$

resulting in

$$h_{233} = \begin{cases} \frac{4}{3}m^4 + \frac{26}{3}m^3 + \frac{56}{3}m^2 + \frac{34}{3} - 21, & m = 25 + 12k \\ 4m^4 + 34m^3 + 100m^2 + 110m + 11, & m = 29 + 12k \end{cases}, \quad (4.87)$$

where $k = 0, 1, 2, \dots$. Equation (4.83) and Equation (4.87) were substituted into

$$\hat{M}_{RSNS} = h_{233} - h_{250} - 1, \quad (4.88)$$

and the resulting expression was simplified to obtain Equation (4.78).

For the other Start Case, Case 252, the data from the algorithm were curve fitted resulting in

$$\hat{M}_{RSNS} = 10m^2 + 30m - 8, \quad (4.89)$$

where $m = \{43 + 12k, 47 + 12k\}$ and $k = 0, 1, 2, \dots$. The data points generated from the efficient algorithm and Equation (4.89) are plotted in Figure 4.13. To solve for h_{252} , a similar approach was taken as for the previous sets of values. The solution to the congruence equations for Case 252 is

$$h_{252} = a_1 4m_2 m_4 + h_{s_{252}} - 4m_1 m_3. \quad (4.90)$$

The shift value, $h_{s_{252}}$, is determined by solving the congruence equations,

$$\begin{aligned} \frac{h_{s_{252}} - 2}{4} &\equiv 0 \pmod{m_2} \\ \frac{h_{s_{252}} + 2}{4} &\equiv 0 \pmod{m_4} \end{aligned}. \quad (4.91)$$

The CRT is applied to Equation (4.91) to obtain

$$h_{s_{252}} = 2m^2 + 14m + 22. \quad (4.92)$$

By curve fitting the solutions for a_1 derived from the values of h_1 , the following expressions for

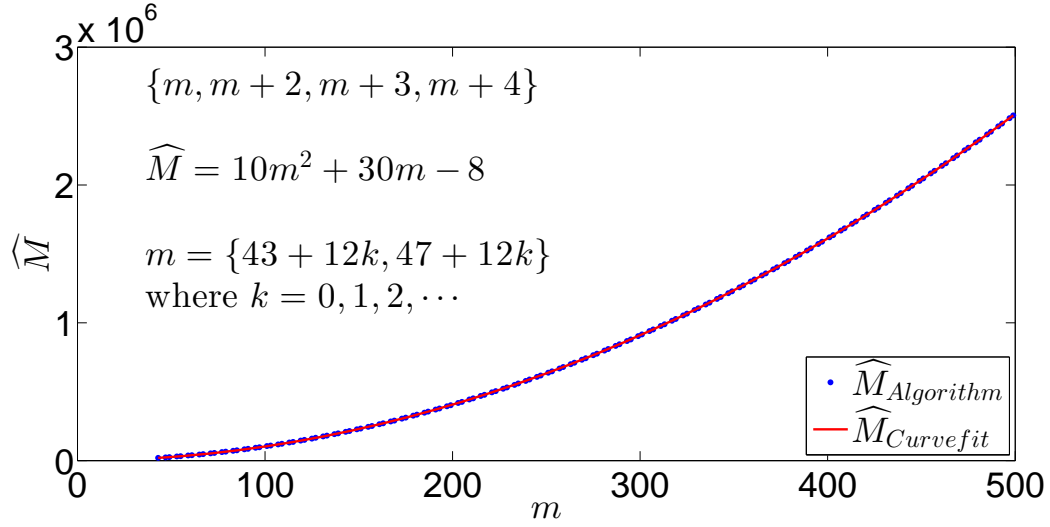


Figure 4.13: Curve fitting results plotted against algorithm results for the dynamic range of the robust symmetrical number system \widehat{M}_{RSNS} when the moduli $m_i = \{m, m+2, m+3, m+4\}$ where $m = \{25 + 12k, 29 + 12k, 31\}$ where $k = 0, 1, 2, \dots$.

a_1 were determined

$$a_1 = \begin{cases} \frac{11}{24}m^2 + \frac{2}{3}m - \frac{9}{8}, & m = 43 + 24k \\ \frac{5}{8}m^2 + \frac{3}{2}m - \frac{1}{8}, & m = 47 + 24k \\ \frac{5}{6}m^2 + \frac{5}{3}m - \frac{3}{2}, & m = 55 + 24k \\ \frac{1}{8}m^2 - \frac{1}{8}, & m = 59 + 12k. \end{cases} \quad (4.93)$$

Equation (4.93) is substituted into Equation (4.90) and the resulting expression is simplified to obtain

$$h_{252} = \begin{cases} \frac{11}{6}m^4 + \frac{41}{3}m^3 + \frac{145}{6}m^2 - \frac{11}{3}m - 14, & m = 43 + 24k \\ \frac{5}{2}m^4 + 21m^3 + \frac{107}{2}m^2 + 47m + 18, & m = 47 + 24k \\ \frac{10}{3}m^4 + \frac{80}{3}m^3 + \frac{176}{3}m^2 + \frac{58}{3}m - 26, & m = 55 + 24k \\ \frac{1}{2}m^4 + 3m^3 + \frac{3}{2}m^2 - m + 18, & m = 59 + 12k \end{cases} \quad (4.94)$$

where $k = 0, 1, 2, \dots$.

For the Stop Case, Case 233, the solution to the congruence equation for h_{233} is Equation (4.80)

where $h_{s_{233}} = -1$. The same procedure is used as in the previous cases to solve for a_2 producing

$$a_2 = \begin{cases} \frac{11}{24}m^2 + \frac{9}{8}m - \frac{5}{6}, & m = 43 + 24k \\ \frac{5}{8}m^2 + \frac{17}{8}m + \frac{1}{2}, & m = 47 + 24k \\ \frac{5}{6}m^2 + \frac{5}{6}m - \frac{4}{3}, & m = 55 + 24k \\ \frac{1}{8}m^2 + \frac{1}{8}m + \frac{1}{2}, & m = 59 + 12k \end{cases}. \quad (4.95)$$

Equation (4.95) is substituted into Equation (4.80) to obtain

$$h_{233} = \begin{cases} \frac{11}{6}m^4 + \frac{41}{3}m^3 + \frac{205}{6}m^2 + \frac{79}{3}m - 21, & m = 43 + 24k \\ \frac{5}{2}m^4 + 21m^3 + \frac{127}{2}m^2 + 77m + 18, & m = 47 + 24k \\ \frac{10}{3}m^4 + \frac{80}{3}m^3 + \frac{206}{3}m^2 + \frac{148}{3}m - 33, & m = 55 + 24k \\ \frac{1}{2}m^4 + 3m^3 + \frac{23}{2}m^2 - 29m + 11, & m = 59 + 12k \end{cases}. \quad (4.96)$$

Equation (4.96) and Equation (4.94) are substituted into

$$\widehat{M}_{RSNS} = h_{233} - h_{252} - 1 \quad (4.97)$$

to obtain Equation (4.89) verifying the results produced from curve fitting.

One Even and Three Odd Sequential Coprime Moduli (Odd, Odd, Odd, Even)

The next case examined was the case where four sequential coprime moduli were used of the form $\{m, m+2, m+4, m+5\}$ where $m \geq 39$, $\gcd(m, 5) = 1$, and m is odd. A sample of the data used in curve fitting is illustrated in Table 4.13, and the curve fitting results are displayed in Figure 4.14. Curve fitting resulted in

$$\widehat{M}_{RSNS} = 10m_2 + 54m + 20. \quad (4.98)$$

For the set of moduli examined, the Start Case is Case 231, and the Stop Case is Case 232. From Table 3.6,

$$\widehat{M}_{RSNS} = h_{s_{232}} + 4m_1m_4 - h_{s_{231}} - 1. \quad (4.99)$$

Table 4.13: Sample of data used in curve fitting for sequential coprime moduli of form, $\{m, m+2, m+4, m+5\}$, with m odd, $m \geq 39$, and $\gcd(m, 5) = 1$.

m	$m+2$	$m+4$	$m+5$	$h_1 + 1$	Start Case	$h_2 - 1$	Stop Case	\hat{M}_{RSNS}
39	41	43	44	2637638	231	2654973	232	17336
41	43	45	46	9234018	231	9253061	232	19044
47	49	51	52	1509618	231	1534265	232	24648
51	53	55	56	10844038	231	10872821	232	28784
53	55	57	58	5053866	231	5084837	232	30972
57	59	61	62	5010070	231	5045657	232	35588
59	61	63	64	2813346	231	2851361	232	38016
63	65	67	68	31530486	231	31573597	232	43112
69	71	73	74	20898166	231	20949521	232	51356
71	73	75	76	18045918	231	18100181	232	54264
77	79	81	82	50219694	231	50283161	232	63468
81	83	85	86	35416458	231	35486461	232	70004
83	85	87	88	57030606	231	57103997	232	73392

The shift values are determined by solving the congruence equations based on Equation (3.28).

The congruence equations for solving $h_{s_{231}}$ are

$$\begin{aligned} \frac{h_{s_{231}} - 1}{4} &\equiv 0 \pmod{m_2} \\ \frac{h_{s_{231}} - 1}{4} &\equiv 0 \pmod{m_3} \end{aligned} \quad , \quad (4.100)$$

and the congruence equations for $h_{s_{232}}$ are

$$\begin{aligned} \frac{h_{s_{232}} - 2}{4} &\equiv 0 \pmod{m_2} \\ \frac{h_{s_{232}} + 2}{4} &\equiv 0 \pmod{m_3} \end{aligned} \quad . \quad (4.101)$$

Equation (4.100) and Equation (4.101) are solved using the CRT and result in

$$h_{s_{231}} = 1 \quad \text{and} \quad (4.102)$$

$$h_{s_{232}} = 2m^2 + 14m + 22. \quad (4.103)$$

Equation (4.98) is obtained by substituting Equation (4.102) and Equation (4.103) into Equation (4.99) and simplifying the resulting expression.

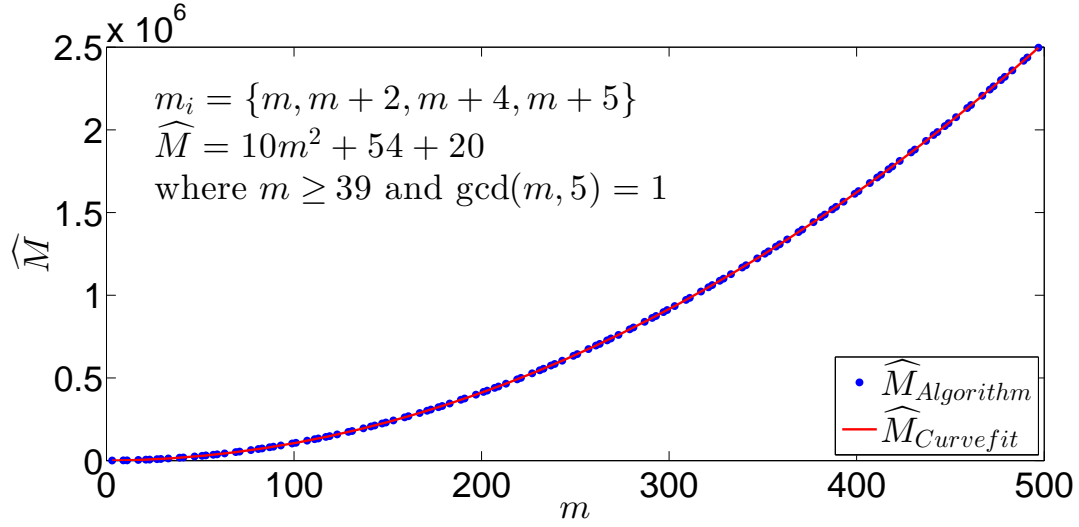


Figure 4.14: Curve fitting results plotted against algorithm results for the dynamic range of the robust symmetrical number system \widehat{M}_{RSNS} when the moduli $m_i = \{m, m+2, m+4, m+5\}$ where with m is odd, $m \geq 39$, and $\gcd(m, 5) = 1$.

Four Sequential Odd Coprime Moduli

A four-sequence RSNS is examined with coprime odd moduli, $m_i = \{m, m+2, m+4, m+6\}$. It was determined when $m \geq 13$ and $\gcd(m, 3) = 1$ that the Start Case is Case 260 and the Stop Case is Case 261 as illustrated in Table 4.14. The data generated using the efficient algorithm described in Section 4.1.2 were curve fit and resulted in

$$\widehat{M}_{RSNS} = 10m^2 + 38m + 56. \quad (4.104)$$

The data and Equation (4.104) are plotted in Figure 4.15.

To verify that the expression, \widehat{M}_{RSNS} is derived from the solutions to the congruence equations in Table 3.6. From these solutions,

$$\widehat{M}_{RSNS} = h_{s_{261}} + 8m_1m_2 - 1. \quad (4.105)$$

The shift value $h_{s_{261}}$ is determined by solving the congruence equations, Equation (4.70), using the CRT to obtain

$$h_{s_{261}} = 2m^2 + 22m + 57. \quad (4.106)$$

Equation (4.106) is substituted into Equation (4.105) resulting in Equation (4.104).

The new closed-form expressions for \widehat{M}_{RSNS} for $N = 4$ are summarized in Table 4.15.

Table 4.14: Sample of data used in curve fitting for sequential coprime moduli odd moduli of form, $m_i = \{m, m+2, m+4, m+6\}$, with m odd, $m \geq 13$, and $\gcd(m, 3) = 1$.

m	$m+2$	$m+4$	$m+6$	h_1+1	Start Case	h_2-1	Stop Case	\widehat{M}_{RSNS}
13	15	17	19	61237	260	63476	261	2240
17	19	21	23	2573	260	6164	261	3592
19	21	23	25	456105	260	460492	261	4388
23	25	27	29	35285	260	41504	261	6220
25	27	29	31	69221	260	76476	261	7256
29	31	33	35	171965	260	181532	261	9568
31	33	35	37	249729	260	260572	261	10844
35	37	39	41	346601	260	360236	261	13636
37	39	41	43	2088673	260	2103824	261	15152
41	43	45	47	1490369	260	1508792	261	18424

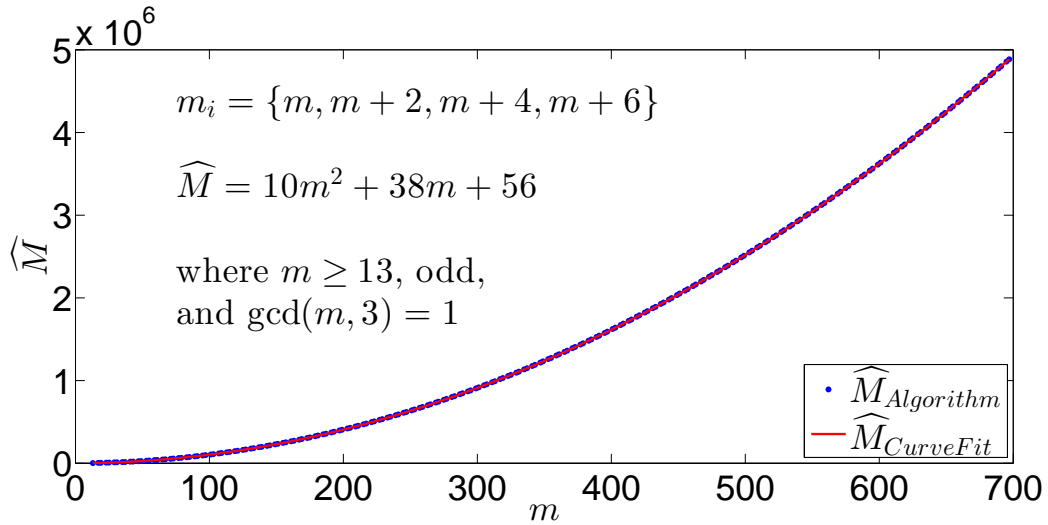


Figure 4.15: Curve fitting results plotted against algorithm results for \widehat{M}_{RSNS} when the moduli $m_i = \{m, m+2, m+4, m+6\}$ where with m is odd, $m \geq 13$, and $\gcd(m, 3) = 1$.

Table 4.15: New closed-form expressions for the dynamic range of four-sequence robust symmetrical number systems, from [68].

m_i	\hat{M}_{RSNS}	m
$\{m-1, m, m+2, m+4\}$	$10m^2 + 6m + 20$	$m \equiv 3 \pmod{6}$ or $m \equiv 5 \pmod{6}$ with $m \geq 15$ and $m \neq \{29, 33\}$
$\{m, m+1, m+2, m+4\}$	$10m^2 + 22m + 20$	$m \equiv 1 \pmod{6}$ or $m \equiv 3 \pmod{6}$ and $m \geq 15$
$\{m, m+2, m+3, m+4\}$	$10m^2 + 30m - 6$ $10m^2 + 30m - 8$	$m = \{25 + 12k, 29 + 12k, 31\}$ where $k = 0, 1, 2, \dots$, $m = \{43 + 12k, 47 + 12k\}$ and $k = 0, 1, 2, \dots$
$\{m, m+2, m+4, m+5\}$	$10m^2 + 54m + 20$	$m \geq 39$, $\gcd(m, 5) = 1$, and m is odd
$\{m, m+2, m+4, m+6\}$	$10m^2 + 38m + 56$	$m \geq 13$ and $\gcd(m, 3) = 1$

4.4 Concluding Remarks

This chapter presented an efficient algorithm for determining \hat{M}_{RSNS} with a significant reduction in computational complexity compared to a naïve search algorithm. The efficient algorithm was used to examine various combinations of moduli sets for $N = 3$ and $N = 4$ RSNS sequences and to develop analytical closed-form expressions for \hat{M}_{RSNS} by identifying the moduli sets with the same case numbers for the beginning and ending points of the RSNS sequences. The closed-form analytical expressions were then proven using the solutions to the congruence equations that identify the ambiguity locations, listed in Table 3.6. The new closed-form analytical expressions for \hat{M}_{RSNS} provide an expanded set of moduli sets for which a closed-form analytical expression for \hat{M}_{RSNS} exist, allowing \hat{M}_{RSNS} to be easily calculated for a wide variety of moduli sets.

The method for determining the new closed-form analytical expressions for \hat{M}_{RSNS} presented in this chapter can be used to determine additional expressions for RSNS sequences with $N > 4$. As an example, for an $N = 5$ RSNS sequence consisting of four sequential odd and one even coprime moduli of the form, $\{m, m+2, m+3, m+4, m+6\}$ with m odd, there are several different cases to examine that have the same Start and Stop Case Numbers. For the sequences with a Start Case Number equal to 380 and a Stop Case Number equal to 313, when $m = 109 + 72k$ and $m = 133 + 72k$ for $k = 0, 1, 2, \dots$,

$$\hat{M}_{RSNS} = \frac{5}{3}m^3 + 10m^2 + \frac{205}{3}m + 152. \quad (4.107)$$

The data points produced from the efficient algorithm are plotted with the curve fit solution for \hat{M}_{RSNS} in Figure 4.16. Equation (4.107) can be proven using the methods described in Section 4.3.1 and Section 4.3.2. Determining additional sets of closed-form analytical expressions for \hat{M}_{RSNS} leading to a general closed-form expression is one area of continuing research.

In the next chapter, RSNS preprocessing is used in a photonic DF linear antenna array. The RSNS allows for a small baseline array while maintaining fine frequency resolution. The photonic implementation enables wide band DF using phase interferometry without the requirement to down convert the SOI.

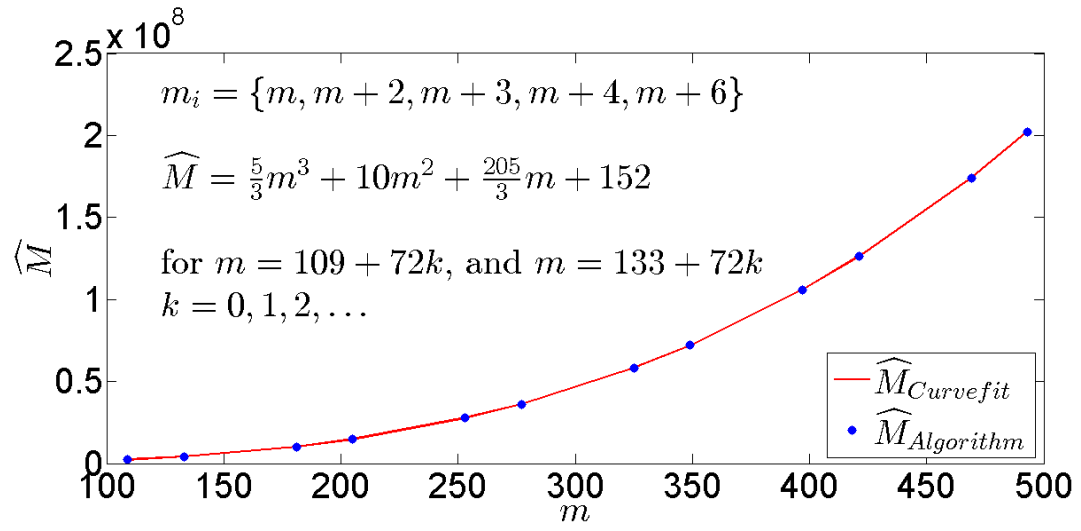


Figure 4.16: Curve fitting results and algorithm results for \widehat{M} when the moduli $m_i = \{m, m+2, m+3, m+4, m+6\}$ when $m = 109 + 72k$ and $m = 133 + 72k$ and $k = 0, 1, 2, \dots$

CHAPTER 5:

Photonic Direction Finding Array with Robust Symmetrical Number System Preprocessing

Direction finding (DF) methods are used to measure the direction-of-arrival (DOA) θ of an incident radio frequency (RF) wave and are also referred to as radio-location systems. Direction finding systems estimate the geographical direction or true bearing of an emitter and have applications in navigation, targeting, law enforcement and wildlife management. Other applications include electronic signal intelligence, electronic warfare (EW), signal identification, search and rescue, propagation analysis, and ionospheric research. The DF processing may be accomplished by using a separate subsystem that is not involved in the signal acquisition and analysis processing (tasked DF) or as part of the signal acquisition process. High performance DF arrays are characterized by a high angular (spatial) resolution, a wide frequency BW, a wide field of view (FOV), a minimum number of array elements, and a minimum baseline length.

Several techniques can be used to determine the DOA of a incident RF signal. They include amplitude comparison [71], phase interferometry [72]–[74], combining amplitude comparison and phase interferometry [75], and super-resolution techniques [76]–[79]. Each technique offers specific advantages and disadvantages. For detecting a single signal, conventional DF techniques typically involve a linear or circular interferometer to measure the incident wave's phase and/or amplitude at each antenna element. For multiple signals, super-resolution DF techniques are often used. These techniques can be categorized as beam-forming super-resolution techniques (maximum likelihood methods, adaptive angular response, thermal noise algorithm) or eigenvalue-based super-resolution techniques (multiple signal classification (MUSIC), Root-MUSIC, estimation of signal parameters via rotational invariance techniques (ESPRIT).

In EW systems, amplitude and phase measurement interferometer systems are typically the methods of choice since they are easier to implement and have good resolution capabilities. However, using these methods can result in ambiguities that must be resolved efficiently. When multiple signals are present, amplitude and phase measurement systems can produce erroneous results due to interference between the signals. This problem is often solved by channelizing the receiver's BW into channels with a narrow BW so that there is a high probability that only one emitter is present in each channel. By comparison, super-resolution techniques are com-

putationally complex, but can determine the DOA with a high degree of accuracy for multiple signals. A disadvantage to super-resolution techniques is that errors can result due to an incorrect estimate of the model order (number of signals present) or inaccurate characterization of antenna array response. In addition, element matching requirements are difficult to realize in a cluttered environment, and multi-path effects can lead to poor DF results. Super-resolution methods are also unattractive for RF DF with array antennas because each antenna requires a matched receiver channel to support simultaneous sampling. Additionally, the matched receivers require calibration to achieve accurate results [80].

Wideband optical technology now plays a significant role in many DF and digital receiver architectures. Especially important in DF applications is the use of the Mach-Zehnder modulator (MZM) built using $LiNbO_3$ technology. The use of the MZM for wideband fiber-optic DF applications is described in [81] where it is used as an optical down conversion circuit at the antenna and as a means to efficiently couple the local oscillator into the optical domain. Accuracy of better than 0.1 deg is achieved at 10 GHz with a BW capability of 2 - 18 GHz. In [82], optical Bragg cells are explored for DF applications. A laser is split between two Bragg cells whose outputs are Fourier transformed by a lens and detected by a channelized phase detector. In [83], a photonic approach is used to measure the DOA for a RF signal. Two cascaded MZMs, biased at the minimum transmission point, are used to modulate a continuous wave (CW) laser. Identical RF signals with a given phase shift are applied to the electrode of each MZM. The phase difference between the signals is determined by measuring the optical signal's power. In [84], a technique for detecting the DOA of broadband microwave (MW) signals in phased-array antennas is proposed. The technique is based upon a two-tap photonic transversal MW filter and measuring the frequency of the notches produced over the broadband signal using a spectrum analyzer.

In this chapter, a novel photonic, wideband, four-element, phase sampling, linear DF antenna array using an RSNS preprocessing technique is presented. A dual electrode Mach-Zehnder modulator (DE-MZM) is used to modulate the intensity of a CW laser to generate a signal that is a function of the phase difference between the phase shifted signals applied to the electrodes of the DE-MZM. The modulated optical signal is converted back to the electrical domain by a photodetector (PD) and is passed through a direct current (DC) block leaving a sinusoidal signal whose magnitude is dependent upon the phase difference ψ_i between the RF signals applied to the DE-MZM electrodes. The magnitude of the signal in each channel is determined through envelope detection, and the normalized envelope is applied to separate comparator networks to

generate the RSNS symmetrical residues that are used in decoding the DOA.

Considering that the BW of a $LiNbO_3$ DE-MZM is on the order of 40 GHz, the use of DE-MZMs provides wideband DF capability without having to down convert a high frequency input signal (e.g. 10 GHz pulsed radar signal) to an intermediate frequency. The use of photonics also allows transfer of the signals to a central location for signal processing due to the reduced weight, low loss, and immunity to EMI of fiber-optic cables compared to those of metallic waveguides and RF cables [9], [85]. Additionally, narrow band signal processing techniques can be applied to wideband RF signals in the optical region due to the optical carrier being in the THz range. The application of RSNS preprocessing allows obtaining an unambiguous DOA with fine spatial resolution while using a smaller array size than conventional linear arrays. Robust symmetrical number system preprocessing decomposes the spatial filtering operation into a number of parallel suboperations (moduli) that are of smaller computational complexity [57]. The inherent integer Gray code property of the RSNS can also be used for error detection and correction when tracking the DOA of a moving target.

The remainder of this chapter is organized as follows. In Section 5.1, phase sampled DF concepts are presented and the concept of using a DE-MZM in phase interferometry applications is developed. Simulation and experimental results are also presented to demonstrate the concept. In Section 5.2, the design of a four-element photonic DF array with RSNS preprocessing is presented, and simulation results are provided in Section 5.3. Experimental results for the RSNS based photonic DF array are provided in Section 5.4. In Section 5.5, simulations are conducted to demonstrate the performance of the array when the signal environment consists of multiple pulsed emitters. The final section provides concluding remarks and discusses potential applications and future research areas.

5.1 Use of a Dual Electrode Mach Zehnder Modulator in Phase Interferometry

For a two-element photonic DF linear array shown in Figure 5.1, the DOA of a RF emitter is determined by detecting the phase difference between the narrow band signals received at a reference antenna element and a measurement antenna element separated by a distance, d . The phase angle ψ between the signals arriving at the two antennas is related to the DOA θ by

$$\psi = \frac{2\pi}{\lambda} d \sin \theta, \quad (5.1)$$

where λ is the wavelength of the incident RF wave.

If the signal at the reference antenna element is $V_1(t) = A \cos(\Omega t)$ and the signal at the measurement antenna element is $V_2(t) = A \cos(\Omega t - \psi)$, θ is calculated by solving Equation (5.1) for θ ,

$$\theta = \arcsin \left(\frac{\psi \lambda}{2\pi d} \right). \quad (5.2)$$

To prevent ambiguous DOA results, $d \leq \lambda/2$ for a FOV of 180deg. If the FOV is reduced, the maximum distance between antenna elements can be increased by a scaling factor [57]

$$\xi = \frac{1}{\sin(FOV/2)}. \quad (5.3)$$

In Figure 5.1, the DC component of the PD output is blocked, and the magnitude of the alternating current (AC) component is determined from the output of an envelope detector. The

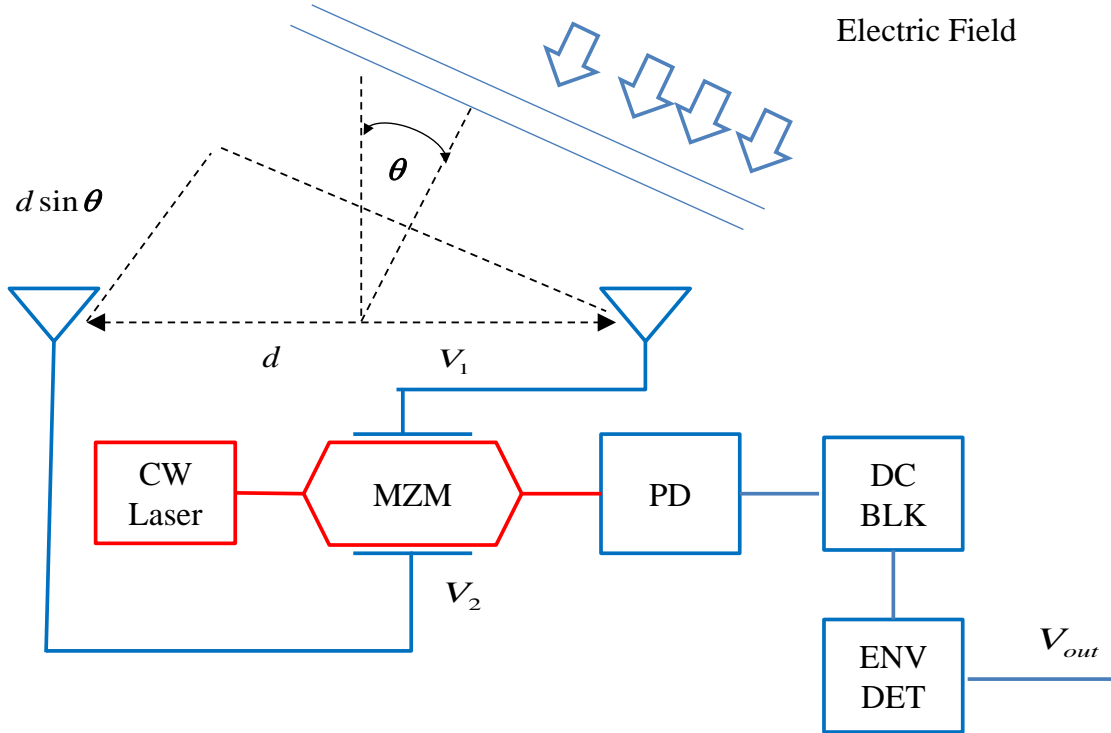


Figure 5.1: Block diagram of a two-element photonic direction finding linear array.

normalized output voltage of the envelope detector V_{out} is demonstrated below to be a function of the phase angle ψ .

The transmission factor T of a DE-MZM is a function of the difference between the voltages, V_1 and V_2 , applied to its electrodes and is expressed as

$$T = \frac{1}{2} \cdot \left[1 + \cos \left(\pi \cdot \frac{V_1 - V_2}{V_\pi} + \phi_b \right) \right], \quad (5.4)$$

where

$$\phi_b = 2\pi \frac{\Delta_{nL}}{\lambda} + \pi \frac{V_b}{V_\pi} \quad (5.5)$$

is the phase bias, V_π is the half-wave switching voltage of the DE-MZM, and $\Delta_{nL} = n_2 L_2 - n_1 L_1$ is the path length mismatch between the two arms of the interferometer [86], [87]. If equal amplitude phase shifted sinusoids, $V_1 = V \cos(\Omega t)$ and $V_2 = V \cos(\Omega t + \psi)$, are applied to the electrodes of the DE-MZM, the difference term in Equation (5.4) is

$$V_1 - V_2 = 2V \sin(\psi/2) \sin(\Omega t + \psi/2). \quad (5.6)$$

As a result, Equation (5.4) can be recast as

$$T = \frac{1}{2} \left[1 + \cos \left(\underbrace{\frac{2V \sin \frac{\psi}{2}}{V_\pi} \pi \sin \left(\Omega t + \frac{\psi}{2} \right)}_x + \underbrace{\phi_b}_y \right) \right]. \quad (5.7)$$

Applying the identity [70],

$$\cos(x + y) = \cos x \cos y - \sin x \sin y, \quad (5.8)$$

to Equation (5.7), the transmission factor can be expressed as

$$T = \frac{1}{2} \left[1 + \cos \phi_b \cos \left(z \sin \left(\Omega t + \frac{\psi}{2} \right) \right) - \sin \phi_b \sin \left(z \sin \left(\Omega t + \frac{\psi}{2} \right) \right) \right], \quad (5.9)$$

where

$$z = \frac{2V \sin \frac{\psi}{2}}{V_\pi} \pi. \quad (5.10)$$

The result in Equation (5.9) can be expressed as a summation of the harmonics of the input

signal by applying the identities [70],

$$\cos(z \sin \theta) = J_0(z) + 2 \sum_{k=1}^{\infty} J_{2k}(z) \cos(2k\theta) \quad (5.11)$$

and

$$\sin(z \sin \theta) = 2 \sum_{k=0}^{\infty} J_{2k+1}(z) \sin((2k+1)\theta), \quad (5.12)$$

where $J_v(z)$ is the Bessel function of the first kind of order v , to Equation (5.9). As a result,

$$T = \frac{1}{2} \left[1 + \cos \varphi_b \left(J_0(z) + 2 \sum_{k=1}^{\infty} J_{2k}(z) \cos \left(2k \sin \left(\Omega t + \frac{\psi}{2} \right) \right) \right) \right. \\ \left. - 2 \sin \varphi_b \sum_{k=0}^{\infty} J_{2k+1}(z) \sin \left((2k+1) \left(\Omega t + \frac{\psi}{2} \right) \right) \right]. \quad (5.13)$$

If the DE-MZM is biased at the quadrature point, $V_b = V_\pi/2$, $\varphi_b \approx \pi/2$. As a result, the even numbered harmonics are suppressed, and Equation (5.13) simplifies to

$$T = \frac{1}{2} - \sum_{k=0}^{\infty} J_{2k+1}(z) \sin \left((2k+1) \left(\Omega t + \frac{\psi}{2} \right) \right). \quad (5.14)$$

Therefore, the output of the PD consists of a DC component plus a summation of the odd harmonics of the RF signal. The amplitudes of the sinusoidal components are a function of $\sin(\psi/2)$. If $V \ll V_\pi$, z is small, and $J_1(z) \gg J_{2k+1}(z)$ where $k = 1, 2, \dots, \infty$. As a result, the magnitude of the AC component of the modulated signal may be approximated as $|J_1(z)|$. When the argument, z , is small, the Bessel function of the first kind may be approximated as [70],

$$J_v(z) \approx (0.5z)^v / \Gamma(v+1), \quad (5.15)$$

where Γ is the Gamma function defined as

$$\Gamma(v) = (v-1)! \quad (5.16)$$

if v is a positive integer. Applying Equation (5.15), the normalized value of $|J_1(z)|$ can be approximated as $|\sin(\psi/2)|$ when $V \ll V_\pi$. The two functions are plotted versus θ in Figure 5.2

when $V = 0.1$ and $V_\pi = 2.6$ and $d = \lambda/2$. The functions are approximately equal with a maximum error, $\epsilon_{max} = 2.8 \times 10^{-3}$ and a mean squared error, $MSE = 2.4 \times 10^{-6}$. Therefore, the normalized value of V_{out} can be approximated as

$$\frac{V_{out}}{\max(V_{out})} \approx |\sin(\psi/2)| \quad (5.17)$$

and can be used to determine θ , from Equation (5.1) provided $V \ll V_\pi$. Note that the peak value in Figure 5.2a corresponds to $\psi = \pm 180^\circ$ and $\theta = \pm 90^\circ$. To have the peak value of occur at $\theta = 0^\circ$ which corresponds to $\psi = 0^\circ$, a 180° phase shift can be applied to the voltage at terminal number (2) of the DE-MZM. This result in $V_{out} \approx \cos(\psi/2)$.

RSOFT Design Group's OptSim software package was used to simulate the two-element photonic DF array (Figure 5.1) with antenna spacing equal to $\lambda/2$ through the PD output using ideal components in a noise free environment. The simulation was conducted for $-90^\circ \leq \theta \leq 90^\circ$ in one degree increments. Figure 5.3a and Figure 5.3b display the output of the DE-MZM and PD respectively when $\theta = 90^\circ$. The waveform is a sinusoid centered about a positive DC value as predicted by the above analysis. The OptSim data was exported to MATLAB where the mean value was determined and subtracted from the data to simulate the DC blocking capacitor, and the normalized magnitude was derived simulating the normalized envelope detector output. In Figure 5.2b, the results of the simulation are plotted against $|\sin(\psi/2)|$ demonstrating the use of a DE-MZM in phase interferometry to determine θ . The simulation results and the theoretical approximation of the normalized envelope detector output, $|\sin(\psi/2)|$, are approximately equal.

The theoretical and simulations results were verified experimentally using the equipment setup displayed in Figure 5.4. A 2.4 GHz CW signal was generated with a Hewlett Packard HP 83711B synthesized CW generator. The input signal passed through a 4-to-1 splitter prior to being applied to the electrodes of the DE-MZM (Fujitsu FTM9712ER) via mechanical phase shifters. The phase shift applied to the signal at the second electrode was varied between 0 and -180 degrees. A CW optical carrier signal was provided by a distributed feedback (DFB) high power laser diode (EM4) operated at a wavelength of 1550 nm. The PD used was a high speed, InGaAs PD (Newport Model 1014). The low noise amplifier (LNA) was a RF-Bay LNA-2700 designed for operation between 2.3 and 3.2 GHz.

The results are presented for an input signal power level of 3 dBm and 6 dBm in Figure 5.5a

and Figure 5.5b respectively, where the normalized peak-to-peak voltage at the output of the LNA is plotted against the theoretical and simulation results. The experimental data closely approximates the theoretical and simulation results. The minimum normalized voltage level is above 0 VDC due to several factors including a difference in magnitude between the signals applied to the electrodes of the DE-MZM, the extinction ratio of the DE-MZM, noise in the

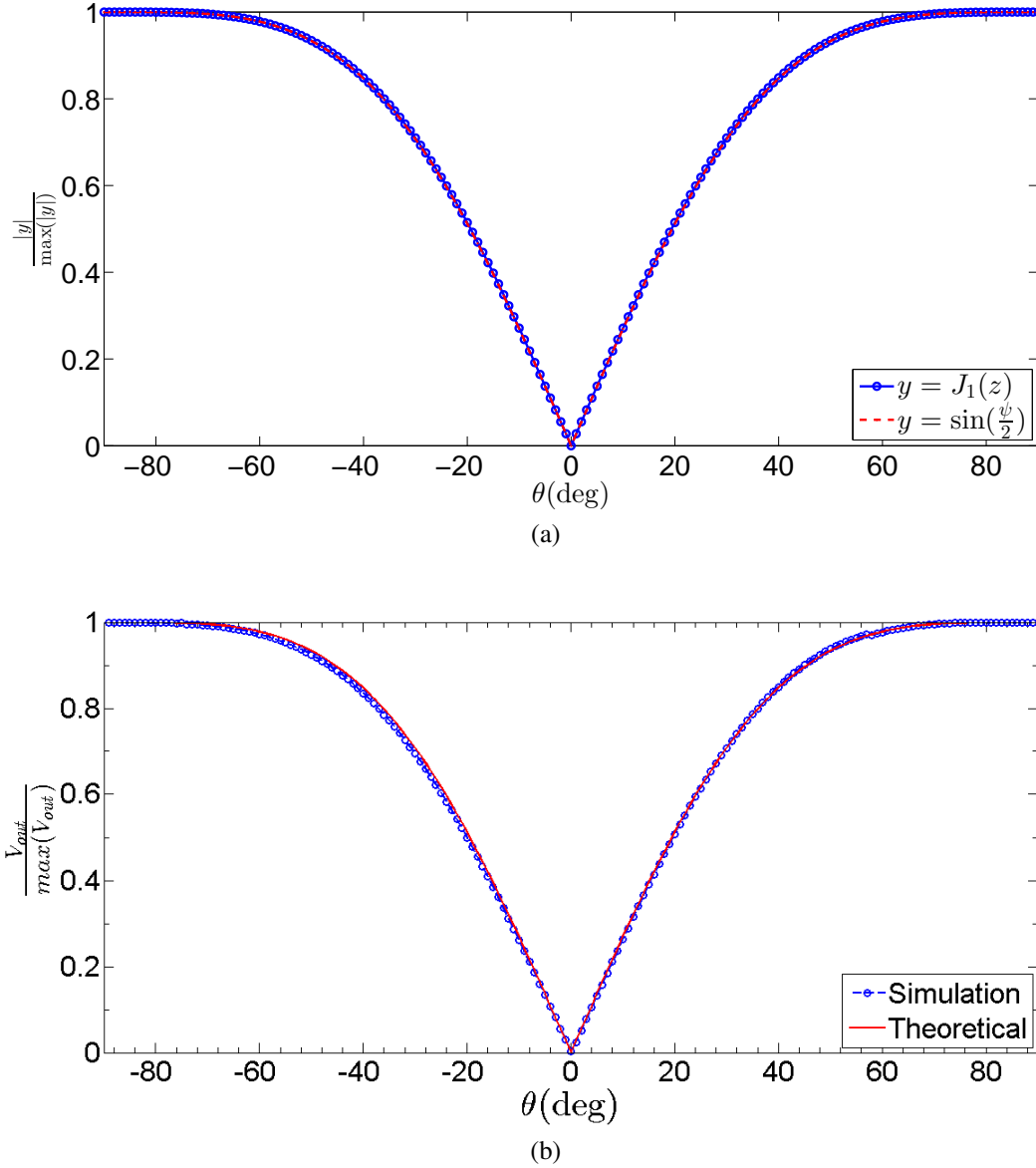


Figure 5.2: Normalized transmission coefficient vs. phase angle. In (a), the blue curve with “o” markers graphs the function $|J_1(z)|/\max(|J_1(z)|)$. The red dashed line graphs the function $|\sin(\psi/2)|$. (b) is $V_{out}/(\max(V_{out}))$ vs. DOA (θ deg) for DE-MZM biased at quadrature point, $V_b = V_\pi/2$. Red solid line graphs the theoretical results, the blue dashed line plots the simulation results.

signal, and the dark current of the PD. The experimental data confirms that the DE-MZM can be used in a phase interferometry application.

If the DE-MZM is biased at its minimum transmission point, $V_b = KV_\pi$, where K is an even

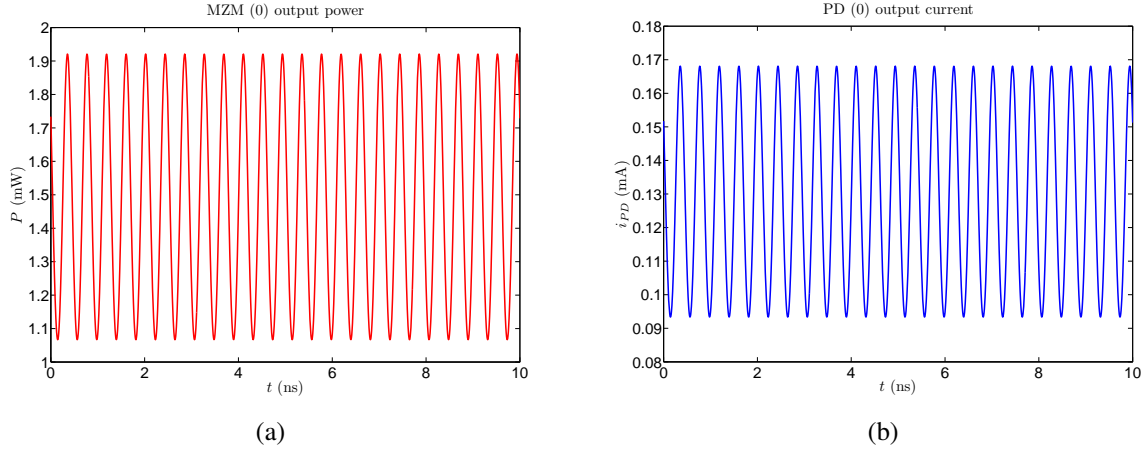


Figure 5.3: (a) displays the DE-MZM output for a DOA of 90deg. (b) displays the PD output for a DOA of 90deg.

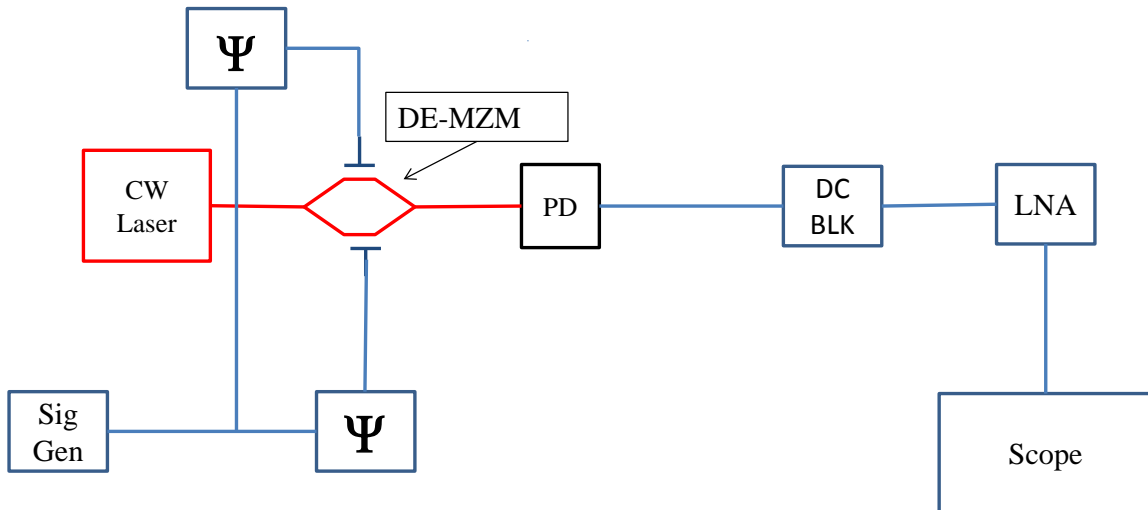
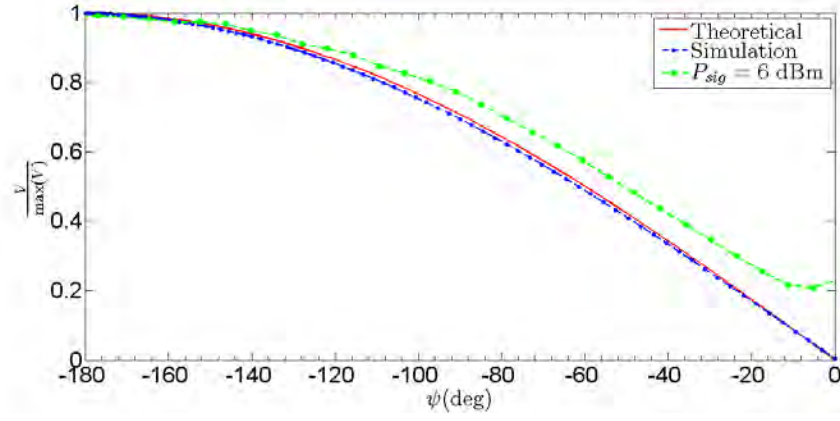
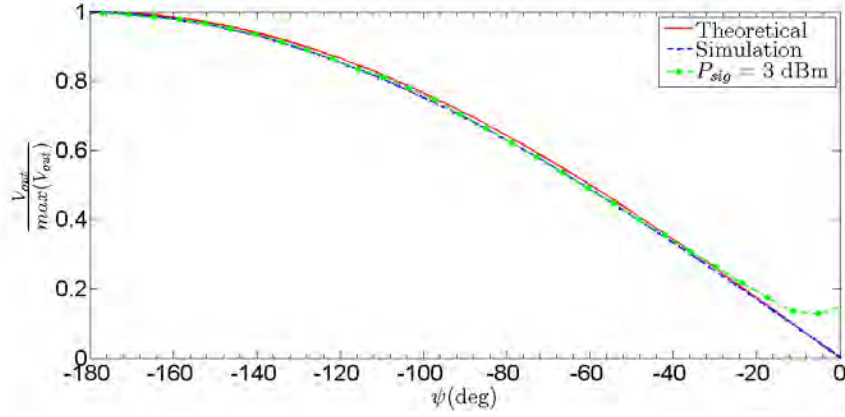


Figure 5.4: Block diagram of experimental setup for testing of a dual electrode Mach-Zehnder modulator in phase interferometry application.



(a)



(b)

Figure 5.5: Experimental results for two element array (bench test):(a) $P_{sig} = 6$ dBm, (b) $P_{sig} = 3$ dBm.

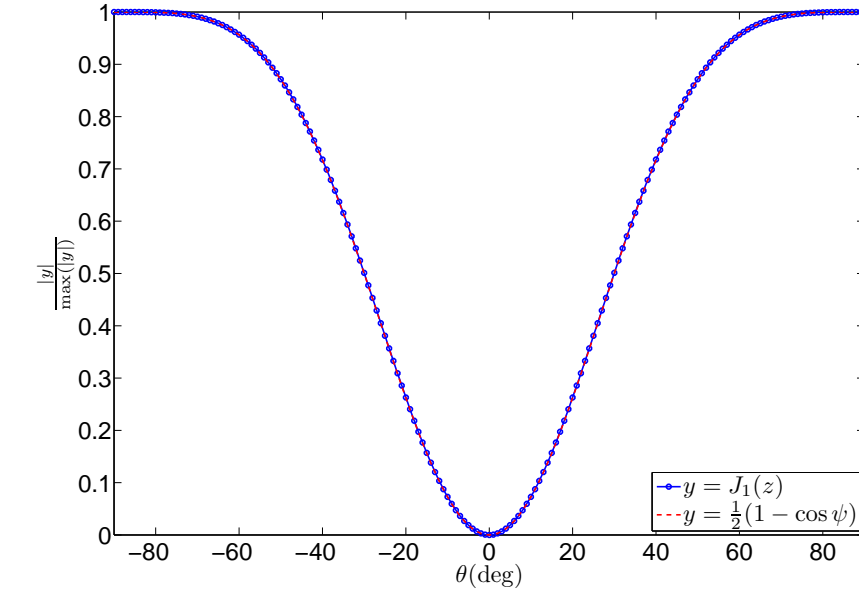
integer, the odd harmonics are suppressed. In this case, Equation (5.13) reduces to

$$T = \frac{1}{2} \left[1 + J_0(z) + 2 \sum_{k=1}^{\infty} J_{2k}(z) \cos \left(2k \sin \left(\Omega t + \frac{\Psi}{2} \right) \right) \right]. \quad (5.18)$$

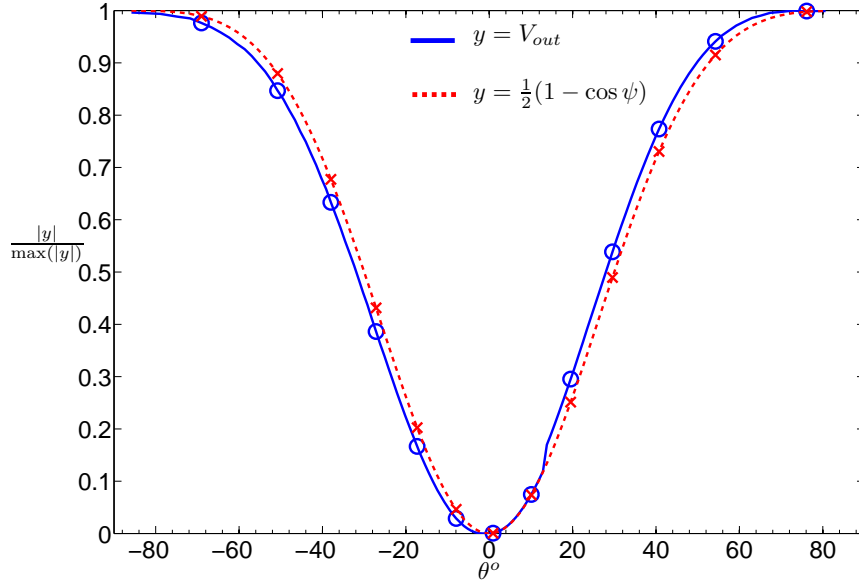
If $V \ll V_{\pi}$, $V_{out} \approx |J_2(z)|$. As a result, the normalized value of V_{out} may be approximated as $(1 - \cos \psi)/2$. The normalized values of $|J_2(z)|$ and the function $(1 - \cos \psi)/2$ are plotted versus θ in Figure 5.6a. The two curves are approximately equal with a maximum error $\epsilon_{max} = 0.012$ and mean square error $MSE = 4.2064 \times 10^{-7}$. The normalized envelope detector output voltage, therefore, can be approximated as

$$\frac{V_{out}}{\max(V_{out})} \approx \frac{1}{2} (1 - \cos(\psi)). \quad (5.19)$$

Simulations were also performed for this case where the DE-MZM is biased at the minimum transmission point using ideal components in a noise-free environment. The simulation results are plotted against the approximation of Equation (5.19) in Figure 5.6b. The curves provide similar results and demonstrate the use of a DE-MZM biased at the minimum transmission point for phase interferometry applications. Experimental results are not provided for this case due to the low voltage levels at the PD output.



(a)



(b)

Figure 5.6: Normalized transmission coefficient vs. phase angle. In (a), the blue solid line curve graphs with "o" markers the function $|J_2(z)|/\max(|J_2(z)|)$. The red dashed line curve with "x" markers graphs the function $(1 - \cos \psi)/2$. (b) plots $V_{out}/\max(V_{out})$ versus θ (deg) for DE-MZM biased at quadrature point, $V_b = KV_\pi$ where K is an even integer. The blue solid line curve with "o" markers graphs the simulation results. The red dashed line with "x" markers is the estimate $(1 - \cos \psi)/2$.

5.2 Photonic Implementation of a Robust Symmetrical Number System-based Direction Finding Array

A block diagram of a photonic RSNS based DF array is shown in Figure 5.7. A CW laser source is used, and the optical signal is passed through a 3:1 optical splitter. The intensity of the optical signal applied to each DE-MZM is modulated by the RF signals applied to its electrodes. The RF input signal received at the reference antenna is applied to electrode one of each of the three DE-MZMs. An identical phase shifted RF signal is received at each measurement antenna element and applied to electrode two of the associated DE-MZMs. The signals applied at electrode two of the DE-MZMs are shifted in phase to align the folding wave forms generated by the array with the RSNS sequences used in coding and quantizing the DOA. The output of the DE-MZMs are converted to electrical signals using a PD.

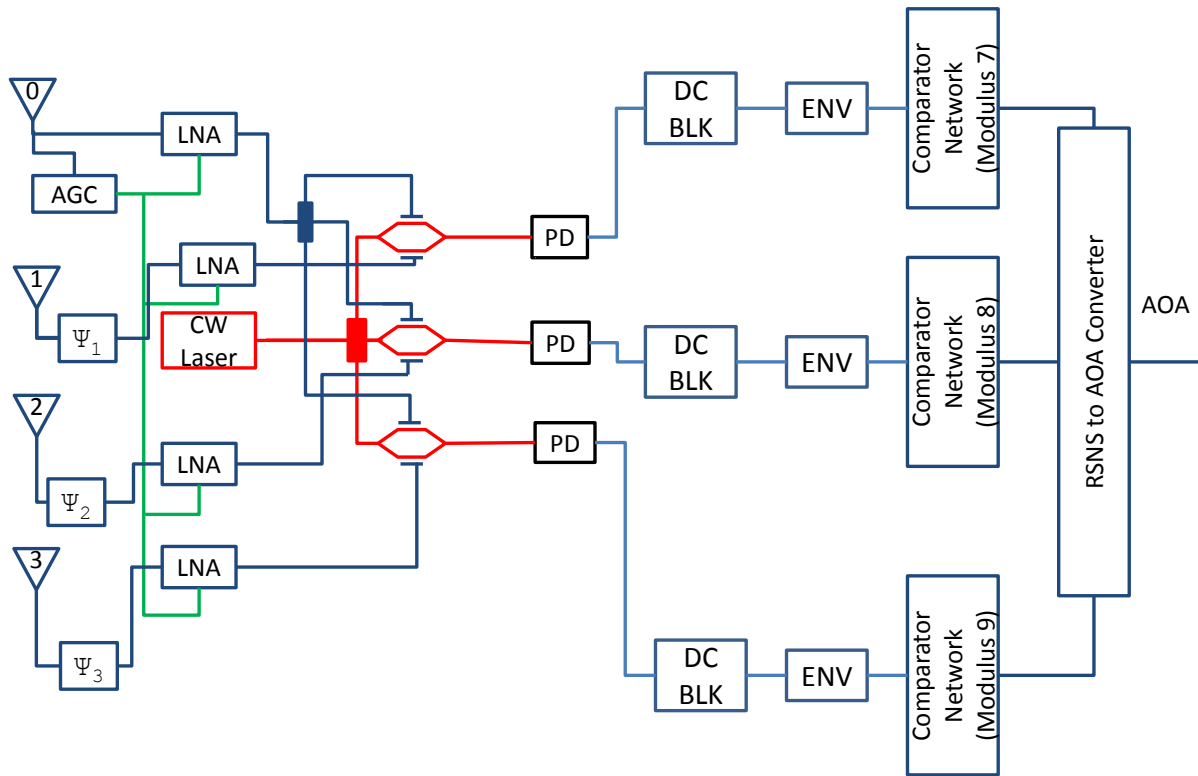


Figure 5.7: Block diagram of the photonic direction finding antenna array using a robust symmetrical number system preprocessing.

The distance of each measurement element antenna from the reference antenna is based on the RSNS moduli and the number of folds within the dynamic range \hat{M}_{RSNS} [57]. For a given modulus m_i the number of folds within \hat{M}_{RSNS} is

$$n_i = \frac{\hat{M}_{RSNS}}{2m_iN}, \quad (5.20)$$

and the distance d_i between each measurement element and the reference element is equal to

$$d_i = \frac{\hat{M}_{RSNS}\lambda}{4m_iN} \xi. \quad (5.21)$$

A right shifted RSNS with $m_i = \{7, 8, 9\}$ with a $\hat{M}_{RSNS} = 133$ is used to represent $-60 \text{ deg} \leq \theta \leq 60 \text{ deg}$ at the design frequency f_{max} . The RSNS folding sequences are plotted against the DOA in Figure 5.8. Each RSNS channel's residue values are determined by applying the normalized envelope detector output voltage V_i to a comparator network where the comparator reference

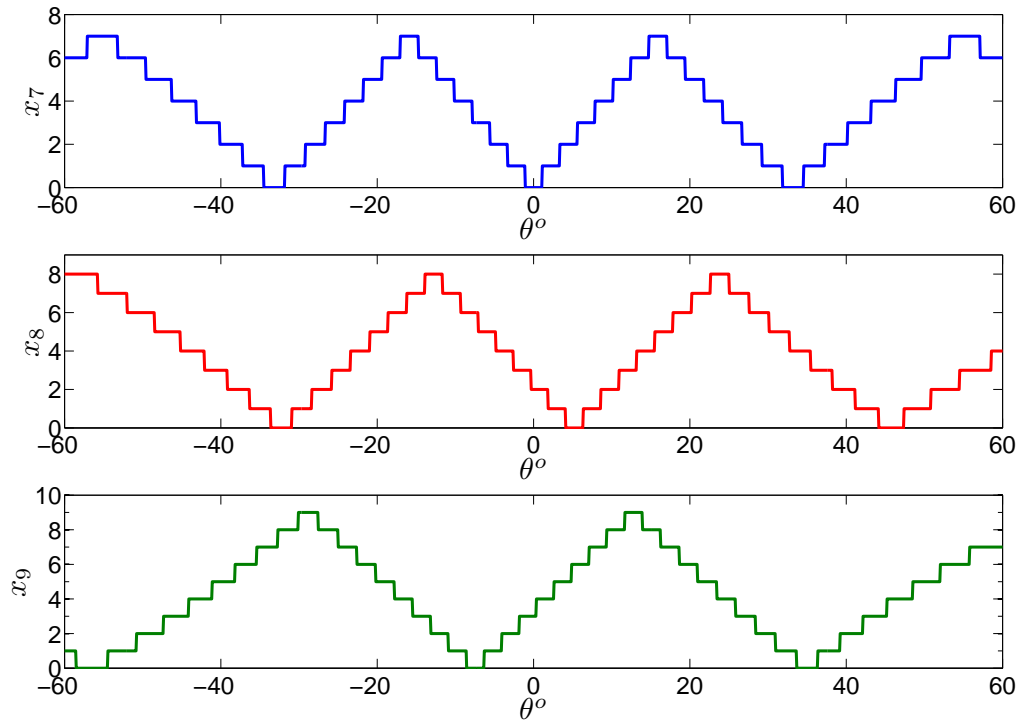


Figure 5.8: Robust symmetrical number system residues versus direction of arrival, θ deg.

values are

$$V_{j,m_i} = \sin\left(\frac{2m_i - 2j + 1}{4m_i}\pi\right). \quad (5.22)$$

The RSNS represents the continuous DOA by sorting the DOA into \widehat{M}_{RSNS} discrete DOA bins where the DOA bin center $\widehat{\theta}_k$ is

$$\widehat{\theta}_k = \arcsin\left(\frac{2k + 1}{\xi \widehat{M}_{RSNS}} - \frac{1}{\xi}\right), \quad (5.23)$$

and the bin width r_k is

$$r_k = \arcsin\left(\frac{2k - \widehat{M}_{RSNS} + 2}{\xi \widehat{M}_{RSNS}}\right) - \arcsin\left(\frac{2k - \widehat{M}_{RSNS}}{\xi \widehat{M}_{RSNS}}\right). \quad (5.24)$$

Phase shifts listed in Table 5.1 are applied to the signals received at each measurement element to align the folding waveforms generated by the array with the RSNS folding sequences shown in Figure 5.8. The folding waveforms generated by the array are plotted both with and without the applied phase shifts in Figure 5.9a through Figure 5.9d. With the phase shifts applied, the arrays folding waveforms align with the RSNS sequences.

Table 5.1: Required phase shifts to match folding wave forms to robust symmetrical number system's waveforms for $m_i = \{7, 8, 9\}$.

m_i	7	8	9
φ_i deg	0	-52.5	-293.33

If the frequency of the incident RF wave is less than f_{max} , the folding waveforms will expand over a larger FOV. To determine the effect on the array transfer function, Equation (5.21) is inserted into Equation (5.1), and the wavelength is expressed as $\lambda = c/f$ to yield

$$\psi_i = \xi \frac{\widehat{M}_{RSNS} f}{2m_i N f_{max}} \pi \sin(\theta). \quad (5.25)$$

The ratio, f/f_{max} , in Equation (5.25) changes the scaling of the folding waveforms. Therefore, a new scaling factor,

$$\tilde{\xi} = \xi \frac{f}{f_{max}} \quad (5.26)$$

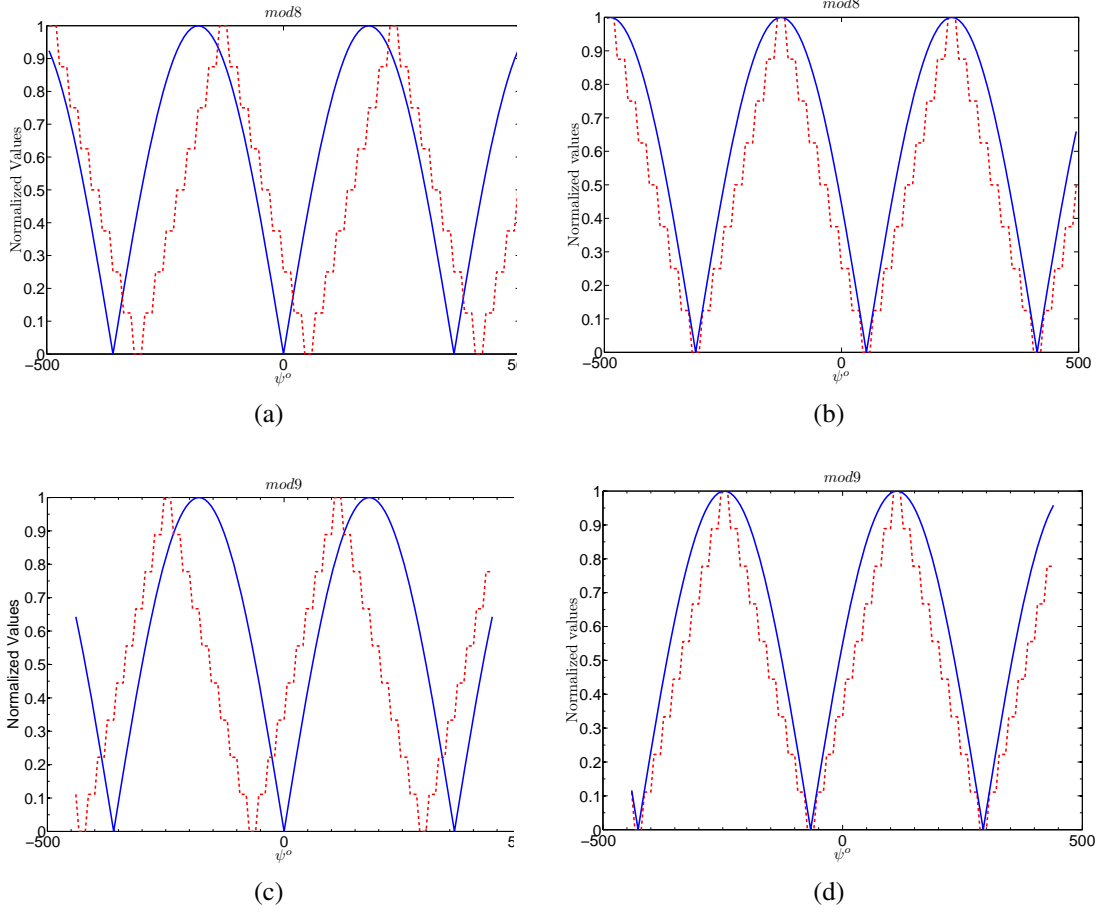


Figure 5.9: Alignment of linear array folding waveforms with the RSNS folding waveforms. (a). For $m_i = 8$, (b) is without phase shift, (d) is with phase shift applied. For $m_i = 9$, (c) is without the phase shift and (d) is with the phase shift applied. The blue solid line curves are the folding waveforms and the red dotted line curves are the associated RSNS folding waveform normalized.

is used to determine θ_k in Equation (5.23) and the corresponding angular resolution r_k in Equation (5.24). For example, if the array is designed for a $FOV = 120^\circ$ at $f_{max} = 8$ GHz and a signal with a frequency, $f = 6$ GHz, is received, the folding waveforms will expand as shown in Figure 5.10. The array's transfer function will also expand over a larger FOV reducing the angular resolution of the array which is illustrated by comparing Figure 5.11a and Figure 5.11b. The spatial resolution provided by Equation (5.24) decreases as the DOA moves further from broadside which can be seen in the insets of Figure 5.11a and Figure 5.11b.

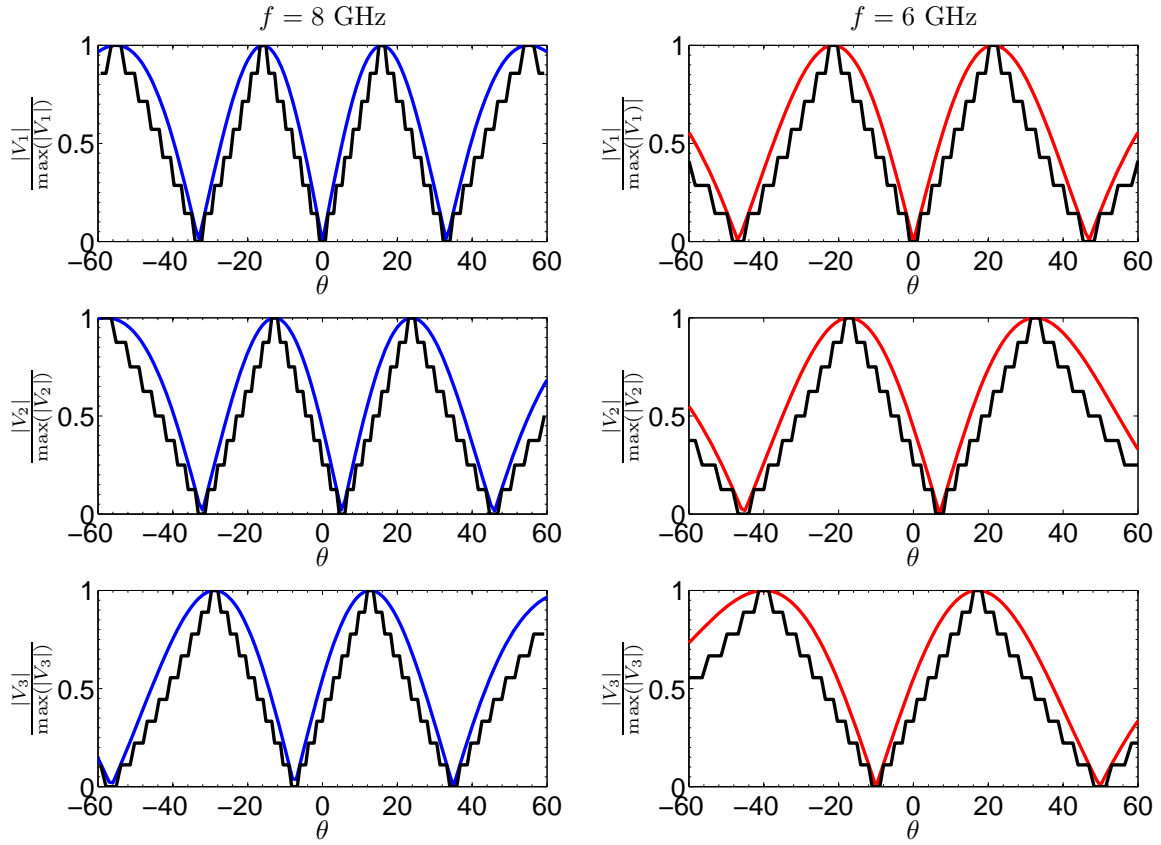
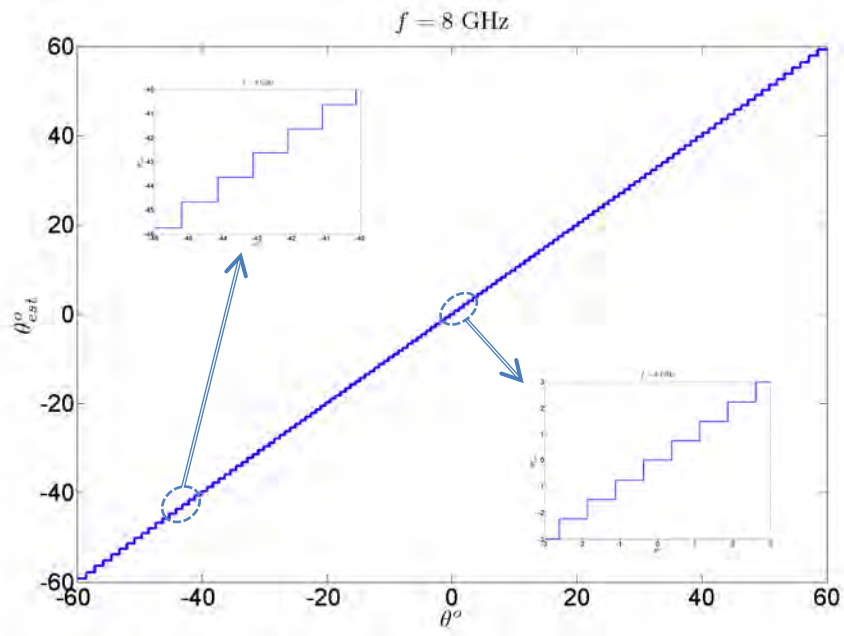
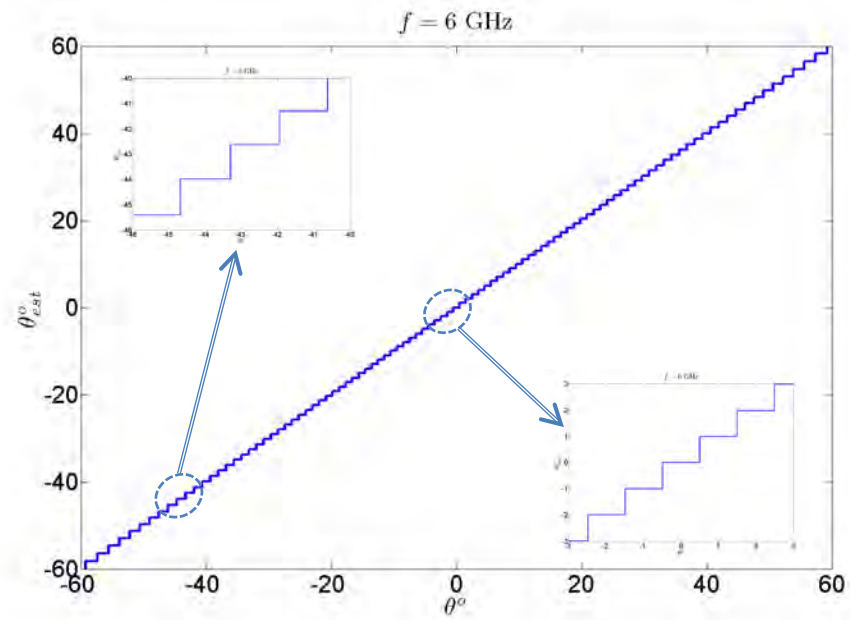


Figure 5.10: Comparison of folding waveforms for each channel at a design of $f = 6$ GHz compared to those resulting from an incident wavefront at $f = 8$ GHz. The RSNS folding waveforms are plotted normalized by the modulus value to demonstrate the alignment of the waveforms.



(a)



(b)

Figure 5.11: Effect of signal frequency on Photonic RSNS DF Array transfer function. (a) is the transfer function when the frequency of the incident RF signal is equal to the design frequency (in this case $f = 8$ GHz). (b) shows the transfer function for a lower frequency ($f = 6$ GHz).

5.3 Simulation Results for Photonic Direction Finding Array with Robust Symmetrical Number System Preprocessing

Simulation of the photonic DF array with RSNS preprocessing displayed in Figure 5.7 was conducted using RSOF Design Group's OptSim software for the components up to and including the PDs. OptSim is a computer software package that enables modeling of fiber-optic networks and fiber-optic circuits. The user friendly features of OptSim enable design and simulation of photonic systems in a similar manner as SIMULINK by MathWorks. OptSim contains models for most of the common electro-optical components and allows interfacing directly with MATLAB to import models for use in simulations or to export and import data and results.

The front-end components (antennas, phase shifters, and LNAs) are simulated using phase shifted sinusoids with a magnitude of 0.1 V and a frequency of 2.4 GHz corrupted with AWGN as the electrical input signals applied to the DE-MZM electrodes. The phase shifts ($\psi_i + \phi_i$) are based on each antenna's distance from the reference antenna and the phase shifts listed in Table 5.1 that are required to align the array's folding waveforms with the RSNS sequences in Figure 5.8. The optical source used in the simulation is a CW laser with a wavelength of 1550 nm and a 20 mW power output. For the DE-MZMs, $V_\pi = 2.6$ V. The output data from the PDs is exported to MATLAB where the mean value is subtracted from each signal to simulate the DC blocking capacitor, and the signal's envelope is determined. The signal at the envelope detector output is normalized and applied to a comparator network to determine the RSNS symmetrical residues.

Simulations using ideal components in a noise-free environment are performed to demonstrate the concept. Additional simulations are then presented to analyze the photonic RSNS DF array's performance when non-ideal components are used in a signal environment corrupted by AWGN. For the DE-MZM, the extinction ratio and excess loss are considered, and for the PDs, the effects of quantum noise, non-ideal responsivity, and dark current are examined. The simulations are conducted for a FOV of $-60\text{deg} \leq \theta \leq 60\text{deg}$ in 0.075deg increments. In the simulations, the DE-MZMs are biased at the quadrature point.

5.3.1 Simulation Results Using Ideal Components in a Noise-free Environment

A CW sinusoidal signal is used as a reference signal which is applied to electrode (1) of each DE-MZM. Identical phase shifted signals are applied to electrode (2) of the corresponding

DE-MZMs simulating the arrival of an RF wavefront at the antennas of the array. Simulations were conducted for $-60\text{deg} \leq \theta \leq 60\text{deg}$ and compared to the theoretical folding waveforms defined by

$$x_i = \left| \sin\left(\frac{\psi_i}{2} + \varphi_i\right) \right| \quad (5.27)$$

where ψ_i is defined by Equation (5.1) and the values for φ_i are defined in Table 5.1. The theoretical and simulated folding waveforms are displayed in Figure 5.12a. The simulation results closely approximate the theoretical approximation of Equation (5.17) demonstrating the ability to use a DE-MZM in a phase interferometry role.

The RSNS residues produced for each value of θ are plotted in Figure 5.12b. The simulated data closely approximates the theoretical curves. In Figure 5.13, the simulation results are plotted against the array's theoretical transfer function. The transfer function generated by the simulation closely approximates the theoretical curve.

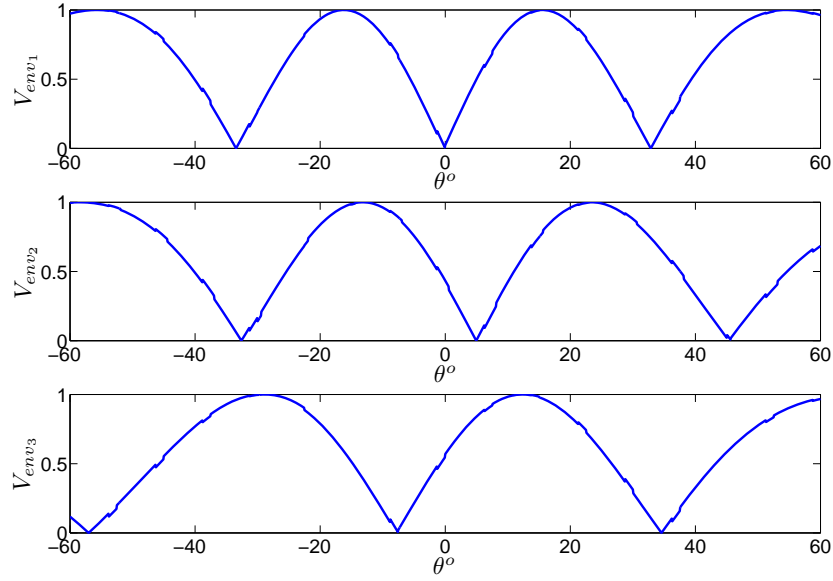
5.3.2 Simulation results for non-ideal components

Simulations were also performed using non-ideal components for a signal environment corrupted by AWGN. An extinction ratio of 25 dB and an insertion loss of 3 dB are used for the DE-MZMs. For the PDs, a dark current of 0.1 nA, quantum efficiency of 0.7, and a 20 GHz BW are specified. Also, electrical and quantum noise are included in the OptSim modeling. The maximum value of the envelope detector used in normalizing the output values for each channel was generated by using a separate identical channel with a constant phase shift of 180deg from the reference signal in the simulation and averaging the value over time. Simulations were conducted for two signal-to-noise ratios (SNRs), $SNR = 30\text{ dB}$ and $SNR = 20\text{ dB}$.

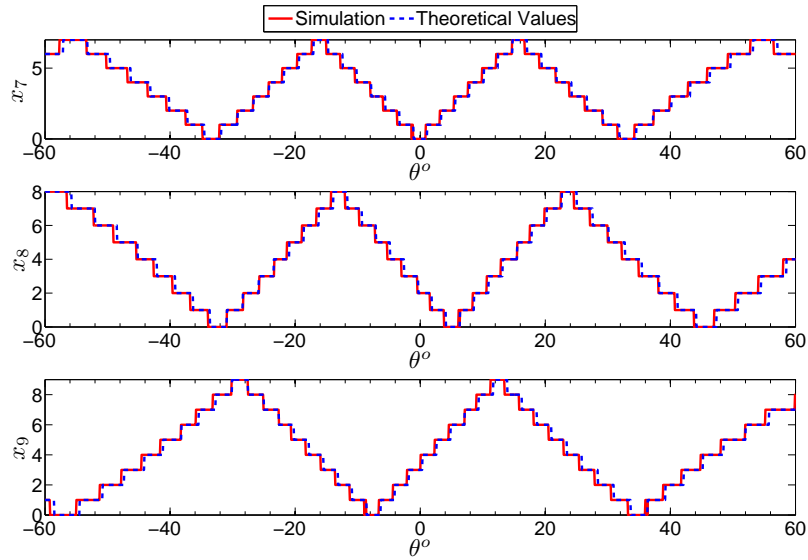
The results for a $SNR = 30\text{ dB}$ are presented in Figure 5.14 and Figure 5.15. The folding waveforms generated by each channel of the DF array for $-60\text{deg} \leq \theta \leq 60\text{deg}$ are displayed in Figure 5.14a. Due to the extinction ratio of the DE-MZM, the minimum value of the normalized envelope is greater than zero. In Figure 5.14a, there are several discontinuities in the curve derived from the element associated with the modulus, $m = 8$. The discontinuities occurred at the points where the data was concatenated to form the output vector. The OptSim simulations were performed in 7.5 deg blocks due to the amount of computer memory required for each simulation. These discontinuities did not significantly impact evaluation of the results. The folding waveforms of Figure 5.14a resemble those of Figure 5.12a.

The values of the symmetrical residues were determined by applying the normalized envelope

detector's output value at each time instant to the comparator network. The residue values for 100 time instances were averaged and rounded to the nearest integer. The residues resulting



(a)



(b)

Figure 5.12: (a) displays the normalized envelope detector output versus the direction of arrival, θ deg (b) displays the resolved RSNS residues for each channel. Theoretical data is plotted with a blue dashed line, simulated data is plotted with a solid red line.

from the simulation and those based on theoretical calculations are shown in Figure 5.14b. From Figure 5.14b, it is observed that the residue values do not match the theoretical values exactly; however, the overall staircase type waveform is preserved. The RSNS vector generated for each DOA is converted to a decimal bin number that is represented by a quantized DOA $\hat{\theta}_k$. The estimated DOA θ_{est} is plotted against the DOA θ in Figure 5.15. The theoretical transfer function is also plotted in Figure 5.15. The simulated curve shows six values that produce invalid RSNS codes for which the values of θ_{est} were set to zero degrees. Two insets are provided to show the details in the curves and how the simulation closely approximates the theoretical transfer function. Examination of the inset around $\theta = 0$ deg reveals an erroneous value for $\hat{\theta}_k$. This error corresponds to the discontinuity that was noted in the folding waveform for the $m = 8$ curve at 0 deg shown in Figure 5.14a and resulted in an erroneous residue value shown in Figure 5.14b.

Simulations were also conducted when the $SNR = 20$ dB. The normalized envelope detector output voltage is plotted along with the theoretical folding waveforms in Figure 5.16a. As seen

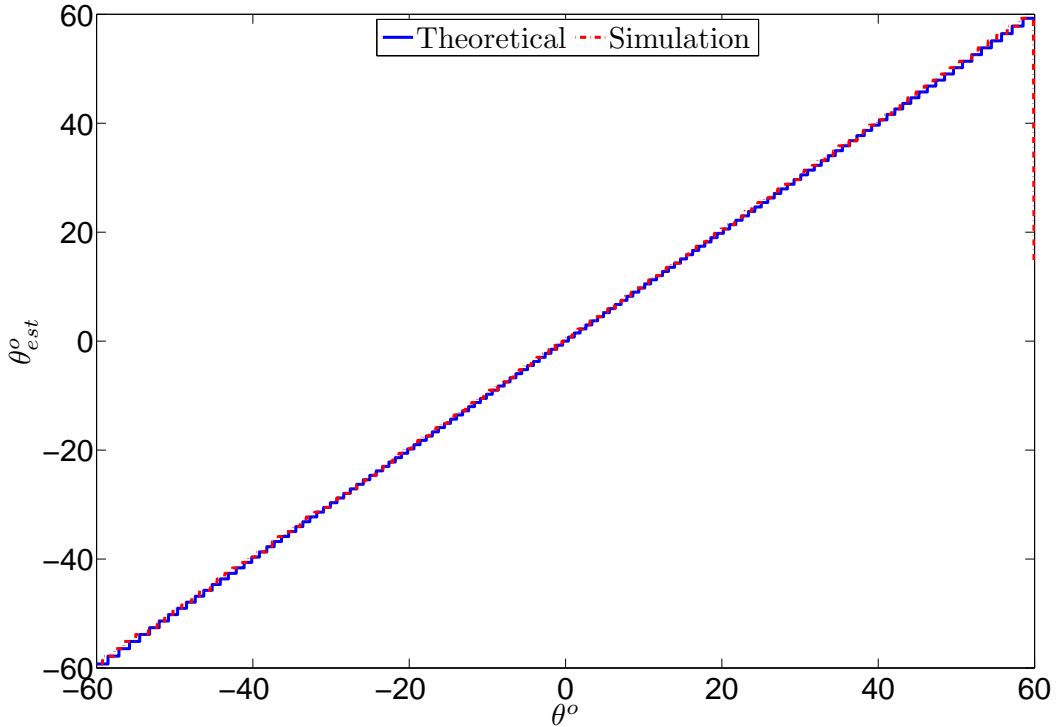


Figure 5.13: Estimated direction of arrival θ_{est} deg versus direction of arrival θ deg using ideal components.

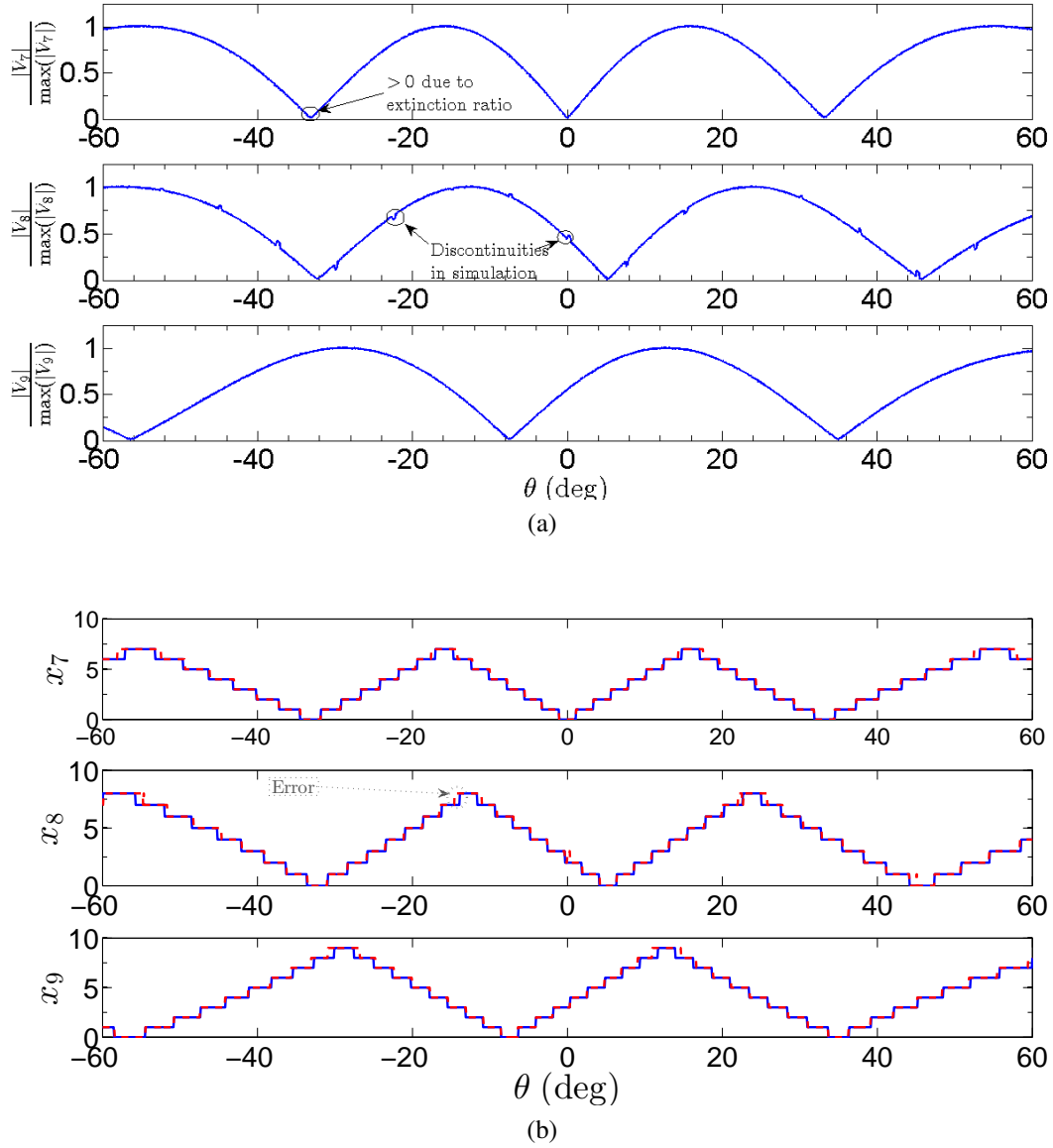


Figure 5.14: Simulation using non-ideal components and $SNR = 30$ dB: (a) normalized envelope detector output voltages, (b) residues versus direction of arrival, theoretical data is the blue solid line, the simulated data is the red dashed line.

in the previous simulations for $SNR = 30$ dB, the envelope detector output voltage does not go to zero due to the extinction ratio and the AWGN. As a result, several errors occur in the resolved residues which are shown in Figure 5.16b. The errors in the residues are carried forward in the transfer function, presented in Figure 5.17. These errors result in either invalid RSNS code values that were set to zero degrees or erroneous codes resulting in decoding errors. Comparing the results for a $SNR = 30$ dB to those with a $SNR = 20$ dB, the performance is degraded as the

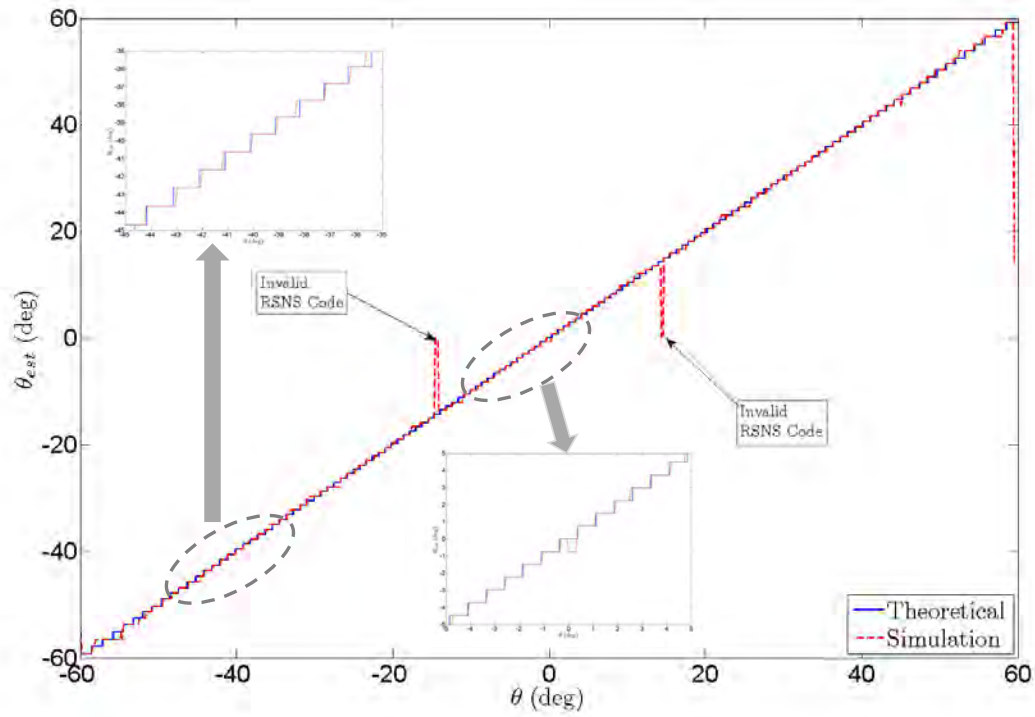
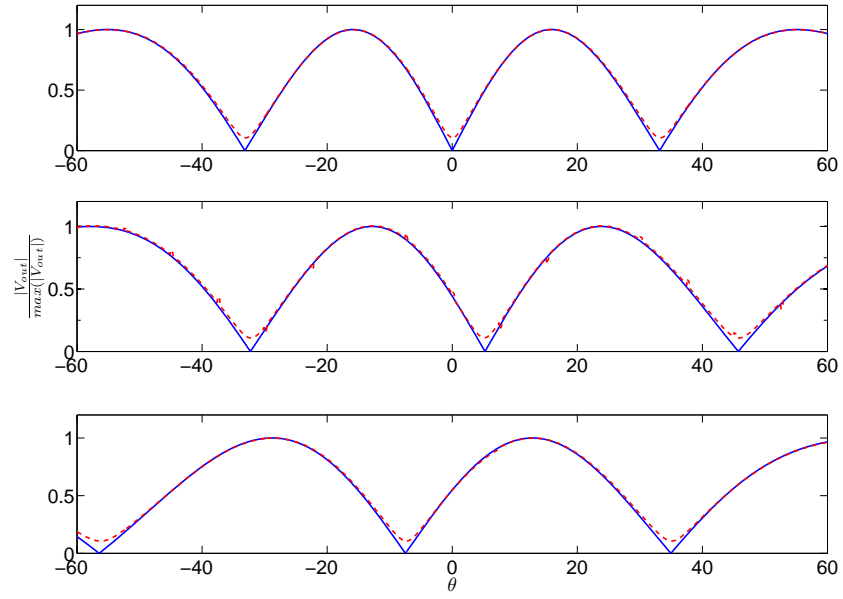
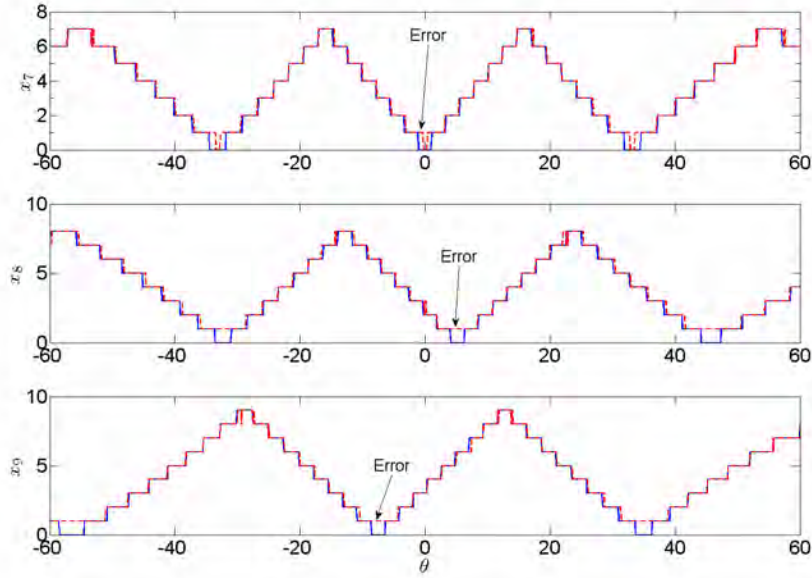


Figure 5.15: Transfer function of photonic direction finding array with robust symmetrical number system for SNR=30 dB.

SNR degrades.



(a)



(b)

Figure 5.16: Simulation results for nonideal components and $SNR = 20$ dB, (a) normalized envelope detector output, (b) residues versus direction of arrival. Blue solid line represents the theoretical values, and the red dashed line represents the simulation results.

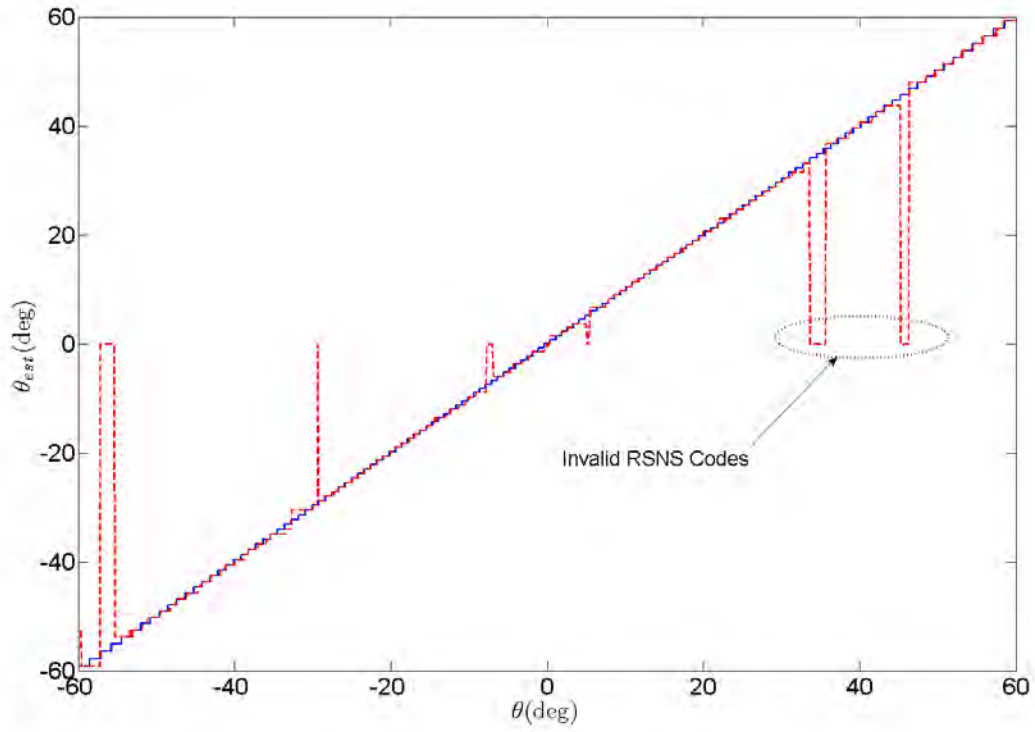


Figure 5.17: Transfer function of photonic direction finding array with robust symmetrical number system preprocessing for $SNR = 20\text{dB}$. Blue solid line is theoretical transfer function, red dashed line represents the simulation results.

5.4 Experimental Results

In this section, experimental testing results are presented for a photonic DF array with RSNS preprocessing. The block diagram for equipment configuration used for the bench testing is shown in Figure 5.18. A 2.4 GHz CW sinusoidal signal with a 6 dBm power level was provided by a Hewlett Packard (HP) 83711B synthesized CW generator. Narrow band testing was conducted to prove the concept due to the cost constraints imposed by wideband components, i.e. antennas, and LNAs. The CW signal was routed to electrode one of each DE-MZM and also to the input of each manual phase shifter used to generate the required phase shift for the signal received at electrode two of each DE-MZM (Fujitsu FTM9712ER). The optical source was provided by a high power 1550 nm wavelength DFB laser at a constant power level of 60 mW. The optical signal was split and routed to each DE-MZM where the optical signal's intensity was modulated by the voltage difference between the DE-MZM's electrodes. The modulated

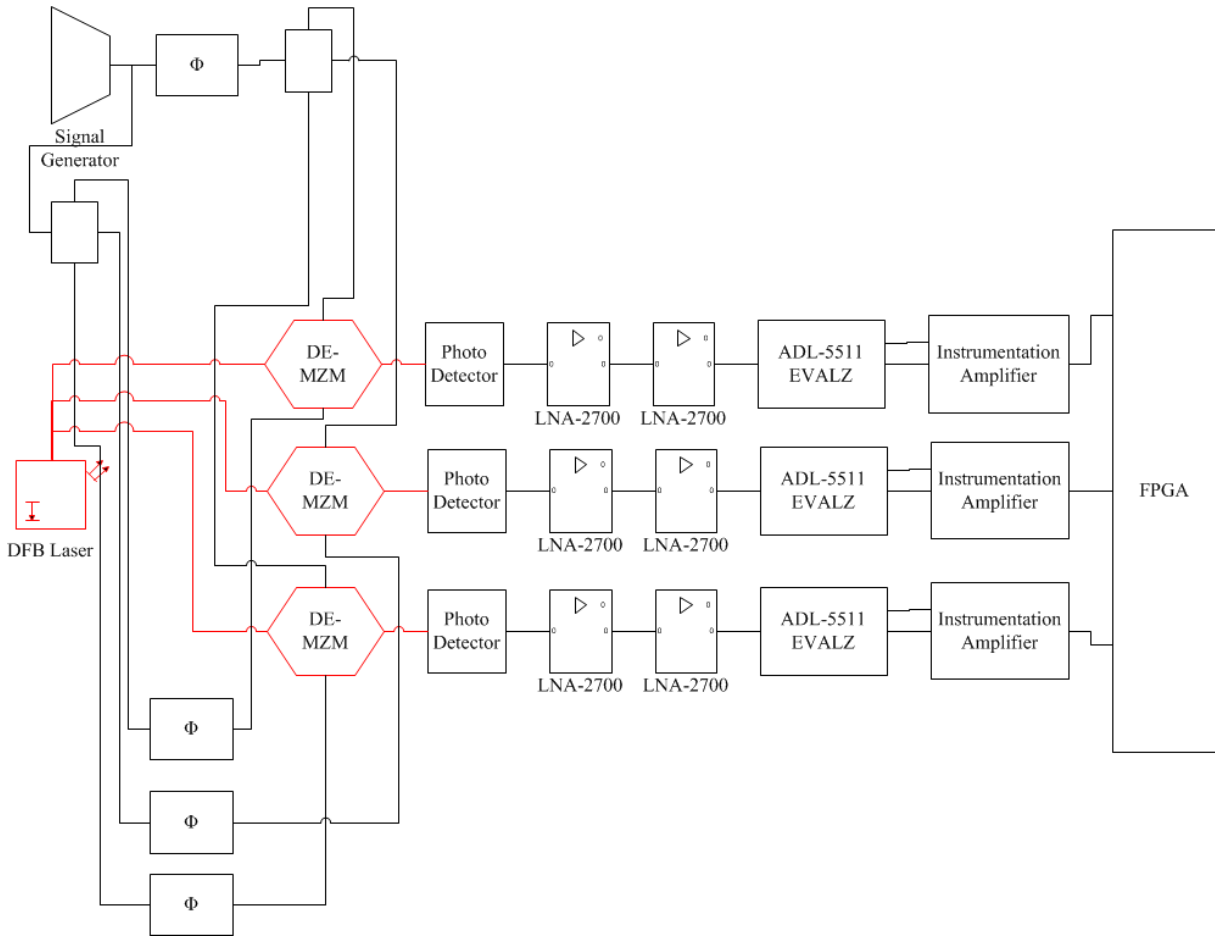
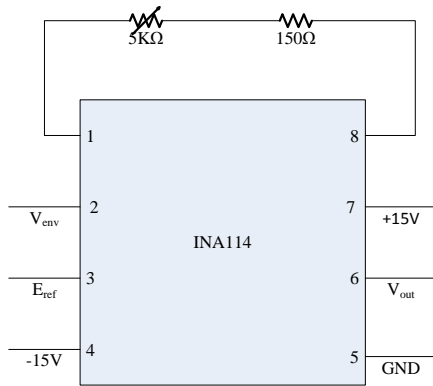


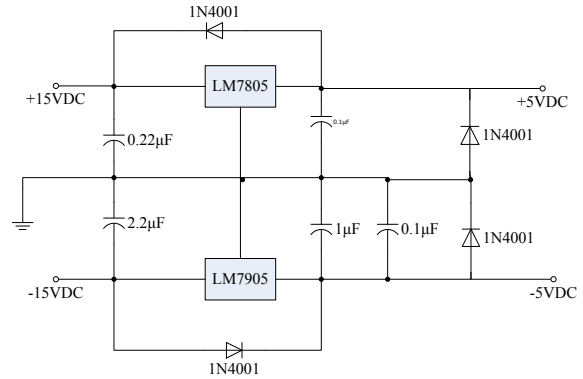
Figure 5.18: Block diagram of equipment setup for bench testing.

optical signal in each channel was detected and converted back to an electrical signal using high speed InGaAs PDs (Newport Model 1014).

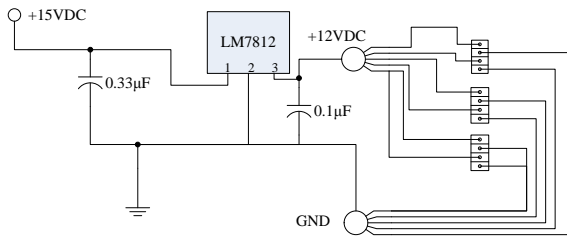
The output of the PDs was passed through a DC blocking capacitor and then amplified using two cascaded LNAs (RF-BAY LNA-2700) prior to envelope detection using an Analog Devices envelope detector evaluation board (ADL 5511-EVALZ). The envelope signal output V_{env} is biased on a reference voltage E_{ref} which is also available as an output. The true envelope was provided by subtracting E_{ref} from V_{env} using an instrumentation amplifier (INA114) circuit shown in Figure 5.19a. The bias voltages supplied to the DE-MZMs are provided by the circuit shown in Figure 5.19b, and the 12 VDC and 5 VDC power supplies required for the LNAs and envelope detector circuits are shown in Figure 5.19c and Figure 5.19d. The output of the instrumentation amplifier was sent to an field programmable logic device (FPGA) (National Instruments Virtex-5 LX30 Compact RIO Reconfigurable Chassis and NI cRIO 9012 Real time



(a)

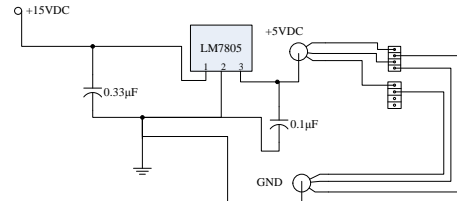


(b)



+12 VDC Power Supply for LNA-2700

(c)



+5 VDC Power Supply for Envelope Detector Board

(d)

Figure 5.19: (a) Instrumentation amplifier circuit, (b) 12 VDC power supply circuit, (c) 5 VDC power supply circuit, and (d) bias voltage power supply circuit.

controller). The FPGA implemented a comparator network and a RSNS to binary algorithm. The **FPG!** (**FPG!**) output was the DOA bin number that was converted to an angular value via a lookup table. In order to use the FPGA code developed in [88], a left shifted RSNS code with $m_i = \{7, 8, 9\}$ was used with the code length truncated to a length of 131 instead of using the right shifted RSNS discussed in Section 5.2 and Section 5.3.

Manual phase shifters (Sage Laboratories Model 6708) were used to insert a phase shift between the sinusoidal signals applied at the two electrodes of each DE-MZM to simulate the phase shift ψ_i that would be present for a given DOA. A rotational turn counter was attached to the shaft of each phase shifter to allow for repeatability in the measurements. The phase shifters were calibrated using a vector network analyzer (VNA) (HP 8517A S-parameter test set and HP 8510C Network Analyzer). The data points were curve fitted to a linear equation for each phase shifter. The linear curves for the phase shifters are displayed in Figure 5.20. Due to the phase shifters providing only 180 degrees of phase shift at the signal frequency of 2.4 GHz and the symmetrical transfer function of the DE-MZMs, phase angles between 180 degrees and 360 degrees were simulated by inserting a phase shift of $360 - \psi_i$.

Data was taken for DOA between -60deg and $+60\text{deg}$ in 0.2deg increments. The residue

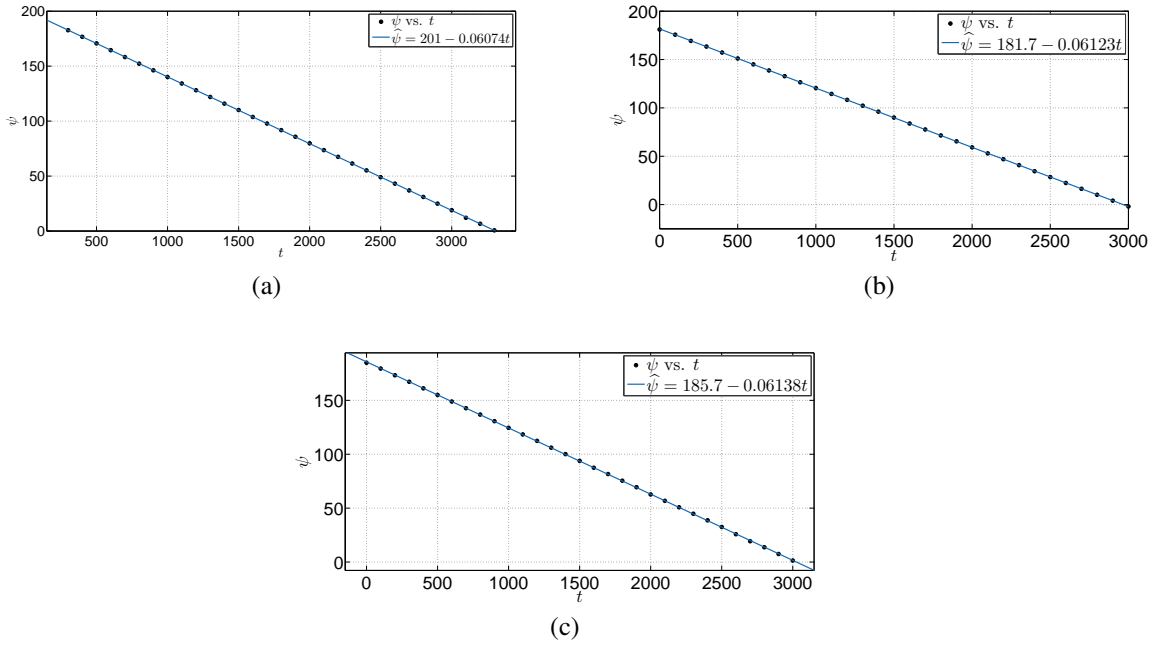


Figure 5.20: Phase Shifter transfer functions, (a) ψ_7 , (b) ψ_8 and (c) ψ_9 .

values resulting in each channel were recorded and graphed against the expected residue values based on the theoretical predictions provided by Equation (5.17) and Equation (5.22). Examining Figure 5.21, the experimental data follow a staircase waveform similar to that followed by the theoretical predictions. There are several points where the transitions between values do not occur when expected or where the tread of the experimental stair case wave form is either wider or narrower than the theoretical curves. These errors are attributed to the drifting the modulator bias point and the amplifier circuits' gain with temperature. To compensate for this drift in output voltage, pauses were made during data collection to adjust the gain of the instrument amplifier circuit so that the maximum output voltage, corresponding to a phase shift of 180 degrees, remained at the maximum value of 4 VDC. Also, to minimize system drift due to temperature, the data was collected during the evening when the temperature in the laboratory was more stable and remained relatively constant.

The estimated direction of arrival for each data point is plotted against the theoretical transfer function of the photonic DF array with RSNS preprocessing in Figure 5.22. The experimental data closely approximates the theoretical transfer function. A few of the RSNS code results were invalid and were set to 0deg. The detail of the curves are displayed in Figure 5.22b and Figure 5.22c where it can be seen that the experimental results follow the theoretical results, but the transitions between the DOA bins do not occur at the proper locations resulting in some DOA bins that are narrower or wider than the theoretical curve. The error signal, $(\theta_{est} - \theta)$, is displayed in Figure 5.23. The mean value and standard deviation were determined for the error signal, neglecting the data points that resulted in invalid RSNS code vectors and the outlying values at $\theta = \{-59.8\text{deg}, -59.6\text{deg}\}$. The errors in the experimental transfer function results are attributed to the voltage drift of the modulator bias point and the amplifiers experienced during the bench testing. Use of a DE-MZM bias control circuit and amplifiers with increased stability and/or adaptive gain features would allow for more stable system performance.

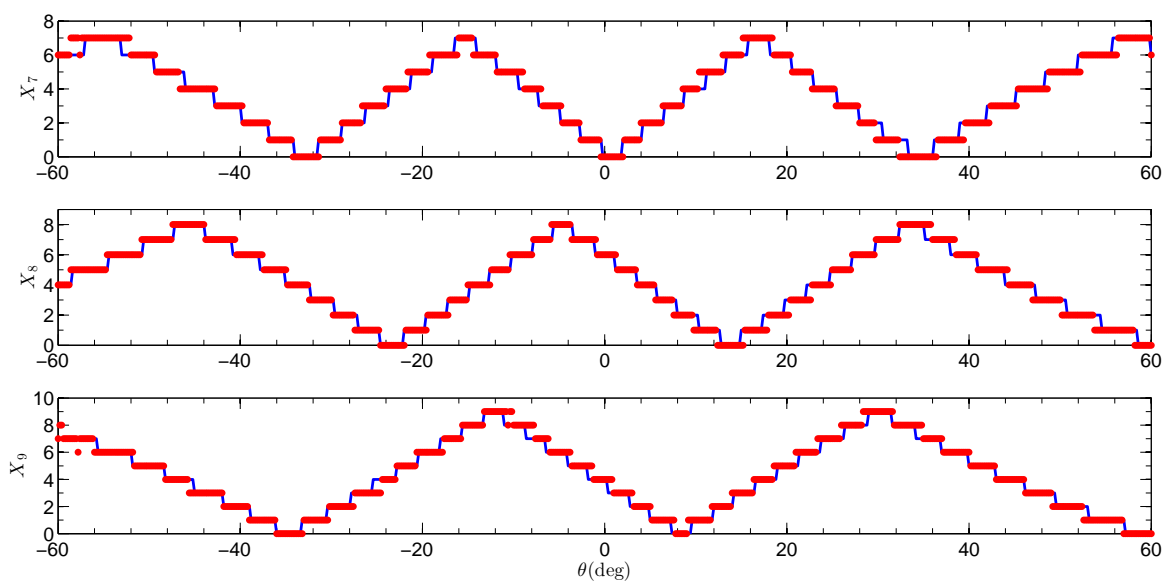


Figure 5.21: Theoretical residues versus experimental residues.

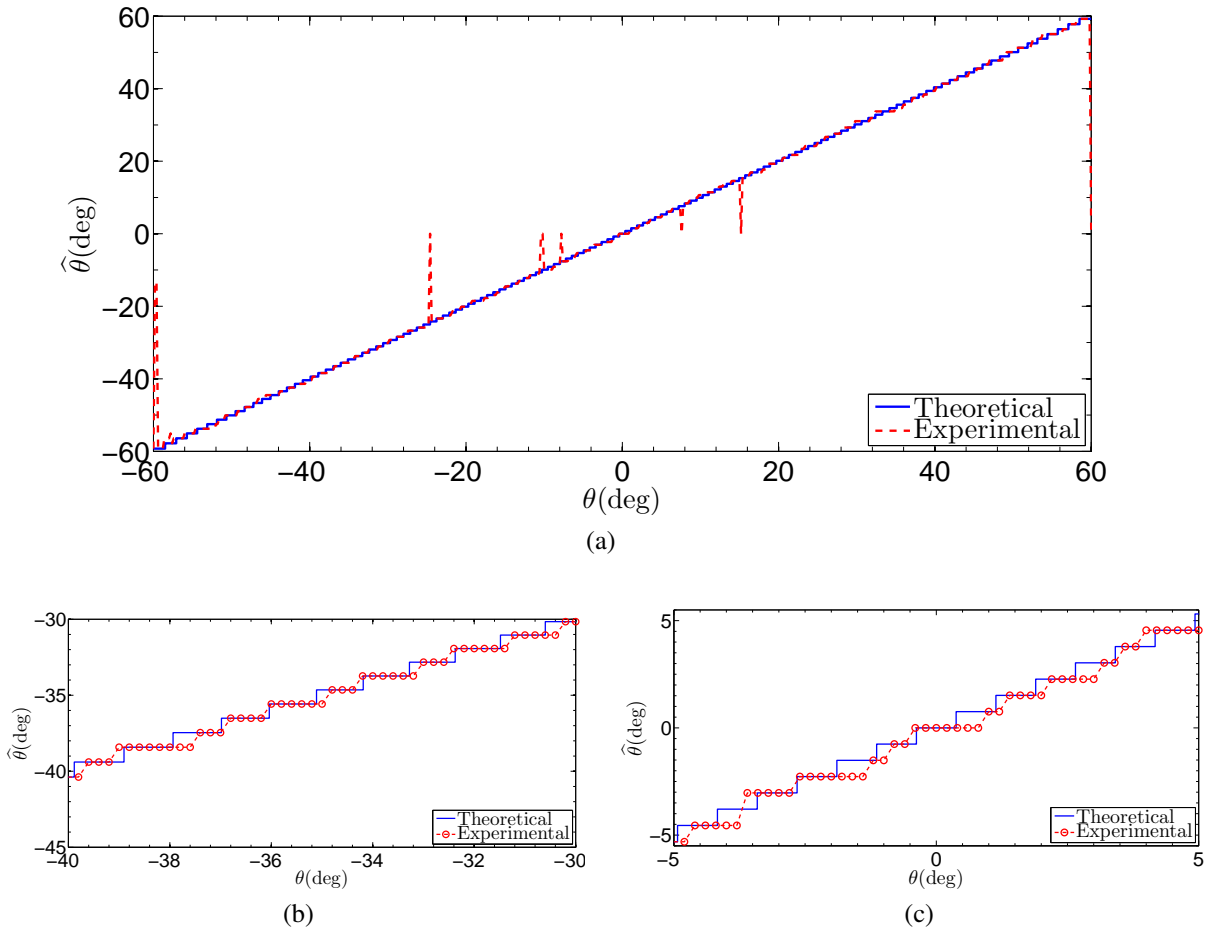


Figure 5.22: Theoretical direction finding array transfer function versus experimental results is displayed in (a). (b) and (c) display details of (a).

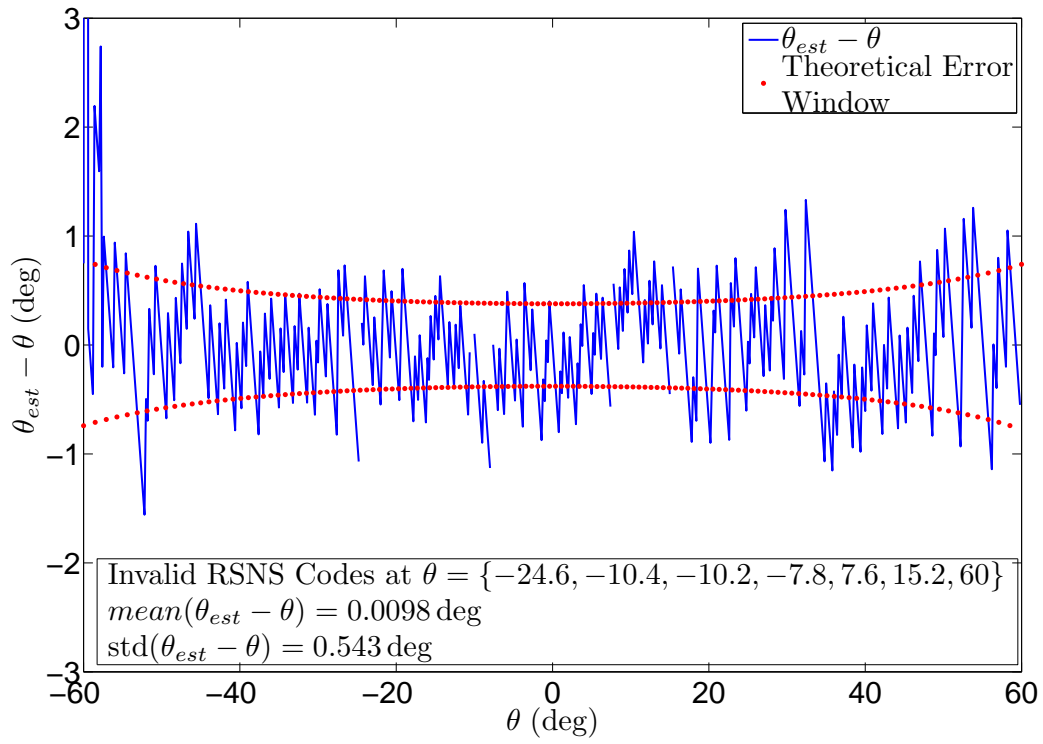


Figure 5.23: Experimental Results - $\theta_{est} - \theta$. Experimental data are represented by the solid blue line, theoretical error envelope represented by red dots.

5.5 Simulation of Multiple Pulsed Signals

The majority of radar systems are based on pulsed sinusoidal signals. The pulse repetition rate can be either constant, staggered, or jittered [89]–[91]. If more than one emitter is present, the received pulses must be sorted based on the signal parameters including the carrier frequency (f_c), PW, PRF, pulse amplitude, and DOA [89] to identify the individual emitters. In EW receivers, time-of-arrival (TOA) measurement is usually the most accurate parameter available. Time-of-arrival analysis is therefore commonly used to determine the PRF and perform the sorting of pulses known as de-interleaving [92]. De-interleaving may also be performed by using multiple parameter algorithms that use several parameters such as DOA, f_c , and PW. These algorithms cluster or group pulses with common parameters, typically DOA and f_c , prior to de-interleaving the pulses in each cluster using TOA data. Emitters are identified by comparing the parameters of each signal that form an emitter descriptive vector by correlating them with a library of known emitters. The use of vector neural networks for emitter identification has also been investigated in [93]–[97].

The simulations and experimental testing discussed in Section 5.3 and Section 5.4 demonstrated the performance of the photonic DF array with RSNS preprocessing when receiving a narrow band CW signal. As discussed in Section 5.2, DE-MZMs have BWs on the order of 40 GHz. This allows the intercept of signals over large BW, for example 2-18 GHz commonly seen in modern EW receivers, without the requirement to down-convert the signal or channelize the signals. The DF antenna spacing is based on the maximum design frequency. If the frequency of the intercepted signal is less than the maximum design frequency, the folding waveforms expand changing the DOA mapping of the RSNS vectors and reducing the angular resolution of the array. Therefore, the frequency of each received pulse must be determined and used in the array signal processing to calculate the DOA. Also, if more than one emitter is present, some pulses will interfere with each other causing errors in RSNS residues and subsequently either invalid RSNS codes or erroneous values for the estimated DOA.

To demonstrate the performance of the photonic DF array with RSNS preprocessing, simulations were conducted in MATLAB. The simulation flow chart is shown in Figure 5.24. A signal consisting of two pulsed sinusoidal signals was simulated at the output of each PD based on the theoretical results presented in Section 5.1 and Section 5.2. The carrier frequencies of the signals were in the MHz range to limit the computer resources required to conduct the simulations over a time period of several milliseconds. The design frequency for the array in the

simulations is 100 MHz. The reference antenna signal was processed separately to determine f_c that applies to each DOA pulse through examination of the periodogram and spectrogram. The periodogram was produced using the Welch method employing a Hamming window, a 2048 point FFT, and 50 percent overlap. The spectrogram was determined using a 2048 point FFT with Hamming window and 75 percent overlap. A hard threshold equal to twenty times the median value was applied to the power spectrum represented by the spectrogram to determine the frequency of the pulses and the time values corresponding to the pulses. The results were applied to the decimal values corresponding to the RSNS vectors after the mode function was applied to select the value that occurs most frequently in the samples that are contained within each pulse. Two separate examples are shown below to demonstrate the performance of the photonic array and the processing of two pulsed emitters. A third example is also presented when three pulsed emitters are present.

The first example consists of two emitters whose parameters are listed in Table 5.2. A graphical representation of the input signal is shown in Figure 5.25a. An example of the interference that occurs when two pulses are received simultaneously is shown in Figure 5.25b. The carrier frequencies of the two pulsed sinusoids were determined from the periodogram of the signal using the Welch method. The spectrogram of the signal was also used to determine the location of the pulses in a time-frequency representation. The spectrogram and periodogram are displayed in Figure 5.26. From the periodogram shown in Figure 5.26b, the carrier frequencies of the two pulsed waveforms were estimated to be equal 60.2 MHz and 29.2 MHz. From the spectrogram data, the time sequences corresponding to the received pulses and their frequencies were applied to Equation (5.26) and Equation (5.23) to determine the DOA versus time plot. An estimate of the PW and PRF can be obtained from the spectrogram; however, more accurate algorithms exist based on TOA data. From the spectrogram shown in Figure 5.26a, the PRF for emitter number one is estimated to be 8 KHz, and for emitter number two the PRF is estimated to be 7 KHz.

The resulting DOA versus time plots are displayed in Figure 5.27. In order to resolve the DOA for each pulse and remove errors associated with noise or invalid RSNS codes, the mode

Table 5.2: Multiple pulsed emitters—example 1: signal parameters.

Emitter	PRF (kHz)	PW (μ s)	f_c (MHz)	DOA (deg)
1	8	6	60.2	30
2	7	8	29.1	-10

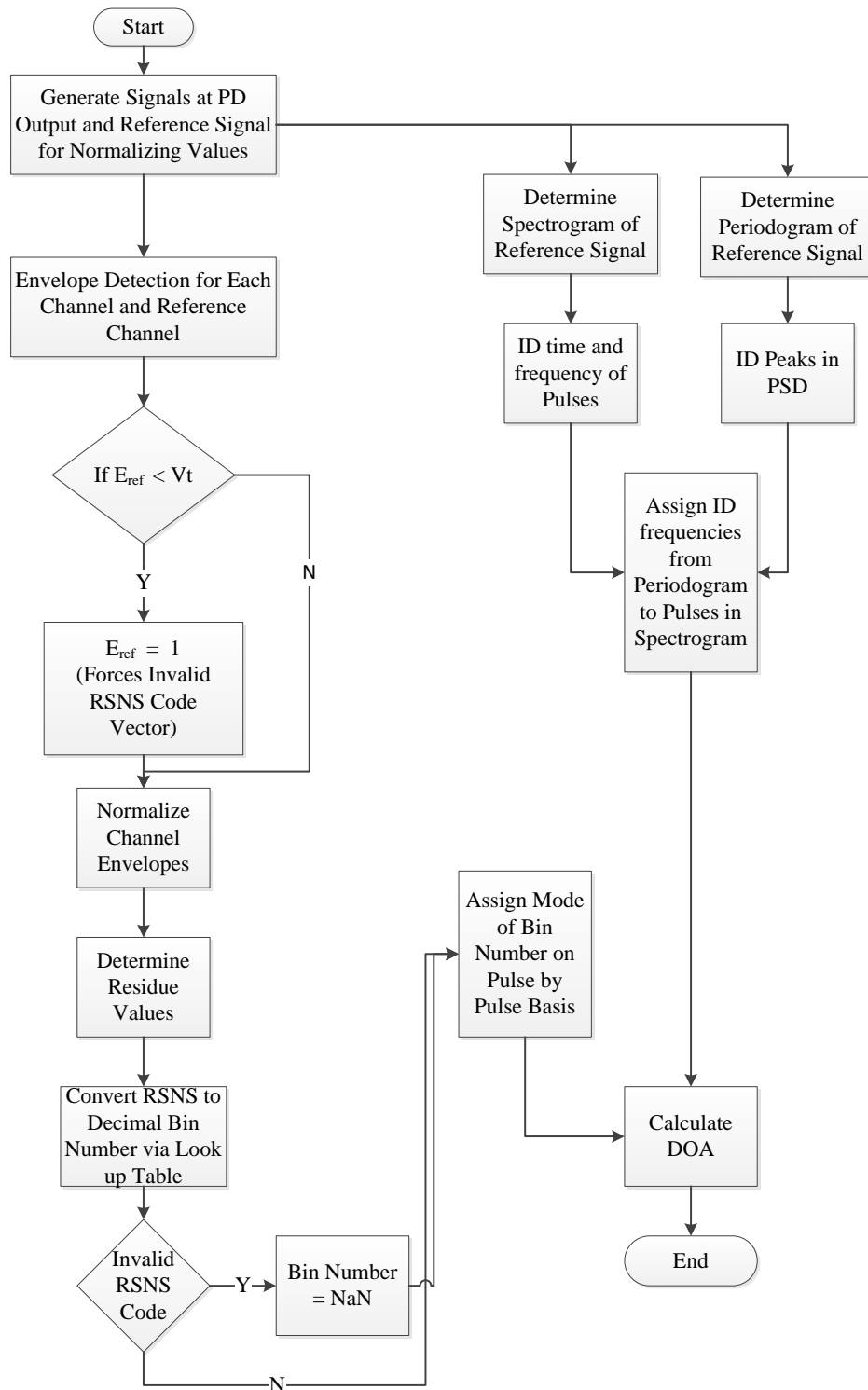


Figure 5.24: Simulation flow chart for multiple emitter direction of arrival determination.

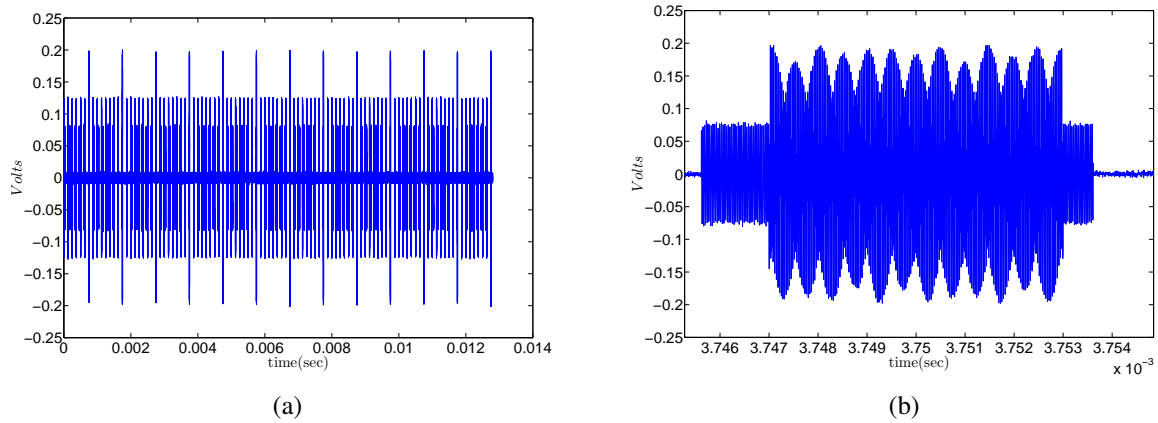


Figure 5.25: Multiple pulsed signals example 1 (a) Input signal. (b) Interference of pulses.

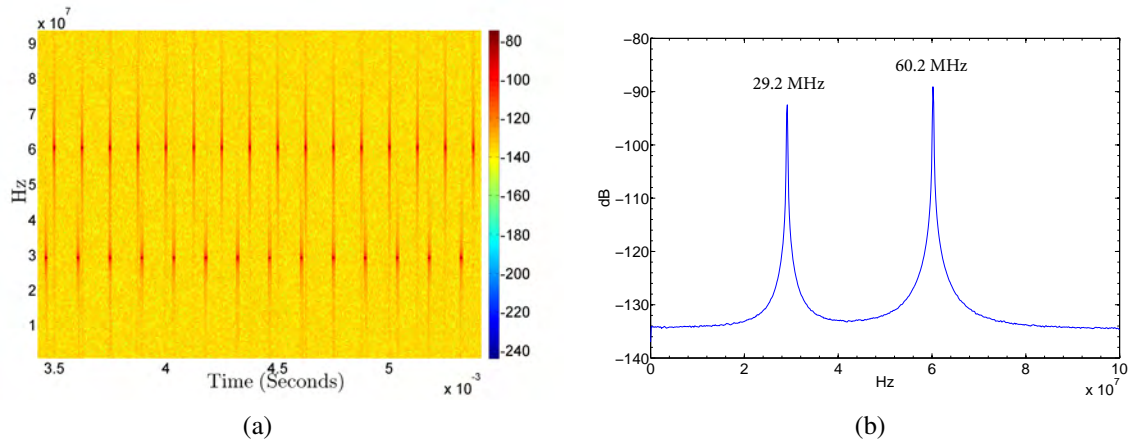


Figure 5.26: Spectrogram and periodogram for example 1 ($PRF_1 = 8$ kHz, $PW_1 = 6 \mu s$, $f_{c1} = 60.2$ MHz, $PRF_2 = 7$ kHz, $PW_2 = 8 \mu s$, $f_{c2} = 29.1$ MHz). (a) Spectrogram of two pulsed sinusoidal signals. (b) Periodogram of input signal using Welch method with 2048 point FFT, 50 percent overlap and Hamming window.

function that selects the value that occurs most often in the set of data was applied to the decimal value representing the decoded RSNS vector within the spectrogram time slots corresponding to each pulse. From the results in Figure 5.27, the estimated DOA for each pulse is approximately equal to the DOA of the transmitted signals.

For the second example, two pulsed emitters with the parameters listed in Table 5.3 are used. The input signal is shown in Figure 5.28. The carrier frequencies of the two pulsed sinusoids was determined from the periodogram of the signal using the Welch method. The spectrogram of the signal was also used to determine the location of the pulses in a time-frequency

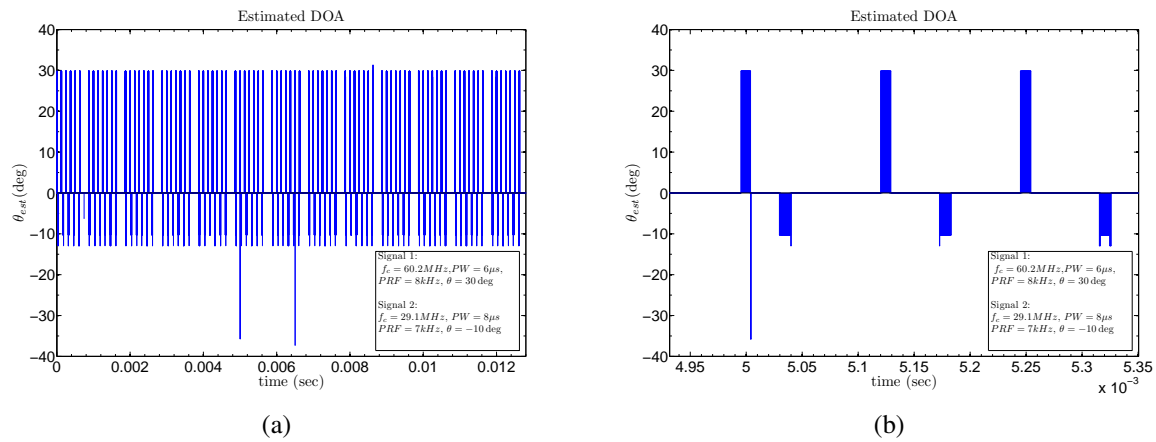


Figure 5.27: Multiple pulsed signal example 1—two pulsed signals, one with a DOA of 30 degrees and one with a DOA of -10 degrees. (a) Direction of Arrival v.s. time. (b) Magnified view of (a).

representation. The spectrogram and periodogram are displayed in Figure 5.29. From the periodogram shown in Figure 5.29b, the carrier frequencies of the two pulsed signals are estimated as $\hat{f}_{c1} = 95.8$ MHz and $\hat{f}_{c2} = 55.6$ MHz. From the spectrogram data, the time sequences corresponding to the received pulses and their frequencies were applied to Equation (5.26) and Equation (5.23) to determine the DOA versus time plot. From the spectrogram displayed in Figure 5.29a, the PRF of emitter number one is estimated to be 10 kHz, and the PRF of emitter number two is estimated to be 2 kHz. The resulting DOA versus time plots are displayed in Figure 5.30. From the results in Figure 5.30, the estimated DOA for each pulse is approximately equal to the DOA of the transmitted signals.

A third example is provided where three pulsed emitters are present. The parameters of the three emitters are provided in Table 5.4. The reference antenna signal is displayed in Figure 5.31 and the spectrogram displaying the time versus frequency information is provided in Figure 5.32. Examining Figure 5.32a, three separate pulsed signals are shown. The periodogram in Figure 5.32b shows two peaks at 48.5 MHz and 7.76 MHz. Due to the proximity of the carrier frequencies of emitters number one and number two, only two peaks are shown in the periodogram of the reference signal. From the spectrogram shown in Figure 5.32a, three pulsed

Table 5.3: Multiple pulsed emitters—example 2: signal parameters.

Emitter	PRF (kHz)	PW (μ s)	f_c (MHz)	DOA (deg)
1	10	10	95.9	20
2	2	7	55.6	-20

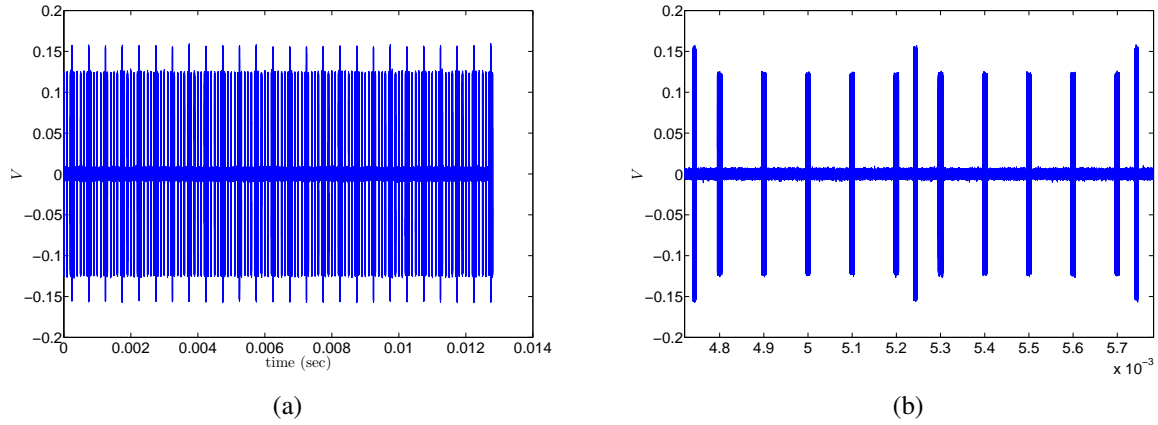


Figure 5.28: Multiple pulsed signals example 2—input, (a) Simulation PD output signal composed of two pulsed sinusoids plus AWGN. (b) Magnified view of signal in (a).

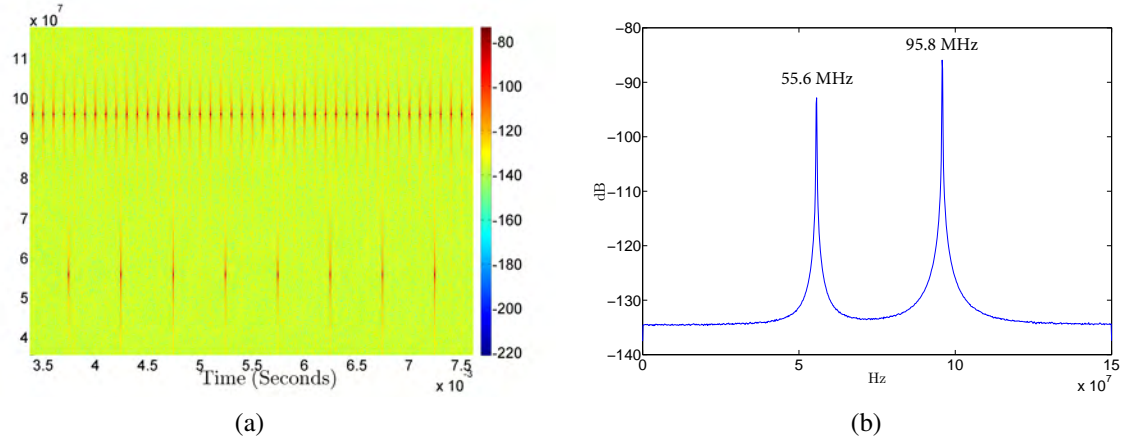


Figure 5.29: Spectrogram and periodogram for example 2 ($PRF_1 = 10$ kHz, $PW_1 = 10 \mu s$, $f_{c_1} = 95.9$ MHz $PRF_2 = 2$ kHz, $PW_2 = 7 \mu s$, $f_{c_2} = 55.6$ MHz). (a) Spectrogram of two pulsed sinusoidal signals. (b) Periodogram of input signal using Welch method with 2048 point FFT, 50 percent overlap and Hamming window.

Table 5.4: Multiple pulsed emitters—example 3: signal parameters.

Emitter	PRF (kHz)	PW (μs)	f_c (MHz)	DOA (deg)
1	5	10	48.5	10
2	2	5	48.7	-10
3	3	3	7.81	45

signals are observed. The PRF of emitter number one is estimated to be 5 kHz; the PRF of emitter number two is estimated to be 2 kHz, and the PRF of emitter number three is estimated to be 3 kHz. The DOA versus time data is plotted in Figure 5.33. Although the the DOA is

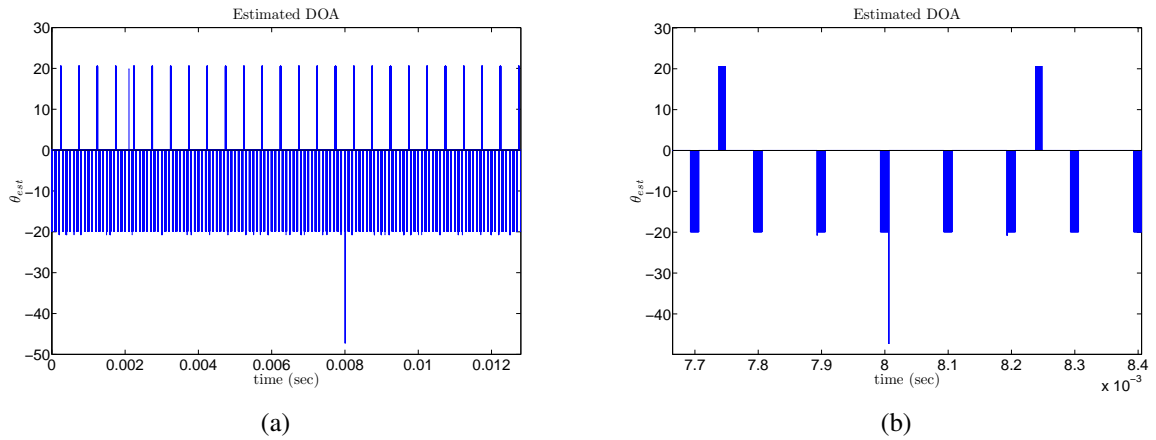


Figure 5.30: Multiple pulsed signals example 2—two pulsed signals, one with $DOA = 20\text{deg}$ and one with $DOA = -20\text{deg}$. (a) Direction of Arrival v.s. time. (b) Magnified view of (a).

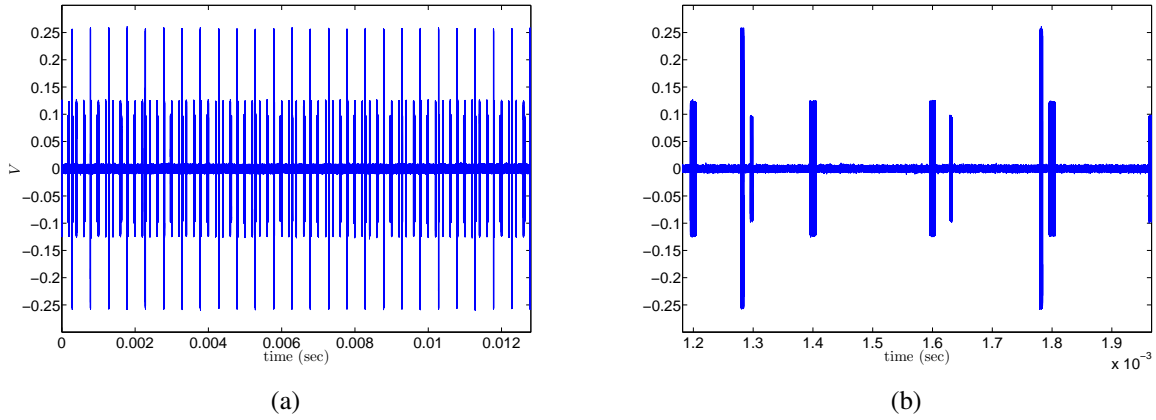


Figure 5.31: Multiple pulsed signals example 3, (a) input signal, (b) magnified view of input signal.

resolved, some errors result at the beginning and ending points of the pulses which can be seen in Figure 5.33b. These errors are most likely due to the errors in the residues resulting from the Gibbs effect due to the filtering operations involved with the envelope detection.

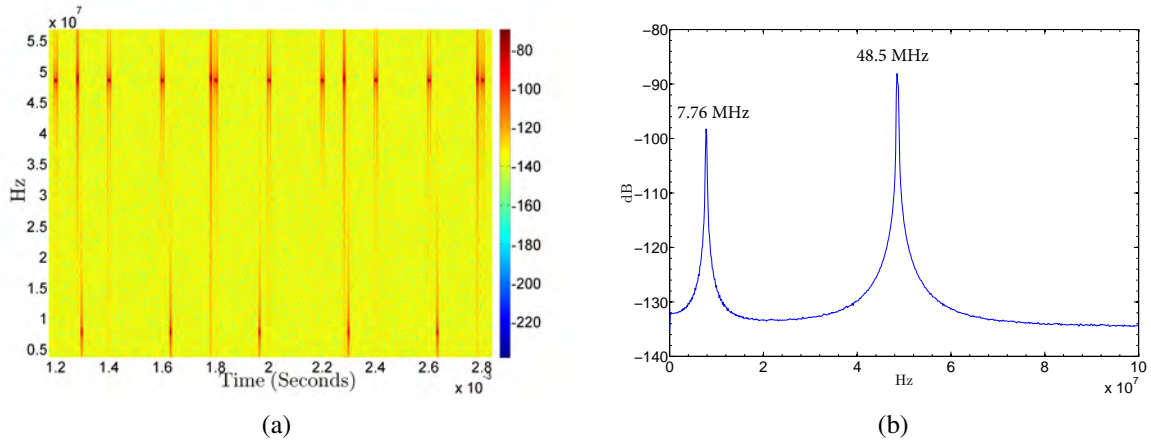


Figure 5.32: Spectrogram and periodogram for example 3 ($PRF_1 = 5$ kHz, $PW_1 = 10 \mu s$, $f_{c1} = 48.5$ MHz, $PRF_2 = 2$ kHz, $PW_2 = 5 \mu s$, $f_{c2} = 48.7$ MHz, $PRF_3 = 3$ kHz, $PW_3 = 4 \mu s$, $f_{c3} = 7.81$ MHz). (a) Spectrogram of three pulsed sinusoidal signals. (b) Periodogram of input signal using Welch method with 2048 point FFT, 50 percent overlap and Hamming window.

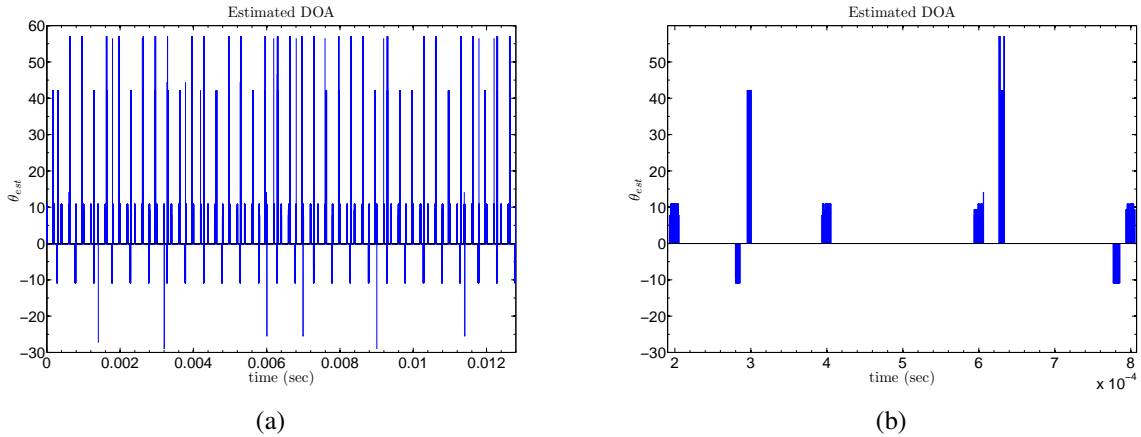


Figure 5.33: Multiple pulsed signals example 3, (a) DOA versus time, (b) magnified view of (a).

5.6 Concluding Remarks

In this chapter, the ability to use a DE-MZM in phase interferometry DF applications was proved theoretically and demonstrated through simulations and experimental testing. A four element photonic DF array with RSNS preprocessing was designed and tested via simulation using RSOFT's OptSim software and MATLAB. The concept was then demonstrated satisfactorily by bench testing the hardware configuration displayed in Figure 5.18. In Section 5.5, the performance of the array was investigated when multiple pulsed emitters are present. The DF array was shown to accurately resolve the DOA of the emitters when the carrier frequency of

each pulse is provided to the array's DOA processing. The NYFR receiver is one example of a CS receiver that is ideally suited to provide the frequency information to the DOA processing due to its wide BW and less complex signal processing algorithms.

The photonic DF array with RSNS preprocessing can be used to monitor a wide BW to determine the DOA of pulsed emitters. The components used in the hardware design can be modified to use wide band antennae and amplifier circuits. Also, adaptive gain amplifiers can be used to ensure the signals applied to the DE-MZM electrodes are of equal amplitude allowing for simpler normalization and comparator level assignment. Also, a bias control circuit for the DE-MZMs can be used to compensate for temperature drift of the DE-MZM bias points. Among the challenges to implementing a wideband photonic DF array with RSNS preprocessing is the close spacing of array antennas at high frequencies and the comparatively large footprint of wideband spiral antennas. As a result the antenna arrays may require being staggered in height. Further investigation of this concept including testing in an anechoic chamber and field testing against pulsed and CW emitters is warranted.

CHAPTER 6:

Symmetrical Number System - Compressive Sensing Cueing Receiver

In addition to the CS receiver architectures presented in Chapter 2, there are many undersampled receiver concepts that rely on coprime sampling rates to resolve frequency ambiguities resulting from aliasing [51], [98]–[102]. In [98]–[100], CRT-based algorithms are used to determine a signal’s frequency components. Another technique that implements coprime undersampling and applies CS theory in a cognitive radio application is presented in [101]. This architecture models spectrum aliasing as a linear projection from the Nyquist rate sampled spectrum to the undersampled spectrum and applies CS theory to resolve the signal’s frequency spectrum using Basis Pursuit. In [102], a receiver architecture that requires only two coprime sampling rates is presented. The algorithm forms appropriate difference sets from the samples and estimates the signal’s autocorrelation function. From this estimate, the power spectral density is determined using the MUSIC algorithm.

An undersampled receiver architecture that uses the SNS to resolve a single frequency ambiguity due to undersampling is presented in [51]. It was demonstrated in [51] that the DFT naturally encodes real signal frequency information into the same format as the SNS. Consequently, a single frequency ambiguity that results from undersampling can be resolved exactly using $r \geq 2$ channels provided the signal’s frequency is less than the dynamic range of the SNS \hat{M}_{SNS} . The receiver architecture presented in [51] undersamples an input signal with sampling frequencies equal to the SNS moduli, m_i . In each channel, a m_i point DFT is performed, and the DFT bin containing the signal’s energy is identified. The corresponding *DFT bin numbers* (symmetrical residues) for each channel form the SNS vector representing the frequency of the signal. The SNS vector is then converted to a more convenient integer representation.

In this chapter, a novel SNS-CS cueing receiver architecture is presented that allows accurate signal frequency identification in a sparse signal environment. The SNS-CS cueing receiver forms a measurement vector \mathbf{y} by collating the samples obtained through coprime undersampling with sampling rates equal to the SNS moduli m_i . The SNS-CS cueing receiver also forms a deterministic partial IDFT sensing matrix \mathbf{A} based on the receiver’s sampling rates, and applies CS recovery algorithms such as the LASSO algorithm to estimate the frequency spectrum

X. The SNS-CS cueing receiver's performance is examined through Monte Carlo simulations and is compared to the performance achieved when a random sensing matrix is used in the CS recovery algorithm. The performance of the SNS-CS cueing receiver is shown to be comparable to that of a random sensing CS receiver architectures in identifying the frequencies of sinusoids in a sparse signal environment.

The major contributions presented in this chapter are that the SNS-CS cueing receiver is demonstrated to allow the identification of an increased number of sinusoids than the CRT-based algorithm described in [100] and the algorithm in [51] for a fixed number of coprime sampling rates. Also, the SNS-CS cueing receiver is demonstrated to allow accurate frequency identification consistent with the theoretical predictions in [35], and its performance is demonstrated to be comparable to the performance achieved when using a random sensing matrix. Additionally, unlike some random sensing CS receiver architectures such as the random demodulator [40] and the RADC [46], the SNS-CS cueing receiver simplifies the sampling process and does not require Nyquist rate components. It also generates a partial IDFT sensing matrix based upon the SNS moduli that is not required to be stored in memory. These advantages make the SNS-CS cueing receiver attractive for use in wideband applications.

6.1 Symmetrical Number System - Compressive Sensing Cueing Receiver Concept and Theoretical Development

A r -channel SNS-CS cueing receiver is presented as a means of simplifying the sampling process by using uniform coprime undersampling while leveraging compressive sensing theory to identify more tonal signals than can be identified using CRT-based algorithms. The block diagram of a r -channel SNS-CS cueing receiver architecture is shown in Figure 6.1. The input signal $x(t)$ is undersampled using coprime sampling frequencies equal to the SNS moduli m_i and the samples, from the r -channels, are collated in the time domain to form the measurement vector \mathbf{y} . The compressive sensing signal processing uses the measurement vector \mathbf{y} to produce an estimate of the frequency spectrum $\tilde{\mathbf{X}}$ from which the frequency components of the signal within the bandwidth of the receiver are identified.

The sensing matrix \mathbf{A} used in the SpARSA algorithm [10], is formed by selecting the rows of an $N \times N$ unitary IDFT basis matrix Ψ^{-1} that correspond to the SNS-CS cueing receiver's sample

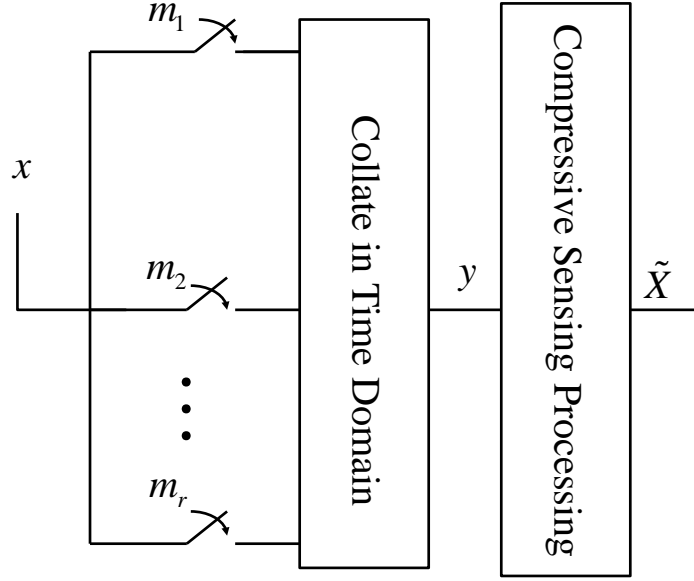


Figure 6.1: Block diagram of a r -channel SNS-CS cueing receiver.

times. A unitary IDFT matrix Ψ^{-1} is defined as

$$\Psi^{-1} = \frac{1}{\sqrt{N}} \begin{bmatrix} 1 & 1 & \dots & \dots & 1 \\ \vdots & \psi & \psi^2 & \dots & \psi^{N-1} \\ \vdots & \psi^2 & \psi^4 & \dots & \psi^{2(N-1)} \\ \vdots & \vdots & \vdots & \ddots & \vdots \\ 1 & \psi^{N-1} & \dots & \dots & \psi^{(N-1)^2} \end{bmatrix} \quad (6.1)$$

where $\psi = e^{j2\pi/N}$ and $j = \sqrt{-1}$. The set of row numbers g_i of Ψ^{-1} that correspond to the sample times for each modulus m_i are calculated as

$$g_i = \{ \lfloor (lN/m_i) \rfloor + 1 \}, \quad (6.2)$$

where $1 \leq g_i \leq N$, l is an integer and $l \geq 0$, $i = 1 \dots r$, and $\lfloor \bullet \rfloor$ represents rounding to the nearest integer value. From Equation (6.2), the set, G , of L unique row numbers consisting of

the elements that belong to all g_i is formed as

$$G = \bigcup_{i=1}^r g_i. \quad (6.3)$$

The $L \times N$ measurement basis matrix, Φ , is formed by selecting the row vectors of an $N \times N$ identity matrix \mathbf{I} such that

$$\Phi_k = \mathbf{I}_{G_k} \text{ where } k = 1, 2, \dots, L \quad (6.4)$$

and \mathbf{I}_{G_k} is the G_k -th row of \mathbf{I} . The selection of the rows of Ψ^{-1} is accomplished by pre-multiplying Ψ^{-1} by Φ or

$$\mathbf{A} = \Phi \Psi^{-1}. \quad (6.5)$$

For convenience, the signal observation period is set equal to one second. As a result, the length N of the discrete signal \mathbf{x} is equal to the ideal sampling frequency of \mathbf{x} . If $N = \prod_{i=1}^r m_i$, the SNS samples will lie on integer multiples of the sampling period of \mathbf{x} , $T_x = 1/N$. However, if $N \neq C \prod_{i=1}^r m_i$, where C is a positive integer, the SNS-CS cueing receiver sample times will not fall on integer multiples of T_x . In this case, the rounding operation, $\lfloor \bullet \rfloor$, in Equation (6.2) is used to select the rows of Ψ^{-1} that most closely approximate the SNS-CS cueing receiver's sample times.

Two examples are shown in Figure 6.2. In the first example, $N = \prod_{i=1}^r m_i$, and in the second example, $N = 2 \left(\hat{M}_{SNS} - 1 \right) < \prod_{i=1}^r m_i$. For example, if a SNS with $m_i = \{3, 4\}$, $\hat{M}_{SNS} = 5$ and $N = \prod_{i=1}^2 m_i = 12$, from Equation (6.2)

$$g_1 = \{1, 5, 9\} \text{ and}$$

$$g_2 = \{1, 4, 7, 10\}.$$

From Equation (6.3), $G = \{1, 4, 5, 7, 9, 10\}$, and from Equation (6.4)

$$\Phi = \begin{bmatrix} 1 & 0 & 0 & 0 & 0 & 0 & 0 & 0 & 0 & 0 & 0 & 0 \\ 0 & 0 & 0 & 1 & 0 & 0 & 0 & 0 & 0 & 0 & 0 & 0 \\ 0 & 0 & 0 & 0 & 1 & 0 & 0 & 0 & 0 & 0 & 0 & 0 \\ 0 & 0 & 0 & 0 & 0 & 0 & 1 & 0 & 0 & 0 & 0 & 0 \\ 0 & 0 & 0 & 0 & 0 & 0 & 0 & 0 & 1 & 0 & 0 & 0 \\ 0 & 0 & 0 & 0 & 0 & 0 & 0 & 0 & 0 & 1 & 0 & 0 \end{bmatrix}.$$

Then, from Equation (6.5),

$$\mathbf{A} = \frac{1}{2\sqrt{3}} \begin{bmatrix} 1 & 1 & \dots & 1 & 1 \\ 1 & \psi^3 & \psi^{3 \cdot 2} & \dots & \psi^{3(11)} \\ 1 & \psi^4 & \psi^{4 \cdot 2} & \dots & \psi^{4(11)} \\ 1 & \psi^6 & \psi^{6 \cdot 2} & \dots & \psi^{6(11)} \\ 1 & \psi^8 & \psi^{8 \cdot 2} & \dots & \psi^{8(11)} \\ 1 & \psi^9 & \psi^{9 \cdot 2} & \dots & \psi^{9(11)} \end{bmatrix}.$$

A signal $x(t) = \sin(8\pi t + \pi/6)$ and the discrete time samples obtained when sampling at m_i samples per second in the above example are shown in Figure 6.2a. Each sample of $x(t)$ that forms \mathbf{y} corresponds exactly to a sample obtained when sampling at N samples per second.

Now, consider the second example where $N = 2(\hat{M}_{SNS} - 1) = 8$. The SNS-CS cueing receiver's sample times correspond to rows $G = \{1, 3, 4, 6, 7\}$ of \mathbf{I} producing

$$\Phi = \begin{bmatrix} 1 & 0 & 0 & 0 & 0 & 0 & 0 & 0 \\ 0 & 0 & 1 & 0 & 0 & 0 & 0 & 0 \\ 0 & 0 & 0 & 1 & 0 & 0 & 0 & 0 \\ 0 & 0 & 0 & 0 & 1 & 0 & 0 & 0 \\ 0 & 0 & 0 & 0 & 0 & 1 & 0 & 0 \\ 0 & 0 & 0 & 0 & 0 & 0 & 1 & 0 \end{bmatrix}.$$

From Equation (6.5),

$$\mathbf{A} = \frac{1}{2\sqrt{2}} \begin{bmatrix} 1 & 1 & \dots & 1 & 1 \\ 1 & \psi^2 & \psi^{2 \cdot 2} & \dots & \psi^{2(7)} \\ 1 & \psi^3 & \psi^{3 \cdot 2} & \dots & \psi^{3(7)} \\ 1 & \psi^4 & \psi^{4 \cdot 2} & \dots & \psi^{4(7)} \\ 1 & \psi^5 & \psi^{5 \cdot 2} & \dots & \psi^{5(7)} \\ 1 & \psi^6 & \psi^{6 \cdot 2} & \dots & \psi^{6(7)} \end{bmatrix}.$$

As seen in Figure 6.2b, the SNS undersampling and shows that the samples for $f_s = 3$ Hz do not equal integer multiples of T_x ; therefore, the closest sample times of \mathbf{x} are used to select the appropriate rows of \mathbf{I} to form Φ . However, the sample values obtained with a sampling frequency of $f_s = 3$ Hz are not representative of the sample values of \mathbf{x} . For example, the sample of $x(t)$ at $t = 0.375$ seconds is not representative of the sample value at $t = 1/3$ seconds.

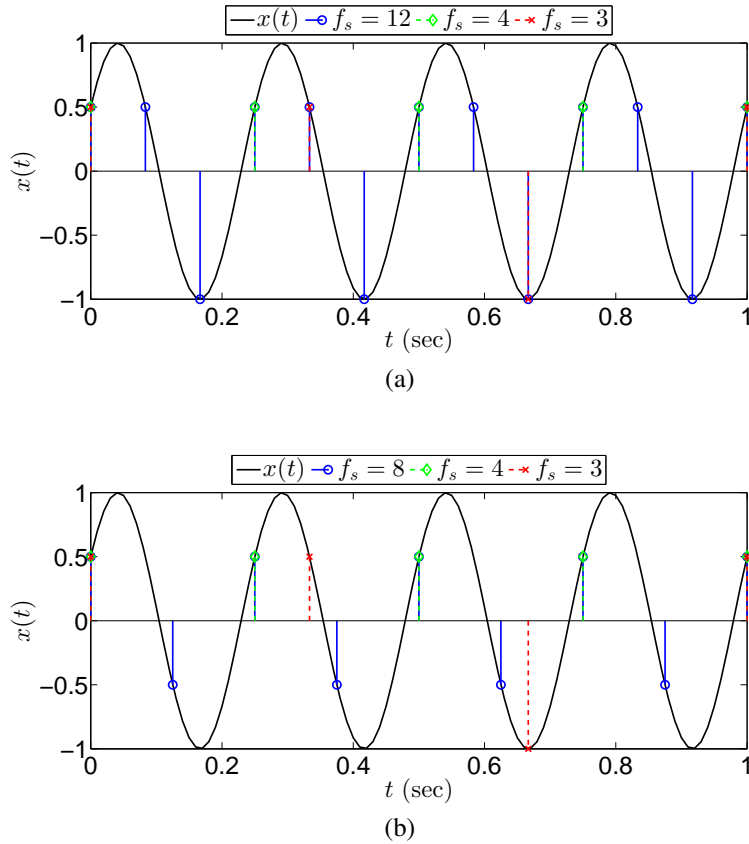


Figure 6.2: Example of SNS based undersampling with (a) $N = \prod_{i=1}^2 m_i = 12$ and (b) $N = 2 \left(\hat{M}_{SNS} - 1 \right) = 8$.

As a result, errors in the reconstructed frequency spectrum occur. To ensure that the sample values that form \mathbf{y} are representative of samples of \mathbf{x} , the sensing matrix dimension, N , must be sufficiently large compared to the maximum signal frequency f_{max} . The ratio of the sensing matrix dimension to f_{max} is defined as

$$\zeta = \frac{N}{2f_{max}}. \quad (6.6)$$

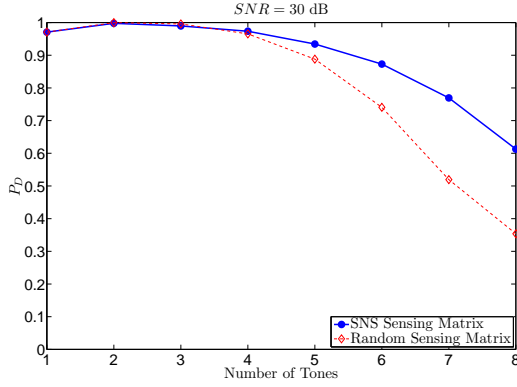
The effect of ζ on the performance of the SNS-CS cueing receiver is also examined through performing Monte Carlo simulations. The Monte Carlo simulation methodology and results are presented in the following section.

6.2 Monte Carlo Simulations

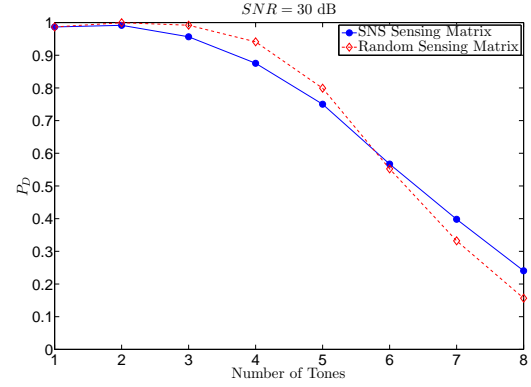
The performance of the SNS-CS cueing receiver is compared to the random sensing approach through Monte Carlo simulations. Several SNS-CS cueing receiver architectures based on different SNS moduli sets and subsequently different sensing matrices are evaluated. Each SNS-CS cueing receiver architecture is examined to determine its performance for different levels of signal sparsity in the frequency domain. Five thousand trials were conducted for each set of simulations where the signal \mathbf{x} is a summation of equal magnitude sinusoids with random integer frequencies, $0 \leq f_0 \leq f_{max} \leq \hat{M}_{SNS} - 1$, and uniformly distributed phase angles, $\theta \sim \mathcal{U}[0, 2\pi)$.

Three different moduli sets are examined, $m_i = \{21, 22, 23\}$, $m_i = \{21, 22, 23, 25\}$, and $m_i = \{21, 22, 23, 25, 29\}$ when $N = 1024$. The performance of the SNS-CS cueing receiver is also compared when $\zeta \in \{8, 16\}$ to demonstrate the impact of ζ on system performance. The SpaRSA algorithm is used to recover the estimated magnitude spectrum $|\tilde{X}(k)|$. The estimated magnitude spectrum $|\tilde{X}(k)|$ is compared to the signal's magnitude spectrum $|X(k)|$ and the probability of correctly detecting the frequencies transmitted within the bandwidth, $f \leq f_{max}$, without false detections is presented. A fixed threshold of 40 dB below the magnitude of the peak values in $|X(k)|$ is used to determine whether a peak exists in $|\tilde{X}(k)|$. The sinusoids are considered to be successfully resolved if the peaks of $|\tilde{X}(k)|$ occur at the same frequencies as $|X(k)|$. Monte Carlo simulations are also performed using normally distributed random sensing matrices of equal size, and the results are compared to those of the SNS-CS cueing receiver.

A SNS-CS cueing receiver with $m_i = \{21, 22, 23\}$ and $\hat{M} = 254$ is examined in Figure 6.3 through Figure 6.5 for $N = 1024$, $\zeta = 16$ and $\zeta = 8$, corresponding to $f_{max} = 32$ Hz and $f_{max} =$

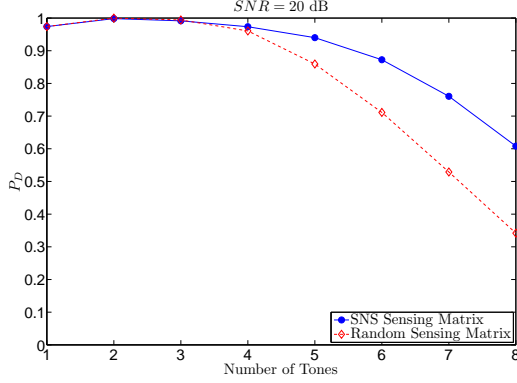


(a)

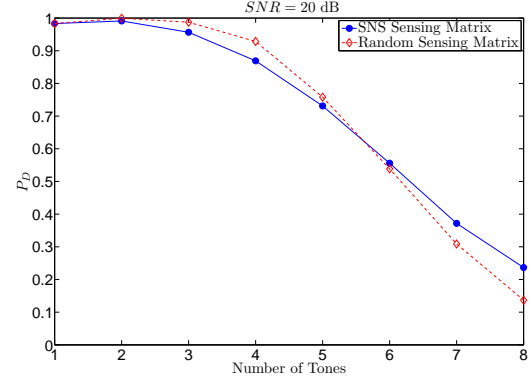


(b)

Figure 6.3: SNS-CS cueing receiver performance: probability of detecting signal frequencies for $m_i = \{21, 22, 23\}$ and $SNR = 30$ dB for (a) $N = 1024$, $f_{max} = 32$ Hz, and (b) $N = 1024$, $f_{max} = 64$ Hz.



(a)



(b)

Figure 6.4: SNS-CS cueing receiver performance: probability of detecting signal frequencies for $m_i = \{21, 22, 23\}$ and $SNR = 20$ dB for (a) $N = 2048$, $f_{max} = 128$ Hz, and (b) $N = 1024$, $f_{max} = 64$ Hz.

64 Hz. From Equation (6.2) and Equation (6.3), \mathbf{A} is a 64×1024 partial IDFT sensing matrix. From Equation (2.17), \mathbf{A} can reconstruct a sparse signal consisting of $S < 8$ complex exponential sinusoids or ≤ 4 real sinusoids. Comparing the results in Figure 6.3a through Figure 6.5b, the P_D is degraded with lower SNR as expected. Also, as the value of ζ lowered, performance degraded which is also expected because the sample values composing \mathbf{y} are more likely to be inconsistent with the Nyquist rate samples. The SNS-CS cueing receiver's performance is shown to be comparable to that achieved using a random sensing matrix with regard to the probability of detection, P_D .

Symmetrical number system - compressive sensing cueing receiver was also examined when

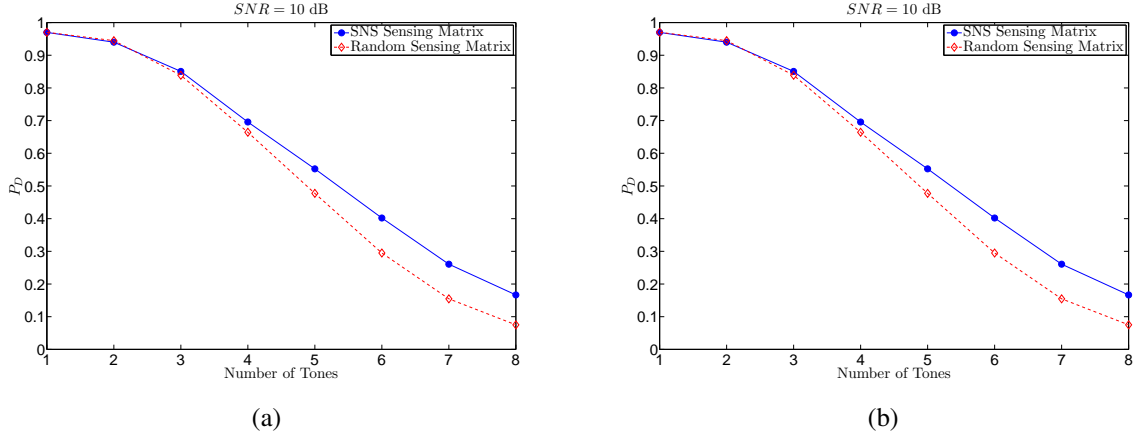


Figure 6.5: SNS-CS cueing receiver performance: probability of detecting signal frequencies for $m_i = \{21, 22, 23\}$ and $SNR = 10$ dB for (a) $N = 1024$, $f_{max} = 32$ Hz and $N = 1024$, $f_{max} = 64$ Hz.

$m_i = \{21, 22, 23, 25\}$. The Monte Carlo simulations were conducted under the same conditions as the previous case ($N = 1024$ and $\zeta = \{8, 16\}$). Figure 6.6 through Figure 6.8 display the results comparing the results obtained when using the SNS-CS cueing receiver to those obtained when a random sensing matrix is used. For each SNR examined, the SNS-CS cueing receiver's performance was comparable to that of the random sensing matrix. Also, its performance degraded more gracefully when the number of tones exceeded the theoretical predictions obtained from Equation (2.17). As seen for the previous case, both compressive sensing architectures' performance improved when the SNR was higher ($SNR \geq 20$ dB). The SNS-CS receiver's performance also improved when ζ was larger due to the SNS sample values more closely approximating the sample values corresponding to those taken at N samples per second.

The next set of moduli examined were $m_i = \{21, 22, 23, 25, 29\}$. Monte Carlo simulations were conducted for the same conditions examined for the previous two moduli sets. As shown in Figure 6.9 through Figure 6.11, the performance of the SNS-CS cueing receiver systems closely approximated the performance of CS systems using equally sized random sensing matrices. Comparing the results for the three different moduli sets, the increased number of samples due to additional coprime moduli, increases the number of sinusoids that can be detected as predicted by Equation (2.17). Also, as shown in Figure 6.3 through Figure 6.11, the SNS-CS cueing receiver's performance degrades more gracefully than random sensing matrix approaches as the number of sinusoids present exceeds the maximum value of sparsity from Equation (2.17). The performance of the three SNS-CS cueing receivers examined are summarized in Table 6.1 and Table 6.2 which list the number of sinusoids that each SNS-CS cueing receiver can resolve

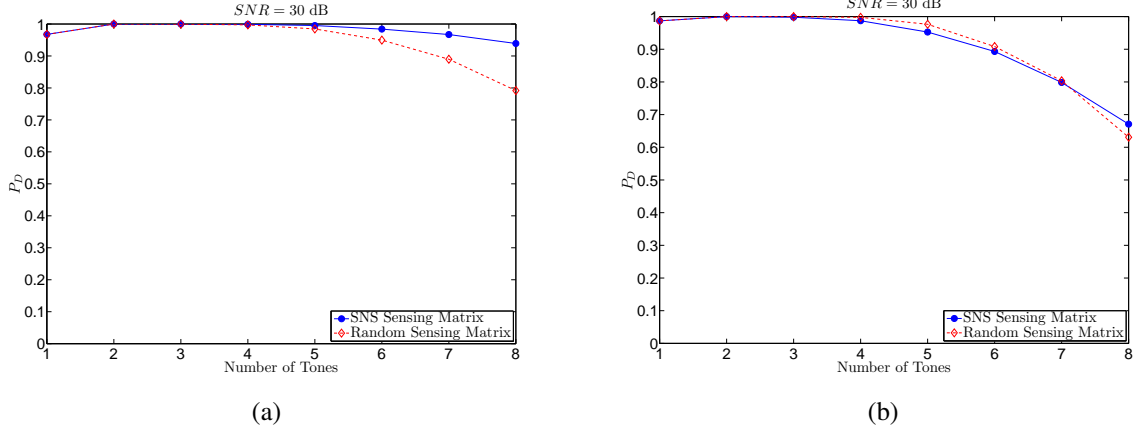


Figure 6.6: SNS-CS cueing receiver performance: probability of detecting signal frequencies for $m_i = \{21, 22, 23, 25\}$ and $SNR = 30$ dB, for (a) $N = 1024$ and $f_{max} = 32$ Hz and (b) $N = 1024$ and $f_{max} = 64$ Hz.

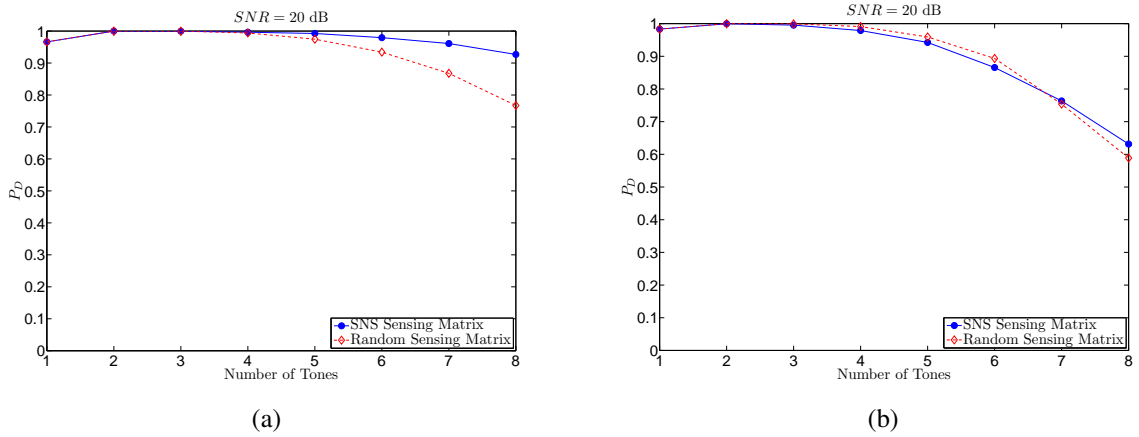


Figure 6.7: SNS-CS cueing receiver performance: probability of detecting signal frequencies for $m_i = \{21, 22, 23, 25\}$ and a $SNR = 20$ dB for (a) $N = 1024$, and $f_{max} = 32$ Hz, and (b) $N = 1024$, and $f_{max} = 64$ Hz.

with a $P_D > 0.9$ for an SNR of 30 dB, 20 dB, and 10 dB. The theoretical predictions from Equation (2.17) are also presented. The performance of the SNS-CS cueing receiver is comparable to the theoretical predictions when the SNR is high and when $\zeta = 16$, the performance exceeded the theoretical predictions. The number of sinusoids that can be detected decreased with the SNR as expected. In Figure 6.3 through Figure 6.11, the P_D is lower for a signal consisting of one tone compared to that for a signal consisting of two tones in some of the simulations. Examining the results of the simulations, this anomaly is due to the SpaRSA algorithm failing to converge for a limited number of trials resulting in erroneous frequency values being identified.

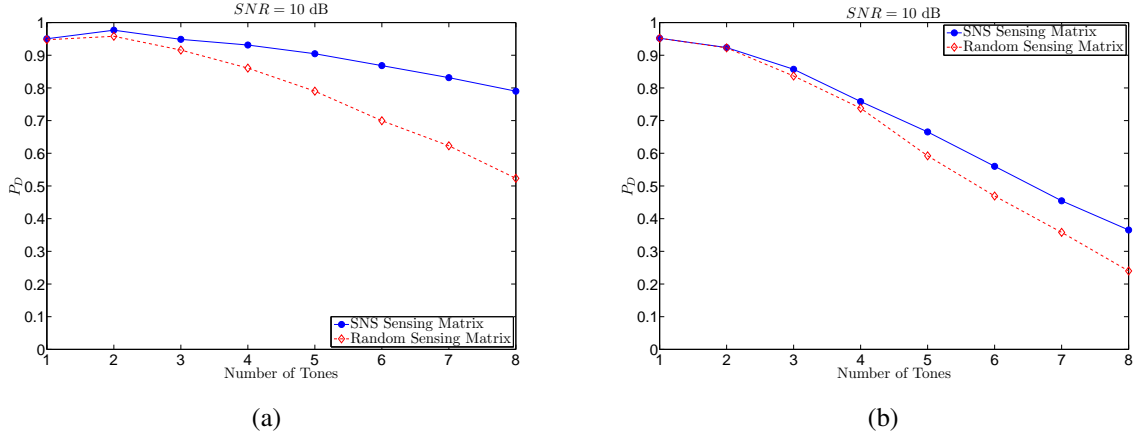


Figure 6.8: SNS-CS cueing receiver performance: probability of detecting signal frequencies for $m_i = \{21, 22, 23, 25\}$ and $SNR = 10$ dB for (a) $N = 1024$, and $f_{max} = 32$ Hz and (b) $N = 1024$, and $f_{max} = 64$ Hz.

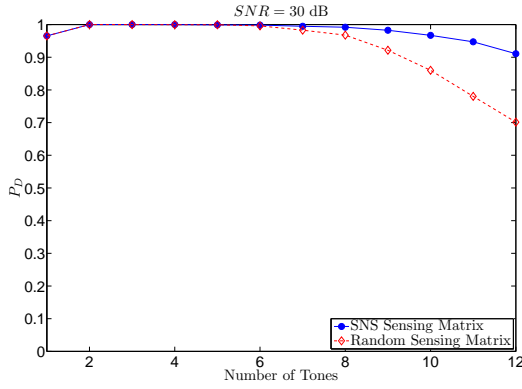
Table 6.1: Number of sinusoids that can be detected with a probability of detection $P_D \geq 0.9$ with $N = 1024$, $f_{max} = 32$ Hz.

m_i	SNR			
	30 dB	20 dB	10 dB	From Equation (2.17)
$\{21, 22, 23\}$	5	5	4	4
$\{21, 22, 23, 25\}$	8	8	5	6
$\{21, 22, 23, 25, 29\}$	12	11	4	8

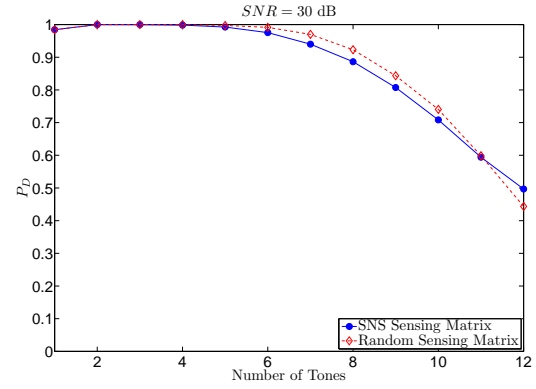
For the case of a single tone being present, the algorithm used in [51] can be used to determine frequencies $\leq \hat{M}_{SNS}$.

Monte Carlo simulations were also performed for the same moduli sets and values of ζ with $N = 2048$. The results are presented at the end of this chapter in Figure 6.13 through Figure 6.15 and Table 6.4 and Table 6.5. The results are similar to those presented when $N = 1024$, meeting or exceeding the predictions of Equation (2.17) when the SNR was high ($SNR > 20$ dB). The results also are approximately equal to those obtained when using a random sensing matrix.

The performance of the SNS-CS cueing receiver for each moduli set examined when the SNR equals 30 dB for $N = 1024$ and $N = 2048$ are displayed in Figure 6.12. The curves demonstrate the advantage of using additional coprime moduli as well as the impact of Equation (2.17) on the receiver architecture's performance.

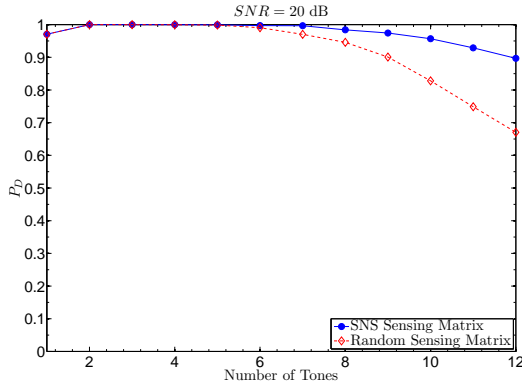


(a)

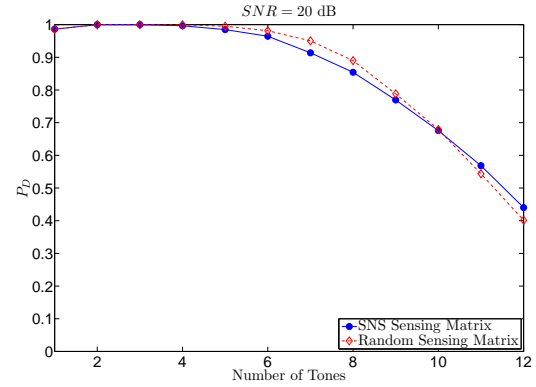


(b)

Figure 6.9: SNS-CS cueing receiver performance: probability of detecting signal frequencies for $m_i = \{21, 22, 23, 25, 29\}$ and $SNR = 30$ dB for (a) $N = 1024$ and $f_{max} = 32$ Hz and (b) $N = 1024$ and $f_{max} = 64$ Hz.



(a)



(b)

Figure 6.10: SNS-CS cueing receiver performance: probability of detecting signal frequencies for $m_i = \{21, 22, 23, 25, 29\}$ and $SNR = 20$ dB for (a) $N = 1024$, and $f_{max} = 32$ Hz and (b) $N = 1024$, and $f_{max} = 64$ Hz.

Table 6.2: Number of sinusoids that can be detected with a probability of detection $P_D \geq 0.9$ with $N = 1024$, $f_{max} = 64$ Hz.

m_i	SNR			From Equation (2.17)
	30 dB	20 dB	10 dB	
$\{21, 22, 23\}$	3	3	2	4
$\{21, 22, 23, 25\}$	5	5	2	6
$\{21, 22, 23, 25, 29\}$	7	7	0	8

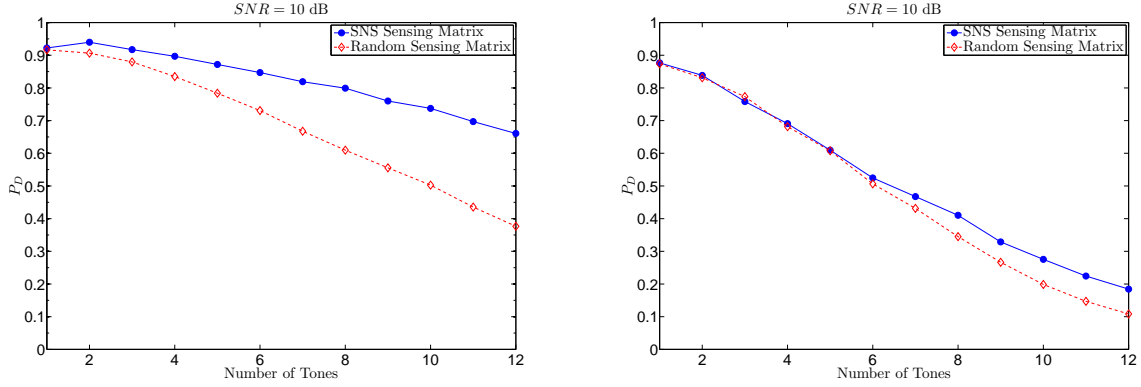


Figure 6.11: SNS-CS cueing receiver performance: probability of detecting signal frequencies for $m_i = \{21, 22, 23, 25, 29\}$ and $SNR = 10$ dB for (a) $N = 1024$ and $f_{max} = 32$ Hz and (b) $N = 1024$ and $f_{max} = 64$ Hz.

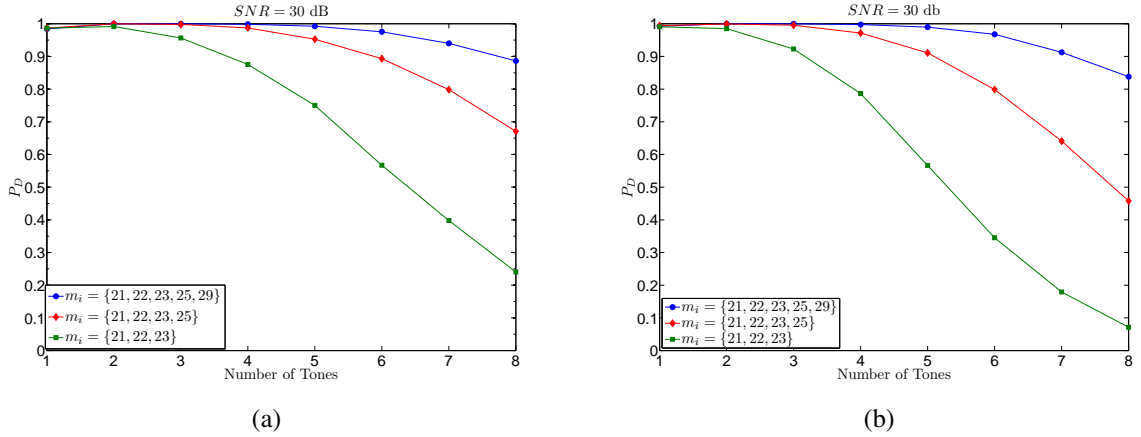


Figure 6.12: Symmetrical number system-compressive sensing cueing receiver performance: (a) $N = 1024$ and $f_{max} = 64$, (b) $N = 2048$ and $f_{max} = 128$.

Comparing the results obtained using SNS-CS cueing receiver architecture to the number of sinusoids that can be resolved using CRT-based algorithms, the SNS-CS cueing receiver provides a significant improvement compared to the results in [51] where only a single frequency alias can be resolved. The SNS-CS cueing receiver also provide improvement compared to the algorithm presented in [100]. The CRT-based algorithm described in [100] states that if a complex-valued waveform $x(t)$ contains ρ different frequencies, the ρ frequencies can be resolved provided the number of coprime sampling rates r is

$$r = \eta\rho + \theta, \quad 0 \leq \theta < \rho \quad (6.7)$$

Table 6.3: Comparison of the maximum number of sinusoids that are able to be detected by the SNS-CS cueing receiver to the performance of the CRT based algorithm of [100].

\mathbf{m}_i	SNS-CS Cueing Receiver		CRT Algorithm of [100]			
	Frequencies	f_{\max}	Frequencies	f_{\max}	Frequencies	f_{\max}
$\{21, 22, 23\}$	3	128	3	23		
$\{21, 22, 23, 25\}$	5	128	4	25	2	462
$\{21, 22, 23, 25, 29\}$	7	128	5	29	2	462

where η is a nonnegative integer, and

$$f_{\max} < \max \{m, m_1, \dots, m_r\}, \quad (6.8)$$

$$m \triangleq \begin{cases} \min_{1 \leq i_1 \leq \dots \leq i_\eta \leq r} \text{lcm}\{m_{i_1}, \dots, m_{i_\eta}\}, & \text{if } \eta > 0 \\ 0, & \text{otherwise} \end{cases}, \quad (6.9)$$

and $\text{lcm}\{\bullet\}$ is the least common multiple function. As an example, when using coprime sampling rates, $m_i = \{21, 22, 23, 25\}$, from (6.7) through (6.9), four sinusoids can be detected with $f_{\max} < 21$ or two sinusoids with $f_{\max} = 462$. Comparatively, the SNS-CS cueing receiver allows detecting up to five sinusoids with $f_{\max} = 128$ with a $P_D > 0.9$ through the use of compressive sensing as demonstrated in Figure 6.14b and Table 6.4. The results for the other two moduli sets that were examined are presented in Table 6.3. In each case, the SNS-CS cueing receiver is capable of identifying more frequencies than the CRT-based algorithm in [100].

Table 6.4: Number of sinusoids that can be detected with a probability of detection $P_D \geq 0.9$ with $N = 2048$, $f_{\max} = 128$ Hz.

\mathbf{m}_i	SNR			
	30 dB	20 dB	10 dB	From Equation (2.17)
$\{21, 22, 23\}$	3	3	2	4
$\{21, 22, 23, 25\}$	5	5	3	5
$\{21, 22, 23, 25, 29\}$	7	7	4	7

Table 6.5: Number of sinusoids that can be detected with probability of detection $P_D \geq 0.9$ with $N = 2048$, $f_{max} = 64$ Hz.

$\mathbf{m_i}$	SNR			
	30 dB	20 dB	10 dB	From Equation (2.17)
$\{21, 22, 23\}$	4	4	3	4
$\{21, 22, 23, 25\}$	6	6	5	5
$\{21, 22, 23, 25, 29\}$	9	9	6	7

6.3 Concluding Remarks

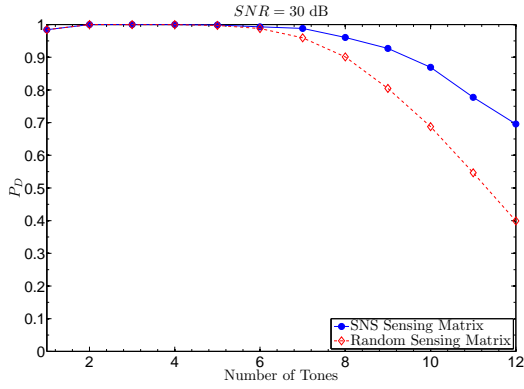
This chapter examined the performance of the SNS-CS cueing receiver architecture and its ability to identify the frequency components of a signal with a sparse representation in the frequency domain. Several SNS-CS cueing receiver architectures were examined, and their performance was compared to theoretical predictions and the performance of random sensing matrices. It was demonstrated through Monte Carlo simulations that the SNS-CS cueing receiver can identify the frequency components of signals sparse in the frequency domain and that they performed within the parameters predicted by CS theory. Their performance was also comparable to that of equally sized random sensing matrices with $\zeta \geq 16$, and the performance of the SNS-CS cueing receiver degraded more gracefully than the random sensing matrix approaches as the number of sinusoids present exceeded the value predicted by Equation (2.17). The performance of the SNS-CS cueing receiver was also examined for different levels of SNR. When the SNR was large, the SNS-CS cueing receiver performance was near the predictions from Equation (2.17); however, for low values of SNR, the performance was unsatisfactory resulting in a low probability of detection due to erroneous frequencies being identified.

The SNS-CS cueing receiver architecture was also compared to the performance of CRT-based algorithms. It was demonstrated that the SNS-CS cueing receiver allows resolving more frequencies with less channels than the CRT-based algorithms. Therefore, by placing the SNS into a CS framework, the ability of SNS based undersampling to resolve frequency ambiguities resulting from aliasing was expanded allowing the identification of an increased number of sinusoids using a fixed moduli set. However, the requirement to limit the signal bandwidth based on a required ζ prevented use of the full dynamic range of the SNS. The bandwidth limitation imposed by the requirement of maintaining a sufficiently large ζ is not encountered when using a random sensing matrix. Therefore, CS receiver architectures employing random sensing

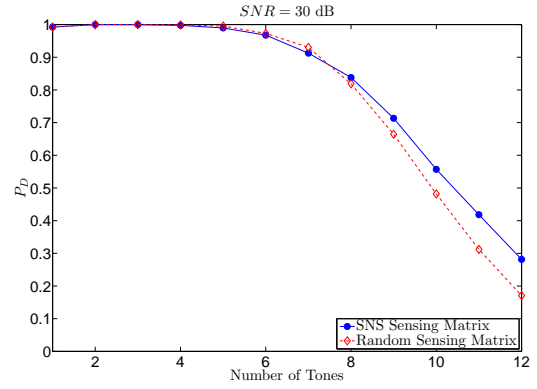
matrices can recover sinusoids within a bandwidth equal to $N/2$ which is one advantage of CS receiver architectures using random sensing matrices compared to the SNS-CS cueing receiver.

The SNS-CS cueing receiver architecture allows for detection of the frequencies in a sparse signal environment and has potential applications as a cueing receiver in EW systems. It also can be employed in cognitive radio systems to sense the frequency spectrum and determine which frequency bands are in use. The reduced bandwidth of the SNS-CS cueing receiver in comparison to that achievable by CS receiver architectures employing random sensing matrices is a drawback; however, it is offset by the reduced complexity of the sampling process and the ease of constructing the sensing matrix.

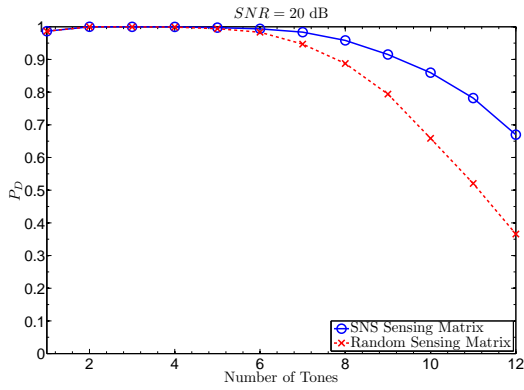
Areas of future research include determining the minimum acceptable value for ζ and the minimum acceptable SNR that provide satisfactory system performance. Investigation of system performance when the signal is composed of sinusoids with non-integer valued frequencies is another area that requires further research. Additional research areas include implementation of an SNS-CS cueing receiver in hardware and conducting experimental testing.



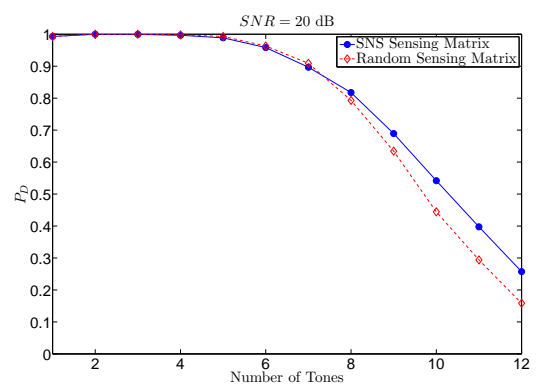
(a)



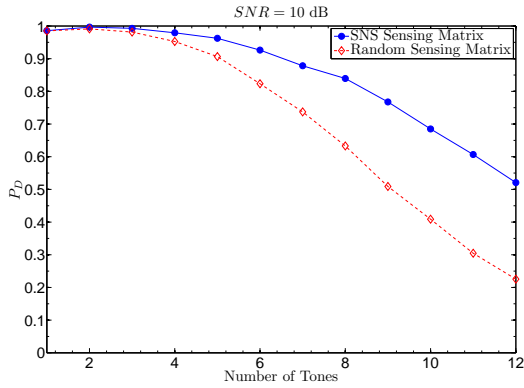
(b)



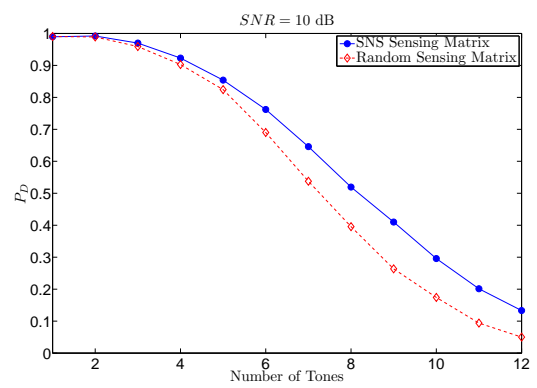
(c)



(d)

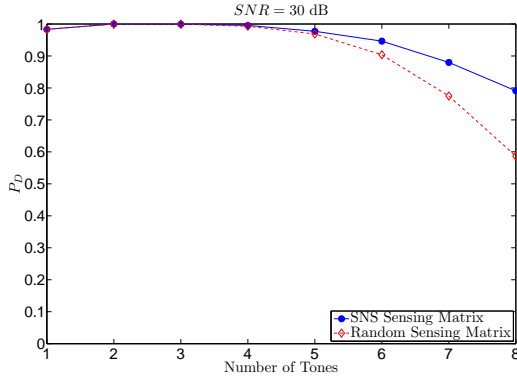


(e)

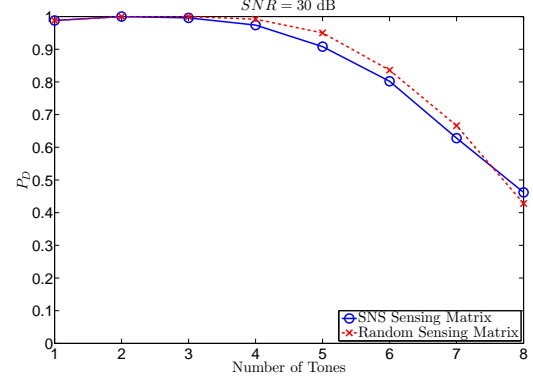


(f)

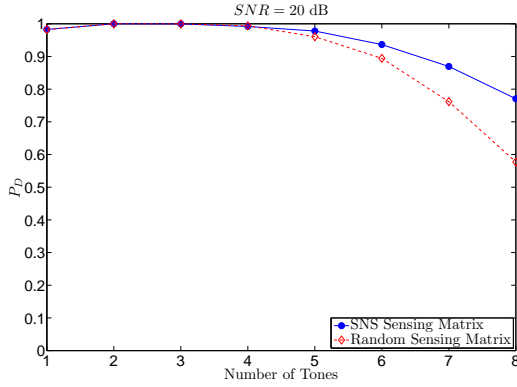
Figure 6.13: Probability of detection for SNS-CS cueing receiver with $m_i = \{21, 22, 23, 25, 29\}$ and $N = 2048$. $f_{max} = 64$ Hz for (a), (c), and (e). $f_{max} = 128$ Hz for (b), (d), and (f). $SNR = 30$ dB in (a) and (b), $SNR = 20$ dB in (c) and (d), and $SNR = 10$ dB in (e) and (f).



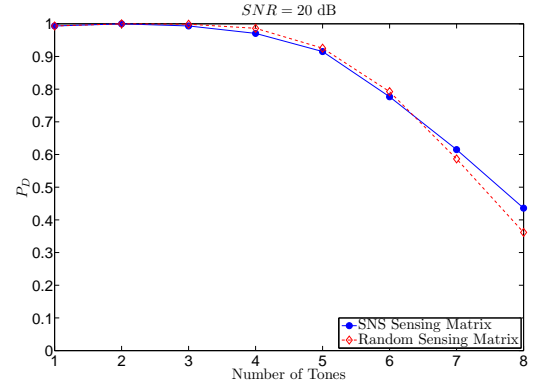
(a)



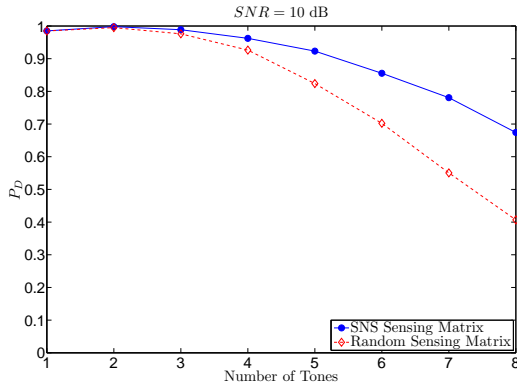
(b)



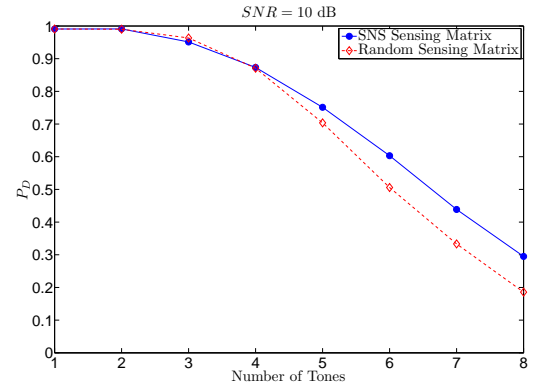
(c)



(d)

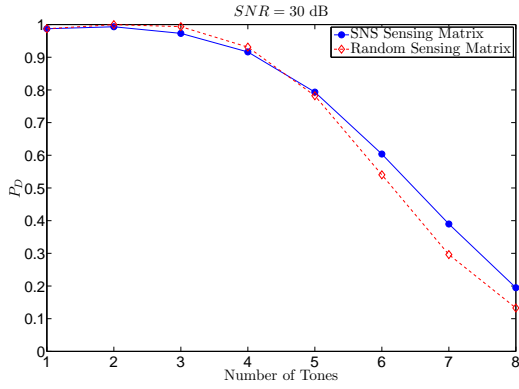


(e)

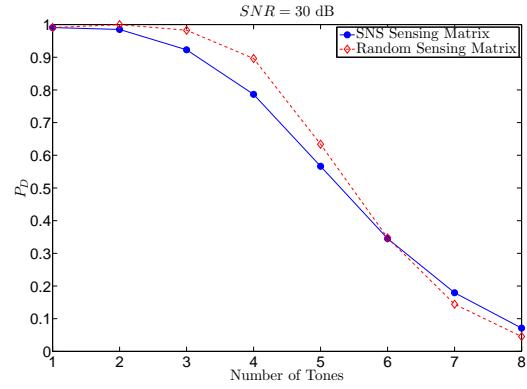


(f)

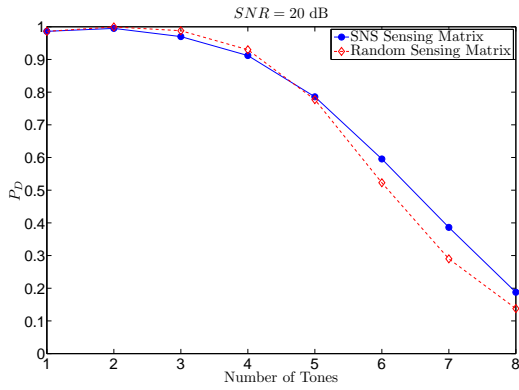
Figure 6.14: Probability of detection for SNS-CS cueing receiver with $m_i = \{21, 22, 23, 25\}$ and $N = 2048$. $f_{max} = 64$ Hz for (a), (c), and (e). $f_{max} = 128$ Hz for (b), (d), and (f). $SNR = 30$ dB in (a) and (b), $SNR = 20$ dB in (c) and (d), and $SNR = 10$ dB in (e) and (f).



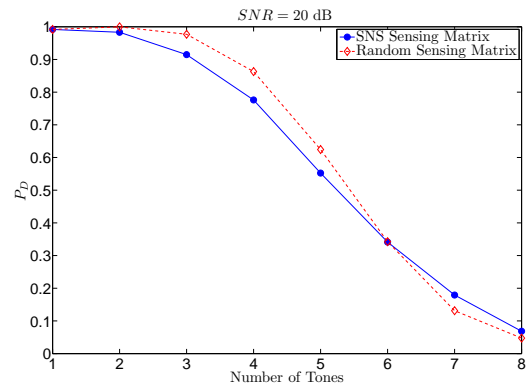
(a)



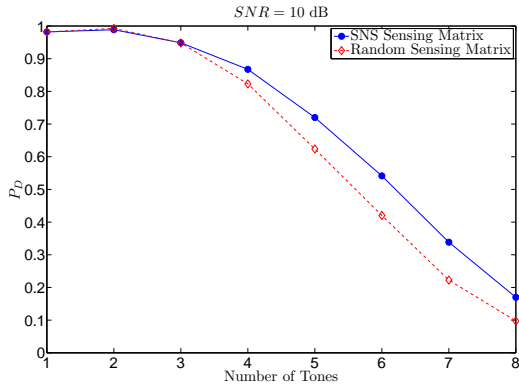
(b)



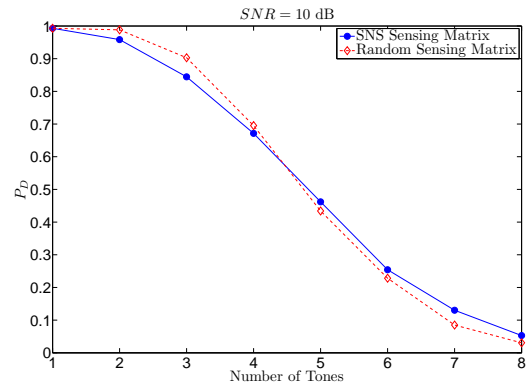
(c)



(d)



(e)



(f)

Figure 6.15: Probability of detection for SNS-CS cueing receiver with $m_i = \{21, 22, 23\}$ and $N = 2048$. $f_{max} = 64$ Hz for (a), (c), and (e). $f_{max} = 128$ Hz for (b), (d), and (f). $SNR = 30$ dB in (a) and (b), $SNR = 20$ dB in (c) and (d), and $SNR = 10$ dB in (e) and (f).

THIS PAGE INTENTIONALLY LEFT BLANK

CHAPTER 7:

Symmetrical Number System - Nyquist Folding Receiver

This chapter examines a multi-channel NYFR architecture with uniform coprime sampling (NYFR-B) as an alternate architecture to a single channel NYFR architecture using a non-uniform sampling as discussed in Section 2.2.7. The NYFR-B architecture uses uniform sampling based on coprime moduli and resolves the signal's frequency using the properties of the SNS and the folding receiver. The relationship between the frequency spectrum obtained using an SNS-based undersampling receiver and that obtained using the NYFR-B architecture is examined. It is demonstrated that the NYFR-B architecture and the SNS undersampling receiver architecture produce frequency spectra for each channel where the signal's energy is concentrated in the identical positive digital frequency bin k representing the same baseband frequency for both receiver architectures. This fact allows the use of a constant radix FFT for all channels allowing faster computations and signal processing compared to that of a multi-channel undersampling receiver architecture using different radix DFTs. An envelope approximation detector (EAD) with GO-CFAR processing [103] is adapted to estimate the magnitude spectrum and detect the peak values. The use of GO-CFAR processing provides an adaptive detection threshold to compensate for either a colored noise spectra, band limited barrage noise jamming, or a noise distribution that is not wide sense stationary. The use of the SNS to resolve multiple frequencies is also examined and the conditions for unambiguous frequency identification are presented.

7.1 Symmetrical Number System - Nyquist Folding Receiver (NYFR-B) Concept

A NYFR architecture can be used in a multi-channel undersampling receiver implementation using uniform coprime sampling rates based upon the SNS moduli. Such a receiver, which is subsequently referred to as the NYFR-B, allows resolution of frequency ambiguities within the dynamic range of the SNS \hat{M}_{SNS} while allowing the use of a constant radix FFT across all the receiver channels. The use of the FFT allows for increased computation speed and reduced signal processing complexity when compared to a multi-channel SNS-based undersampling receiver that requires the use of a different radix DFT in each channel. The NYFR-B also allows simpler implementation and Nyquist zone determination as compared to conventional

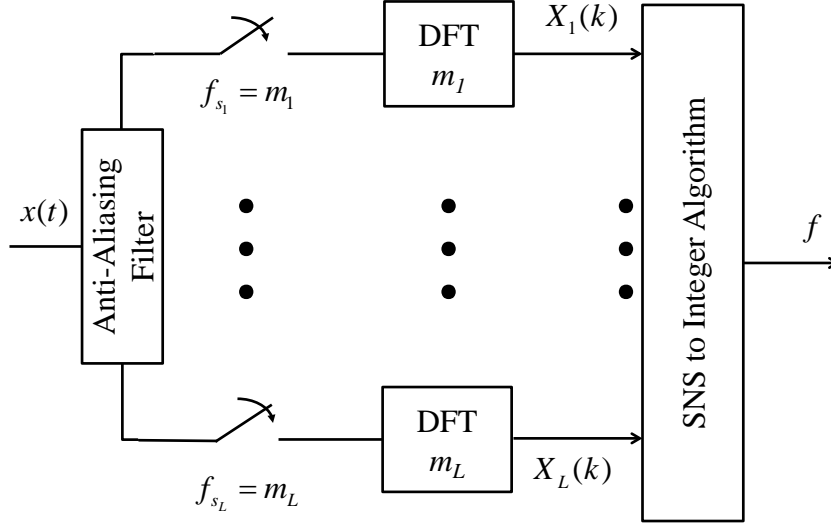


Figure 7.1: L -channel symmetrical number system undersampling receiver. After [51].

single channel NYFR implementation using non-uniform sampling. It is demonstrated that the frequency spectra obtained by using a set of SNS-based sampling frequencies in an L -channel undersampling receiver shown in Figure 7.1 is equivalent to that obtained by a NYFR-B receiver architecture shown in Figure 7.2 where the front-end sampling frequencies f_{s_1}, \dots, f_{s_L} are equal to the set of SNS-based co-prime sampling frequencies and the uniform sampling rate at the ADC is $f_{s_{ADC}}$ and $f_{s_{ADC}} \geq f_{s_l}$, where $l \in \{1, 2, \dots, L\}$.

Examining a single channel of an SNS-based undersampling receiver without the use of a windowing function, if an input signal $x(t)$ is sampled at constant co-prime sampling rate f_{s_l} where $l \in \{1, 2, 3, \dots, L\}$, the resulting signal is

$$x(nT_l) = x(t) \sum_{n=-\infty}^{+\infty} \delta(t - nT_l). \quad (7.1)$$

The Fourier transform of Equation (7.1) is

$$X_{s_l}(f) = X(f) * f_{s_l} \sum_{k=-\infty}^{+\infty} \delta(f - kf_{s_l}) \quad (7.2)$$

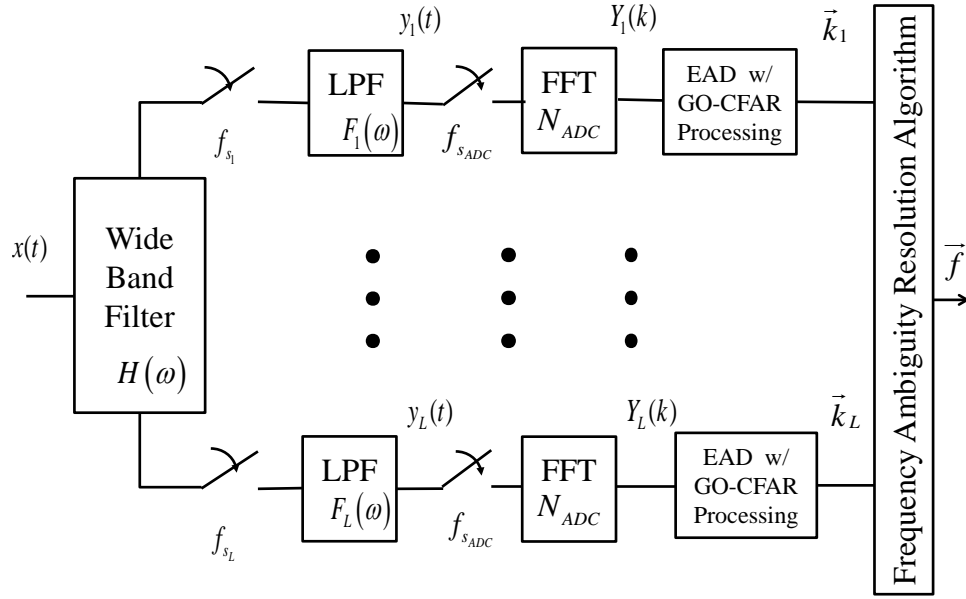


Figure 7.2: SNS-based NYFR (NYFR-B).

which is equal to

$$X_{s_l}(f) = f_{s_l} \sum_{k=-\infty}^{+\infty} X(f - kf_{s_l}). \quad (7.3)$$

As seen in Equation (7.2), the frequency spectrum $X(f)$ is repeated at multiples of the sampling frequency; therefore, if $f_{s_l}/2 < f_{max}$, aliasing occurs mapping frequency components greater than $f_{s_l}/2$ into the band $|f| \leq f_{s_l}/2$ which corresponds to the digital frequency band of $-\pi \leq \omega \leq \pi$. The DFT of the signal $x_l(n)$ is equal to

$$X_l(k) = \sum_{n=0}^{N_l-1} x_l[n] e^{-\frac{j2\pi kn}{N_l}} \quad (7.4)$$

for $k = 0, 1, \dots, N_l - 1$.

In the NYFR-B implementation using a set of SNS-based front-end sampling frequencies, the frequency spectrum of the signal entering the analog low pass filter (LPF) is equal to $X_{s_l}(f)$. The LPF acts as an anti-aliasing filter for the uniform sampler at $f_{s_{ADC}}$ limiting the frequency spectrum to the frequencies composing $x(t)$ and their aliases that lie in the frequency band,

$|f| \leq f_{s_l}/2$. The frequency spectrum of the output of the LPF is

$$Y_l(f) = f_{s_l} \sum_{k=-\infty}^{+\infty} X(f - kf_{s_l}) F_l(f), \quad (7.5)$$

where $F_l(f)$ is an ideal LPF with BW equal to $f_{s_l}/2$. The output frequency spectrum is equal to

$$Y_{s_l}(f) = f_{s_{ADC}} Y_l(f) * \sum_{k=-\infty}^{+\infty} \delta(f - kf_{s_{ADC}}). \quad (7.6)$$

And, since no aliasing occurs,

$$Y_{s_l}(f) = f_{s_{ADC}} f_l \sum_{k=-\infty}^{+\infty} X(f - kf_{s_l}) F_l(f). \quad (7.7)$$

The DTFT of the signal $y_{s_l}(n)$ is equal to

$$Y_l(k) = \sum_{n=0}^{N_{ADC}-1} y_{s_l}[n] e^{\frac{-j2\pi kn}{N_{ADC}}} \quad (7.8)$$

for $k = 0, 1, \dots, N_{ADC} - 1$. The inverse Fourier transform (IFT) of Equation (7.6) is

$$y_{s_l}(nT_{ADC}) = \left[\sum_{n=-\infty}^{+\infty} x(nT_l) \text{sinc}(f_l(t - nT_l)) \right] \times \sum_{l=-\infty}^{+\infty} \delta(t - lT_{ADC}) \quad (7.9)$$

Equation (7.9) is simplified resulting in

$$y_{s_l}(nT_{ADC}) = x_l(t) \sum_{l=-\infty}^{+\infty} \delta(t - lT_{ADC}) = x_l(nT_{ADC}). \quad (7.10)$$

Therefore,

$$Y_{s_l}(k) = \sum_{n=0}^{N_{ADC}-1} x_l[nT_{ADC}] e^{-j2\pi kn/N_{ADC}} \quad (7.11)$$

for $k = 0, 1, \dots, N_{ADC} - 1$.

The DFTs of Equation (7.4) and Equation (7.11) produce spectra with energy concentrated in identical bins provided that f_{s_l} and $f_{s_{ADC}}$ are integer multiples of a base frequency f_0 and N_l and

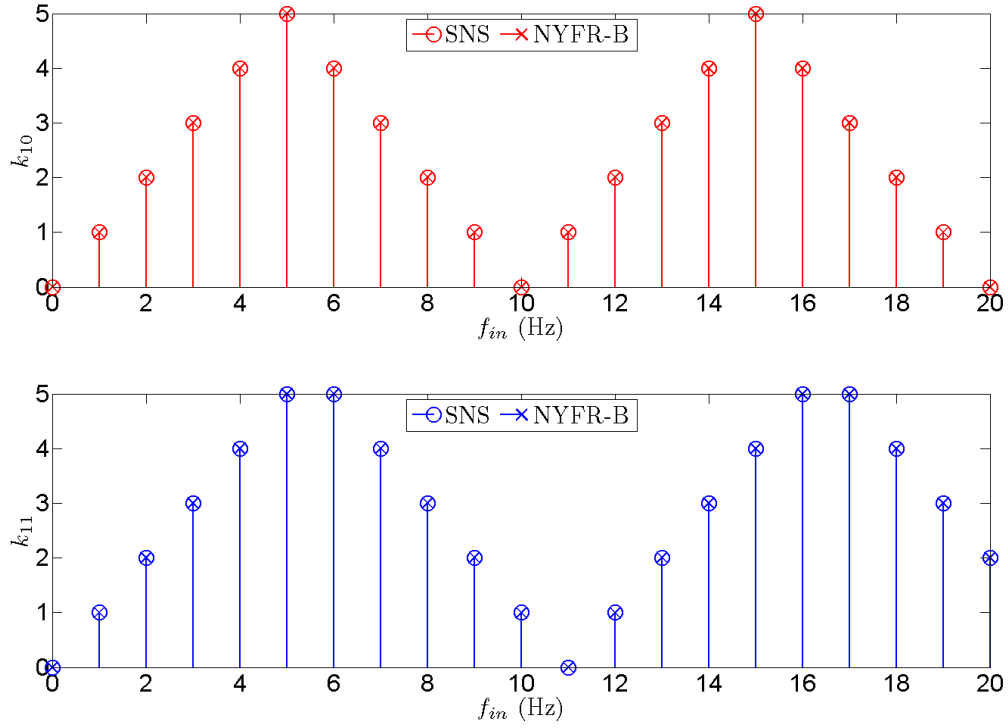


Figure 7.3: Comparison of the symmetrical residues resulting from a symmetrical number system (SNS) undersampling receiver and a SNS - Nyquist Folding Receiver (NYFR-B) architecture.

N_{ADC} are equal to Cf_{s_l} and $Cf_{s_{ADC}}$ where C is an integer constant. The amplitudes of the spectra differ by a scaling factor. The symmetrical residues for a two channel SNS implementation and SNS folded receiver implementation are displayed in Figure 7.3 where $f_{s_l} = \{10, 11\}$ and $f_{s_{ADC}} = 16$ and the DFT sizes used are $N_l = \{10, 11\}$ and $N_{ADC} = 16$. As seen in Figure 7.3, the NYFR-B and the SNS undersampling receiver produce identical symmetrical residues.

7.2 Detection of Multiple Signals Using the Symmetrical Number System

The SNS was demonstrated to have the capability of resolving single frequency ambiguities within \hat{M}_{SNS} in [51]. Similarly, an RNS based receiver concept was shown to be able to resolve single frequency ambiguities within its dynamic range M . However, if ρ frequencies are present and a L -channel undersampling receiver is used, each channel will detect potentially ρ frequencies represented by the residues of the respective SNS or RNS. Therefore, there will be ρ^L possible combinations of the L -length vectors to represent the ρ frequencies. As a result,

more than ρ possible valid SNS or RNS vectors may be formed producing ambiguous results.

In [99], the problem of determining multiple frequencies from a L -channel undersampling receiver using coprime sampling rates was examined when using the RNS. It was proven that ρ frequencies can be unambiguously identified provided that

$$L \geq \eta\rho + \theta \quad (7.12)$$

where η is a nonnegative integer and the maximum frequency contained in the signal is

$$f_{max} < \max(m, m_1, m_2, \dots, m_L) \quad (7.13)$$

where $m = lcm(m_1, m_2, \dots, m_\eta)$. Since the moduli are coprime, the above statement is equivalent to f_{max} being less than the dynamic range of a RNS, composed of the smallest η moduli. As an example, if $L = 4$, $\rho = 2$, and $m_i = \{19, 20, 21, 23\}$, the maximum frequency that can be detected unambiguously is $f_{max} < 380$ Hz.

The dynamic range of the SNS \hat{M}_{SNS} was shown to be equal to Equation (3.6) and Equation (3.7). The proof of the expressions for \hat{M}_{SNS} involves the solution of systems of linear congruence equations using the CRT [51]. Therefore, the conditions in Equation (7.12) can be used for an undersampling receiver using the SNS provided that the f_{max} is less than \hat{M}_{SNS} derived from the smallest η coprime moduli. Simulations were conducted to verify the above conjecture. For an $L = 4$ SNS, 1016 different co-prime moduli sets were tested and were verified to unambiguously resolve all possible permutations of two integer frequencies that are less than \hat{M}_{SNS} based on the smallest two moduli. Testing was also conducted for an $L = 6$ SNS, for two tones being present with $f_{max} < \hat{M}_{SNS}$ based on the smallest three moduli. All of the 286 moduli sets tested were determined to unambiguously resolve two integer frequencies.

7.3 Symmetrical Number System - Nyquist Folding Receiver (NYFR-B) Detection and Frequency Resolution Using an Envelope Approximation Detector with Greatest of Constant False Alarm Rate Processing

The NYFR-B architecture shown in Figure 7.2 uses an EAD with GO-CFAR processing in each channel. The input to the GO-CFAR processing is the envelope approximation of the frequency

spectrum of its associated NYFR-B channel. Greatest of constant false alarm rate processing is conducted for each FFT bin and a vector of frequency bin locations \mathbf{k} is output for each channel. The envelope approximation is equal to

$$Y_{EAD} = a \max(|I|, |Q|) + b \min(|I|, |Q|) \quad (7.14)$$

where I is the in-phase or real component of the frequency spectrum $Y_m(k)$, Q is the quadrature or imaginary component of the frequency spectrum $Y_m(k)$ and a and b are constants [103]. Alternately, if software is used for signal processing, the magnitude or envelope of the frequency spectrum could be used and is determined as

$$Y_{ENV} = \sqrt{I^2 + Q^2}. \quad (7.15)$$

A signal is detected if the envelope approximation of the test cell is greater than an adaptively set threshold value determined by the GO-CFAR processing. A schematic of GO-CFAR processing is shown in Figure 7.4. The threshold value is adaptively set based on the greatest of the average values of the envelope or envelope approximation of two sets of reference cells that are separated from the test cell by a small guard band. This value estimates the square root of the noise power in the signal which is multiplied by a threshold multiplying constant T to establish the threshold value, V_T .

The probability of false alarm (PFA) for an EAD using GO-CFAR processing was examined in [103], and closed-form analytical expressions for the PFA and the threshold multiplier T were derived through the use of numerical methods and curve fitting techniques. In [103], the analysis was conducted for an input of AWGN with distribution $\mathcal{N}(0, 1)$. The analysis shown below is for an input of zero mean AWGN with an variance equal to σ^2 . The PFA is equal to

$$PFA_{a,b} = 2 \int_0^\infty p_{y,n}(z) \left\{ \int_0^z p_{y,n}(y) dy \right\} \times \left\{ \int_{T \frac{z}{n}}^\infty p_c(x) dx \right\} dz \quad (7.16)$$

where $p_{y,n}(y)$ is the probability density function (pdf) of the sum of reference cells shown in Figure 7.4 which is an n -fold convolution of the pdf of the test cell or an individual reference cell,

$$p_c(x) = C e^{D(x)} [\Phi(f_1(x)) + \Phi(f_2(x))] u(x), \quad (7.17)$$

where

$$C = \sqrt{\frac{2}{\pi\sigma^2\sqrt{a^2+b^2}}}, \quad (7.18)$$

$$D(x) = -\frac{x^2}{2b^2\sigma^2} + \frac{a^2x^2}{2b^2\sigma^2(a^2+b^2)}, \quad (7.19)$$

$$f_1(x) = \left(\frac{a}{b}\right) \frac{x}{\sqrt{2\sigma^2\sqrt{a^2+b^2}}}, \quad (7.20)$$

$$f_2(x) = \left(\frac{b}{a}\right) \frac{x}{\sqrt{2\sigma^2\sqrt{a^2+b^2}}}, \quad (7.21)$$

$\Phi(\bullet)$ is the error function,

$$\Phi(\gamma) = \frac{2}{\sqrt{\pi}} \int_0^\gamma e^{-t^2} dt \quad (7.22)$$

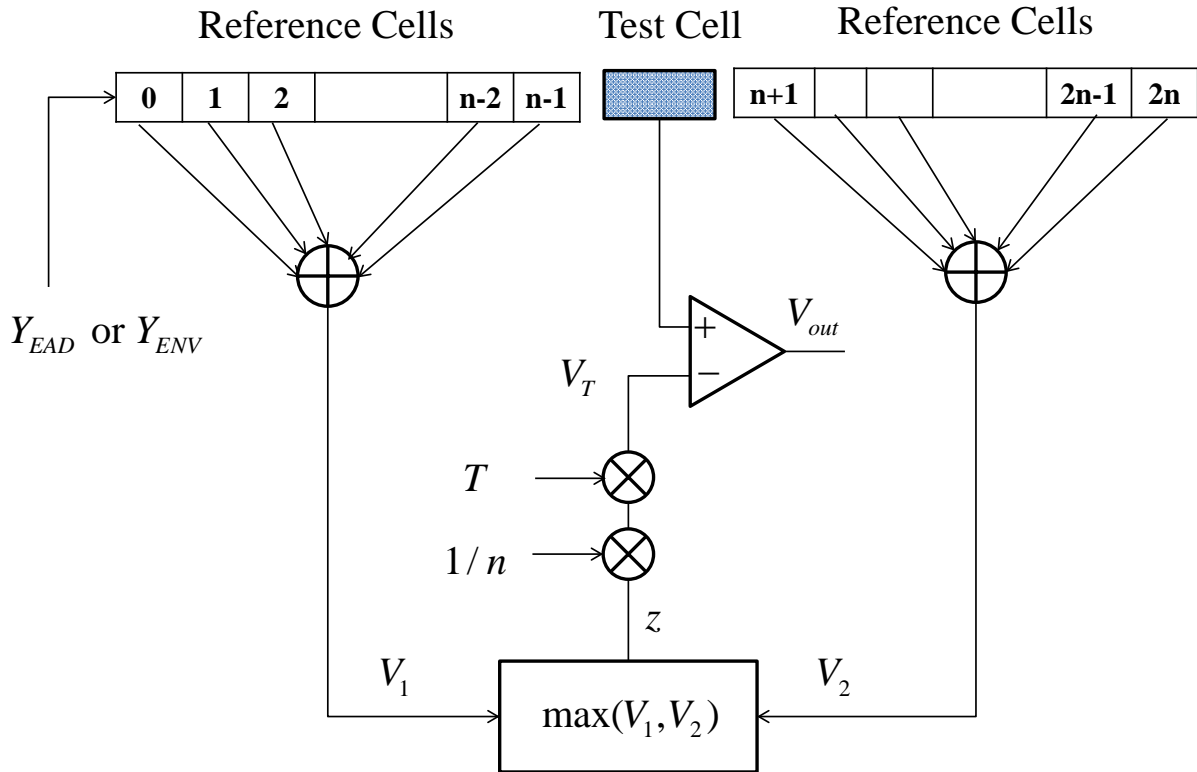


Figure 7.4: Greatest of constant false alarm rate processing. After [103].

and, $u(x)$ is the unit step function.

The analysis in [103] is valid for the DFT or FFT of the input signal due to the DFT and FFT being linear transforms that sum a large number of independent identically distributed random variables. As a result of the central limit theorem, the DFT or FFT of AWGN is normally distributed with zero mean and variance equal to $N\sigma^2$, if the transform length N is large.

In the simulations conducted, $a = 1$ and $b = 1$. Under these conditions, the pdf for a test cell can be expressed as shown in Equation (7.17) and Equation (7.18) through Equation (7.21). These equations reduce to:

$$C = \sqrt{\frac{\sqrt{2}}{N\sigma^2\pi}} \quad (7.23)$$

$$D(x) = \frac{-x^2}{4N\sigma^2} \quad (7.24)$$

$$f_1(x) = \frac{x}{2\sqrt{N\sigma^2}} \quad (7.25)$$

$$f_2(x) = \frac{x}{2\sqrt{N\sigma^2}} \quad (7.26)$$

Substituting Equation (7.23) through Equation (7.26) into Equation (7.17) and simplifying results in,

$$p_c(x) = 2\sqrt{\frac{\sqrt{2}}{N\sigma^2\pi}} e^{\frac{-x^2}{4N\sigma^2}} \Phi\left(\frac{x}{2\sqrt{N\sigma^2}}\right) u(x). \quad (7.27)$$

In [103], an analytical formula was determined to calculate the threshold multiplying factor, T ,

$$\hat{T} = \tilde{a} - \tilde{b}/\beta + \tilde{c}\beta, \quad (7.28)$$

where

$$\beta = \left\{ \tilde{d} - \ln(PFA) + \sqrt{\tilde{e} + \tilde{f} \ln(PFA) + \ln(PFA)^2} \right\}^{1/3} \quad (7.29)$$

for the number of reference cells, $n \leq 2$. When $n > 2$,

$$\hat{T} = \left| \tilde{a} - \frac{\sqrt{-3}}{2} \left(\frac{\tilde{b}}{\beta} + \tilde{c}\beta \right) - \frac{1}{2} \left(\frac{-\tilde{b}}{\beta} + \tilde{c}\beta \right) \right|, \quad (7.30)$$

where

$$\beta = \left\{ \tilde{d} + \ln(PFA) + \sqrt{\tilde{e} + \ln(PFA)} \sqrt{\tilde{f} + \ln(PFA)} \right\}^{1/3}, \quad (7.31)$$

and \tilde{a} , \tilde{b} , \tilde{c} , \tilde{d} , \tilde{e} , and \tilde{f} are the applicable constant values listed in Tables IIB through IXB in [103]. In the case where a real signal is used and a N -point FFT is performed, a False Alarm is defined as a detection above the threshold for any of the $N/2$ positive digital frequency bins when only noise is present. Therefore, the value of the PFA used in Equation (7.29) and Equation (7.31) must be modified. Since each frequency bin can be considered independent, the probability of no false alarm for one frequency bin is

$$P(\text{no alarm}) = 1 - PFA. \quad (7.32)$$

The probability of no alarm in $\frac{N}{2}$ frequency bins for a real signal is equal to

$$P\left(\text{no alarm in } \frac{N}{2} \text{ bins}\right) = (1 - PFA)^{\frac{N}{2}}, \quad (7.33)$$

and the PFA therefore is

$$PFA^* = 1 - (1 - PFA)^{\frac{N}{2}}. \quad (7.34)$$

Solving for PFA in Equation (7.34) yields the value used in Equation (7.29) and Equation (7.31)

$$PFA = 1 - (1 - PFA^*)^{\frac{2}{N}} \quad (7.35)$$

where PFA^* is the desired probability of false alarm for the detector.

To resolve the frequency ambiguities due to undersampling, the base band frequencies in each channel are unfolded through the Nyquist zones that comprise the bandwidth of the wideband input filter $H(\omega)$ shown in Figure 7.1. The possible frequencies corresponding to the baseband frequencies in each channel are calculated as

$$\vec{f}_m = \begin{cases} lf_{sm} - \vec{f}_{bb}, & l \text{ odd} \\ lf_{sm} + \vec{f}_{bb}, & l \text{ even} \end{cases} \quad (7.36)$$

where $l = \{0, 1, 2, \dots, L_m\}$, $L_m = \lceil BW/f_{sm} \rceil$, $\lceil \bullet \rceil$ is the ceiling operator that rounds the argument up to the next integer value, and BW is the bandwidth of the filter $H(\omega)$. The values

of the resolved frequency ambiguities are determined by comparing the elements of the frequency vectors \vec{f}_m for each channel and determining which frequencies are common among the channels within the resolution of the FFT.

7.4 Simulation Results

To demonstrate the performance of the NYFR-B receiver concept, Monte Carlo simulations were conducted using MATLAB for a different moduli sets and different PFAs. The first set of moduli examined were $m_i = \{97, 98, 99, 101\}$. The $N = 4$ SNS sequence enables detection of up to two frequencies. If the sampling frequencies for each channel are equal to the corresponding moduli, $f_{max} = 145$ Hz, an increase in receiver bandwidth of approximately 287% compared to the highest SNS-based sampling rate. The sampling rate of the ADC in each channel is simulated at $f_{sADC} = 128$ Hz. The Monte Carlo simulations results when a signal consisting of a single sinusoidal tone with an random integer valued frequency, $f \leq f_{max}$, are displayed in Figure 7.5. A reference cell length of 16 cells and a guard band length of four cells were used in the GO-CFAR processing. The probability of detecting the tone and identifying its frequency correctly is displayed in Figure 7.5a, and the probability of a missed detection is shown in Figure 7.5b. Monte Carlo simulations were also performed for a signal consisting of two random integer valued frequency tones with $f_n \leq f_{max}$, and the results are presented in Figure 7.6. The probability of correctly detecting and determining the frequencies contained in the signal is shown in Figure 7.6a, and the probability of a missed detection is displayed in Figure 7.6b. The simulations were performed for a $PFA = 1 \times 10^{-2}$ (1×10^5 trials), $PFA = 1 \times 10^{-3}$ (1×10^5 trials), and $PFA = 1 \times 10^{-4}$ (1×10^6 trials). Comparing the curves in Figure 7.5 and Figure 7.6, an increase in SNR of approximately 2 dB is required for a given probability of detection as the number of sinusoids contained in the signal increases from one to two. As the SNR, increases the probability of detection approaches a value of $1 - PFA$.

Monte Carlo simulations were also performed for a six channel NYFR-B receiver with $m_i = \{97, 98, 99, 101, 103, 107\}$ and three frequency tones present. The maximum signal frequency is $f_{max} = 145$ Hz increasing the bandwidth by 271 % compared to Nyquist rate sampling for the largest moduli. In both the four channel and six channel approach the increase in receiver BW compared to the ADC sampling frequency is 227%. The results for this case using the same number of reference cells and guard band length as in the previous case are displayed in Figure 7.7 through Figure 7.9. As seen in the four channel NYFR-B, approximately a 2 dB increase in SNR is required to detect each additional tone for a specific PFA. The performance

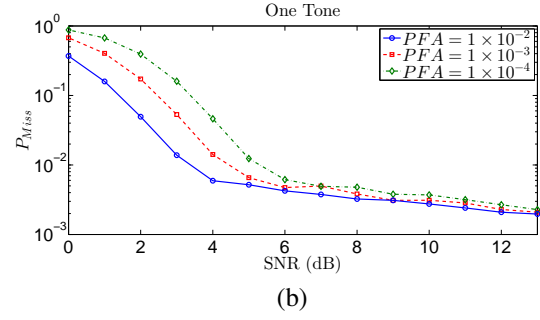
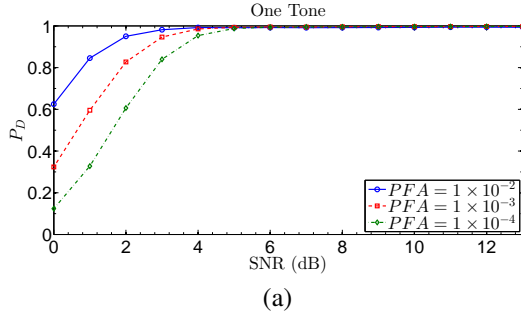


Figure 7.5: Four channel NYFR-B: one transmitted tone, (a) probability of detection, (b) probability of a missed detection.

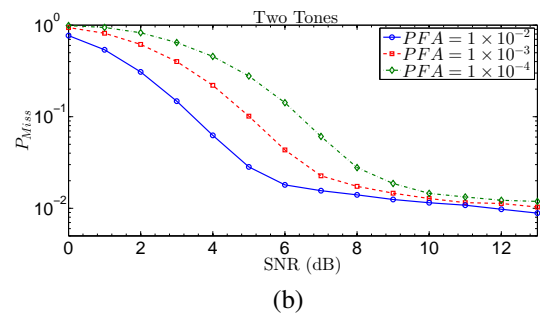
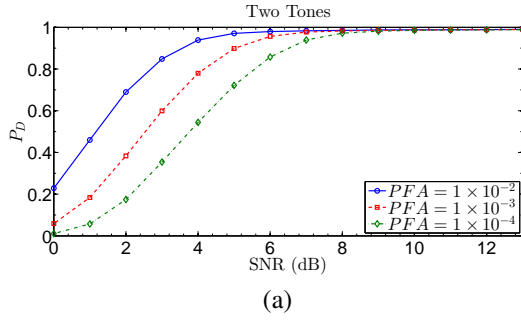


Figure 7.6: Four channel NYFR-B: two transmitted tones, (a) probability of detection, (b) probability of a missed detection.

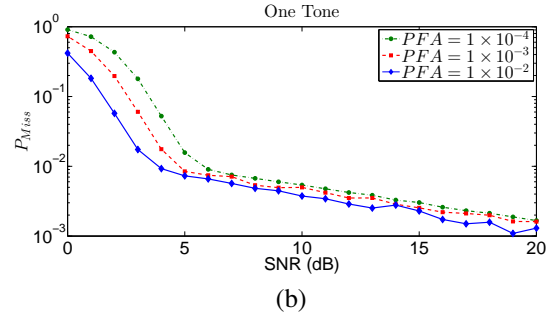
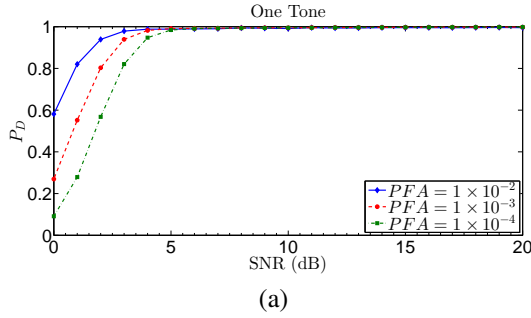


Figure 7.7: Six channel NYFR-B: one transmitted tone, (a) probability of detection, (b) probability of a missed detection.

curves for a four-channel and six-channel NYFR-B are displayed for a $PFA = 1 \times 10^{-3}$. Comparing the curves, the six-channel NYFR-B requires additional SNR to achieve the same P_D as the four-channel NYFR-B.

In the simulation results presented above, the plotted SNR is that of the time domain signal. However, P_D was determined in the frequency domain by comparing each FFT bin to an adap-

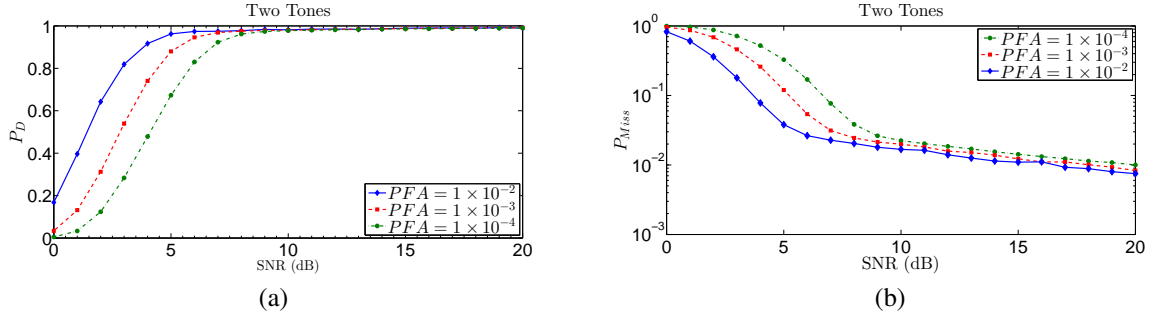


Figure 7.8: Six channel NYFR-B: two transmitted tones, (a) probability of detection, (b) probability of a missed detection.

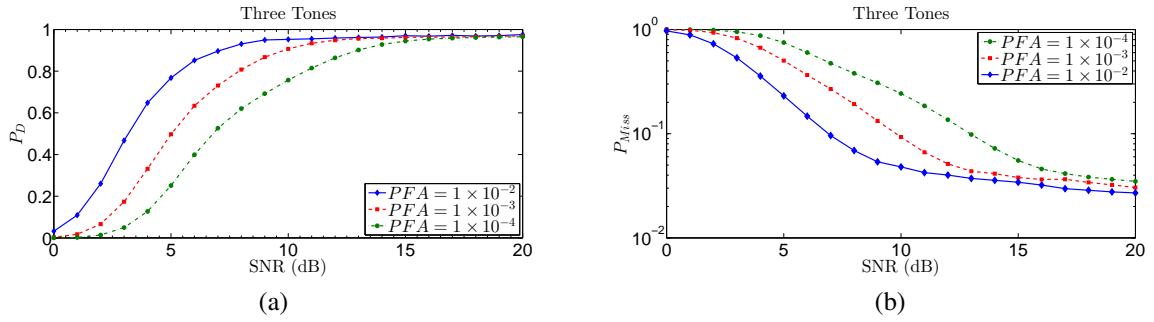


Figure 7.9: Six channel NYFR-B: three transmitted tones, (a) probability of detection, (b) probability of a missed detection.

tive threshold based on a specified CFAR by adapting the EAD with GO-CFAR processing to the frequency domain. Therefore, when comparing the results to benchmarks such as those of a matched filter, the processing gain of the FFT must be considered. The FFT processing gain depends on the size of the FFT. In the Monte Carlo simulations performed, a 128-point FFT was used resulting in a processing gain of approximately 21 dB.

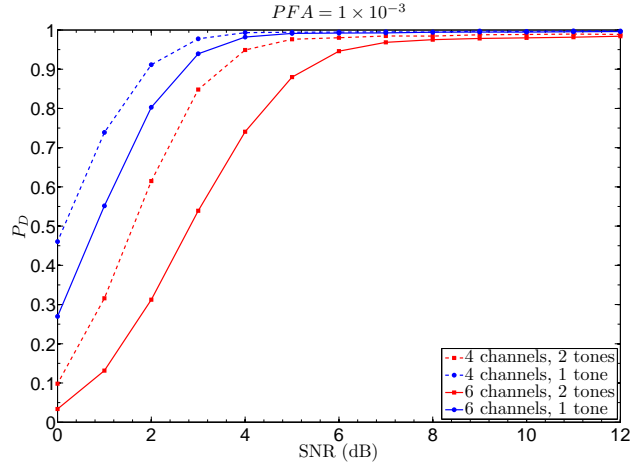


Figure 7.10: Comparison of four and six channel NYFR-B performance.

7.5 Concluding Remarks

In this chapter, it was demonstrated that the residue structure of the SNS is retained when a multi-channel NYFR architecture is used with constant coprime sampling rates based on the SNS moduli. This fact allows use of a constant radix FFT across the channels of the receiver increasing signal processing speeds at the expense of additional hardware when complexity when compared to the undersampling receiver architecture implementation of [51]. The receiver architecture utilized an EAD with GO-CFAR processing to estimate the magnitude spectrum and provide a variable threshold for peak detection. To enable use of the GO-CFAR processing of the estimated magnitude spectrum, the results presented in [103] were modified through applying the central limit theorem based on the DFT and FFT being linear transforms. Due to the different permutations of valid SNS vectors that may exist if more than one frequency is present, the full range of \hat{M}_{SNS} was not able to be exploited. To determine the number of frequencies that the receiver could identify unambiguously, a theorem applicable to a RNS was modified and applied to the SNS. Monte Carlo simulations were then performed for two separate NYFR-B receiver architectures to develop the performance curves.

The restriction of f_{max} to allow the unambiguous determination of multiple frequencies using the SNS reduces the overall advantage gained since the full dynamic range of the L -sequence SNS is not available. Also, the increase in the hardware requirements are significant for a modest increase in the number of frequency tones the receiver could detect. To allow use of the full dynamic range of the SNS, a means of resolving the ambiguities that result from the permutations of the symmetrical residues is required. One potential avenue that could resolve

this ambiguity issue is to determine the Nyquist zone of the signals through modulating one of the NYFR-B channels as described in Section 2.2.7. Further research is required in this area.

THIS PAGE INTENTIONALLY LEFT BLANK

CHAPTER 8:

Concluding Remarks

To effectively counter threat emitters, an EW receiver must accurately determine the emitter's location and the signal's frequency components. Due to the continued evolution of threat emitters that have adopted complex modulations schemes and low-probability-of-intercept techniques, EW receivers are required to obtain these parameters while monitoring an expanding BW which can exceed 20 GHz. Emerging wideband technologies such as CS and photonics demonstrate great potential for use in wideband EW receiver systems. Symmetrical number systems have also been employed in various EW receiver applications such as frequency ambiguity resolution due to undersampling and minimizing DF antenna array sizes. In this dissertation, symmetrical number systems were employed with photonics and CS to address the emerging requirements of EW receivers to monitor wider BWs as threat emitters evolve.

One of the most powerful symmetrical number systems is the RSNS due to its inherent integer Gray code property that can be used to identify and correct coding errors. However, unlike other symmetrical number systems or residue number systems, there is not a general closed-form analytical expression for \hat{M}_{RSNS} , and closed-form expressions exist for only a few specific cases. In Chapter 4, an efficient search algorithm was presented for determining \hat{M}_{RSNS} and its computational complexity was examined. The efficient algorithm was then applied to generate data for different families of moduli sets. Curve fitting algorithms contained in MATLAB's curve fitting tool box were then applied to the data to develop polynomial expressions for \hat{M}_{RSNS} for three sequence and four sequence RSNSs. The polynomial expressions for \hat{M}_{RSNS} were verified to satisfy the solutions to the congruence equations defining the ambiguity locations. Previously published work contains only two specific cases for which closed-form expressions for \hat{M}_{RSNS} exist, Equation (3.21) and Equation (3.22). Chapter 4 presented closed-form expressions for four additional moduli families for a three-sequence RSNSs. Also, closed-form expressions for five different families of moduli sets for four-sequence RSNSs were developed and presented. These are the only identified closed-form solutions for \hat{M}_{RSNS} that have been developed for four-sequence RSNSs. Future work in this area encompasses identifying additional specific closed-form expressions for \hat{M}_{RSNS} for different families of moduli sets focused upon identifying a general closed-form expression for the \hat{M}_{RSNS} for a general set of N coprime moduli.

In Chapter 5, it was demonstrated theoretically and verified through simulations and experi-

mentation that a DE-MZM can be used to perform phase interferometry. Using DE-MZMs, a linear four-element photonic DF antenna array with RSNS preprocessing was designed, and its performance was examined through simulations and experimental testing. It was demonstrated that the photonic DF array provided accurate DOA estimation with fine angular resolution while maintaining a small array size. The simulations and experimental testing was performed for a narrow band CW signal at 2.4 GHz. Simulations were also performed in MATLAB to demonstrate the signal processing required to determine the DOA of more than one pulsed sinusoidal signal. The results contained in Chapter 5 successfully demonstrate photonic DF array with RSNS preprocessing concept which warrants future investigation and development for future use in EW receiver systems. Future work to further develop and mature the application of this concept include anechoic chamber testing using narrow band components, and modification of the circuit to use wideband components followed by bench testing and anechoic chamber testing. Experimental testing with multiple pulsed emitters is also required. Also, integration of the photonic DF array with RSNS preprocessing with a wide band CS receiver such as the NYFR and further development of pulse sorting signal processing algorithms provide avenues for future research.

The use of the SNS was examined in CS receivers to take advantage of the relationship between the SNS and the DFT [51]. In Chapter 6, a SNS-CS cueing receiver was investigated. The SNS-CS cueing receiver forms the measurement vector by collating the samples obtained using coprime sampling rates equal to the SNS moduli. The sensing matrix was formed by deterministically retaining the rows of a unitary DFT matrix that most closely correspond to the sample times. The SpaRSA algorithm was applied to estimate the frequency spectrum of the signal from which the frequency tones composing the signal were identified. The performance of the SNS-CS cueing receiver was examined through Monte Carlo simulations and the results were compared to those obtained when a random orthonormal sensing matrix was used. The results demonstrated that the SNS-CS cueing receiver was capable of accurately resolving the number of frequencies predicted by CS theory and was comparable to that of random sensing techniques. Future work includes determining the SNS-CS cueing receiver's performance when using greedy recovery algorithms such as OMP, and hardware implementation.

In Chapter 7, a multi-channel NYFR architecture using deterministic coprime sampling based on the moduli of a SNS was examined. Using a NYFR architecture enabled the use of a common radix FFT to calculate the residues in each channel instead of different radix DFTs in each channel. The constant sampling rates also allowed for a simpler implementation of the

sampling process when compared to the conventional NYFR architecture that uses a modulated RF sampling clock. The SNS residues, aliased frequencies, were identified in each channel by adapting a EAD with GO-CFAR processing for use in the frequency domain to allow an adaptive threshold to be applied to compensate for a colored noise spectrum, band limited barrage noise jamming, or a noise distribution that is not wide sense stationary. From the residues, the actual transmitted frequencies were identified by leveraging the folding properties of the receiver to identify the common frequency to which each aliased frequency unfolds. Due to the possibility that permutations of the residues could represent more than one valid SNS code, the full dynamic range of the SNS could not be exercised and a smaller dynamic range based on applying Equation (7.12) and Equation (7.13) to the SNS was used. Monte Carlo simulations were conducted and performance curves were presented for a four-channel and six-channel NYFR-B receiver architecture. Future research in this area includes examining methods that can be employed to allow taking advantage of the entire bandwidth provided by the \hat{M}_{SNS} of all moduli used. By doing so, the number of channels required to identify multiple signals can be reduced significantly. One potential method is to apply a modulation to one of the channels of the NYFR to isolate the Nyquist zone that each sinusoid resides to allow resolution of each signals frequency and eliminate permutations of the residues that are correspond to frequencies outside of the identified Nyquist zone. Simulations and hardware testing can also be accomplished to further develop this CS receiver concept.

THIS PAGE INTENTIONALLY LEFT BLANK

List of References

- [1] C. L. Davies and P. Hollands, “Automatic processing for ESM,” *Communications, Radar and Signal Processing, IEE Proc. F*, vol. 129, pp. 164–171, Jun. 1982.
- [2] “Navy.mil - view image.” [Online]. Available: <http://www.navy.mil/viewGallery.asp>
- [3] C. E. Shannon, “Communication in the presence of noise,” *Proceedings of the IRE*, vol. 37, pp. 10–21, Jan. 1949.
- [4] R. H. Walden, “Analog-to-digital converter survey and analysis,” *IEEE J. Sel. Areas Commun.*, vol. 17, pp. 539–550, Apr. 1999.
- [5] ———, “Performance trends for analog to digital converters,” *IEEE Commun. Mag.*, vol. 37, pp. 96–101, Feb. 1999.
- [6] B. Murmann, “A/D converter trends: Power dissipation, scaling and digitally assisted architectures,” *Proc. IEEE Custom Integrated Circuits Conf.*, pp. 105–112, 2008.
- [7] B. Jonsson, “A survey of A/D-converter performance evolution,” *Proc. 17th IEEE Int. Conf. Electronics, Circuits, and Systems (ICECS '10)*, pp. 766–769, Dec. 2010.
- [8] B. L. Luke and P. E. Pace, “N-sequence RSNS ambiguity analysis,” *IEEE Trans. Inf. Theory*, vol. 53, pp. 1759–1766, May 2007.
- [9] J. Capmany, B. Ortega, and D. Pastor, “A tutorial on microwave photonic filters,” *J. Lightw. Technol.*, vol. 24, pp. 201–229, Jan. 2006.
- [10] S. J. Wright, R. D. Nowak, and M. A. T. Figueiredo, “Sparse reconstruction by separable approximation,” *Proc. IEEE Int. Conf. Acoustics, Speech and Signal Processing*, pp. 3373–3376, 2008.
- [11] Y. C. Eldar and E. G. Kutyniok, *Compressed Sensing: Theory and Applications*. New York: Cambridge University Press, 2012.
- [12] H. Chen, N. Xi, B. Song, L. Chen, J. Zhao, K. W. C. Lai, and R. Yang, “Infrared camera using a single nano-photodetector,” *IEEE Sensors J.*, vol. 13, no. 3, pp. 949–958, Mar. 2013.

- [13] M. F. Duarte, M. A. Davenport, D. Takhar, J. N. Laska, S. Ting, K. F. Kelly, and R. G. Baraniuk, "Single-pixel imaging via compressive sampling," *IEEE Signal Process. Mag.*, vol. 25, pp. 83–91, Mar. 2008.
- [14] M. Lustig, D. Donoho, and J. M. Pauly, "Sparse MRI: The application of compressed sensing for rapid MR imaging," *Magnetic resonance in medicine*, vol. 58, pp. 1182–1195, Dec. 2007.
- [15] J. Provost and F. Lesage, "The application of compressed sensing for photo-acoustic tomography," *IEEE Trans. Med. Imag.*, vol. 28, pp. 585–594, Apr. 2009.
- [16] A. Budillon, A. Evangelista, and G. Schirinzi, "Three-dimensional SAR focusing from multipass signals using compressive sampling," *IEEE Trans. Geosci. Remote Sens.*, vol. 49, pp. 488–499, Jan. 2011.
- [17] X. X. Zhu and R. Bamler, "Super-resolution power and robustness of compressive sensing for spectral estimation with application to spaceborne tomographic SAR," *IEEE Trans. Geosci. Remote Sens.*, vol. 50, pp. 247–258, Jan. 2012.
- [18] R. Maleh, G. L. Fudge, F. A. Boyle, and P. E. Pace, "Analog-to-information and the Nyquist folding receiver," *IEEE J. Emerging Select. Topics Circuits Syst.*, vol. 2, pp. 564–578, Sep. 2012.
- [19] M. Mishali, Y. C. Eldar, O. Dounaevsky, and E. Shoshan, "Xampling: Analog to digital at sub-nyquist rates," *IET Circuits, Devices & Syst.*, vol. 5, no. 1, pp. 8–20, 2011.
- [20] W. U. Bajwa, J. Haupt, A. M. Sayeed, and R. Nowak, "Compressed channel sensing: A new approach to estimating sparse multipath channels," *Proceedings of the IEEE*, vol. 98, pp. 1058–1076, Jun. 2010.
- [21] J. Meng, W. Yin, Y. Li, N. T. Nguyen, and Z. Han, "Compressive sensing based high-resolution channel estimation for OFDM System," *IEEE J. Sel. Topics Signal Process.*, vol. 6, pp. 15–25, Feb. 2012.
- [22] M. A. Herman and T. Strohmer, "High-resolution radar via compressed sensing," *IEEE Trans. Signal Process.*, vol. 57, pp. 2275–2284, Jun. 2009.
- [23] V. M. Patel, G. R. Easley, D. M. Healy Jr., and R. Chellappa, "Compressed synthetic aperture radar," *IEEE J. Sel. Topics Signal Process.*, vol. 4, pp. 244–254, Apr. 2010.

- [24] E. J. Candes and M. B. Wakin, “An introduction to compressive sampling,” *IEEE Signal Processing Mag.*, vol. 25, pp. 21–30, Mar. 2008.
- [25] R. G. Baraniuk, “Compressive sensing [lecture notes],” *IEEE Signal Process. Mag.*, vol. 24, pp. 118–121, Jul. 2007.
- [26] K. H. Rosen, *Discrete Mathematics and Its Applications, 4th Edition*. Boston: WCB McGraw-Hill, 1999.
- [27] D. L. Donoho, “Compressed sensing,” *IEEE Trans. Inf. Theory*, vol. 52, pp. 1289–1306, Apr. 2006.
- [28] R. Tibshirani, “Regression shrinkage and selection via LASSO,” *J. R. Statist. Soc. B*, vol. 58, no. 1, pp. 267–288, 1996.
- [29] S. S. Chen, D. L. Donoho, and M. A. Saunders, “Atomic decomposition by basis pursuit,” *SIAM J. Scientific Computing*, vol. 20, no. 1, pp. 33–61, 1998.
- [30] —, “Atomic decomposition by basis pursuit,” *SIAM Review*, vol. 43, no. 1, pp. 129–159, 2001. [Online]. Available: <http://epubs.siam.org/doi/abs/10.1137/S003614450037906X>
- [31] J. A. Tropp, “Greed is good: Algorithmic results for sparse approximation,” *IEEE Trans. Inf. Theory*, vol. 50, pp. 2231–2242, Oct. 2004.
- [32] J. A. Tropp and A. C. Gilbert, “Signal recovery from random measurements via orthogonal matching pursuit,” *IEEE Trans. Inf. Theory*, vol. 53, pp. 4655–4666, Dec. 2007.
- [33] M. A. T. Figueiredo, R. D. Nowak, and S. J. Wright, “Gradient projection for sparse reconstruction: Application to compressed sensing and other inverse problems,” *IEEE J. Sel. Topics in Signal Process.*, vol. 1, pp. 586–597, Dec. 2007.
- [34] D. Needell and J. Tropp, “CoSaMP: Iterative signal recovery from incomplete and inaccurate samples,” *Applied and Computational Harmonic Analysis*, vol. 26, no. 3, pp. 301 – 321, 2009. [Online]. Available: <http://www.sciencedirect.com/science/article/pii/S1063520308000638>
- [35] R. Calderbank, S. Howard, and S. Jafarpour, “Construction of a large class of deterministic sensing matrices that satisfy a statistical isometry property,” *IEEE J. Sel. Topics Signal Process.*, vol. 4, pp. 358–374, Apr. 2010.

- [36] J. Haupt, L. Applebaum, and R. Nowak, "On the restricted isometry of deterministically subsampled Fourier matrices," *Proc. 44th Annu. Conf. Information Science and Systems*, pp. 1–6, Mar. 2010.
- [37] R. G. Baraniuk, V. Cevher, M. F. Duarte, and C. Hegde, "Model-based compressive sensing," *IEEE Trans. Inf. Theory*, vol. 56, pp. 1982–2001, Apr. 2010.
- [38] M. F. Duarte and Y. C. Eldar, "Structured compressed sensing: From theory to applications," *IEEE Trans. Signal Process.*, vol. 59, no. 9, pp. 4053–4085, 2011.
- [39] J. A. Tropp, M. B. Wakin, M. F. Duarte, D. Baron, and R. G. Baraniuk, "Random filters for compressive sampling and reconstruction," *Proc. IEEE Int. Conf. on Acoustics, Speech and Signal Processing*, vol. 3, pp. 872–875, 2006.
- [40] J. A. Tropp, J. N. Laska, M. F. Duarte, J. K. Romberg, and R. G. Baraniuk, "Beyond nyquist: Efficient sampling of sparse bandlimited signals," *IEEE Trans. Inf. Theory*, vol. 56, pp. 520–544, Jan. 2010.
- [41] J. P. Slavinsky, J. N. Laska, M. A. Davenport, and R. G. Baraniuk, "The compressive multiplexer for multi-channel compressive sensing," *Proc. IEEE Int. Conf. Acoustics, Speech and Signal Processing*, pp. 3980–3983, 2011.
- [42] G. L. Fudge, R. E. Bland, M. A. Chivers, S. Ravindran, J. Haupt, and P. E. Pace, "A Nyquist folding analog-to-information receiver," *Conf. Rec. 42nd Asilomar Conf. on Signals, Systems and Computers*, pp. 541–545, 2008.
- [43] P. E. Pace, A. Kusmanoff, and G. L. Fudge, "Nyquist folding analog-to-information receiver: Autonomous information recovery using quadrature mirror filtering," *Conf. Rec. 43rd Asilomar Conf. Signals, Systems. and Computers*, pp. 1581–1585, 2009.
- [44] K. W. Forsythe, J. I. Goodman, M. R. Green, B. A. Miller, G. M. Raz, and J. H. Jackson, MIT Lincoln Laboratory, Tech. Rep. PR-A21- 1, Oct. 2007.
- [45] A. Harms, W. U. Bajwa, and R. Calderbank, "A constrained random demodulator for sub-nyquist sampling," *IEEE Trans. Signal Process.*, vol. 61, pp. 707–723, Feb. 2013.
- [46] J. Laska, S. Kirolos, Y. Massoud, R. Baraniuk, A. Gilbert, M. Iwen, and M. Strauss, "Random sampling for analog-to-information conversion of wideband signals," *IEEE*

Dallas/CAS Workshop on Design, Application, Integration and Software (DCAS '06), pp. 119–122, Oct. 2006.

- [47] A. Ahmed and J. Romberg, “Compressive multiplexers for correlated signals,” *Conf. Rec. 46th Asilomar Conf. Signals, Systems and Computers*, pp. 963–967, 2012.
- [48] M. Mishali and Y. C. Eldar, “From theory to practice: Sub-nyquist sampling of sparse wideband analog signals,” *IEEE J. Sel. Topics Signal Process.*, vol. 4, pp. 375–391, Apr. 2010.
- [49] X. Kong, P. Petre, R. Matic, A. C. Gilbert, and M. J. Strauss, “An analog-to-information converter for wideband signals using a time encoding machine,” *IEEE Digital Signal Processing Workshop and IEEE Signal Processing Education Workshop*, pp. 414–419, 2011.
- [50] X. Kong, R. Matic, Z. Xu, V. Kukshya, P. Petre, and J. Jensen, “A time-encoding machine based high-speed analog-to-digital converter,” *IEEE J. Emerging and Select. Topics in Circuits and Syst.*, vol. 2, no. 3, pp. 552–563, Sep. 2012.
- [51] P. E. Pace, R. E. Leino, and D. Styer, “Use of the symmetrical number system in resolving single-frequency undersampling aliases,” *IEEE Trans. Signal Process.*, vol. 45, pp. 1153–1160, May 1997.
- [52] P. E. Pace and D. D. Styer, “High-resolution encoding process for an integrated optical analog-to-digital converter,” *Opt. Eng.*, vol. 33, pp. 2638–2645, Aug. 1994. [Online]. Available: <http://dx.doi.org/10.1117/12.173559>
- [53] P. Pace, J. L. Schafer, and D. Styer, “Optimum analog preprocessing for folding ADCs,” *IEEE Trans. Circuits Syst. II*, vol. 42, pp. 825–829, Dec. 1995.
- [54] D. Styer and P. E. Pace, “Two-channel RSNS dynamic range,” *IEEE Trans. Circuits Syst. I*, vol. 49, pp. 395–397, Mar. 2002.
- [55] B. L. Luke and P. E. Pace, “N-sequence RSNS redundancy analysis,” *Proc. IEEE Int. Symp. Information Theory*, pp. 2744–2748, 2006.
- [56] —, “Computation of the robust symmetrical number system dynamic range,” *Proc. IEEE Information Theory Workshop*, pp. 1–5, 2010.

- [57] P. E. Pace, D. Wickersham, D. C. Jenn, and N. S. York, "High-resolution phase sampled interferometry using symmetrical number systems," *IEEE Trans. Antennas Propag.*, vol. 49, pp. 1411–1423, Oct. 2001.
- [58] M. R. Arvizo, J. Calusdian, K. B. Hollinger, and P. E. Pace, "Robust symmetrical number system preprocessing for minimizing encoding errors in photonic analog-to-digital converters," *Optical Engineering*, vol. 50, pp. 084 602–1–084 602–11, Aug. 2011.
- [59] A. P. Hiltgen, K. G. Paterson, and M. Brandestini, "Single-track gray codes," *IEEE Trans. Inf. Theory*, pp. 1555–1561, May 1996.
- [60] B. L. Luke, "Architecture of an integrated microelectronic warfare system on a chip and design of key components," Ph.D. dissertation, Naval Postgraduate School, 2004.
- [61] D.-M. Pham, A. Premkumar, and A. S. Madhukumar, "Efficient sample rate conversion in software radio employing folding number system," *Proc. IEEE Int. Conf. Communications*, pp. 1–5, 2009.
- [62] P. E. Pace, D. Styer, and I. A. Akin, "A folding ADC preprocessing architecture employing a robust symmetrical number system with gray-code properties," *IEEE Trans. Circuits Syst. II*, vol. 47, pp. 462–467, May 2000.
- [63] I.-H. Wang and S.-I. Liu, "A CMOS 5-bit 5GSample/sec analog-to-digital converter in 0.13 μm CMOS," *J. Semiconductor Technol. and Sci.*, pp. 28–35, Mar. 2007.
- [64] M. Wicht, M. Schott, and P. E. Pace, "Increasing the flux measurement range of an RF-SQUID resonant detection circuit using the robust symmetrical number system," *IEEE Trans. Appl. Supercond.*, vol. 23, pp. 1 602 910–1 602 910, Feb. 2013.
- [65] D.-M. Pham, A. B. Premkumar, and A. S. Madhukumar, "Error detection and correction in communication channels using inverse Gray RSNS codes," *IEEE Trans. Commun.*, vol. 59, pp. 975–986, Apr. 2011.
- [66] Y. Jakop, A. S. Madhukumar, and A. B. Premkumar, "A robust symmetrical number system based parallel communication system with inherent error detection and correction," *IEEE Trans. Wireless Commun.*, vol. 8, pp. 2742–2747, Jun. 2009.
- [67] N. Paepolshiri, P. E. Pace, and D. C. Jenn, "Extending the unambiguous range of polyphase P4 CW radar using the robust symmetrical number system," *IET Radar, Sonar & Navigation*, vol. 6, pp. 659–667, Jul. 2012.

- [68] P. E. Pace, P. Stănică, B. L. Luke, and T. W. Tedesso, "Extended closed-form expressions for the robust symmetrical number system dynamic range and an efficient algorithm for its computation," *IEEE Trans. Inf. Theory*, accepted for publication.
- [69] H. Dubner, "Factorial and primorial primes," *J. Rec. Math.*, pp. 197–203, 1987.
- [70] M. Abramowitz and E. I. A. Stegun, *Handbook of Mathematical Functions with Formulas, Graphs, and Mathematical Tables*, 9th ed. New York: Dover Publications, INC., 1965.
- [71] P. Hajiani, H. Habibi, M. Hakkak, and F. Mazlumi, "Accuracy in wideband direction of arrival system," *Proc. 4th IEEE Int. Symp. Electromagnetics Compatibility*, pp. 394–397, 2007.
- [72] J. S. Lim, C.-G. Jung, and G. S. Chae, "A design of precision RF direction finding device using circular interferometer," *Proc. IEEE Int. Symp. Intelligent Signal Processing and Communication Systems*, pp. 713–716, 2004.
- [73] R. Shar, "Simulation of polarizer impact on circular interferometer performance," *Proc. 11th IEEE Computer Society Int. Conf. Computational Science and Engineering*, pp. 334–339, 2008.
- [74] X. Yang and C. Zhang-Zhong, "Two-dimensional circular array real-time phase interferometer algorithm and its correction," *Proc. 2nd IEEE Computer Society Int. Congr. Image and Signal Processing*, pp. 1–5, 2009.
- [75] C. Brinegar, "Passive direction finding: combining amplitude and phase based methods," *Proc. IEEE National Aerospace and Electronics Conf.*, pp. 78–84, 2000.
- [76] C. J. Tarran, "Operational HF DF systems employing real time superresolution processing," *Proc. 7th Int. Conf. HF Radio Systems and Techniques, (Conf. Publ. No. 441)*, pp. 311–319, 1997.
- [77] R. L. Johnson and G. E. Miner, "Comparison of superresolution algorithms for radio direction finding," *IEEE Trans. Aerosp. Electron. Syst.*, vol. AES-22, pp. 432–442, Apr. 1986.
- [78] A. Ferreol and M. Chenu-Tournier, "Space-frequency direction finding in wideband and multi-path contexts," *Proc. IEEE Int. Conf. Acoustics, Speech, and Signal Processing*, vol. 5, pp. 3113–3116, 2000.

- [79] M. Hajian, C. Coman, and L. P. Ligthart, "Comparison of circular, uniform and non-uniform Y-shaped array antenna for DOA estimation using MUSIC algorithm," *Proc. 9th European Conf. Wireless Technology*, pp. 143–146, 2006.
- [80] J. G. Worms, "RF direction finding with a reduced number of receivers by sequential sampling," *Proc. IEEE Int. Conf. Phased Array Systems and Technology*, pp. 165–168, 2000.
- [81] P. D. Biernacki, R. Madara, L. T. Nichols, A. Ward, and P. J. Mathews, "A four channel angle of arrival detector using optical downconversion," *IEEE MTT-S Int. Microwave Symp. Dig.*, vol. 3, pp. 885–888, 1999.
- [82] H. L. Levitt, E. M. Alexander, A. Y. Tse, and A. E. Spezio, "Superresolution precision direction-finding techniques and measurements," *Proc. SPIE 2489, Transition of Optical Processors into Systems*, vol. 2489, pp. 95–106, 1995.
- [83] X. Zou, W. Li, W. Pan, B. Luo, L. Yan, and J. Yao, "Photonic approach to the measurement of time-difference-of-arrival and angle-of-arrival of a microwave signal," *Opt. Lett.*, vol. 37, pp. 755–757, Feb. 2012.
- [84] B. Vidal, M. A. Piqueras, and J. Marti, "Direction-of-arrival estimation of broadband microwave signals in phased-array antennas using photonic techniques," *J. Lightw. Technol.*, vol. 24, pp. 2741–2745, Jul. 2006.
- [85] J. P. Yao, "A tutorial on microwave photonics - Part I," *IEEE Photon. Soc. Newsletter*, vol. 26, pp. 4–12, Apr. 2012.
- [86] R. Becker, "Broad-band guided-wave electrooptic modulators," *IEEE J. Quantum Electron.*, vol. 20, pp. 723 – 727, Jul. 1984.
- [87] B. Hraimel, M. O. Twati, and K. Wu, "Closed-form dynamic range expression of dual-electrode mach-zehnder modulator in radio-over-fiber WDM system," *J. Lightw. Technol.*, vol. 24, pp. 2380–2387, Jun. 2006.
- [88] H. W. Lim, "FPGA implementation of robust symmetrical number system in high-speed folding analog-to-digital converters," Master's thesis, Naval Postgraduate School, 2010.
- [89] H. E. Hassan, "A new algorithm for radar emitter recognition," *Proc. 3rd Int. Symp. Image and Signal Processing and Analysis*, vol. 2, pp. 1097–1101, 2003.

- [90] ———, “Joint deinterleaving/recognition of radar pulses,” *Proc. Int. Radar Conf.*, pp. 177–181, 2003.
- [91] A. W. Ata’a and S. N. Abdullah, “Deinterleaving of radar signals and PRF identification algorithms,” *IET Radar, Sonar Navig.*, vol. 1, pp. 340–347, Oct. 2007.
- [92] P. S. Ray, “A novel pulse TOA analysis technique for radar identification,” *IEEE Trans. Aerosp. Electron. Syst.*, vol. 34, pp. 716–721, Jul. 1998.
- [93] H. J. Liu, Z. Liu, W.-L. Jiang, and Y.-Y. Zhou, “Incremental learning approach based on vector neural network for emitter identification,” *IET Signal Process.*, vol. 4, no. 1, pp. 45–54, 2010.
- [94] H.-J. Liu, Z. Liu, W.-L. Jiang, and Y.-Y. Zhou, “Approach based on combination of vector neural networks for emitter identification,” *IET Signal Process.*, vol. 4, no. 2, pp. 137–148, 2010.
- [95] J. A. Anderson, M. T. Gately, P. A. Penz, and D. R. Collins, “Radar signal categorization using a neural network,” *Proceedings of the IEEE*, vol. 78, pp. 1646–1657, Oct. 1990.
- [96] X. Chen and W. D. Hu, “Approach based on interval type-2 fuzzy logic system for emitter identification,” *Electronics Letters*, vol. 48, no. 18, pp. 1156–1158, Aug. 2012.
- [97] C.-S. Shieh and C.-T. Lin, “A vector neural network for emitter identification,” *IEEE Trans. Antennas Prop.*, vol. 50, pp. 1120–1127, Aug. 2002.
- [98] X. Li, H. Liang, and X.-G. Xia, “A robust chinese remainder theorem with its applications in frequency estimation from undersampled waveforms,” *IEEE Trans. Signal Process.*, vol. 57, pp. 4314–4322, Nov. 2009.
- [99] X. G. Xia, “An efficient frequency-determination algorithm from multiple undersampled waveforms,” *IEEE Signal Process. Ltrs.*, vol. 7, pp. 34–37, Feb. 2000.
- [100] X.-G. Xia, “On estimation of multiple frequencies in undersampled complex valued waveforms,” *IEEE Trans. Signal Process.*, vol. 47, pp. 3417–3419, Dec. 1999.
- [101] H. Sun, D. I. Laurenson, and J. S. Thompson, “Cooperative compressive spectrum sensing by sub-nyquist sampling,” *Proc. 1st UK-India Int. Workshop Cognitive Wireless Systems*, pp. 1–5, 2009.

- [102] P. P. Vaidyanathan and P. Pal, “Sparse sensing with co-prime samplers and arrays,” *IEEE Trans. Signal Process.*, vol. 59, pp. 573–586, Feb. 2011.
- [103] P. E. Pace and L. L. Taylor, “False alarm analysis of the envelope detection GO-CFAR processor,” *IEEE Trans. Aerosp. Electron. Syst.*, vol. 30, pp. 848–864, Jul. 1994.

Initial Distribution List

1. Defense Technical Information Center
Ft. Belvoir, Virginia
2. Dudley Knox Library
Naval Postgraduate School
Monterey, California